Dielectric Coatings for High Voltage Gas Insulated Switchgear

van der Born, Dennis

DOI
10.4233/uuid:4f1b06bc-3d01-4107-8c85-21c0e278c4bd

Publication date
2017

Document Version
Final published version

Citation (APA)
van der Born, D. (2017). *Dielectric Coatings for High Voltage Gas Insulated Switchgear*. [Dissertation (TU Delft), Delft University of Technology]. https://doi.org/10.4233/uuid:4f1b06bc-3d01-4107-8c85-21c0e278c4bd

Dielectric Coatings for High Voltage Gas Insulated Switchgear

DENNIS VAN DER BORN

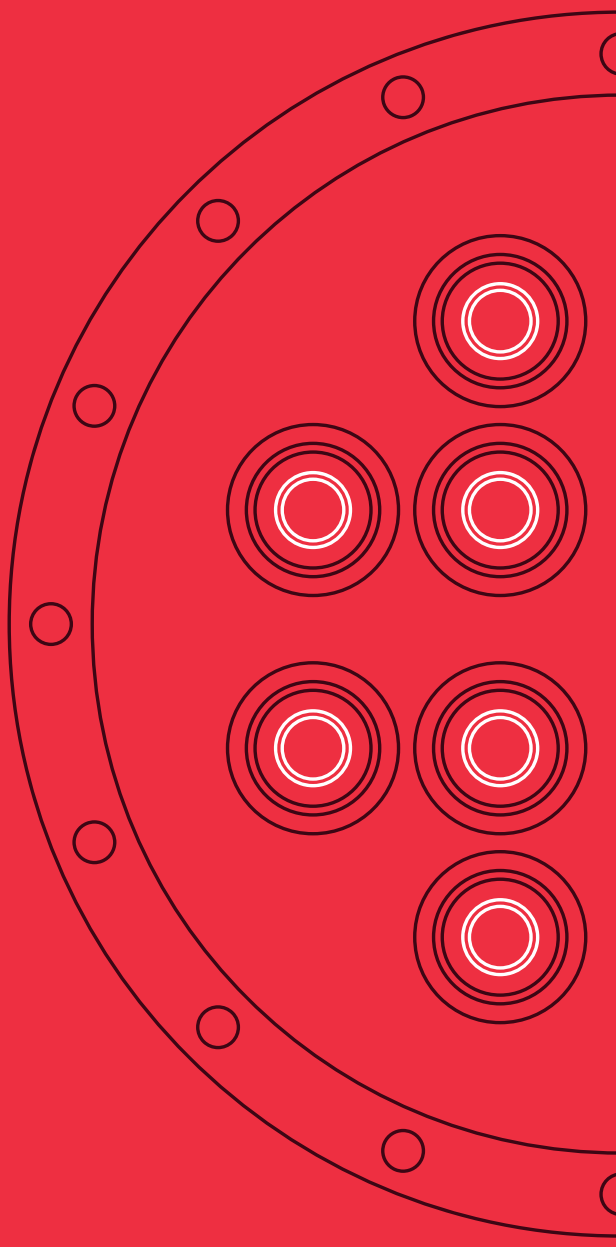

Dielectric Coatings for High Voltage Gas Insulated Switchgear

Dennis van der Born

This research was financially supported by GE Grid Solutions
(Villeurbanne, France)

The cover page was designed by: Optima Grafische Communicatie – *ogc.nl*
Layout and Printing: Ridderprint BV – *www.ridderprint.nl*

ISBN 978-94-6299-576-5
An electronic version of this dissertation is available at *http://repository.tudelft.nl/*

Dielectric Coatings for High Voltage Gas Insulated Switchgear

PROEFSCHRIFT

ter verkrijging van de graad van doctor
aan de Technische Universiteit Delft,
op gezag van de Rector Magnificus prof. ir. K.C.A.M. Luyben,
voorzitter van het College voor Promoties,
in het openbaar te verdedigen op 11 april 2017 om 15:00 uur
door

Dennis VAN DER BORN
elektrotechnisch ingenieur
geboren te Alphen aan den Rijn, Nederland

Dit proefschrift is goedgekeurd door de promotor:
Promotor: Prof. dr. J.J. Smit

Samenstelling promotiecommissie:
Rector Magnificus, voorzitter
Prof. dr. J.J. Smit, Technische Universiteit Delft, promotor
Onafhankelijke leden:
Prof. dr. A. Beroual, École Centrale de Lyon, France
Prof. dr. M. Haddad, Cardiff University, United Kingdom
Prof. dr. P. Palensky, Technische Universiteit Delft
Prof. dr. ir. P. Bauer, Technische Universiteit Delft
Prof. dr. R. Ross, Technische Universiteit Delft / TenneT TSO B.V., Arnhem
Dr. Y. Kieffel, General Electric, Aix les Bains, France

To my parents, brothers and my friends,
who inspired and encouraged me

Summary

In the 1960's, gas insulated switchgear (GIS), gas insulated busbar (GIB) and other gas insulated substation components were developed to overcome several disadvantages of air insulated substations. Gas insulated substations, although more expensive than the air insulated counterparts, are almost insusceptible to atmospheric conditions such as precipitation, pollution and ice formation. Moreover, the surface area of gas insulated substations is significantly smaller than that of air insulated substations at the same voltage level and power rating. The direct influence of gas insulated substations on the environment is also small compared to air insulated substations because of the lack of corona and thus audible noise and radio frequency interference, especially in wet weather conditions.

From the above mentioned advantages it seems that gas insulated substations are advantageous with respect to air insulated substations. However, the main disadvantage, next to the construction costs, is the fact that almost all GIS is filled with sulphur hexafluoride (SF_6) as an insulation gas, which has a very high global warming potential of roughly 23,000 times that of CO_2. The global warming potential of SF_6 has resulted in strict governmental regulations on the usage and storage of SF_6. Therefore, the urge from the industry to replace SF_6 with a more environmentally friendly insulation gas has become very strong over the past years.

Unfortunately, most readily available and environmentally friendly insulation gases have a relatively low electrical breakdown strength, which would require the operating pressure or the dimensions of GIS to be significantly increased. Increasing the operating pressure or the dimensions of GIS would be unfeasible. Therefore, the main challenge in the field of GIS is to improve the electrical breakdown strength of GIS without increasing the size or raise the operating pressure above the current design limits.

The investigation into the improvement of the breakdown strength of GIS has taken two main paths. Firstly, ongoing research is being conducted to develop a new replacement gas which has a breakdown strength comparable to that of SF_6. This research has recently led to several replacement candidates. Secondly, research has shown that the

breakdown strength of GIS can also be improved by the introduction of a dielectric coating layer on the electrodes inside GIS. This thesis focusses on the improvement of the breakdown strength of GIS with the application of a coating layer.

In this thesis the lightning impulse breakdown voltage of gas-coating insulation systems is evaluated with the use of lightning impulse breakdown tests on a rod-plane electrode configuration. These tests include a wide variety of coating materials with a wide range of material properties and are mainly conducted in dry air as an insulating gas. Next to the breakdown tests, a range of material characterisation experiments are performed to obtain more information on the coating material structure and to find a relation between the coating material parameters and the breakdown strength of the gas-coating insulation system. The material characterisation experiments include dielectric spectroscopy, surface roughness measurements, conduction current measurements, electrical breakdown tests and optical microscopy.

The results of the above mentioned experiments have shown that a significant improvement of the lightning impulse breakdown voltage of GIS can be obtained with the application of a coating. The maximum obtained improvement is 34% for 1 cm thick coating layers and 15% for thin coating layers with a thickness smaller than 1 mm. Furthermore, a set of requirements has been determined, with respect to the coating material characteristics, which should be met to obtain an effective improvement of the lightning impulse breakdown strength of GIS. Another important observation is the fact that gas-coating insulation can in some cases exhibit temporary self-restoring and improving behaviour. In these special cases the breakdown voltage of a gas-coating insulation is not reduced to the level of an uncoated gas insulation after the first breakdown has occurred. The breakdown voltage is even higher with an increase in the number of breakdowns after the first breakdown.

Finally, four breakdown models were developed with which the 50% lightning impulse breakdown voltage of several GIS configurations can be predicted. These GIS configurations include both uncoated configurations and configurations coated with a coating layer of at least 1 cm thickness. The models are able to predict the breakdown voltage of GIS filled with dry air and SF_6. The verification of the breakdown models with lightning impulse breakdown tests has shown that the models have an inaccuracy ranging up to 6.3%, depending on the applied gas type, gas pressure and electrode configuration.

Samenvatting

In de Jaren '60 zijn gasgeïsoleerde schakelaars en spanningsrails ontwikkeld om verschillende nadelen van openlucht schakelstations weg te nemen. Hoewel gasgeïsoleerde schakelstations duurder zijn dan de openlucht varianten, zijn deze vrijwel ongevoelig voor atmosferische condities zoals neerslag, vervuiling en ijsvorming. Daarnaast is het benodigde grondoppervlak van een gasgeïsoleerd schakelstation relatief klein in vergelijking met openlucht schakelstations voor hetzelfde spanningsniveau en vermogen. De directe invloed van gasgeïsoleerde schakelstations op de omgeving is ook klein in vergelijking met openlucht schakelstations, in het bijzonder in natte weersomstandigheden, dankzij het ontbreken van corona, hoorbare ruis en radiofrequente interferentie.

Op basis van bovenstaande voordelen lijkt het dat gasgeïsoleerde schakelstations gunstig zijn ten opzichte van openlucht schakelstations. Echter, het grootste nadeel, naast de bouwkosten, is het feit dat bijna alle gasgeïsoleerde schakelaars gevuld zijn met zwavelhexafluoride (SF_6) als isolatiegas. Dit gas heeft een aardopwarmingsvermogen (GWP – Global Warming Potential) welke 23.000 maal groter is dan die van CO_2. Het aardopwarmingsvermogen van SF_6 heeft ertoe geleid dat strenge regels en richtlijnen zijn opgesteld inzake het gebruik en de opslag van SF_6. Daarom is de drang om SF_6 te vervangen door een milieuvriendelijker isolatiegas zeer sterk geworden in de afgelopen jaren.

Helaas hebben de meeste beschikbare milieuvriendelijke isolatiegassen een relatief lage elektrische doorslagsterkte, wat zou vereisen dat de gasdruk significant verhoogd wordt. Daarom is de belangrijkste uitdaging in dit vakgebied het vergroten van de doorslagsterkte van gasgeïsoleerde schakelaars zonder de afmetingen aanzienlijk te vergroten of de gasdruk te verhogen tot boven de ontwerplimiet.

Het onderzoek met betrekking tot de verbetering van de doorslagsterkte van gasgeïsoleerde schakelaars is twee hoofdwegen ingeslagen. Ten eerste wordt voortschrijdend onderzoek uitgevoerd voor het ontwikkelen van een nieuw vervangingsgas welke een met SF_6 vergelijkbare doorslagsterkte heeft. Dit onderzoek heeft recentelijk verschillende mogelijke vervangingsgassen opgeleverd. Ten tweede is uit onderzoek gebleken dat de

doorslagsterkte van gasgeïsoleerde schakelaars verbeterd kan worden door het aanbrengen van een diëlektrische coating op het oppervlak van de elektrodes. Dit proefschrift richt zich op de verbetering van de doorslagsterkte van gasgeïsoleerde schakelaars door middel van het toepassen van een 'coating'.

In dit proefschrift wordt de doorslagspanning van gas-coating isolatiesystemen geëvalueerd met behulp van bliksemstootspanningsproeven aan een staaf-plaat elektrodeconfiguratie. Deze proeven omvatten een reeks coatingmaterialen met een grote variatie in materiaaleigenschappen en worden uitgevoerd in droge lucht als isolatiegas. Naast de doorslagproeven wordt ook een scala aan materiaalproeven uitgevoerd teneinde meer informatie te verkrijgen omtrent de materiaalstructuur en om een correlatie te vinden tussen de materiaalparameters en de doorslagspanning van de gas-coatingisolatie. De materiaalproeven omvatten diëlektrische spectroscopie, oppervlakteruwheidsmetingen, lekstroommetingen, doorslagproeven en optische microscopie.

De resultaten van de hierboven genoemde experimenten hebben aangetoond dat een significante verbetering van de doorslagspanning van gasgeïsoleerde schakelaars kan worden behaald door het toepassen van een coating, in het geval van bliksemstootspanning. De grootst behaalde verbetering is 34% in het geval van 1 cm dikke coatings en 15% in het geval van dunne coatings met een dikte kleiner dan 1 mm. Daarnaast is er een lijst van voorwaarden opgesteld, met betrekking tot de materiaaleigenschappen van een coating, om een effectieve verbetering van de doorslagsterkte onder bliksemstootspanning van gasgeïsoleerde schakelaars te kunnen realiseren. Een andere belangrijke waarneming is het feit dat, in een aantal gevallen, gas-coating isolatiesystemen zelfherstellend en zelfs verbeterd doorslaggedrag laten zien. In deze bijzondere gevallen is de doorslagspanning niet verminderd tot het niveau van een ongecoat isolatiesysteem na het optreden van de eerste doorslag. De doorslagspanning neemt zelfs toe met een toename van het aantal doorslagen.

Verder zijn er een viertal doorslagmodellen ontwikkeld waarmee de 50% doorslagspanning van een aantal gasgeïsoleerde configuraties voorspeld kan worden, in het geval van bliksemstootspanning. Deze configuraties betreffen zowel ongecoate systemen als systemen met een coating van tenminste 1 cm dikte. De modellen kunnen de doorslagsterkte voorspellen van gasgeïsoleerde schakelaars gevuld met SF_6 of droge lucht. De verificatie van de modellen met bliksemspanningsproeven heeft laten zien dat de onnauwkeurigheid van de modellen kleiner of gelijk is aan 6.3%, afhankelijk van de gassoort en de elektrodeconfiguratie.

TABLE OF CONTENTS

1

Introduction

1.1 GAS INSULATED SUBSTATIONS

Gas insulated substations are in use in built-up areas due to fact that the required surface area is relatively small compared to open air substations, which require a relatively large amount of surface area. Further advantages of gas insulated substations compared to air insulated substations are the relative insusceptibility with respect to atmospheric conditions (e.g. wind, precipitation and ice formation) and the possibility of incorporating a substation inside an office building or construction of a substation underground. The main disadvantage of gas insulated substations is the construction and operating costs which are significantly higher than that of open air substations. Therefore, a trade-off is made between construction costs, the available surface area and the corresponding land prices.

In metropolitan regions the available surface area is very small and the power consumption is continuously increasing, as is the case in other regions. Therefore it is necessary to increase the system voltage to limit the increase in losses which coincide with the increase in power consumption. To accommodate a higher system voltage, the gas insulated switchgear (GIS) in the gas insulated substation should be upgraded, which can be difficult due to the limited space available.

Next to the increase in power consumption, the size constraints of gas insulated substations are becoming more strict. Less land area is available for construction of new substations due to the increase in the population density. Therefore, the development of GIS with smaller dimensions is favourable. The desired reduction of GIS dimensions and the desired increase in system voltage are conflicting. The solution of this conflict should be found in the improvement of the breakdown strength of GIS without significantly increasing the size of GIS.

1.2 REPLACEMENT OF SF_6 AS AN INSULATION GAS

In GIS the most commonly used insulation gas is sulphur hexafluoride (SF_6). The reason why this gas is so often used can be found in the electrical and thermal properties. Firstly, the electrical breakdown strength is relatively high due the strong electronegativity of the gas. Secondly, the arc extinguishing and cooling properties are good compared to other insulation gases. Next to the favourable electrical and thermal properties, the gas is also non-toxic, is not ozone depleting and has a relatively low boiling point compared to other electronegative gases.

Unfortunately, SF_6 also has some disadvantages. Firstly, the gas has a Global Warming Potential (GWP) which is 23,000 times higher than that of CO_2 [1]. Because of this, the legal regulations on emission of SF_6 are now very strict. Users of SF_6, such as grid operators and high voltage laboratories, are obligated to keep a detailed record of the amount of SF_6 in storage. Secondly, the gas is dissociated into harmful by-products during arcing. These by-products can damage spacers and can be toxic. Thirdly, the production costs are relatively high and the disposal and handling costs are high due to the above mentioned regulations.

Therefore, it is favourable to replace SF_6 with an alternative gas which is environmentally friendly and relatively inexpensive. Unfortunately, most readily available environmentally friendly alternatives, such as dry air, CO_2 or N_2, also show a relatively low breakdown strength.

1.3 IMPROVEMENT OF THE BREAKDOWN STRENGTH OF GIS

In sections 1.1 and 1.2 it was explained that it is favourable to increase the breakdown strength of GIS because of the desired size reduction, system voltage increase or replacement of SF_6 as an insulation gas. Currently, the latter is the strongest factor in the desire of an improved GIS.

The breakdown strength of GIS filled with an alternative gas could be improved with two methods. Firstly, an alternative gas can be developed which is environmentally friendly and has a breakdown strength comparable to that of SF_6. Research related to the development of such a gas has recently delivered suitable replacement candidates such as G^3 gas developed by Alstom [2] and C5 FK gas developed by ABB [3]. G^3 gas consists of CO_2 gas mixed with 3M Novec 4710, which is a fluoronitrile and C5 FK gas consists of dry air mixed with 3M Novec 5110, which is a fluoroketone.

This thesis does not cover the development of a replacement gas. Instead, the focus is on inexpensive and readily available gases such as dry air or N_2. The second method to improve the breakdown strength of GIS, while using such an environmentally friendly but

weak insulation gas, is the application of a dielectric coating on parts of the electrodes inside GIS. Prior research has shown that the application of a dielectric coating on (parts of) the electrode surfaces inside GIS can lead to a significant increase in the breakdown strength of GIS [4]–[26].

1.4 CHALLENGES IN THE FIELD OF GAS-COATING INSULATION

Up to now it has been shown that there is a potential for an improvement in the breakdown strength of GIS by application of a coating layer on (parts of) the electrode surfaces. The range of applied dielectric coating materials in literature has been limited to roughly insulator grade epoxy, silicone rubber and polyethylene[5], [9]–[12], [20], [26]. To find a suitable coating material for the improvement of GIS it is necessary to significantly increase the range of materials used in experiments.

Although the improving potential of coatings in GIS has been shown [5], [9]–[12], [20], [26] it is not clearly known which physical factors influence the breakdown strength of a coated gas insulated system. Consequently it is also unknown what the influence of the coating material parameters is on the possible improvement of GIS. Therefore, the influence of the coating and gas parameters on the breakdown strength of gas-coating insulation has to be investigated. This investigation should include possible self-restoring properties of coating-gas insulation because up to now it is assumed that gas-coating insulation is always non-self-restoring.

Following on the above mentioned investigation into the influence of material parameters on the breakdown behaviour of coated GIS, it is interesting to investigate the possibility of developing a mathematical model which can predict the breakdown strength of coated and uncoated GIS, based on coating material and gas parameters and the GIS geometry. Up to now several attempts were made to develop such a model. However, these models either lack the influence of electrode surface roughness, prediction of the breakdown path or the addition of a coating material on the electrode surface.

1.5 THESIS GOALS AND APPROACH

The main objectives of this thesis are threefold. The first objective is to find one or more suitable coating materials with which the breakdown strength of GIS can be successfully improved. The second objective is to obtain more insight into the material requirements of a suitable coating for the improvement of the breakdown strength of GIS. Finally, the third objective is to develop a mathematical model which can predict the breakdown

voltage of coated and uncoated GIS filled with either dry air or SF_6. The model should include the prediction of the breakdown path.

To accomplish the first objective, a large amount of breakdown voltage measurements are performed on both uncoated and coated GIS configurations. The breakdown voltage measurements include a wide range of coating materials to maximize to probability of finding one or more suitable coating materials.

The second objective will be accomplished by extending the above mentioned breakdown experiments with a wide range of coating material characterisation measurements. The coating material parameters of interest are the relative permittivity, dielectric losses, electrical conductivity, surface roughness, layer thickness and electrical breakdown strength. The relative permittivity and dielectric losses are evaluated with dielectric spectroscopy and the electrical conductivity is evaluated with conduction current measurements. Moreover, the roughness profiles of the coating material surfaces and uncoated electrode surfaces are obtained with tactile surface roughness measurements. The coating layer thickness is measured using a thickness gauge of the eddy current type and a micrometer screw gauge and the coating. Finally, the breakdown strength of the coating materials is evaluated with breakdown experiments on coating material samples.

The third objective is accomplished by developing a breakdown model from the available theory on gas breakdown and theory on the breakdown of coating-gas insulation. Subsequently, the model is validated and tuned using breakdown voltage measurements on coated and uncoated GIS configurations, filled with dry air or SF_6 at varying gas pressures. The GIS configurations include a wide range of coating materials.

1.6 THESIS OUTLINE

This thesis consists of 7 chapters including the introduction. **Chapter 2** describes the background theory on the improvement of GIS with the application of a coating layer on (parts of) the electrode surfaces inside GIS. The measurement setups, equipment and procedures used for the breakdown tests on coated and uncoated GIS configurations and the material characterisation measurements are presented in **Chapter 3**. In **Chapter 4**, the results of the breakdown voltage tests on coated and uncoated GIS configurations are presented and discussed. **Chapter 5** describes the material characterisation measurement results. This chapter also contains an in-depth discussion on material characterisation including the correlation with the results of the breakdown measurements on coated and uncoated GIS configurations, presented in chapter 4. The development of the breakdown model is described in **Chapter 6**, including the tuning and validation with extra breakdown voltage measurements on GIS configurations. Finally, **Chapter 7**

contains the conclusions on this research and the recommendations for future research, the application of coatings in GIS and the application of the breakdown model.

2

Gas insulated switchgear with coated electrodes

In this chapter several methods of improving the breakdown strength of gas insulated switchgear (GIS) with the help of coatings are discussed. Section 2.1 contains an overview of the available literature on coatings in gas insulated systems. In section 2.2 the dielectric performance of available alternative gases and gas mixtures is described.

In section 2.3 it is explained how the electric field distribution in the gas gap can be modified with the application of a coating. The breakdown strength of the system can be increased by correctly modifying the electric field distribution. Section 2.4 describes the influence of coatings on electron field emission and ionization in the gas gap. Both physical phenomena have a large influence on the electrical breakdown of gases. Section 2.5 describes the influence of coatings on particle movement inside GIS. The presence of particles near spacers and other critical locations is an important cause of switchgear failure. Particle contamination and the subsequent movement of particles thus have a large influence on the breakdown strength of GIS.

2.1 LITERATURE SPECTRUM

In literature, a wide range of sources can be found on the improvement of the breakdown strength of GIS. The available sources can be categorized in several subjects related to the physical phenomena which influence the breakdown strength of a gas insulated system. These sources also describe how coatings can be used to improve the breakdown strength of GIS by influencing these phenomena.

Physical Phenomena

To improve the breakdown strength of GIS the electric field strength in the gas should be reduced. Two main physical parameters can be modified to accomplish this. First, under normal operating conditions the electric field in the gas can be reduced by applying a dielectric coating of sufficient thickness on the electrodes where the electric field

is most divergent [1–3]. Second, when a unipolar voltage is applied, such as lightning impulse or DC voltage, charges can accumulate on the coating surface. The electric field generated by these charges can reduce the electric field in the gas, provided that the charges are of opposite polarity with respect to the applied voltage. Furthermore, the polarity, magnitude and location of the surface charges are dependent on the applied electric field distribution. The largest charge magnitude can be found at locations where the electric field is most divergent. Electrode surface charges can therefore also cause a homogenization of the electric field [4–8].

The breakdown strength of GIS can also be improved by reducing electron field emission and ionization in the gas. The roughness of electrode surfaces has a direct influence on ionization in the gas gap, especially at high gas pressure. Furthermore, the roughness of the cathode surface also directly influences electron field emission. Covering the electrodes with a coating can reduce the surface roughness and subsequently reduce both ionization and field emission [6, 9–11]. Electron field emission from very smooth electrodes can also be reduced by the application of a dielectric coating [12, 13].

Another important factor in the breakdown of GIS is particle contamination. Small metallic particles present in critical areas such as a spacer surface can significantly reduce the breakdown strength of gas insulated systems. It is not possible to completely prevent particle contamination. Therefore, the probability that a particle appears in a critical region should be minimized. Coatings can be used to reduce particle motion inside GIS and thus reduce the probability of a particle causing a breakdown [14–16].

Coating Types

The available literature sources can also be categorized in two approaches with different layer thickness. Coatings with a layer thickness of three millimetres and larger are referred to as "thick coatings". In [2–5, 7, 8, 17–23] thick coatings are used in breakdown tests and surface potential measurements. Coatings with a thickness up to roughly one millimetre are referred to as "thin coatings". Thin coatings are used in breakdown tests and surface potential measurements in [6, 9–13, 24–29].

Voltage Waveforms

In literature, the results of breakdown tests, withstand tests and surface potential measurements on coated and bare electrodes in gas filled test arrangements are reported. During these experiments a variety of voltage waveforms is applied on the electrodes. Standard lightning impulse voltage is most frequently applied [1–10, 17–29]. Several papers also include the use of AC voltage (50 or 60 Hz) [1, 9, 11, 23, 29]. DC voltage is applied in [4, 5, 11–13]. Results of breakdown tests using standard switching impulse can be found in [15].

Electrode Arrangements

Several different electrode arrangements are used in literature for breakdown tests, withstand tests and surface potential measurements. The most commonly used electrode arrangements are rod-plane [1–3, 7, 8, 10, 11, 18–20, 22, 23], coaxial cylinders [2, 6, 24–27, 29], sphere-plane [9, 17, 21, 28] and parallel flat plates [4, 5, 12, 26]. Also electrodes with a Rogowski profile [29] and configurations containing a spacer [25, 26] are used.

Gas Types

In literature, a variety of insulating gases and gas mixtures is used. The current standard insulating gas in GIS is SF_6. Breakdown test results and surface charge measurements in SF_6 can be found in [1–3, 6, 8, 10, 11, 23–28]. The performance of alternative gases in coated and uncoated systems is also evaluated. These gases include dry air [1, 4, 5, 7, 17–22, 24–26, 28], CO_2 [1, 9, 25, 26, 29] and N_2 [9, 24–26]. Gas mixtures such as SF_6/N_2 (5%, 10% and 50% SF_6), SF_6/air (50%) and N_2/O_2 (20%, 40% and 60% O_2) are tested in [24–26]. In [12] and [13] a vacuum is applied instead of an insulating gas.

Coating Materials

Theoretically, any dielectric material can be used to increase the breakdown strength of GIS. In practice only a small range of dielectric materials is used as a coating because these materials should be suitable to be applied to the electrode surfaces by either spraying, casting or dipping. The most frequently used coating material is epoxy [1–3, 6, 8–11, 17, 19, 21, 23–29] followed by silicone rubber [1, 4, 5, 7, 18, 20–22]. Note that epoxy and silicone rubber represent a variety of related materials with varying material properties. The exact type of epoxy or silicone rubber is rarely mentioned in literature. Other materials used in literature include polyethylene [3, 24], silicon monoxide [12, 13], polyamide 6,6 [26], polyimide [8] and polystyrene [15].

2.2 ENVIRONMENTALLY FRIENDLY GASES

In gas insulated systems SF_6 is generally in use as an insulating gas. The urge to find a suitable replacement gas for SF_6 is becoming stronger because of the environmental constraints.

For a replacement gas to be suitable for use in GIS, certain constraints should be fulfilled. First, the gas should be environmentally friendly and non-toxic. The gas should have no or only a very small global warming potential and the gas should not be ozone depleting. Second, the boiling point of the gas should be low enough to prevent condensation at operating temperatures. Third, the dielectric strength should be high enough to mini-

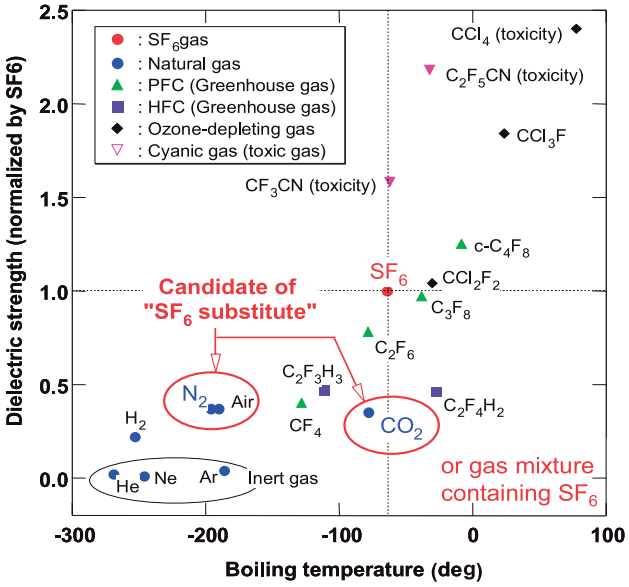

Figure 2.1: SF_6 replacement candidates with dielectric strength and boiling point [34].

mize the size increase of GIS designs containing the candidate gas. Possible replacement gases are shown in Figure 2.1.

Figure 2.1 shows a range of gases which are readily available. Newly designed gas mixtures, such as Alstom G^3 and ABB C5 FK gas are not included. From the figure it can be seen that the gases which have a higher dielectric strength than SF_6 are either toxic, ozone depleting or are greenhouse gases. These gases are therefore unsuitable to replace SF_6.

The gases which fulfil the environmental constraints are air, N_2, CO_2, H_2 and inert gases. Inert gases are however expensive and show a very low dielectric strength. Hydrogen is highly flammable, which makes it unsuitable for switchgear operation. Thus, only air, N_2 and CO_2 can be considered as replacement candidates when Alstom G^3 and ABB C5 FK are excluded.

2.2.1 Dielectric performance

As can already be seen from Figure 2.1 the replacement candidates show a low dielectric strength compared to SF_6 at equal gas pressure. In several papers the dielectric performance of air, N_2, CO_2 and mixtures of those gases including small concentrations of SF_6 is investigated.

In [25, 26] the lightning impulse (LI) breakdown strength of air, N_2, CO_2 and N_2/O_2 mixtures with varying oxygen concentrations is compared. The results are shown in Figure 2.2.

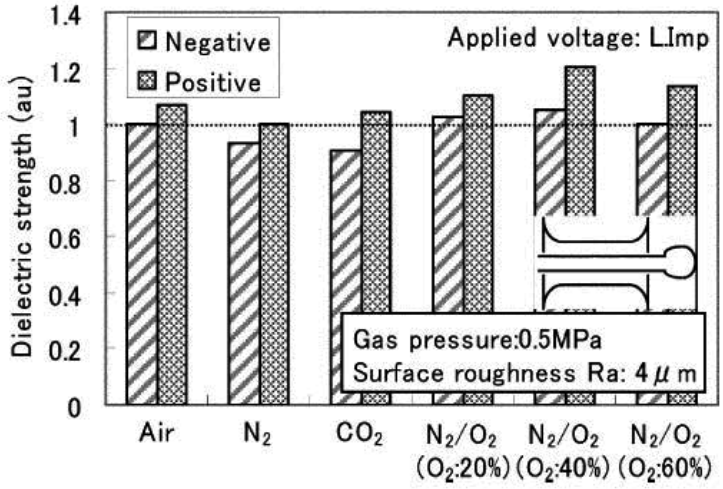

Figure 2.2: Comparison of the lightning impulse breakdown strength of various gases and gas mixtures [19]

For their comparison, lightning impulse breakdown tests were performed on a coaxial electrode arrangement. The gas pressure was kept constant at 0.5 MPa and the roughness of the electrodes was 4 µm. Both positive and negative polarity impulses were applied on the inner electrode.

In Figure 2.2 it can be seen that the dielectric strength at negative lightning impulse is in all cases lower than at positive lightning impulse. Only the negative polarity results will thus be considered. The results show that the dielectric strength of N_2 and CO_2 was roughly 7% lower than the dielectric strength of air. When the O_2 concentration of the N_2/O_2 mixtures was 20% a small increase of the dielectric strength above that of air is visible. For an O_2 concentration of 40% the dielectric strength is roughly 5% higher than that of air. When the oxygen concentration is increased to 60% the dielectric strength is equal to that of air. It seems that there is an optimal concentration of oxygen for N_2/O_2 mixtures which is 40% at 0.5 MPa gas pressure.

The LI breakdown strength of SF_6/N_2 gas mixtures is also evaluated in [19]. Figure 2.3 shows the comparison of the LI breakdown strength of air and SF_6/N_2 gas mixtures. Negative lightning impulse voltage is applied in the breakdown tests.

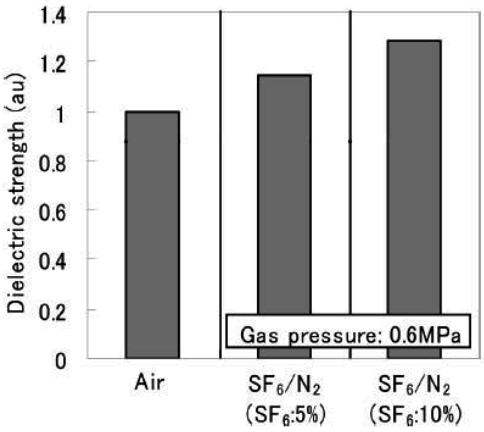

Figure 2.3: Comparison of the LI breakdown strength of air and SF_6/N_2 gas mixtures [19]

Figure 2.3 shows that an SF_6/N_2 gas mixture with an SF_6 concentration of 5% has a dielectric strength which is 15% higher than that of air at 0.6 MPa gas pressure. The highest dielectric strength is obtained when the SF_6 concentration is increased to 10%. In this case, the increase with respect to the dielectric strength of air is roughly 28%.

The dielectric performance of SF_6, CO_2, N_2 and an SF_6/N_2 gas mixture with 10% SF_6 is also evaluated in [35]. For this evaluation, lightning impulse breakdown tests were performed in a coaxial electrode arrangement. The pressure of the alternative gases varies between 0.6 and 1.1 MPa. In Figure 2.4 the 50% breakdown electric field strength

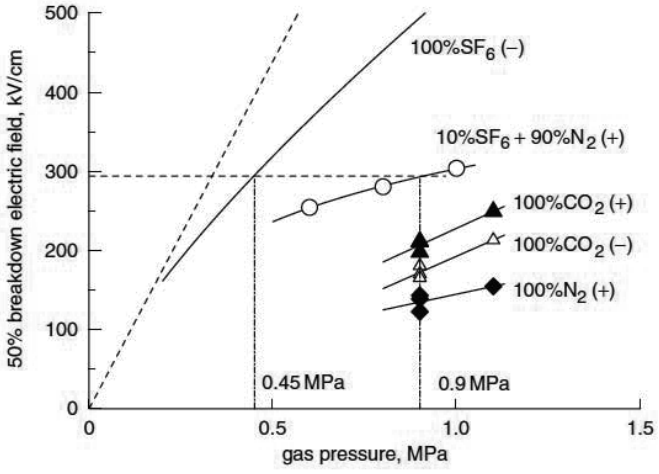

Figure 2.4: 50% BDE of SF_6, CO_2, N_2 and SF_6(10%) /N_2 gas mixture [35]

(BDE) of the alternative gases is shown as a function of gas pressure. The 50% BDE of pure SF_6 is also included.

In the figure it can be seen that the dielectric strength of an SF_6 (10%)/N_2 mixture with a gas pressure of roughly 0.9 MPa is equal to the dielectric strength of pure SF_6 at 0.45 MPa pressure. Therefore, to replace pure SF_6 by an SF_6 (10%)/N_2 gas mixture the gas pressure should roughly be doubled. Unfortunately, for CO_2 the 50% BDE at 0.9 MPa is roughly 40% lower than that of pure SF_6 at 0.45 MPa. The 50% BDE of N_2 is even lower than that of CO_2.

When the results from Figure 2.4 are translated into the design of a coaxial busbar arrangement, the dimensions and applied pressure should be modified for each gas type to obtain a comparable dielectric strength. Table 2.1 displays the necessary dimensions for the use of an alternative gas in a coaxial busbar.

Table 2.1: Comparison of busbar dimensions, LI = Lightning Impulse [35]

	SF_6(100%)	SF_6(10%) + N_2(90%)	CO_2(100%)	N_2(100%)
Gas Pressure (%)	100	200	200	200
Electric Strength (%)	100(LI-)	100(LI+)	62(LI-)	47(LI+)
Inner diameter of tank (%)	100	100	160	210

From the table it can be seen that the dimensions of a busbar filled with the SF_6/N_2 mixture can be equal to the dimensions of an SF_6 filled busbar when the pressure of the gas mixture is twice the pressure of SF_6. When CO_2 or N_2 is applied at twice the pressure of SF_6 the electric strength will be 62% or 47% of the electric strength of SF_6 respectively. When CO_2 or N_2 is used as an SF_6 substitute, the inner diameter of the tank(outer electrode) should be 1.6 or 2.1 times larger than the diameter of an SF_6 filled tank, respectively. With these dimensions and twice the gas pressure of SF_6, a coaxial busbar filled with CO_2 or N_2 will have the same electric strength as an SF_6 filled busbar. Note that the lightning impulse polarities shown in Table 2.1 represent the critical polarity, which is the polarity with the lowest measured breakdown strength for the corresponding gas type.

Summarizing, the results from literature show that air, CO_2 and N_2 are good substitutes for SF_6 with respect to environmental and economic constraints. However, the dielectric strength of these gases is much lower than that of SF_6 resulting in a size increase of GIS designs which would not be favourable. Furthermore, the usage of SF_6/N_2 mixed gases would not be favourable because of the fact that, despite of the significantly lower quantity, SF_6 is still necessary. Existing regulations regarding SF_6 handling would in that case still apply removing the advantage of lower handling costs.

Fortunately, the application of coatings on the electrodes inside GIS might be a solution to overcome the problem of the inferior dielectric strength of these alternative gases.

2.3 IMPROVEMENT OF THE ELECTRIC FIELD DISTRIBUTION

In section 2.2 it was shown that most alternative gases have a low breakdown strength compared to SF_6. Therefore, GIS filled with such alternative gases would require a larger size to obtain a comparable dielectric strength with respect to SF_6 filled GIS. Because increasing the size of GIS would be unfavourable, the breakdown strength needs to be improved.

One of the possibilities to improve the dielectric strength of GIS, without increasing the size, is to reduce the electric field in the gas gap. In this way, the withstand voltage of GIS can be increased. In this section, two methods are described to improve the electric field distribution in gas insulated systems.

2.3.1 Modification of the capacitive electric field distribution

In the case of AC voltage the electric field distribution is dependent on the permittivity of the insulating media. This type of electric field distribution is also known as a capacitive electric field distribution. With the application of a thick dielectric coating layer on one or multiple electrodes in GIS the electric field distribution in the gas gap can be improved.

Consider a rod-plane electrode arrangement as shown in Figure 2.5. The length of the gas gap between the tip of the rod electrode and the plane electrode is set at 23.31 mm. The radius of the rod electrode is 15 mm and both electrodes are uncoated.

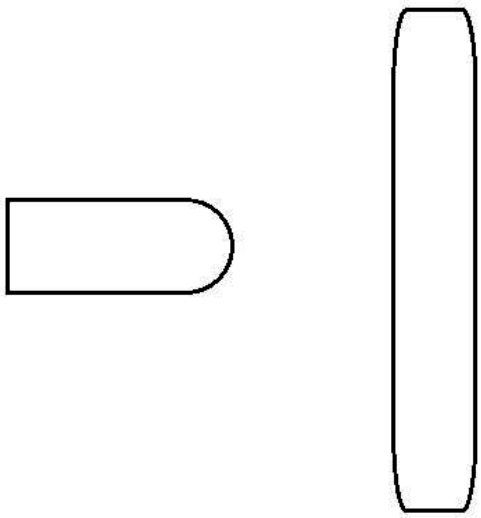

Figure 2.5: Simple rod-plane electrode arrangement

The electric field distribution along a straight line between the rod tip and the plane is represented by the dotted blue line in Figure 2.6. The parameter D on the horizontal axis represents the position in the gas gap. The rod tip is located at D = 0 mm and the surface of the plane electrode is positioned at the right end of the horizontal axis (D = 23.31 mm). The local electric field strength E in kV/mm is displayed on the vertical axis.

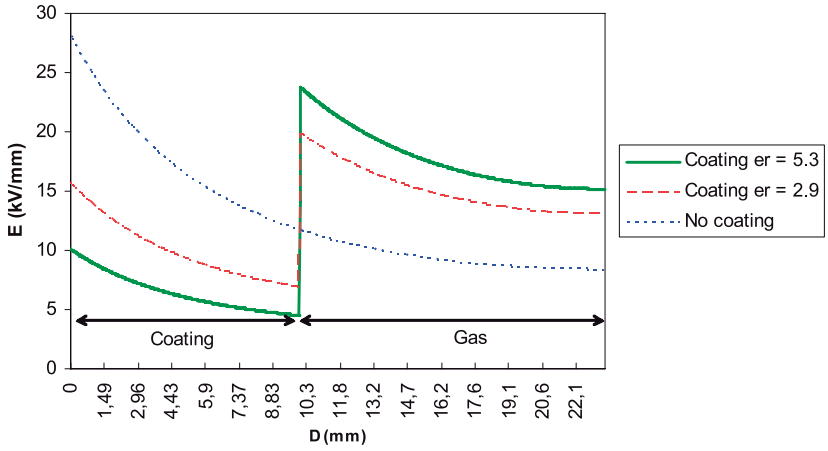

Figure 2.6: Electric field distribution in a rod-plane configuration with and without coating [5]

The highest electric field strength of roughly 28 kV/mm is located at the tip of the rod electrode where the electric field is most divergent. The electric field near the surface of the plane electrode is more homogeneous. There, the lowest field strength of roughly 9 kV/mm is found.

When a 10 mm thick dielectric coating with a relative permittivity of 5.3 is applied on the surface of the rod electrode the electric field distribution changes. Now, the electric field distribution is represented by the solid green line.

In a capacitive electric field distribution the electric field is pushed into regions of low permittivity. Therefore, the electric field at the electrode surface in the coating is lowered because the coating has a higher permittivity than the gas. Furthermore, at the coating-gas interface the electric field strength shows a jump which again is caused by the higher permittivity of the coating.

Even with the jump in the electric field strength at the coating surface, the maximum electric field strength in the gas is lowered with respect to the uncoated situation. The maximum electric field strength in the uncoated situation is roughly 28 kV/mm and in the coated situation it is 24 kV/mm.

The reduction of the maximum electric field strength in the gas is even stronger when the relative permittivity of the coating is lowered as can be seen from the dashed red line in Figure 2.6. Because the difference between the permittivity of the coating and the gas is smaller, the step increase in the electric field strength at the interface is also smaller. This results in an even lower maximum field strength in the gas.

The hypothetical best case would occur when the relative permittivity of the coating is equal to the permittivity of the gas. In this case, the electric field distribution in the gas would be equal to the blue dotted line between D = 10 mm and 23.31 mm. The maximum electric field strength in the gas is then roughly 12 kV/mm which is 43% of the maximum field strength in the uncoated system. Note that, with a lower relative permittivity of the coating, the electric field strength inside the coating is increased. Fortunately, solid dielectric materials have a high electric breakdown strength compared to insulating gases. The best coating candidate would therefore have a relative permittivity which is as close as possible to one.

It is important to see that this modification of the capacitive electric field distribution is only significant when a thick coating is applied. For thin coatings there is no significant change in the capacitive electric field distribution in the gas. Furthermore, this effect is only present in electrode arrangements with an inhomogeneous electric field distribution such as a rod-plane or coaxial arrangement.

2.3.2 Charge accumulation on the coating surface

The electric field in the gas gap can also be reduced with the intentional use of accumulated surface charge. Consider the parallel plane configuration shown in Figure 2.7.

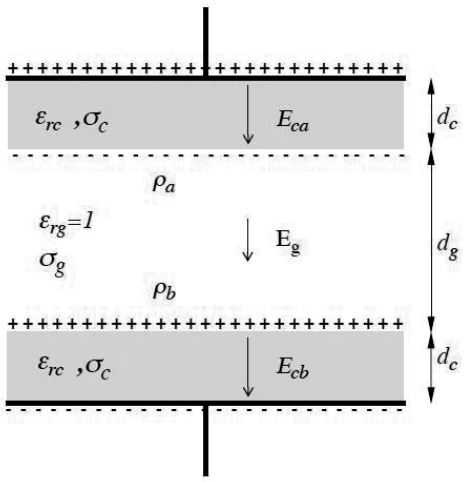

Figure 2.7: Parallel plane configuration with coated electrodes [24].

In this configuration, the electrodes represented by the black lines are covered with a coating layer represented by the grey areas. The gas gap is represented by the white area. Both electrodes are covered with the same coating material. The terms ε_c and ε_g represent the permittivity of the coating layers and the gas respectively. The conductivity of the coating material and the gas is represented by σ_c and σ_g.

When a unidirectional electric field is applied between the electrodes, available free charges in the gas will move in or opposite to the direction of the applied electric field. These charges will accumulate on the coating surfaces. In this case negative charges will move upwards and accumulate on the coating surface of the top electrode and positive charges will accumulate on the bottom coating surface.

These accumulated charges generate an electric field in the gas opposite to the applied electric field. The total electric field in the gas is equal to the applied field plus the charge induced field. Therefore, the field strength in the gas is reduced. As is clear from Figure 2.7, the electric field generated by the surface charges enhances the total electric field strength in the coatings. Fortunately, the breakdown strength of solid insulators is usually significantly higher than that of insulating gases.

The magnitude of the charge induced electric field is positively dependent on the surface charge density designated by ρ_a and ρ_b in Figure 2.7. Therefore, the reduction of the total electric field strength in the gas is dependent on the amount of accumulated charge.

In Figure 2.8, the amplitude of the total electric field in the gas and in the coating is displayed as a function of the surface charge density for the configuration displayed in Figure 2.7. As long as there is a finite electric field in the gas gap and there are enough free charges available in the gas, charges will continue to accumulate on the coating surfaces until the electric field in the gas equals zero. In this case the system is in equilibrium and the total applied voltage is carried by the coatings only. The accumulated surface charge density is then equal to ρ_{eq} in Figure 2.8.

In this equilibrium the accumulated surface charge density ρ_{eq} is given by the following equation [24].

$$\rho_{eq} = V \frac{\varepsilon_0 \varepsilon_c}{2d_c} \quad (1)$$

In this equation V represents the applied voltage between the parallel plates and d_c is the thickness of the coating layers. The required surface charge density to reach zero electric field in the gas gap is dependent only on coating material parameters. To minimize the amount of surface charge necessary for equilibrium the permittivity of the coatings should be as close as possible to one and the thickness of the coatings should be as large as possible.

The accumulation of surface charge is not instantaneous. These charges accumulate with a certain time constant depending on the original source of the charges. The graph in Figure 2.8 thus also represents the change of the electric field in the gas and in the coating over time. In the figure, two further interesting points can be seen. First, the surface charge density necessary to obtain a uniform field strength in the entire arrangement is designated by r_p. Second, the surface charge density accumulated in a resistive electric field distribution is designated by r_{dc}. In a resistive electric field distribution the electric field strength in each medium is dependent only on the conductivity of the materials (in this case σ_c and σ_g). More information on resistive electric field distributions can be found in [36].

Charge sources and transport mechanisms

Free charges in the gas can originate from several different sources. Natural ionization caused by background radiation provides a stable source of charged species. The ion and electron generation rate is in this case relatively low. Electric field dependent processes such as gas ionization and electron field emission from the cathode are also important sources of ions and electrons. When the electric field strength reaches the critical field strength for gas ionization the field dependent processes are the main sources of ions and electrons. In this case the generation rate is relatively high.

Charge transport mechanisms also play an important role in the accumulation of surface charge. Charges can either be transported to the coating surfaces by conduction along the surface of the coatings or by bulk conduction through the coatings. Furthermore, charges can also be transported through the gas by diffusion and drift of ions and electrons. Generally, bulk conduction through a coating is a relatively slow process depending on the conductivity of the coating material. Electron and ion drift can be a very fast transport mechanism depending on the electric field strength in the gas and the mobility of the charged species.

The time constant of surface charge accumulation is dependent on both the charge generation rate of the different sources and the charge transport velocity of the different transport mechanisms. The field reducing effect of surface charge accumulation for different voltage types, such as AC, DC or lightning impulse, is thus dependent on this time constant. For example, consider the application of a DC voltage for several days. In this case, both slow processes, such as natural ionization, bulk conduction and diffusion, and fast processes, such as electron drift and gas ionization can be useful for the accumulation of surface charge. When a lightning impulse is applied only fast processes such as electron drift and gas ionization will play a significant role in the accumulation of surface charge.

Active insulation

Surface charge accumulation could be used as an adaptive form of insulation. The accumulated amount of charge is dependent on the applied voltage. A change in applied voltage is counteracted by a change in accumulated surface charge. To illustrate this effect, several situations will be described.

Consider the parallel plane configuration in Figure 2.7 in which a fast rising voltage is applied. Because there is insufficient naturally available charge in the gas the electric field in the gas gap will also rise. The electric field will continue to rise until the electric field in the gas reaches the critical field strength for ionization. At this instant new charges are generated in the gas and transported to the coating surfaces by the drift mechanism resulting in a reduction of the electric field in the gap. The system is thus self-stabilizing.

In general, the system will try to reach an equilibrium in which the electric field in the gas gap is zero. Normally, this equilibrium is not reached because of a lack of available charges. When the electric field is again below critical and all the newly generated charges have accumulated on the surfaces not enough charge remains in the gas to obtain a zero electric field. If the voltage is still rising, the electric field again reaches the critical value, ionization occurs and once more the electric field strength is reduced to below critical. This phenomena can be present in the front of a lightning impulse and is called a depositing discharge [24].

If a steady state DC voltage is present between the electrodes and the coatings have an ideal conductivity of zero the accumulated charge will remain on the coating surfaces. The electric field in the gap is below critical, so no ionization occurs. The system is in a local equilibrium. However, most coating materials show a very low conductivity. Over time, accumulated charge is removed from the surface via bulk conduction through the coating layer to the electrodes. When charge is drained from the surface, the electric field in the gas will rise until the critical value is reached. Ionization will then be present in the gas resulting in the accumulation of new charge on the coating surfaces. The accumulated surface charge is thus restored to the original amount which is called a restoring discharge [24].

When the voltage is removed or reversed, the accumulated surface charge represents a field enhancement. Locally, the electric field can be higher than critical resulting in a partial discharge of the coating surfaces. This phenomena can be present in the tail of a lightning impulse and is called a relaxing discharge [24].

Measurements

To investigate the theory on the charging of coating surfaces several experiments were performed in [24]. In these experiments a parallel plane electrode configuration, coated with a 3 mm thick layer of silicone rubber, was stressed at AC, DC or lightning impulse voltage. The voltage was applied on the top plane and the lower plane was earthed via

a shunt to measure any currents flowing from the bottom plane to earth. With these current measurements discharge activity in the gas could be recorded.

When a slowly rising AC voltage was applied, intense discharge activity was recorded when the electric field in the gas reached the critical field strength. The discharge activity remained until the voltage was again lowered. No influence of the coating or charge accumulation was visible.

In the second experiment [24] a slowly rising DC voltage was applied. The DC voltage was increased until discharge activity occurred. After several minutes the discharge activity vanished which can be related to depositing discharges. Next, the voltage was further increased until new discharge activity was visible. After another several minutes the voltage was increased again. With this slow stepwise increase, DC voltages between 50% and 250% higher than the voltage level necessary to obtain a critical electric field strength in the gas, according to the capacitive field distribution, were reached within the range of applied gap distances.

At high voltage levels recurring discharges were visible. These discharges can be classified as restoring discharges, which are present due to the increased leakage current through the coating layers. Charge drained from the surfaces is replaced. At the highest voltage levels the discharge activity was continuous, which represents a continuous supply of new charge from the gas to replace the continuously draining surface charge.

For lightning impulse voltage a comparable procedure was used in which each voltage level represents a sequence of five equal impulses. With this method, voltage levels between 70% and 350% higher than the voltage necessary for a critical field strength in the gas, according to the capacitive field distribution, were reached. In further experiments a depositing discharge was recorded on the front of each lightning impulse including the first impulse in a sequence. If the amplitude of the impulse was sufficiently high a train of multiple discharges of opposite polarity was visible on the tail of the impulse. These discharges can be classified as relaxing discharges.

Homogenization

Another important property of active insulation is the fact that free charges experience an electrostatic force in the direction of the area with the highest and most divergent electric field. More charge will accumulate in these regions, which usually are weak spots. Surface charge accumulation will therefore result in a homogenization and reduction of the electric field at this weak spot. The breakdown voltage of the entire system is subsequently increased.

In [24], the applied electric field was in all cases homogeneous. Experiments with an inhomogeneous field distribution were performed in [26]. In this work, discharge activity was recorded in a rod-plane arrangement using current measurements and video im-

ages. The rod electrode was covered with a 3 mm thick layer of silicone rubber. Lightning impulse of positive and negative polarity was applied.

The decay of surface charges on the rod electrode after the voltage was removed was measured with a field mill [26]. The profile of the surface potential along the entire length of the rod was also recorded with a field mill.

2.4 REDUCTION OF ELECTRON FIELD EMISSION AND IONIZATION

In section 2.3 it was shown that the dielectric strength of GIS can be improved by reducing the electric field strength in the gas gap. The breakdown strength of GIS can also be improved with the modification of the starting conditions for an electrical breakdown in the gas gap.

In this section, it is explained how the roughness of the electrode surface can influence these starting conditions. Furthermore, it is explained how the starting conditions can be modified with the application of a coating to obtain an increased breakdown strength.

2.4.1 Electron field emission

Electrical breakdown in gases is initiated by impact ionization of gas molecules or atoms. Impact ionization occurs when electrons with sufficient kinetic energy collide with neutral gas atoms or molecules. Therefore, ionization requires the availability of a free electron in a region of sufficient electric field strength in the gas gap. This minimum electric field strength is called the critical field strength and the region in the gas gap in which the electric field is critical is named the critical region.

Consider the rod plane electrode configuration shown in Figure 2.5 and the corresponding electric field distribution shown as a blue dotted line in Figure 2.6 in section 2.3.1. When the applied voltage on the rod electrode is increased above a certain critical level a critical region will be present in the gas at the tip of the rod electrode. Ionization will start when a single free electron appears inside this critical region.

Free electrons can originate from different sources. First, electrons can be generated by natural ionization of gas molecules due to the presence of background radiation. Second, irradiation of a gas with light can cause ionization of gas molecules resulting in the generation of free electrons. This process is called photo-ionization, because of the collisions between photons and gas molecules. Sources of light can be UV-radiation from the sun or light emitted by gas discharges. Third, electrons can be emitted from the cathode surface.

Electron emission from the cathode is driven by three main processes. First, photons from incident radiation can strike the cathode surface. When these photons have sufficient energy, electrons can be freed from the electrode metal, a process known as

photoemission. Second, when the temperature of the cathode is sufficiently high electrons can gain enough thermal energy to be freed from the metal. This process is called thermionic emission and is used in x-ray generators or cathode ray tubes. Third, electrons in the cathode can also be emitted into the gas when the cathode voltage is sufficiently high. This process is known as electron field emission. Note that the applied voltage in GIS usually is far lower than required for field emission. However, microscopic protrusions at the electrode surface cause electric field enhancements of sufficient magnitude for electron field emission. This effect is explained in section 2.4.2.

In GIS, photo-emission and photo-ionization are negligible because the tank in which the electrodes are located is a dark chamber. Furthermore, thermionic emission is negligible because the conductor temperature is far lower than required for thermionic emission. Therefore, electron field emission and natural ionization are the main sources of free electrons in GIS.

When a negative voltage is applied to the rod electrode in the rod-plane configuration, the rod electrode becomes the cathode. In this case the critical region at the tip of the rod electrode is adjacent to the cathode surface. Electrons are thus emitted from the cathode directly into the critical region. Electron field emission then becomes the main source of electrons which implies that field emission is in this case the main factor in breakdown initiation. Inhibition of electron field emission from the cathode can therefore increase the breakdown strength of GIS.

Application of a coating on the cathode surface can inhibit electron field emission [28]. In [28] the DC breakdown strength of a vacuum gap between coated and uncoated electrodes is evaluated. In this work, a parallel plane configuration is used with a gap distance of 0.2 mm and stainless steel electrodes. In the coated system the cathode is coated with a 2 µm thick layer of SiO. The pressure of the vacuum is in the order of 10^{-7} mbar. Because the test tank is a dark chamber and the electrodes are at room temperature, thermionic emission, photo-emission and photo-ionization are negligible. Furthermore, natural ionization is negligible in a high vacuum. Therefore, electron field emission is the main source of electrons.

The breakdown test results are shown in Figure 2.9. The white dots represent the breakdown field strength for the uncoated situation and the black dots represent the system with a coated cathode. It can be seen from the figure that the application of the coating on the cathode increases the breakdown strength with roughly 100%.

The figure also shows results from [29], which are represented by the triangles on the right side. In this case an aluminium cathode with a Rogowski profile was used and the coating consisted of a 3 µm thick silicon oxide layer. The gap distance was varied between 3 and 8 mm for the coated cathode and was fixed at 6.3 mm for the uncoated cathode. With a gap distance of 3 mm the coated cathode shows an improvement of roughly 130%.

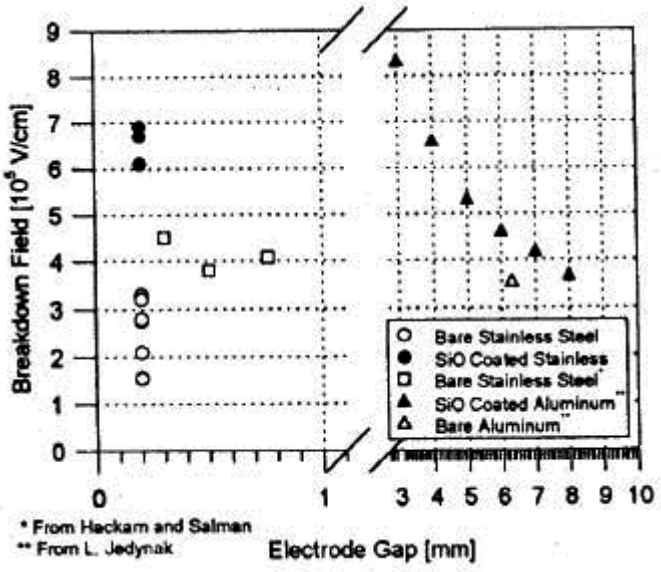

Figure 2.9: Breakdown strength of a vacuum gap with a coated and uncoated cathode [28]

As mentioned in [28], the improvement decreases when the gap distance is increased. This might be caused by the total voltage effect described in [28] and seems to be only present in vacuum systems due to the fact that the electron mean free path is several orders of magnitude longer in vacuum than in a pressurized gas filled system.

Improvement factor

In [28] the expected improvement of the breakdown strength in a vacuum gap with a coated cathode is determined as a function of material parameters. Because in this system electron field emission is the most important cause of breakdown, the expected improvement in breakdown strength is determined by this process.

The current density due to electron field emission can be described by the Fowler-Nordheim tunnelling equation [28], [37]:

$$J = f\frac{E^2}{\Phi}\exp\left(-g\Phi^{3/2}\frac{u}{E}\right) \quad [\mathrm{A/m^2}] \qquad (2)$$

In this equation, f and g are constants and u is a correction factor proportional to E/Φ^2. The terms E and Φ are the electric field strength at the cathode surface and the height of the potential barrier respectively. The field emission current is determined by the height (Φ) and slope of the potential barrier at the metal surface. The potential barrier slope is proportional to the electric field (E) at the metal surface.

In the uncoated case, electrons need to tunnel directly to the vacuum level. In this case the potential barrier height (Φ) is actually the work function of the cathode metal. The work function is the difference in energy level between the conduction band of the metal and the vacuum level.

When a coating is applied on the cathode surface, the electric field at the metal surface is reduced with a factor of $1/\varepsilon_r$ in which ε_r is the relative permittivity of the coating. The slope of the potential barrier is effectively reduced which results in a reduction in emission current.

Furthermore, the potential barrier height is reduced by the energy difference between the vacuum level and the coating conduction band. This energy difference is the electron affinity (χ) of the coating material.

In total, the expected improvement in the breakdown voltage of the vacuum gap can be described by an improvement factor, γ, which is the ratio between the gap voltage of a coated cathode and an uncoated cathode with equal field emission current. The improvement factor is given by the following equation:

$$\gamma = \frac{V_{coated}}{V_{uncoated}} = \frac{\varepsilon_r(\Phi - \chi)^{3/2}}{\Phi^{3/2}} \qquad (3)$$

The ratio γ is thus the predicted increase in breakdown voltage of the vacuum gap when a coating is applied. From the equation it can be seen that the best coating candidates should have a high relative permittivity ε_r and low electron affinity χ. Note that the need for a high relative permittivity in this case opposes the need for a low relative permittivity in the cases mentioned in section 2.3.

2.4.2 Electrode surface roughness

In section 2.4.1 it was described that the occurrence of a free electron in the critical region in the gas gap is necessary to initiate a breakdown. In the critical region the electric field is above the critical value, which is 8.84 [kV/mm bar] for SF_6 [38].

In section 2.4.1 it was always assumed that the surface of the electrodes is smooth. However, in general the surface of the electrode metal is not smooth at a microscopic scale. Grooves and protrusions can be seen through the microscope.

These microscopic protrusions cause local electric field enhancements. Consider a flat plate electrode with a smooth surface on which a voltage is applied. The electric field near this flat plate is homogeneous and the corresponding electric field strength is designated by E_0. When a hemispherical protrusion is present on the electrode surface, the electric field strength at the hemisphere is 3 times higher ($3E_0$) [39].

The presence of microscopic electric field enhancements at the electrode surface can cause local ionization at an applied electric field strength below critical. The critical

value of the macroscopic electric field near the electrode is consequently decreased. This decrease in the critical electric field strength can result in a reduction of the breakdown strength of the system.

In Figure 2.10, the critical electric field strength for SF_6 is shown as a function of the product of gas pressure and electrode surface roughness. As can be seen from the figure, the critical electric field strength decreases when the product of the gas pressure and the coefficient related to the maximum surface roughness R_y, according to the JIS B 0601 standard [40], is increased. When the gas pressure is kept constant the critical electric field strength is only dependent on R_y.

Note that below a threshold of roughly 40 [bar µm] there is no influence of the surface roughness on the critical field strength. Furthermore, this dependence of the critical field strength on the surface roughness is only present in strongly electronegative gases such as SF_6 due to the short attachment length. This dependence is discussed in more detail in chapter 4.

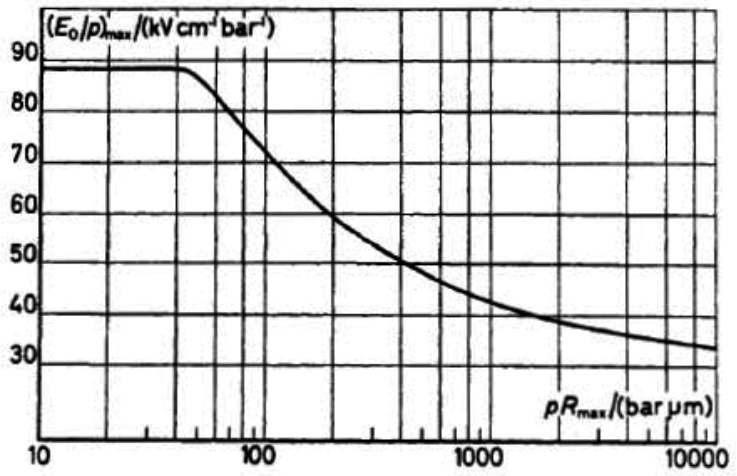

Figure 2.10: Critical electric field strength as a function of gas pressure and surface roughness [38]

Specification of surface roughness

In order to evaluate and compare the influence of electrode surface roughness on the breakdown strength of gas gaps, the surface roughness should be clearly defined according to standards. In [6, 9–11] the mean surface roughness R_z of the electrodes is defined according to standards [40], [41]. To determine the value of R_z, the measured track is divided into 5 equidistant parts. The distance between the highest peak and

deepest valley R_t of each part is calculated. R_z represents the mean value of these five distances as shown in the next equation [9].

$$R_z = \frac{1}{5}\sum_{i=1}^{5} R_{ti} \tag{4}$$

Results from literature

In [10, 11] the breakdown voltage of rod-plane configurations as a function of electrode surface roughness was investigated. The applied gas was SF_6 with a pressure in the range of 0.4 to 0.5 MPa absolute. The plane electrode was in all cases polished to a mean roughness R_z of 5 µm, while the roughness of the rod electrodes was varied between 5 and 80 µm. The rod electrodes have a diameter of 60 mm and the gap distance ranges from 10 to 50 mm.

In Figure 2.11 the breakdown voltage as a function of surface roughness is shown in the case of positive lighting impulse voltage. The polarity refers to the polarity of the rod electrode. It can be seen from the figure that the breakdown voltage decreases with an increase in surface roughness, which is consistent with the theory of Pedersen [38]. Also in the case of positive DC voltage a comparable negative dependence of the breakdown voltage on the surface roughness of the rod electrode was shown [9].

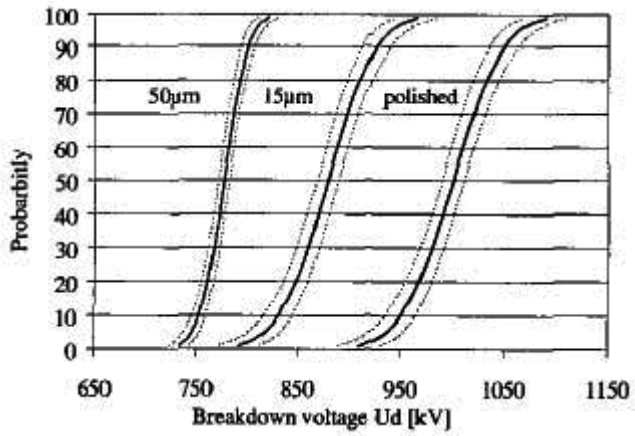

Figure 2.11: Normal distribution of breakdown voltage including 95% confidence intervals, positive LI voltage, s = 40 mm, variation of R_z , uncoated [10]

Figure 2.12 shows the breakdown voltage as a function of surface roughness in the case of negative lightning impulse voltage [10]. In this case, the lowest breakdown voltage can be found for a surface roughness R_z of 15 µm. The electrode with a surface roughness of 50 µm shows a significantly higher breakdown voltage. The breakdown voltage of the polished electrode is only highest for quantiles higher than 50%. These results are not consistent with the theory of Pedersen [38]. In [9], comparable results were found for negative DC voltage.

Another interesting result from [10] is the fact that the breakdown voltage is also dependent on the applied surface treatment method. In Figure 2.13 it is shown that

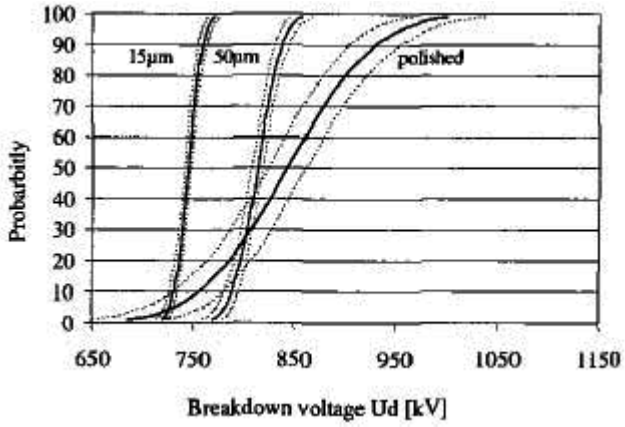

Figure 2.12: Normal distribution of breakdown voltage U_d including 95% confidence intervals, negative LI voltage, s = 40 mm, variation of Rz, uncoated [10]

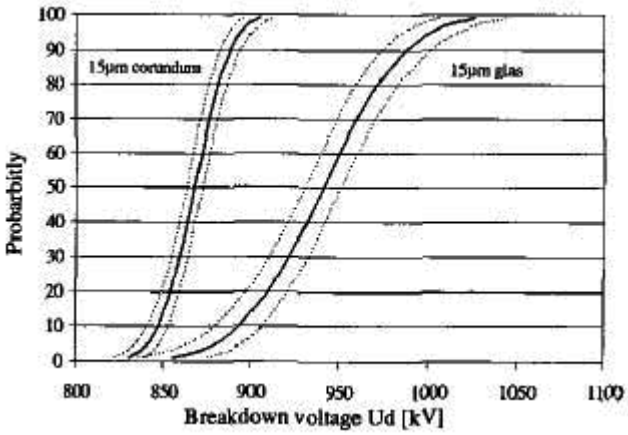

Figure 2.13: Normal distribution of breakdown voltage including 95% confidence intervals, negative LI voltage, s = 50 mm, Rz = 15 µm, varying surface treatment, uncoated [10]

there is a significant difference in breakdown voltage between an electrode blasted with corundum and an electrode blasted with glass pearls, despite the fact that the surface roughness of both electrodes is equal (R_z = 15 µm).

Coatings

The application of a coating can theoretically reduce the influence of electrode surface roughness on the breakdown strength of gas gaps. During application the coating material fills up the unevenness of the electrode surface as shown in Figure 2.14, provided that the layer thickness of the coating is sufficient. The surface of the coating at the coating-gas interface should be significantly smoother, effectively removing the microscopic electric field enhancements from the gas. These field enhancements are now present in the coating material, which usually has a higher dielectric strength than the gas. Furthermore, due to the permittivity of the coating, the electric field at the metal surface is reduced, as explained in section 2.4.1.

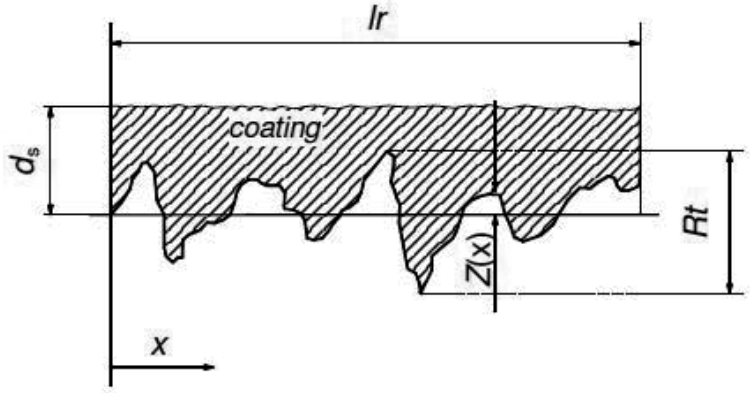

Figure 2.14: Schematic drawing of the cross-section of a coated electrode surface [11]

In [10, 11] the breakdown voltage of epoxy coated rod electrodes was also investigated and compared to uncoated electrodes. For the design of GIS components the 10% quantile of the breakdown voltage is the most important parameter. Figure 2.15 displays the 10% breakdown voltage of coated and uncoated electrodes under positive and negative lightning impulse voltage. As can be seen from the figure, at positive lightning impulse voltage the application of a coating results in a reduction of the 10% breakdown voltage. For negative lightning impulse voltage an increase of roughly 8% was found for a coated electrode. Note that the surface roughness of the coating is always between 6 and 10 µm.

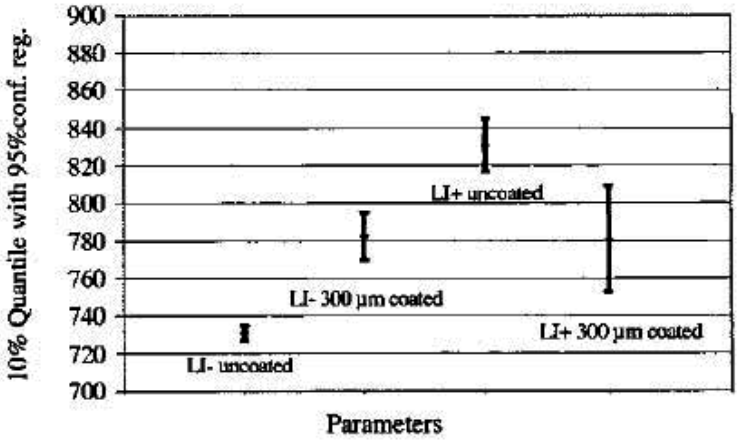

Figure 2.15: 10% quantile with 95% confidence intervals, epoxy coated and uncoated electrodes, Rz = 15 µm, s = 40 mm, coating thickness is 300 µm, positive and negative LI [10]

For DC voltage, comparable results have been found [9]. In this paper it has been shown that the breakdown voltage of coated electrodes is roughly independent of the surface roughness of the underlying rod electrode.

In [11] the breakdown strength of a coaxial electrode arrangement as a function of surface roughness and coating thickness has been investigated. The used gas type is SF_6 at a pressure of 0.5 MPa absolute. The inside of the outer electrode is always polished to a roughness of 5 µm and is uncoated. The inner electrode is either polished (R_z = 5 µm) or trowalized (i.e. barrel finishing, R_z = 25 µm) and is either uncoated or coated with epoxy. The epoxy coating has a layer thickness ranging from 25 µm to 120 µm. The gap distance s is set at 30 mm.

The lightning impulse breakdown voltage shows a different behaviour with respect to the rod-plane arrangement. First, From Figure 2.16 and Figure 2.17 it can be seen that in this case the breakdown voltage for uncoated electrodes is lower at positive polarity than at negative polarity lightning impulse.

Second, at both polarities the uncoated polished electrode shows a significantly higher breakdown voltage than the trowalized electrode. Third, for both polarities the application of a thin coating layer results in a significant increase of the 10% breakdown voltage, independent of the surface roughness of the electrodes.

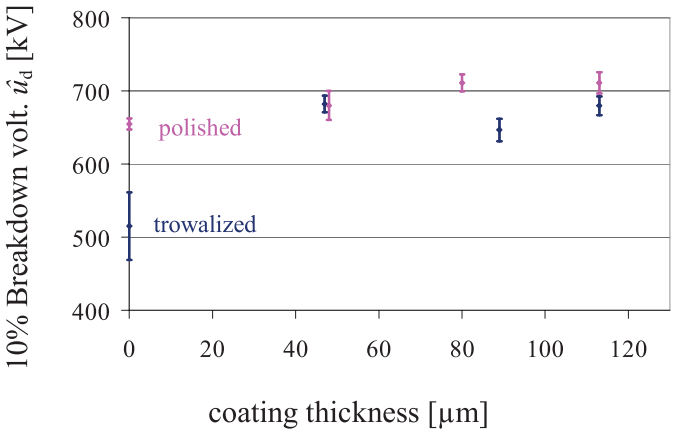

Figure 2.16: 10% quantiles of breakdown voltage with 95% confidence intervals, negative LI, polished and trowalized electrodes, epoxy coated[11]

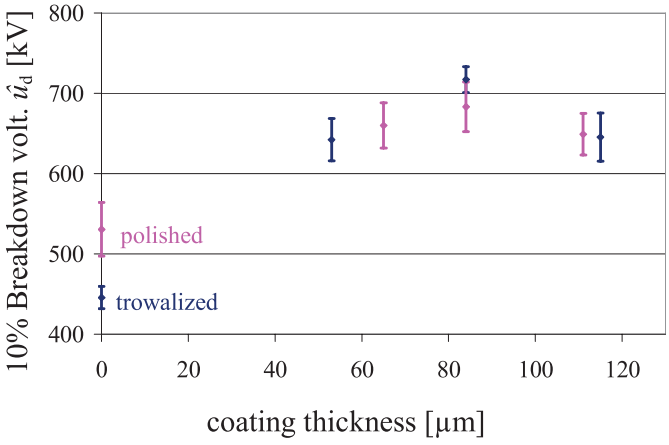

Figure 2.17: 10% quantiles of breakdown voltage with 95% confidence intervals, positive LI, polished and trowalized electrodes, epoxy coated [11]

2.5 INHIBITION OF METALLIC PARTICLE MOVEMENT

In section 2.3 and 2.4 it is shown that the breakdown strength of GIS can be improved by either reduction of the electric field in the gas gap or reduction of electron field emission from the cathode. In these cases it was assumed that gas insulated systems are clean inside. However, GIS can be contaminated with small metallic particles. The presence of these small conductive particles is a major cause of breakdown in GIS. Nearly 50% of all

failures of gas insulated substations is caused by particle induced breakdown[30]. In this section it is explained how the application of a coating can reduce the effect of metallic particle contamination on the breakdown strength of GIS.

2.5.1 Influence of particles on the breakdown strength of GIS

Consider a conductive particle present on the bottom of the tank of a horizontal coaxial electrode arrangement in which the tank is the outer electrode. When an electric field is applied on the system, the particle can acquire charge through the outer electrode. If the particle is charged, electrostatic forces can cause the particle to move in the system.

When the electrostatic force in the radial direction is sufficiently high, the particle can lift-off from the bottom of the tank against the gravitational force. The particle can fully cross the gap and make contact with the centre electrode changing into a protrusion on the electrode surface. This protrusion represents a field enhancement which effectively reduces the breakdown strength of the system. Furthermore, the particle can hover in the high field region near the centre conductor. Also in this case the particle causes a local electric field enhancement in the gas, resulting in a reduction of the corona onset and breakdown voltage.

In literature, extensive research can be found on the influence of particle contamination on breakdown initiation in GIS. For example, the breakdown voltage of contaminated coaxial electrode arrangements is investigated as a function of particle shape, size and material in [35–37]. In these papers the contamination consists of free moving metallic wire particles or spheres with a diameter ranging from 0.1 to 12.7 mm. Both aluminium and copper particles are used. The length of the wire particles varies between 0.8 and 50 mm. Also the diameter of the inner and outer electrode of the coaxial arrangement is varied.

Results obtained in [35–37] show that in the case of wire particles the breakdown voltage has a clear negative dependency with respect to the wire length, as shown in Figure 2.18. The presence of a "sharper" particle results in a lower breakdown voltage. For comparison, the figure also shows the breakdown voltage of a clean system.

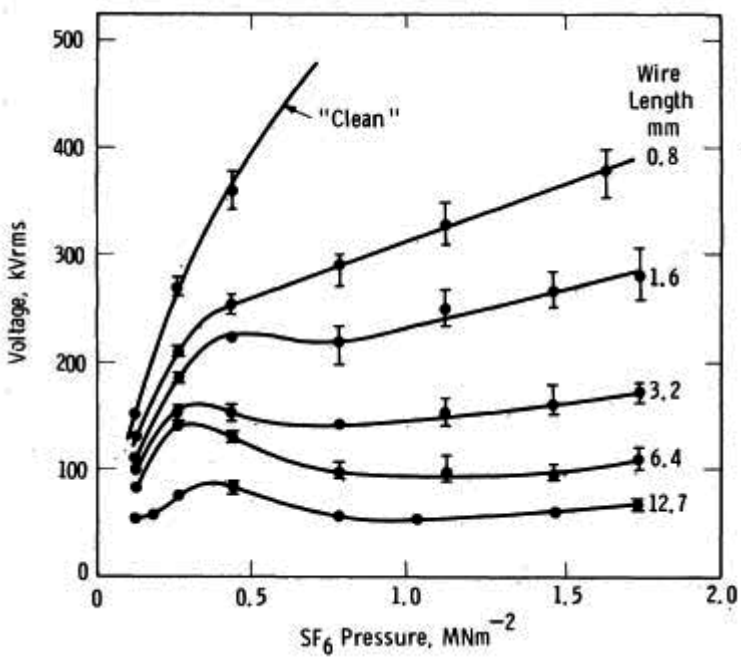

Figure 2.18: Breakdown voltage as a function of gas pressure and wire length, (0.4 mm diameter copper wire particles, AC voltage, 150/250 mm coaxial arrangement)[42]

The wire diameter has a different influence on the breakdown voltage. In [35, 37] it is shown that in most cases the breakdown voltage is reduced when the wire diameter is increased. Therefore, the presence of thicker and thus "less sharp" particles does not imply a higher breakdown voltage. However, these results also show that the breakdown voltage mostly has a negative dependency with respect to particle size (length and diameter). For spherical particles it is found in [35, 37] that the breakdown voltage is reduced when the particle diameter is increased.

Next to free moving particles, the effect of particles adhered to a spacer surface is also investigated [25, 26, 37]. In these papers, particles are fixed to the surface of either a post spacer [25, 26, 37] or a cone spacer [25, 26]. The number of fixed particles and the location varies.

The results in [44] show that in the case of wire particles attached to a post spacer, the breakdown voltage strongly decreases with an increase in wire diameter. Furthermore, the shape of the post spacer and the particle position have a significant influence on the breakdown voltage which is related to the corresponding local electric stress.

Figure 2.19 shows the three different types of post spacer used in [44]. These three spacer types all have a withstand voltage of 560 kV peak AC voltage when there is no particle contamination. Eight copper wire particles with a diameter of 0.45 mm and a

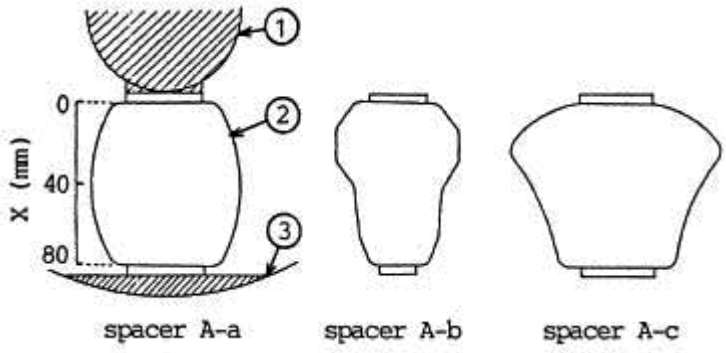

Figure 2.19: Three types of post spacer tested in [44].

length of 5 mm were fixed to the surface of the three spacers. The particle position x, depicted in Figure 2.19, was varied between 0 and 75 mm. The breakdown voltage was then measured as a function of particle position and is shown in Figure 2.20.

As can be seen from Figure 2.20, the presence of particles on the spacer surface can significantly reduce the breakdown voltage. Furthermore, the particle position has a large influence on the breakdown voltage. For example, the breakdown voltage of spacer A-b is the maximum 560 kV peak when the particle is close to the high voltage electrode

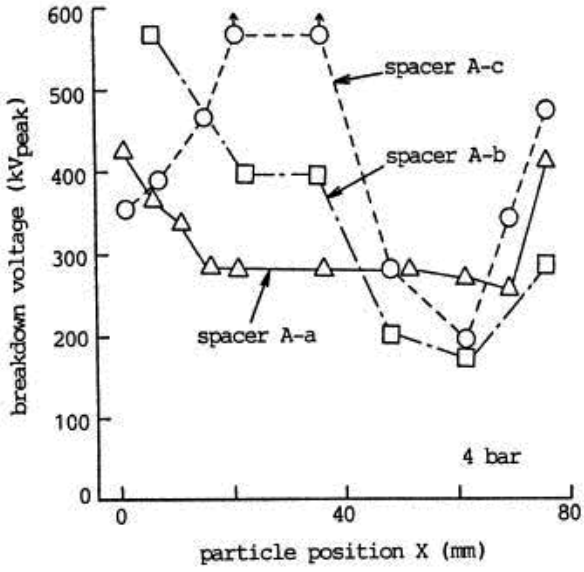

Figure 2.20: Breakdown voltage as a function of particle position for three post spacer types [44].

and is even lower than 200 kV peak when the particle is relatively close to the ground electrode (position X is 60 mm).

Figure 2.20 also shows that the breakdown voltage-position curve (V_{BD}-X) is significantly different for each spacer shape. This difference can be clarified by observing the electric stress distribution along the spacer surface, which is shown in Figure 2.21. In this figure the solid lines represent the total electric stress E_r on the spacer surface. The dashed lines represent the tangential component of the electric stress E_p.

Figure 2.21 and Figure 2.20 show that there is no correspondence between the maximum electrical stress E_r and the minimum breakdown voltage for each spacer. However, the variation in tangential stress component E_p shows a relation with the breakdown voltage. For example, the maximum breakdown voltage of spacer A-c occurs at X = 30 mm. At this location the tangential stress E_p is minimal. It seems that the tangential stress component has a large influence on the surface breakdown of a contaminated spacer. However, the total electric stress is also an important factor in the breakdown process. In [25, 26] it is shown that breakdown of a contaminated cone spacer always originated at the particle location with the highest total electric stress.

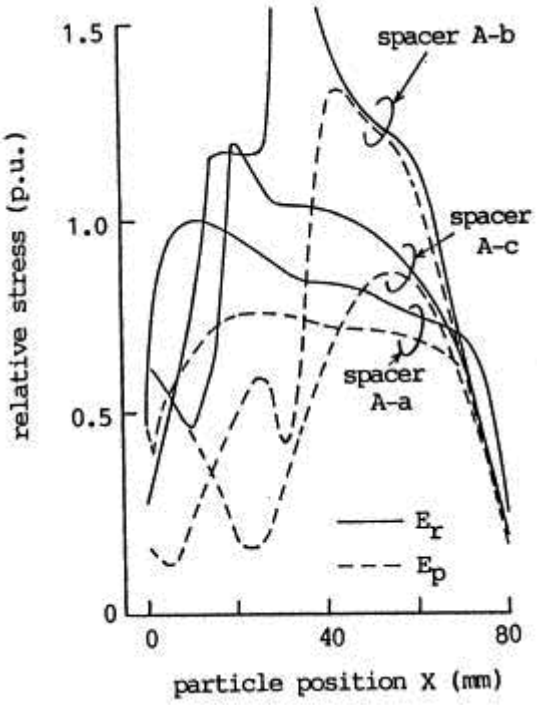

Figure 2.21: Electric stress distribution on spacer surfaces [44]

2.5.2 Dynamics of particle movement

In section 2.5.1 it was shown that both free moving particles and particles attached to a spacer surface can have a detrimental effect on the breakdown strength of a gas insulated system. Unfortunately it is not possible to fully prevent particle contamination of GIS. Therefore, to improve the breakdown strength of GIS, the negative effect of particles should be diminished.

Particle contamination is most harmful when the contamination is present at specific locations in GIS as described in section 2.5.1. To diminish the negative effects, it should be prevented that particles move to these locations. It is therefore important to understand particle movement in GIS.

Consider a coaxial gas insulated bus, which is contaminated with metallic particles. Generally, the particles are present on the bottom of the outer enclosure. When a voltage is applied, the particles acquire a charge Q via the outer enclosure, which is in this case the earth electrode. Because of the charge, the particles experience an electrostatic force in the direction of the centre high voltage electrode. The electrostatic force opposes the gravitational force on the particle as shown in the following equation [30].

$$F_p = k \cdot Q \cdot E - m \cdot g \qquad (5)$$

k is a correction factor between 0 and 1,
Q is the particle charge
E is the applied electric field at the location of the particle
m is the particle mass
g is the gravitational constant

When the applied electric field is strong enough the particle will lift off from the bottom of the tank. The corresponding electric field strength is the lift-off field E_{LO}. When the applied electric field at the enclosure remains below the lift-off field the particles will not move and potentially cause a breakdown of the system.

Therefore, to improve the breakdown strength of a gas insulated system the particle lift-off field should be increased. This can be accomplished by applying a dielectric coating on the outer enclosure[14–16, 38]. When a coating is applied on the inside of the outer enclosure the acquired charge of the particles will be smaller than in a bare enclosure provided that the applied electric field is equal. The coating is effectively an insulator which reduces the charging current.

Figure 2.22 shows an equivalent circuit diagram representing the charging of a particle on top of a coating layer. The lift-off field is in this case dependent on the coating capacity, resistivity and thickness as shown in the following equation [30]. As can be seen from the equation, the lift-off field is proportional to the square root of the coating thickness and resistivity.

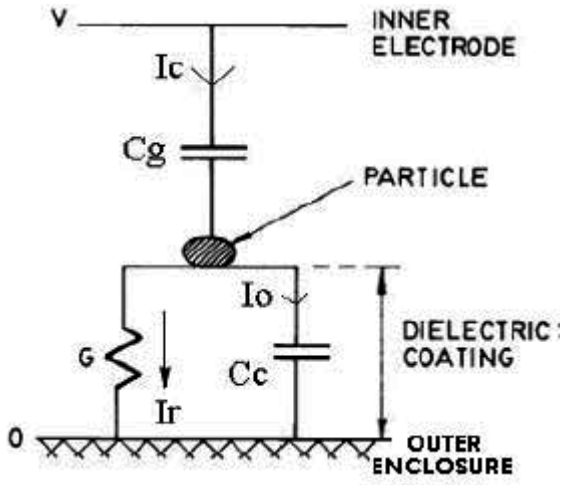

Figure 2.22: Model of particle charging through a coating layer [30].

$$E_{LO} = K\left[\left(1+\frac{C_c}{C_g}\right)^2 + \frac{1}{R^2\omega^2 C_g^2}\right]^{0.25} \cdot \left(\frac{\rho_c T}{S}\right)^{0.5} \qquad (6)$$

Where K is an arbitrary constant

Measurement results from [45] show that the lift-off field is significantly increased when a coating is applied. Figure 2.23 displays the lift-off field for 1.5 mm aluminium spheres on an anodized aluminium electrode in an SF_6 filled enclosure as a function of gas pressure and anodized layer thickness. Note that anodized aluminium is actually aluminium with an insulating aluminium oxide layer. Several manufacturers have produced GIS with anodized enclosures.

The particle jump height is also an important parameter which gives information on particle movement inside a gas insulated system. After lift-off, a particle can reach a certain height from the bottom of the tank which is also described as the maximum radial distance. The particle jump height is positively dependent on the particle charge and the applied electric field. The drag force that the particle experiences when moving and the particle mass reduce the jump height. The drag force on a moving particle is proportional to the particle velocity and gas viscosity.

For example, increasing the gas pressure results in an increase in gas viscosity and thus drag. Consequently, the particle jump height will be reduced. Because the application of a coating on the bottom of the enclosure reduces the acquired charge of a particle,

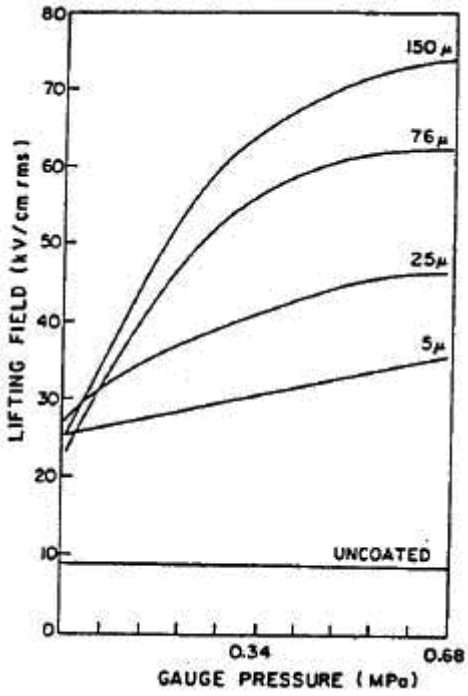

Figure 2.23: Lift-off field as a function of coating thickness and gas pressure. 1.5 mm diameter aluminium spherical particles on an anodized electrode [45].

the particle jump height is also reduced provided that the applied voltage remains unchanged.

Measurements and simulations of particle motion inside a gas insulated bus (GIB) or transmission line (GITL) including jump height can be found in [14–16]. In these papers the motion of metallic particles is measured or calculated for uncoated and coated systems with varying coating thickness and material. Also the particle metal and the applied voltage is varied.

Note that there are also other methods suggested in literature to reduce the motion of particle contaminants in a gas insulated system. Examples of these methods include the application of adhesive coatings, electrostatic trapping and radiative discharging [30].

Another option to control particle induced breakdown of GIS is to monitor particle motion inside the tank. Charging and movement of metallic particles inside a GIS enclosure produce low intensity partial discharges in the gas caused by the strongly enhanced electric field close to the particle. These partial discharges can be recorded by sensors

or UHF electromagnetic sensors (antennas). Extensive research on partial discharge and particle movement detection with UHF systems in GIS can be found in [46].

3

Experimental Methods

This chapter describes the applied experimental procedures, equipment and test specimens. Section 3.1. contains a detailed description of the test setup and equipment used for the gas and gas-coating breakdown tests. In section 3.2 it is shown which test electrodes are used in the breakdown tests. Section 3.3 describes the selected coating materials including material properties. The application procedure of the coatings is also described. Section 3.4 contains an explanation of the applied test procedures and parameters. Section 3.5 describes the material characterisation tests including equipment, procedures and material samples.

3.1 TEST SETUP AND GASES

To investigate the improvement of the electrical breakdown strength of gas insulated switchgear with the application of coatings on (parts of) the electrodes, a special test setup was designed in cooperation with Alstom. The setup mainly consists of a GIS enclosure and bushing as shown in Figure 3.1.

The centre vessel is filled with SF_6 and is used in combination with a bushing to transfer the test voltage to the test chamber on the right. The test chamber can be filled with any type of gas which is not corrosive to the spacer material or the aluminium enclosure. The maximum gas pressure is 1.0 MPa.

For the electrical breakdown tests, a rod-plane electrode arrangement is placed inside the test chamber. The aluminium plane electrode is fixed inside the enclosure and is not easily removed or replaced. The test voltage is applied to the plane electrode.

The test setup has a revolver assembly which can hold up to 12 small size rod electrodes. The electrode arrangement is displayed in Figure 3.2.

Figure 3.1: Picture of test setup GIS enclosure

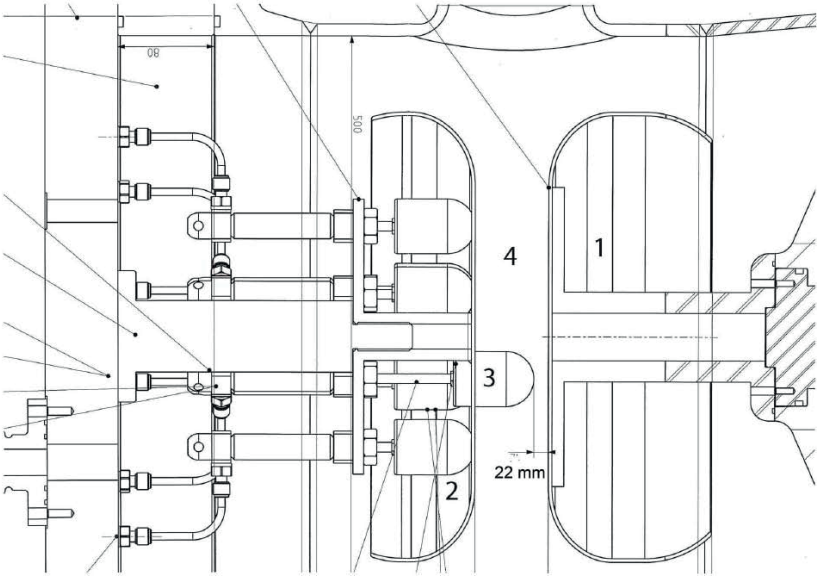

Figure 3.2: Rod-plane electrode arrangement with revolver assembly for the rod electrodes.

In the figure, number 1 represents the plane electrode. On the left side the revolver assembly can be seen. The rod electrodes are represented by number 3 and are all located within another plane electrode represented by 2. Thus, before commencing a breakdown test there are no rod electrodes present in the gas gap (4). The gas gap between the planes is 60.1 mm.

The rod electrodes are mounted on pneumatic pistons which can be actuated by applying gas pressure on the intake valve of each piston. When a certain rod electrode is selected for a test, the corresponding piston is actuated and the rod electrode will be pushed into the gas gap resulting effectively in a rod-plane arrangement. The actual gas gap will then be reduced to a distance between roughly 15 and 25 mm depending on the length of the rod electrode. The ends of the pistons are equipped with a thread. Therefore, the resulting gap distance can be controlled by varying the distance the electrode is screwed onto the piston end.

For the breakdown tests two different revolver assemblies are used. For small electrodes with a diameter up to 48 mm an assembly is used in which 12 electrodes can be mounted. This assembly is shown in Figure 3.3. For electrodes with a diameter up to 90 mm another assembly is applied which can hold up to 4 electrodes and is shown in Figure 3.4. When changing from small electrodes to large electrodes with a diameter larger than 48 mm the revolver assembly in the tank is removed and replaced by the other assembly. The applied rod electrodes are described in section 3.2.

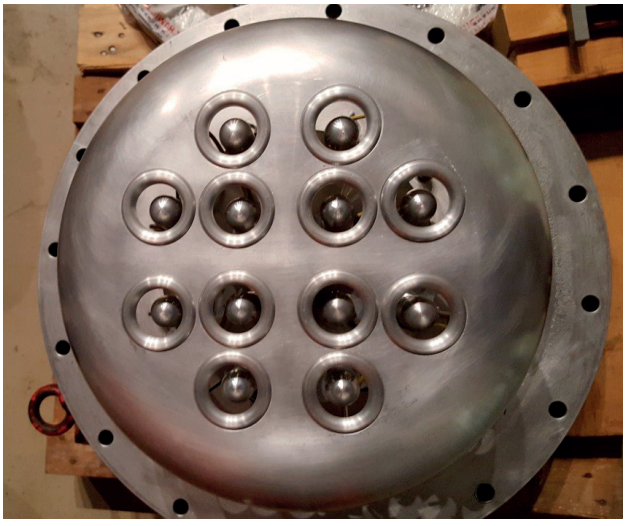

Figure 3.3: Revolver assembly for small rod electrodes.

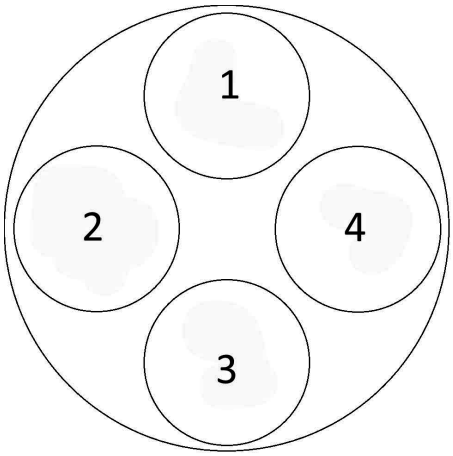

Figure 3.4: Revolver assembly for large rod electrodes.

The coating materials are applied to the rod electrodes. With the revolver assemblies it is possible to test up to 12 samples without evacuating and opening the tank, which results in a significant time gain.

3.1.1 Gases

As explained, the test tank can be filled with any non-corrosive gas up to a pressure of 1.0 MPa. The breakdown tests are conducted in SF_6 and dry air, which is considered as a possible replacement gas for SF_6. For practical reasons the gas pressure of dry air is set to 0.9 MPa for the breakdown tests. Note that it is not expected that the gas pressure in gas insulated systems will increase in the future due to cost constraints related to the required mechanical strength of the enclosure and spacers.

To obtain a good comparison between the breakdown test results in SF_6 and dry air the SF_6 gas pressure is set at 0.34 MPa. At this pressure the dielectric strength of SF_6 is theoretically equal to that of dry air at 0.9 MPa. For the determination of the desired SF_6 gas pressure, the relative dielectric strength is assumed to be 2.65, which was empirically determined with breakdown tests at Alstom. More information on gas breakdown and relative dielectric strength can be found in chapter 6.

For the verification of the breakdown model in chapter 6, extra breakdown tests were performed in SF_6 with a pressure between 0.34 and 0.6 MPa. Extra verification tests were also performed in dry air with a pressure of 8.0 and 9.0 MPa. To obtain reproducible breakdown test results in dry air, the tank is in all cases filled with unused gas from the bottle before the test is commenced. After each test, the dry air is released into the atmosphere.

3.2 ROD ELECTRODES AND GAP DISTANCE

The rod electrodes used in the rod-plane test setup are all aluminium rods with a hemispherical tip which has the same radius as the cylindrical part of the rod. Three different sizes were used for the breakdown tests as shown in Figure 3.5.

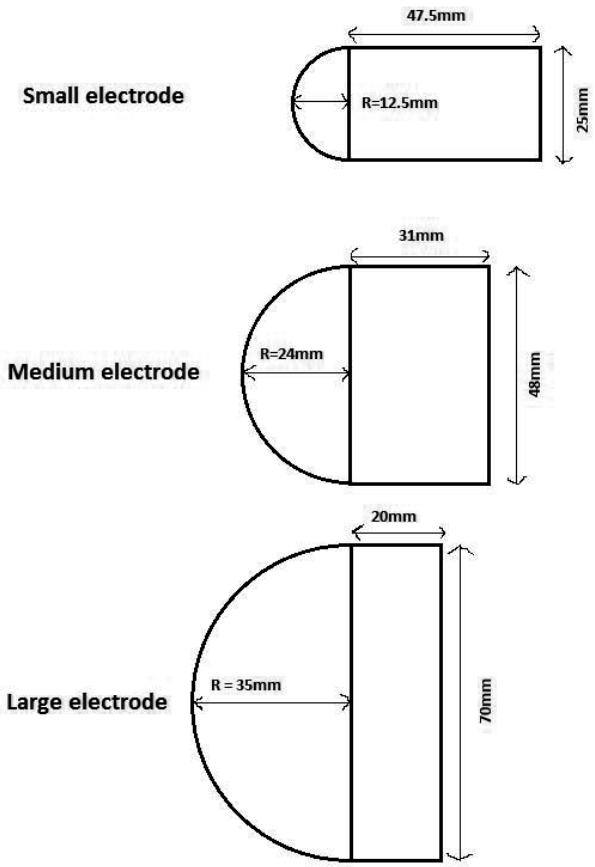

Figure 3.5: Dimensions of the three rod electrode types.

All three electrode types have a total length of 55 mm. The small electrode has a radius of 12.5 mm resulting in a width of 25 mm. The radius of the medium size electrode is 24 mm resulting in an electrode width of 48 mm. Finally, the large electrode has a radius of 35 mm and a width of 70 mm. The electrode dimensions and applied gap distance are based on the electric field distribution inside a 420 kV GIS as follows.

The electric field distribution can be represented by the field utilization factor f. This factor is equal to the average electric field strength divided by the maximum electric field strength present in a gas gap as shown in the equation below. Therefore, a field utilization factor of one represents a homogeneous electric field whereas a field utilization factor close to zero represents a strongly inhomogeneous electric field.

$$f = \frac{E_{av}}{E_{max}} \tag{7}$$

For the determination of the correct electrode dimensions and gap distance, the field utilization factor of certain locations inside the 420 kV GIS is calculated with the use of Finite Element Analysis (FEA). With the obtained utilization factor the correct electrode radius and gap distance are calculated. The test setup then has the same field utilization factor as the corresponding location inside the 420 kV GIS.

For example, consider the area surrounding a cone spacer inside the 420 kV GIS as shown in Figure 3.6. The location with the highest electric field strength is present in this area. To determine the field utilization factor in this area, the electric field is calculated with the use of FEA and a simulation voltage V_{sim} of 420 kV applied to the conductor. The enclosure potential is set at 0 V.

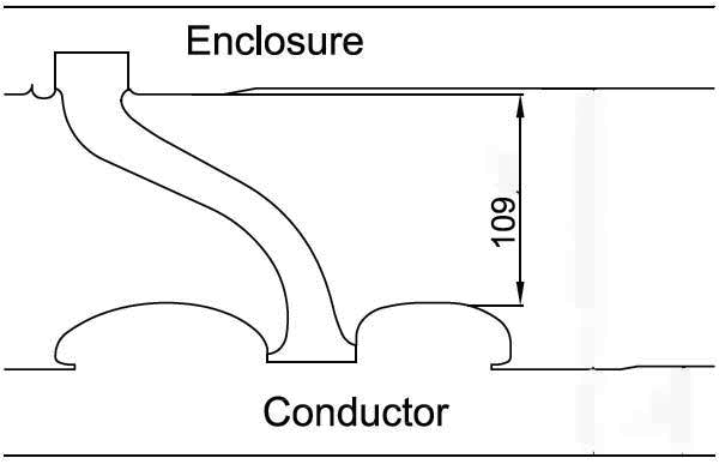

Figure 3.6: Sketch of the area surrounding a cone spacer inside a 420 kV GIS.

The calculation results show that the maximum electric field strength is 8.5 kV/mm. The average electric field strength is determined by dividing the applied voltage by the smallest gap distance d, which is 109 mm as shown in Figure 3.6. The field utilization factor is then calculated with the equation shown below.

$$f = \frac{E_{av}}{E_{max}} = \frac{\frac{V_{sim}}{d}}{E_{max}} = \frac{\frac{420\ [\mathrm{kV}]}{109\ [\mathrm{mm}]}}{8.5\ [\mathrm{kV/mm}]} = 0.45 \qquad (8)$$

The field utilization factor is thus 0.45 for the considered region.

To obtain a comparable electric field distribution in the rod-plane test setup with respect to the above mentioned 420 kV GIS, the correct electrode radius R and gap distance d should be calculated from the desired utilization factor of 0.45. This calculation can be performed with an equation determined by Azer and Comsa for a rod-plane geometry [47]. The equation is rewritten in the form shown below.

$$d = R\left(\sqrt[0.9716]{\frac{1}{f} - 1.1377}\right) \qquad (9)$$

The electrode radius R is set at 12.5 mm because of the size constraints related to the holes in the electrode holding plane and the range of possible gap distances. It should be possible to apply a dielectric layer of 10 mm thickness on the electrodes as described in section 3.3. Now the gap distance is calculated with an R of 12.5 mm and an f of 0.45. The calculation results show a required gap distance of 22 mm.

For the medium and large electrodes a comparable procedure is applied. Inside the 420 kV GIS there are also regions with a more homogeneous electric field distribution where breakdowns have taken place. Therefore it was desirable to include the field utilization factor of these regions in the tests. Also, the electrode surface area is larger than for the small electrodes which might result in a higher probability of defects in the coating layer. Furthermore, there is a larger gas volume in which ionization can occur. These two factors can reduce the breakdown strength of the system.

Unfortunately, the formula derived by Azer [47] is only valid for field utilization factors between 0.043 and 0.61. Therefore, a new formula was necessary for the medium and large size electrodes. Furthermore, the formula of Azer was derived in the 1970's with finite element analysis using a computer with limited computational power. The element size was relatively large resulting in a rough calculation of the electric field. With modern equipment and software the equation can also be refined.

The new formula was derived by performing electric field calculations in Lorentz-E (version 6.2, Integrated Engineering Software), which is also an FEA program. The electric field and the field utilization factor was calculated for a range of electrode radiuses R and gap distances d. The factor d/R was varied between 0.1 and 40 resulting in a field

utilization factor between 0.043 and 0.92. The obtained formula is shown in the equation below.

$$f = 0.7063 \cdot e^{-0.6602 \cdot \frac{d}{R}} + 0.2221 \cdot e^{-0.05532 \cdot \frac{d}{R}} \quad (10)$$

The medium size electrode with a radius of 24 mm and a gap distance of 22 mm has a field utilization factor of 0.60. The field utilization factor of the large size electrode with a radius of 35 mm and a gap distance of 22 mm is equal to 0.68.

3.3 COATING MATERIALS

This section describes the dielectric coatings which are applied on the rod electrodes presented in section 3.2. Three different types of coatings can be distinguished. First, thin coatings with a layer thickness between 25 and 570 µm. Second, double layer coatings consisting of two thin layers with a total thickness ranging from 340 to 590 µm. Third, thick coatings with a fixed thickness of 10 mm. These coatings are tested in the rod-plane electrode arrangement described in section 3.1.

3.3.1 Thin coatings

For the gas-coating breakdown experiments described in section 3.4, a total of seven different thin dielectric coating materials are applied on the rod electrodes. These materials are shown in Table 3.1. All thin coatings are produced by an external company.

Table 3.1: Thin dielectric coating materials.

Coating	Thickness [µm]
Epoxy-A	320
FP-I	420
FP-II	560
FP-III	25
FP-IV	40
PA11	250
Semiconductor A	450

EP-I

EP-I is a thermoset polymer based on epoxy resin and has a green colour as shown in Figure 3.7. For the application of the material on the rod electrodes the electrodes are

first degreased and sandblasted. Next, the coating is applied by dipping the electrodes in a bath containing the liquid resin. The resin is then polymerized at a temperature between 180 ºC and 230 ºC.

Figure 3.7: EP-I coated small size electrodes.

FP-I

FP-I is a thermoplastic fluoropolymer based on ECTFE (Ethylene ChloroTriFluoroEthylene) which is a copolymer of ethylene and monochlorotrifluoroethylene and is generally used in highly corrosive environments. The material is applied by electrostatic spraying at a temperature between 270 ºC and 300 ºC. Before spraying the electrodes are degreased and sandblasted. The material has a greyish green colour as can be seen in Figure 3.8.

Figure 3.8: FP-I coated small size electrodes

FP-II

FP-II is also a thermoplastic fluoropolymer based on ECTFE. However, this material contains an electrically conductive filler and has a black colour as shown in Figure 3.9. The material shows a high resistance to corrosive chemicals and is anti-static. The application procedure consists of electrostatic spraying at a temperature of 270 °C. The electrode pre-treatment consists of degreasing and abrasive blasting.

Figure 3.9: FP-II coated small size electrodes.

FP-III

FP-III consists of a thermoset resin loaded with PTFE filler and pigments resulting in a light blue colour as displayed in Figure 3.10. This material is generally used for dry

Figure 3.10: FP-III coated small size electrodes.

lubrication, electrical insulation and high temperature operation (up to 280ºC). Electrode pre-treatment consists of degreasing and abrasive blasting. The material is applied by pneumatic spraying (not electrostatic) and cures at a temperature of 180 ºC to 220 ºC.

FP-IV

FP-IV consists of a bottom adhesion layer and one or more topcoat layers which consist of FEP (Fluorinated Ethylene Propylene) reinforced with mica particles. This material is anti-adhesive and non-wetting and is suitable for food contact. The colour of the material is in this case olive green as shown in Figure 3.11. The production process consists of pneumatic spraying after which the material cures at a temperature of 400 ºC. Electrode pre-treatment consists of degreasing and micro-abrasive blasting.

Figure 3.11: FP-IV coated small size electrodes.

PA11

PA11 is a thermoplastic material based on polyamide 11, which is produced from castor beans. PA11 can therefore be seen as a bioplastic, although it is non-biodegradable. The material is used for the electrical insulation of cables and has a very smooth surface suitable for lubrication. The smooth surface is also used because of the aesthetic finish. The coating can have any colour from the RAL colour scale. In this case the colour is white as shown in Figure 3.12.

The production process consists of dipping in a bath filled with liquid material. The corresponding production temperature ranges from 260 ºC to 450 ºC. Electrode pre-treatment consists of degreasing, abrasive blasting and the application of a primer.

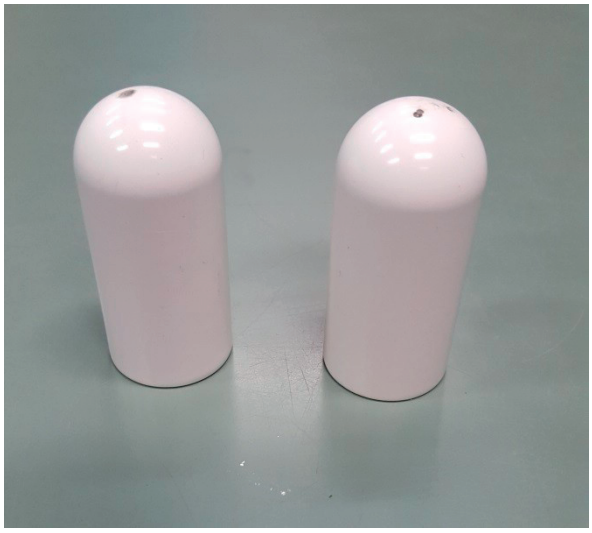

Figure 3.12: PA11 coated small size electrodes.

Semiconductor A

Unfortunately, the contents of this material are classified. However it is disclosed that this material has semiconductive properties. The colour of the material is green as shown in Figure 3.13.

Figure 3.13: Semiconductor A coated small size electrodes.

Table 3.2: Thin double layer coating materials.

Coating	Total thickness [µm]
FP-II + FP-I	590
FP-II + PA11	340

3.3.2 Double layer coatings

Next to the thin coatings, also double layered coatings were tested in the rod-plane test setup. These coatings are shown in Table 3.2.

As can be seen from the table, for both materials the base layer consists of FP-II which can be seen as a semiconductor. For the top layer either PA11 or FP-I is used as shown in Figure 3.14 and Figure 3.15 respectively. The reason to test these coating types was to

Figure 3.14: FP-II + FP-I coated small size electrodes.

Figure 3.15: FP-II + PA11 coated small size electrodes.

reduce the influence of the electrode surface roughness underneath the coating on the breakdown initiation voltage. This method can be compared with the application of a semiconductor layer between the conductor and the insulation of a power cable.

3.3.3 Thick coatings

Four different thick coating materials, which all have a thickness of 10 mm, are applied on the rod electrodes for the gas-coating breakdown experiments. The coatings are nanocomposites based on Huntsman Araldite epoxy resin type CY225 combined with hardener HY225. The coatings are produced at Delft University of Technology according to the production procedure described below. The materials are shown in Table 3.3.

Table 3.3: Thick dielectric coating materials.

Coating	Filler	APS
Neat Epoxy	No Filler	-
Epoxy nanocomposite A	0.2 vol.% hBN	70 nm
Epoxy nanocomposite B	0.2 vol.% cBN	150 nm
Epoxy Nanocomposite C	0.6 vol.% hBN	70 nm

As can be seen from Table 3.3, neat epoxy has no filler and thus only consists of the base material used for the nanocomposites. Nanocomposites A and C are filled with Hexagonal Boron Nitride (hBN) particles with an average particle size (APS) of 70 nm supplied by mk-NANO. The volume concentration of hBN particles in nanocomposite A is 0.2% whereas nanocomposite C has an hBN volume concentration of 0.6%. Nanocomposite B is filled with Cubic Boron Nitride (cBN) particles with an APS of 150 nm supplied by PlasmaChem. Due to the relatively large APS this composite can also be considered a

Figure 3.16: Neat epoxy coated small size electrodes.

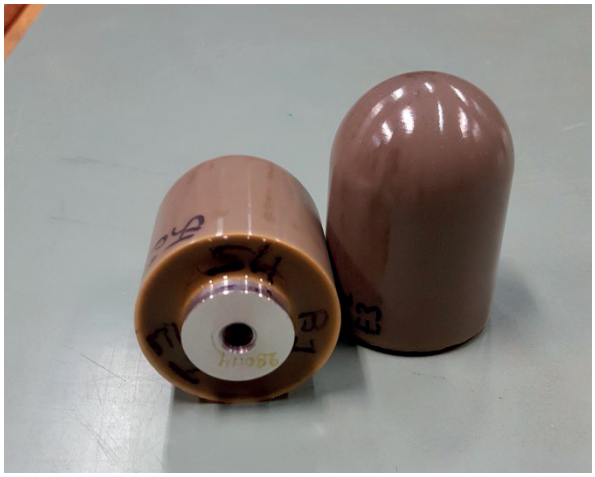

Figure 3.17: Nanocomposite B coated small size electrodes.

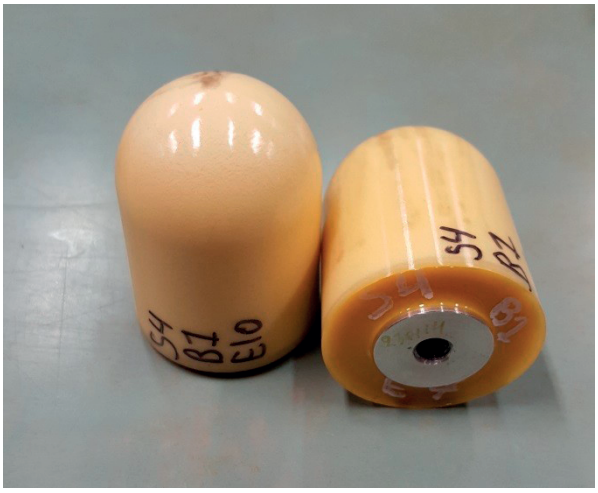

Figure 3.18: Nanocomposite C coated small size electrodes.

mesocomposite [48]. The volume concentration of cBN particles in nanocomposite B is 0.2%. Figure 3.16 shows two samples of small size electrodes coated with neat epoxy. Electrodes coated with nanocomposite B and C are shown in Figure 3.16 and Figure 3.17 respectively. Nanocomposite A has the same appearance as nanocomposite C.

The reason to choose nanocomposites is the fact that it is possible to decrease the relative permittivity of epoxy with the addition of low concentrations of BN nanoparticles [48]. Decreasing the relative permittivity of epoxy would be favourable in terms of breakdown voltage as explained in section 2.3. Furthermore, at Delft University of Technology extensive research was conducted on nanocomposites for high voltage applications and this

application would show that it is possible to produce nanocomposites with a relatively large volume compared to the generally used test samples.

BN nanoparticles are favourable for electrical applications because of the low electrical conductivity, high breakdown strength, high thermal conductivity and low relative permittivity of the particles[48]. The main reason to select cubic BN particles is the fact that these particles have higher thermal conductivity than hexagonal shaped BN particles[48].

Production procedure

The production of neat epoxy coatings starts with the combination of the correct quantities of resin and hardener in a mixing cup followed by thorough manual mixing with a stir bar. The mixture contains a large amount of air bubbles due to the mixing. Therefore, after mixing the epoxy coating is degassed in a vacuum oven for at least 2.5 hours until the air bubbles are visibly removed.

In the case of small size electrodes, the degassed epoxy is poured into the mould shown in Figure 3.19 and Figure 3.20. With this mould it is possible to produce 16 coated small size electrodes in one batch. The correct volume of epoxy is calculated and poured into the cavities in the bottom part of the mould, which is displayed in Figure 3.19. Before pouring the epoxy, silicone release agent is sprayed on the cavity surface to ensure a successful release of the coated electrodes. Furthermore, the mould is preheated to 75

Figure 3.19: Mould for small size electrodes, bottom part.

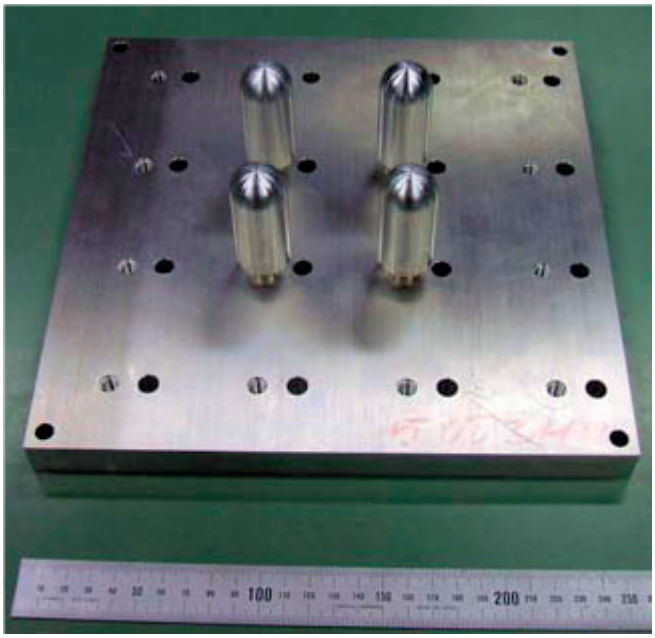

Figure 3.20: Mould for small size electrodes, top part, 4 electrodes mounted.

°C prior to pouring to prevent mechanical stress in the epoxy due to expansion of the mould during heating in the oven.

After pouring the epoxy, the bottom part of the mould is placed in the vacuum oven for 1 hour of degassing to remove the air bubbles formed during pouring. After the second round of degassing the preheated top part, shown in Figure 3.20, is placed gently on top of the bottom part.

The epoxy is now cured inside the oven at a temperature of 140 °C for 3 hours after which the electrodes remain in the mould in the oven at the same temperature for 17 hours of post-curing. After a total duration of 20 hours the oven is automatically switched off to let the mould cool down slowly to a temperature of 110 °C in 3 to 4 hours to prevent excess mechanical stress. When the mould has cooled down to 110 °C, the coated electrodes are removed from the mould. The coated electrodes are then placed in a vacuum desiccator to minimize moisture ingress. When all coatings are produced, the electrodes are placed back in the vacuum oven for a round of conditioning at 140°C for 24 hours to remove absorbed moisture.

For the medium and large size electrodes comparable moulds are used which can provide up to 4 coated electrodes per batch. The bottom and top part of the large size mould are shown in Figure 3.21 and Figure 3.22 respectively.

Figure 3.21: Mould for large size electrodes, bottom part.

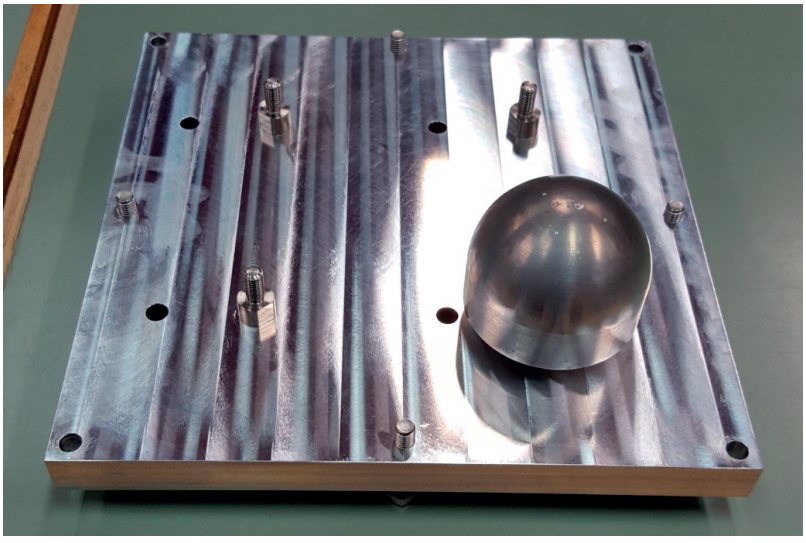

Figure 3.22: Mould for large size electrodes, top part, one electrode mounted.

The production procedure for the nanocomposites A through C is the same with respect to the pouring and curing in the mould. The production of the liquid resin is however more complicated compared to neat epoxy.

Nanocomposite production starts with an evaluation of the morphology and crystal structure of the supplied nanoparticles. The particle shape and size distribution of the nanoparticles were evaluated with Transmission Electron Microscopy (TEM). The applied TEM device is a Philips CM30T electron microscope. The results of the TEM analysis for hBN and cBN nanoparticles are shown in Figure 3.23 and Figure 3.24 respectively.

The results of the TEM analysis show that the hBN particles either have a quasi-spherical or an elongated shape. Moreover, the particle size distribution is broad with a range from 30 to 300 nm and the APS is equal to 70 nm. In the case of cBN particles the results show that the particle size ranges from 10 to 300 nm with an APS of 150 nm. The particle shape shows sharp edges.

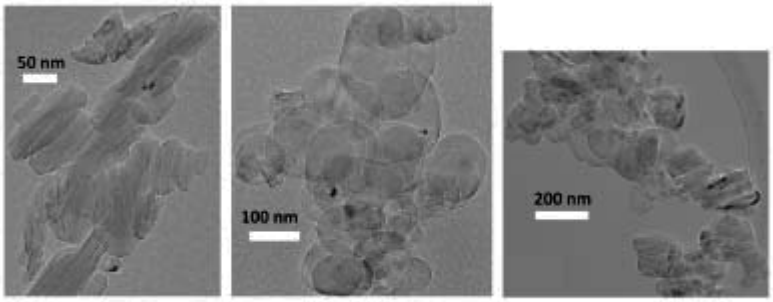

Figure 3.23: TEM analysis of hBN nanoparticles [48].

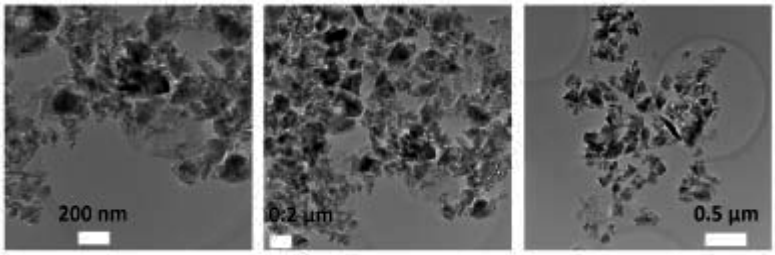

Figure 3.24: TEM analysis of cBN nanoparticles [48].

The crystal structure of the nanoparticles was characterized with X-Ray Diffraction (XRD) measurements using a Bruker AXS D8 Advance Diffractometer. The results of the hBN and cBN particles are displayed in Figure 3.25 and Figure 3.26 respectively. The value of 2q was varied between 5º and 90º with steps of 0.02º. The XRD spectrum of hBN shows a

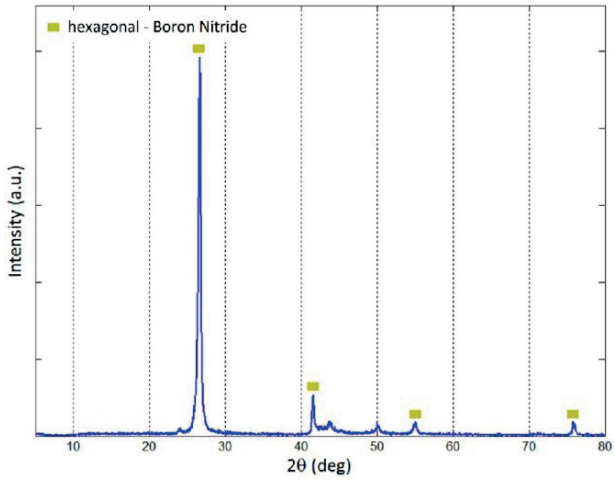

Figure 3.25: XRD spectrum of hBN nanoparticles [48]

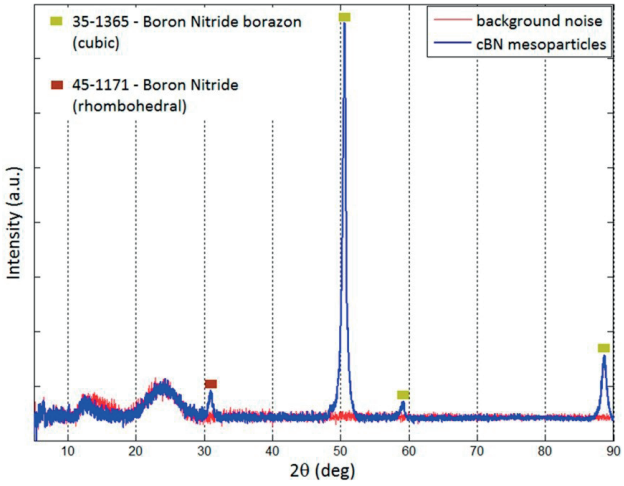

Figure 3.26: XRD spectrum of cBN nanoparticles [48]

match with the spectrum of a hexagonal crystal structure whereas the XRD spectrum of cBN matches with the spectrum of a cubic crystal structure [48].

The second step in the production of the nanocomposites is the modification of the nanoparticle surfaces with a suitable coupling agent to increase the compatibility between the epoxy matrix and the filler[48]. In this case the applied coupling agent is (3-GlycidoxyPropyl)trimethoxySilane (EPPS) which is an epoxy silane coupling agent. The amount of EPPS coupling agent used to modify the surface of both the hBN and cBN particles was 3 wt.% [48].

The determination of the correct amount of coupling agent for the modification of the nanoparticle surfaces is described in [48]. The successful modification of the nanoparticle surfaces was evaluated with Thermogravimetric Analysis (TGA) using a TGA/SDTA851e analyser from Mettler Toledo and Diffuse Reflectance Infrared Fourier Transform Spectrometry (DRIFTS) using a Bruker IFS 66 FT-IR spectrometer [48].

The final step in the production of the liquid nanocomposite resin is the mixing of the functionalized nanoparticles and the epoxy resin and hardener. The nanoparticles were directly mixed with the epoxy resin for 15 minutes in a speedmixer, which is in this case a DAC 150.1 FVZ speedmixer. Next, the correct amount of hardener was added to the mixture and the mixing continued for another 5 minutes. During the mixing process zirconia balls with a diameter of 1.95 mm were added to improve nanoparticle dispersion and distribution. The remaining production procedure, consisting of degassing, moulding, curing and post-curing, is the same as for the neat epoxy samples. Other possible nanocomposite synthesis techniques such as the solvent and nanomizer technique are explained in [48].

3.4 GAS BREAKDOWN EXPERIMENTS

In this section the experimental procedure is explained for the gas and gas-coating breakdown tests conducted in the rod-plane arrangement described in section 3.1. Furthermore, it is described which breakdown tests have been performed regarding the combination of materials, electrode sizes and gas types.

3.4.1 Test procedure

For the gas and gas-coating breakdown tests in the rod-plane arrangement it was decided to only apply standard lightning impulse (LI) voltage according to IEC standard 60060-1 [49]. The wave shape of the standard LI voltage is presented in Figure 3.27.

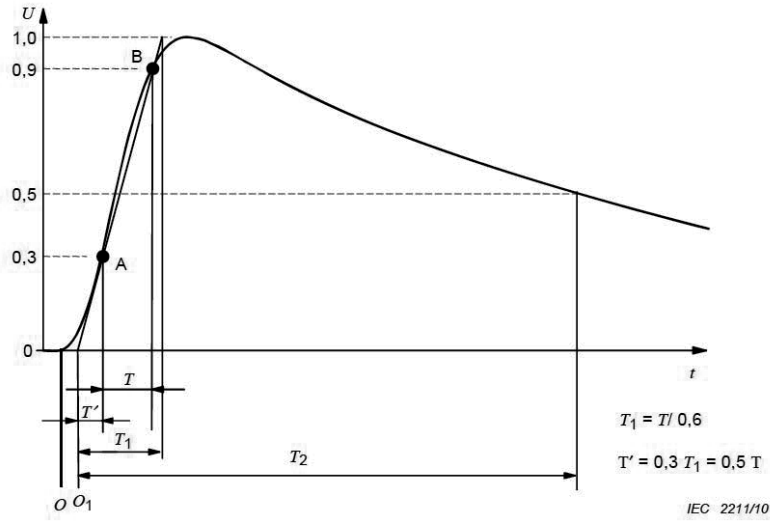

Figure 3.27: Standard Lightning Impulse wave shape including time parameters [49].

The main parameters which determine the shape of the LI voltage are T_1 and T_2. The front time T_1 indicates the steepness of the wave and is determined by first measuring the time difference T between the instant when the voltage reaches 30% of the peak value and the instant when the voltage reaches 90% of peak value (point A and B in the figure respectively). The front time T_1 is now calculated by dividing T by 0.6. The time to half-value T_2 is determined as the time interval between the virtual origin O_1 and the instant when the voltage has decreased to half the peak value. In a standard LI voltage the front time T_1 should be 1.2 µs with a margin of ±30% and the time to half-value T_2 should be 50 µs with a margin of ±20%. When a breakdown occurs during an LI breakdown test the recorded wave shape is different, as depicted in Figure 3.28. On the left side of the figure the wave is chopped by a breakdown on the tail (after the peak). In this case the wave shape is characterised by the front time T1, which is determined in the same way as described above, and the chopping time Tc (time-to-breakdown), which is the time between the virtual origin O_1 and the time instant at which the wave is chopped (point a in the figure). On the right side of Figure 3.28 the wave is chopped on the front (before the intended peak of the lightning impulse). In this case the wave is characterised only by the chopping time Tc.

For impulse voltages both positive and negative polarity can be applied. In this case it is decided to only apply negative lightning impulse voltage. Although the test voltage is applied on the plane electrode in the rod-plane arrangement, the mentioned polarity always refers to the polarity of the rod electrode. In the breakdown tests the rod electrode

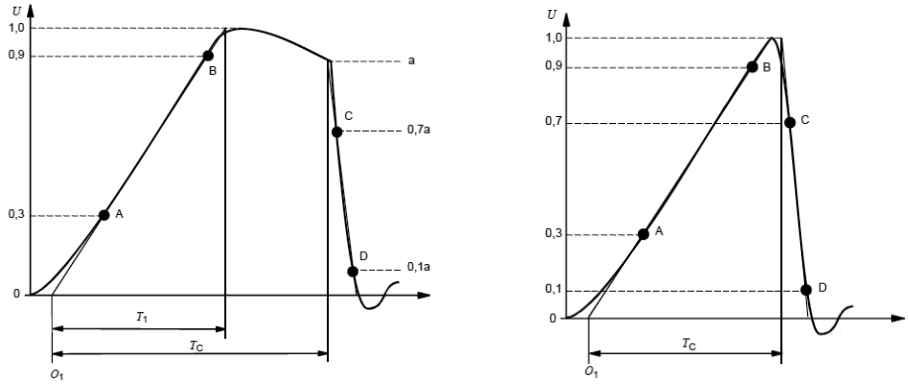

Figure 3.28: Left: Standard lightning impulse wave shape with a breakdown occurring on the tail, Right: Standard lightning impulse wave shape with a breakdown occurring on the front of the wave

is therefore always the cathode. The actual applied LI voltage on the plane electrode always has positive polarity.

The reason to only apply negative polarity standard LI voltage is the fact that for this voltage type, at SF_6 gas pressures above 0.3 MPa and a dry air pressure of 0.9 MPa, the lowest breakdown voltage was measured in the rod-plane arrangement and in Alstom 420 kV GIS. Negative LI is thus the worst-case situation for these systems and gas pressures. The 420 kV GIS is dimensioned to withstand this type of overvoltage. Consequently, the highest improvement in breakdown strength with the application of coatings can be expected for negative LI. The corresponding size reduction of GIS is in this case maximized. Also, by selecting only one voltage polarity and wave shape the available measurement time can be utilized to test a large range of promising coating materials.

To generate the desired test voltage, a Haefely impulse voltage generator is used as shown in Figure 3.29. This generator is a multistage Marx type generator with 20 stages of 200 kV each, reaching a maximum charge voltage of 4 MV. For the breakdown experiments in this research only 10 stages are in use, limiting the maximum charge voltage to 2 MV. The reason for this is the fact that the charging voltage of the capacitors is too low for the desired output voltage when all stages are in use. Reducing the number of stages to 10 ensures simultaneous firing of the sphere gaps in all active stages and thus the successful generation of a lightning impulse.

For the determination of the breakdown voltage of the gas gap between the rod and the plane electrodes and the breakdown voltage of the coating-gas combinations, several test procedures are available. For breakdown tests on the uncoated (bare) rod electrodes, test procedure D in section 7.3.1.4 of IEC standard 60060-1 [49] is applicable. Test procedure D is suitable for the determination of the 10% or 50% breakdown voltage of self-restoring insulation types.

Figure 3.29: 20-stage Haefely impulse voltage generator.

Test procedure D provides three possible test methods (classes) for the determination of the 10% or 50% breakdown voltage. The first test method is the Multiple-Level (Class 1) test in which at least 10 consecutive impulses of equal voltage level are applied after which the applied impulse voltage is raised to the next level and another set of 10 impulses is applied. This procedure is repeated until at least 5 voltage levels have been applied. The voltage difference DU between the levels should be between 1% and 6% of the expected 50% breakdown voltage. Next, the discharge frequency is calculated for each voltage level by dividing the recorded number of disruptive discharges (breakdowns) by the number of impulse applications for each voltage level. The calculated discharge

frequencies are then fitted to a suitable probability distribution function. Finally, the 50% breakdown voltage can be obtained from the determined probability function.

The second test method is the up-down (Class 2) test. This tests starts with a group of n impulse applications at a voltage level close to the expected breakdown voltage. If no disruptive discharge occurs in that group, the voltage level is raised with DU. If a disruptive discharge occurs, the voltage level is directly lowered with DU. After the voltage level is changed, a new group of impulses is applied. This process is repeated until the desired number of stresses has been reached.

The number of impulses (n) in a group is selected for the desired breakdown probability. For the determination of the 10% breakdown voltage the value of n should be 7 and for the 50% breakdown voltage n should be 1. Figure 3.30 shows a schematic representation of a 10% up-down test in which n is 7. The voltage difference between the levels DU should be between 1% and 3% of the expected (i.e. 10% or 50%) breakdown voltage. For the calculation of the 10% or 50% breakdown voltage only the accepted groups are taken into account. An accepted group is a group with a voltage level which occurs at least twice in the test procedure. For example, in Figure 3.30 the groups with a voltage level of 100 kV and 85 kV are not accepted because these levels occur only once in the test. For a correct 50% up-down test the total number of accepted groups (m) should be at least 20.

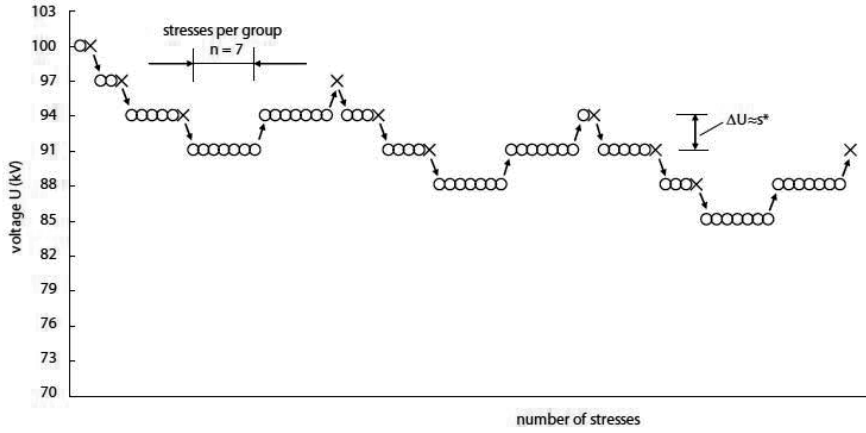

Figure 3.30: 10% Up-Down (Class 2) Test (n = 7, m = 14, DU = 3 kV). Circles represent impulse applications without disruptive discharge, crosses represent disruptive discharges [49].

The IEC standard presents a formula to calculate the 10% or 50% breakdown voltage. In this research, the withstand and breakdown voltages in the accepted groups in a 50% up-down test are fitted to a suitable probability distribution function from which the breakdown voltage of the desired breakdown probability can be determined.

The third test method is the progressive stress (class 3) test. This test starts with the application of an impulse with voltage level U_0. The voltage level of the consecutive impulses is increased step-wise until a disruptive discharge occurs. After the disruptive discharge this step-up to breakdown process is repeated, again starting at U_0. For a correct test, the number of disruptive discharges (n) should be at least 10. Therefore, at least 10 step-up to breakdown sets are required. The acquired breakdown voltages U_1 to U_n are fitted to a suitable probability function. The voltage step size DU should have a value between 1% and 3% of the expected 50% breakdown voltage.

The test procedure for the breakdown tests on the bare rod electrodes was selected by performing a series of breakdown tests using the three different test procedures. The three procedures were evaluated by comparing the acquired 50% breakdown voltage and the time needed to perform a correct test. From the results it was decided to select the 50% Up-Down test as the most suitable test method for the bare electrodes. The results of these preliminary tests are presented in chapter 4.

In the case of coated electrodes a different test procedure should be selected because the gas-solid insulation is non-self-restoring. The IEC standard [49] presents several test procedures for non-self-restoring insulation. Unfortunately, these test procedures are intended to provide pass/fail results and are thus not suitable for the evaluation of the 50% and 10% breakdown voltage. However, the progressive stress (class 3) test in procedure D could also be applied to non-self-restoring insulation. In this case, the sample would be replaced after the disruptive discharge at the end of one step-up to breakdown series. This test procedure is similar to the step-by-step tests in IEC standard 60243-1 [50].

When the progressive stress test is applied to the coated electrodes the breakdown behaviour after the first disruptive discharge is not evaluated. It might be possible that for one or more of the selected materials the breakdown voltage is not reduced after the occurrence of the first disruptive discharge. Therefore, to observe the breakdown behav-

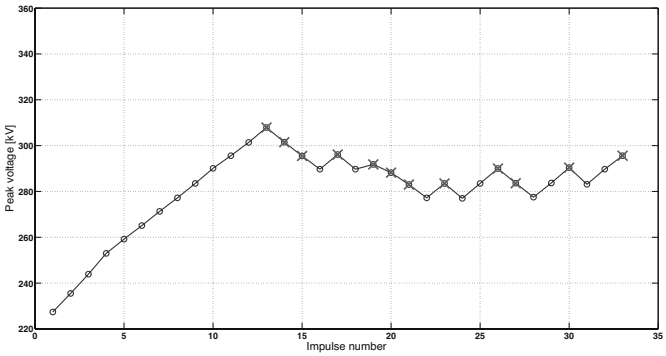

Figure 3.31: Combined test with step-up to breakdown and 50% up-down (the circles represent impulse applications and the crosses represent disruptive discharges).

iour of the coated electrodes after the first breakdown a combined test was composed. The combined test starts with one step-up to breakdown with the same parameters as the progressive stress test. After the first breakdown the test continues with a standard 50% Up-Down test as shown in Figure 3.31.

Waiting time

In the IEC standards no requirements are defined for the waiting time between impulse applications in lightning impulse tests. However, in literature it is stated that the waiting time between impulses can influence the breakdown behaviour of the system [51]. When a gas gap is in an equilibrium it is filled with neutral and charged species such as gas molecules, electrons and negatively and positively charged ions. These species are homogeneously distributed over the gap volume. Electrical breakdown starts with impact ionization of neutral gas molecules by collisions with electrons. The source of these electrons can be free electrons in the gas or negatively charged ions from which the excess electrons are detached through collisions, provided that the gas is electronegative. In equilibrium, there is a certain concentration of negatively charged ions and electrons available to start ionization.

Consider the application of a lightning impulse on the system without causing a disruptive discharge. During the impulse application electrostatic forces cause the charged species to move quickly to the oppositely charged electrode. The charged species are then neutralized upon collision with the electrode surface. Thus, directly after the application of the impulse the gas gap is effectively charge free.

The reestablishment of the equilibrium concentration of charged species directly starts through processes such as photo-ionization and photo-emission by background radiation, electron attachment and recombination processes. The reestablishment of equilibrium is not instantaneous and the related time constant in an SF_6 gap of 26 cm is found to be 2.5 minutes [51]. Therefore, the reestablishment of 90% of the equilibrium concentration takes 6 minutes.

To obtain a test in which the ion concentration is always close to equilibrium just before each impulse application, the waiting time between impulses should be 6 minutes. If the waiting time is significantly shorter than 6 minutes most impulses are effectively applied on a gas gap with a low ion concentration resulting in a higher breakdown voltage [51].

For the tests in the rod-plane gap the difference in breakdown behaviour between tests with 1 minute and 6 minutes waiting time was investigated. This investigation showed that in the rod-plane gap there is no significant difference in breakdown behaviour.

The difference with the experiment in [51] is the fact that the rod-plane gap is a factor 10 shorter. It might be the case that in such a short gas gap the time constant of equilibrium reestablishment is much shorter than 2.5 minutes. The results of the investigation

are presented in chapter 4. Thus, for the gas and gas-coating breakdown tests described in this section the waiting time between impulses is set at 1 minute.

3.4.2 Performed tests

The gas and gas-coating breakdown test performed in the rod-plane arrangement are summarized here.

Determination of test procedure

For the determination of the most suitable test procedure and waiting time between impulses the tests shown in Table 3.4 were performed on small size bare electrodes with a machined finish in dry air at a pressure of 0.9 MPa. The waiting time between impulses is 1 minute.

As explained in section 3.4.1, the number of disruptive discharges in the progressive stress test is represented by the term n, which is in this case 10. The number of impulses in each group in the up-down tests is also represented by n, which is 1 or 7 for the 50% and 10% up-down tests respectively. The number of accepted groups in the up-down tests is represented by the term m, which is 25 for the 50% up-down tests and 15 for the 10% up-down test.

Table 3.4: Tests on small size bare electrodes with machined finish in dry air, 1 min. waiting time.

Test procedure	Number of tests
Progressive stress test (n = 10)	2
50% Up-Down test (n = 1, m = 25)	2
10% Up-Down test (n = 7, m = 15)	1
Multiple Level test	1

Material tests on small size electrodes

For the investigation on the breakdown behaviour of the coated electrodes the tests displayed in Table 3.5 were performed on small size electrodes in dry air at 0.9 MPa using the combined test procedure.

Table 3.5: Tests on small size coated and bare electrodes in dry air, combined test procedure.

Coating	Number of tests
Bare, machined finish (reference)	2
Bare, sand blasted finish (reference)	2
EP-I	6
FP-I	6
FP-II	6
PA11	12
FP-IV	6
FP-III	6
Semiconductor A	6
Neat Epoxy (thick coating)	6
Nanocomposite A (thick coating)	6
Nanocomposite B (thick coating)	6
Nanocomposite C (thick coating)	6

Determination of impulse waiting time

To investigate the difference between the breakdown behaviour in tests with a 1 minute and 6 minutes waiting time the tests listed in Table 3.6 were performed on small size electrodes in dry air at 0.9 MPa using the combined test procedure with a waiting time of 6 minutes.

Table 3.6: Tests on small size electrodes in dry air, combined procedure, 6 min. waiting time.

Coating	Number of tests
Bare, machined finish	3
FP-I	3
FP-II	3
Bare, machined finish (multiple-level test)	1

Extra material tests on small size electrodes

Some materials showed interesting breakdown behaviour compared to the other materials in the breakdown tests with small size electrodes. Therefore, extra tests were performed to investigate this behaviour. The results of these tests are presented in chapter 4. The tests were performed on small size electrodes in dry air at 0.9 MPa and are displayed in Table 3.7.

Table 3.7: Extra tests on small size coated electrodes in dry air, combined test procedure.

Coating	Number of tests
FP-II, used (tested)	3
FP-II, new (50% up-down test)	3
Neat Epoxy, used (tested)	6
Nanocomposite A, used (tested)	6
Nanocomposite B, used (tested)	6
Nanocomposite C, used (tested)	6

Breakdown model verification tests

For the verification of the breakdown model described in chapter 5 the tests shown in Table 3.8 were performed on small size bare electrodes with a machined finish. The verification tests listed in Table 3.9 were performed on medium and large size bare electrodes with a machined finish.

Table 3.8: Verification tests on small size bare electrodes.

Gas type	Gas Pressure	Test Procedure	Number of tests
SF_6	0.34 [MPa]	Combined	3
SF_6	0.4 [MPa]	Combined	3
SF_6	0.5 [MPa]	Combined	1
SF_6	0.5 [MPa]	50% Up-Down	2
SF_6	0.6 [MPa]	50% Up-Down	3

Table 3.9: Verification tests on medium and large size bare electrodes.

Gas type	Gas Pressure	Test Procedure	Number of tests
Dry air	0.9 [MPa]	Combined	2 Medium, 2 Large
Dry air	0.8 [MPa]	Combined	2 Medium, 2 Large
SF_6	0.34 [MPa]	Combined	2 Medium, 2 Large
SF_6	0.4 [MPa]	Combined	2 Medium, 2 Large
SF_6	0.5 [MPa]	Combined	2 Medium, 2 Large
SF_6	0.6 [MPa]	Combined	2 Medium, 2 Large

Material tests on medium and large size electrodes

The influence of the electrode surface area on the breakdown behaviour of coated rod electrodes in the rod-plane arrangement was assessed with the breakdown tests on medium and large size rod electrodes presented in Table 3.10. With these tests the contribution of the electric field homogeneity with respect to the breakdown behaviour

Table 3.10: Tests on coated medium and large size electrodes in dry air, combined test procedure.

Coating	Electrode size	Number of tests
PA11	Medium	8
PA11	Large	8
Neat Epoxy	Medium	8
Neat Epoxy	Large	8

was also evaluated. The breakdown tests were performed in dry air at 0.9 MPa using the combined test procedure.

3.5 MATERIAL CHARACTERISATION

The gas and gas-coating breakdown tests described in section 3.4 were conducted to investigate the breakdown behaviour of coated electrodes and the possible improvement in breakdown voltage with respect to uncoated electrodes. In chapter 2 it is explained that the coating material properties can have an influence on the breakdown behaviour of coated electrodes and the corresponding improvement in breakdown voltage. To investigate the relation between the material properties and the breakdown behaviour it is necessary to define these properties with suitable measurements. This section describes the applied test equipment and procedures to evaluate the applicable material parameters.

3.5.1 Electrode and coating surface roughness

In section 2.4 it is explained that the electrode surface roughness can have a significant influence on the breakdown voltage of a gas insulated system. To investigate the influence of the electrode surface roughness on the breakdown test results, the surface roughness of the rod electrodes should be determined. The surface roughness of the rod electrodes is measured with a Mitutoyo Surftest SJ-301. This device is a tactile surface roughness tester which measures the surface roughness by moving a mechanical detector (stylus) along a straight line on a selected part of the electrode surface.

The device output consists of a roughness profile as shown in Figure 3.32. The figure shows the roughness profile of a bare rod electrode with a machined finish. The total length of the profile is 4 mm divided in 5 sampling lengths of 0.8 mm. To obtain the roughness profile without including long wave components, the input signal is filtered with a cut-off wavelength l_c of 0.8 mm.

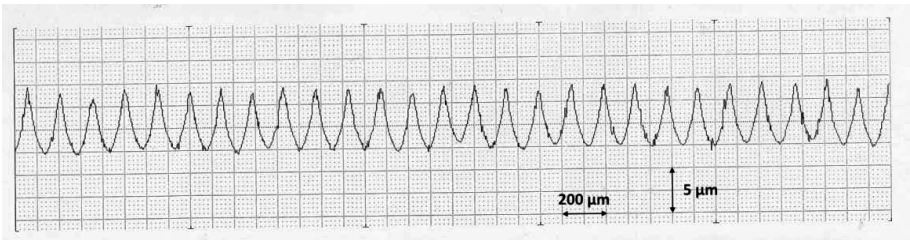

Figure 3.32: Surface roughness profile of a bare electrode with a machined finish.

The measurements are performed according to the JIS B 0601-1994 standard [40] which is comparable to the ISO 4287 standard [41]. Next to the roughness profile the measurement device determines several surface roughness parameters of which two are of interest. First, the maximum height R_y, which represents the difference between the height of the highest peak and the depth of the lowest valley with respect to the average line in one sampling length. Second, the ten point average roughness R_z, which is determined by the sum of the five highest peaks and the five lowest valleys in a sampling length divided by five. Thus, R_z represents the mean value of R_y in a sampling length. The device calculates the average value of R_y and R_z over the five sampling lengths.

With the method described above the surface roughness is evaluated for bare electrodes with a machined and a sand blasted finish. As explained in section 2.4, the application of a coating on the electrode surface can fill up the roughness of the metal surface resulting in a possible increase in breakdown voltage. However, the surface of the coating material also has a certain roughness which could have an influence on the breakdown behaviour of the gas-coating insulation. Therefore, the same surface measurement procedure is also applied on the coated rod electrodes.

3.5.2 Coating Thickness

In chapter 2 it is shown that the thickness of the coating layer can have an influence on the breakdown voltage of the system. Therefore it was desirable to measure the thickness of the coatings on the rod electrodes.

Furthermore, for the evaluation of the breakdown strength of the coating materials several samples were produced by spraying the coating material on a flat aluminium substrate. To correctly evaluate the breakdown strength of these coating materials the electric field strength at the breakdown locations should be acquired. Thus, the thickness of the material at these locations should be measured. The coating breakdown tests are described in section 3.5.5. Furthermore, for the dielectric spectroscopy described in section 3.5.3 and the conduction current measurements in section 3.5.4 the thickness of the coating layer on the flat samples is also required.

The coating layer thickness of the coated rod electrodes was measured with two different measurement methods. Firstly, the coating thickness was measured with a micrometer in two steps. In the first step the diameter of the bare electrodes was measured. The production tolerance of the rod electrodes regarding the rod diameter was found to be within 5 µm.

In the second step the diameter of the coated electrodes was measured at 4 to 6 locations depending on the unevenness of the coating layer. Next, the average diameter was calculated from the measured diameters. Finally, the diameter of the bare electrodes was subtracted from the average diameter of the coated electrodes and divided by two.

Secondly, the coating thickness was measured with a coating thickness gauge of the eddy current type. This type of thickness gauge was selected because the rod electrodes and the flat samples are aluminium which is conductive and non-ferromagnetic. The applied thickness gauge is a DeFelsko IT-826M-1250. Note that for the flat samples only the thickness gauge was used because the thickness of the aluminium substrates was unknown.

3.5.3 Dielectric spectroscopy

The permittivity of the coating material is an important factor with respect to the breakdown behaviour of a coated gas insulated system as explained in chapter 2. Therefore, the relative permittivity of the coating materials was measured using dielectric spectroscopy.

The permittivity of a material is related to the different polarization processes in the material such as dipole relaxation, ionic relaxation and electronic polarization. These processes are frequency and temperature dependent. The dielectric response is the result of these polarization processes and is therefore also dependent on frequency and temperature. The dielectric response can be represented by the relative complex permittivity ε(w, T) as shown in the equation below. The real part of the complex permittivity ε′ is the relative permittivity of the material which is the material parameter of interest. The imaginary part ε″ represents the dielectric losses in the material.

$$\varepsilon(\omega, T) = \varepsilon' - j\varepsilon'' \qquad (11)$$

The complex permittivity was measured as a function of frequency and temperature using a Novocontrol dielectric spectrometer. The spectrometer mainly consists of an impedance analyser (Alpha-A Mainframe combined with a ZGS sample cell) and a temperature control system (Quatro Cryosystem). The impedance analyser measures the complex impedance of the material test specimen according to the measurement circuit depicted in Figure 3.33.

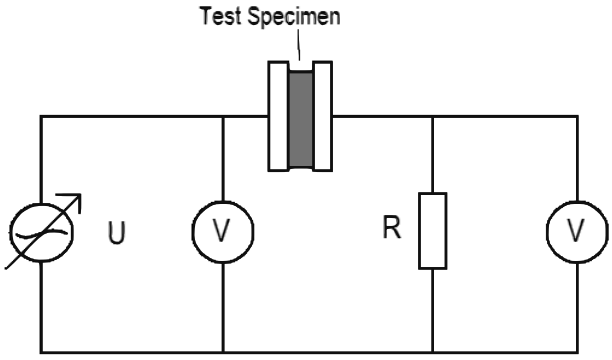

Figure 3.33: Circuit diagram of the impedance analyser.

During a measurement the AC voltage U is applied to the test specimen which is placed between two parallel plane electrodes in the sample cell. The two phase-sensitive voltmeters measure the amplitude and phase of the voltage across the test specimen and the current through the specimen. The resistor R is a shunt resistor for the current measurement. With the measured voltage U and current I the complex impedance can be calculated with the equation below.

$$Z = \frac{U}{I} \qquad (12)$$

From the complex impedance Z the capacitance C can be calculated. Because the test specimen is located between two parallel planes the complex permittivity can be calculated from the capacitance C, the surface area of the electrodes A and the dielectric material thickness d with the equation below.

$$\varepsilon(\omega, T) = \varepsilon' - j\varepsilon'' = C\frac{d}{\varepsilon_0 A} \qquad (13)$$

These calculations are automatically performed by the dielectric spectrometer. For the amplitude of the applied voltage either 1 V or 3 V can be selected. The frequency of the applied voltage can be varied between 3 µHz and 20 MHz to obtain the desired frequency spectrum of the complex permittivity. The impedance measurement range of the analyser is 10^{-2} to 10^{14} W.

The permittivity can also be strongly dependent on temperature. Therefore, the spectrometer system is equipped with a cryostat and temperature control system to accurately control the temperature of the sample cell. The temperature control system and the cryostat are displayed in Figure 3.34.

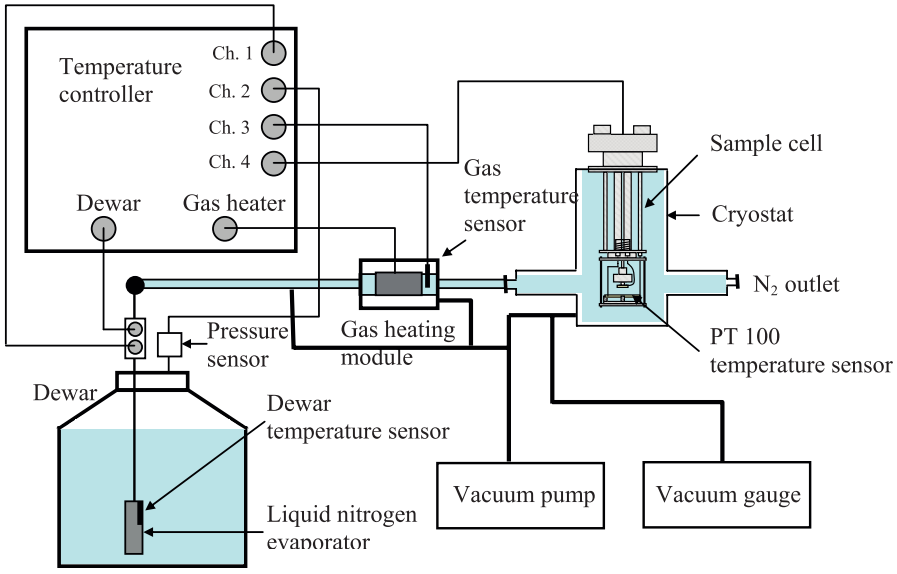

Figure 3.34: Schematic representation of the temperature control system and cryostat [52].

The temperature of the sample is controlled by a flow of nitrogen gas through the cryostat. The nitrogen gas source is a Dewar vessel filled with liquid nitrogen. With a resistive heating element the nitrogen gas flow can be regulated by evaporating liquid nitrogen and building up the desired gas pressure in the Dewar. Channels 1 and 2 measure the temperature and gas pressure inside the Dewar respectively. The Dewar output controls the evaporation rate of the liquid nitrogen. The gas heating module regulates the nitrogen gas temperature and channels 3 and 4 measure the gas temperature and sample cell temperature respectively. With the Quatro cryosystem the temperature of the sample cell can be controlled between -160 and 400 °C with a sensitivity of 0.01 K.

Measurement procedure

For the coating materials the frequency spectrum of the relative permittivity ε' and dielectric losses ε'' is measured within a frequency range of 1 Hz to 1 MHz. The frequency spectrum is recorded for temperatures between -40 °C and 120 °C with a step size of 20 °C. Thus, for each material nine spectra are obtained.

To evaluate the temperature behaviour of the relative permittivity and dielectric losses in more detail, temperature ramp tests were conducted. In a temperature ramp test the applied frequency is fixed and the temperature is increased from -40 °C to 120 °C with a ramp of 1 K/min while recording the relative permittivity and dielectric losses. The output of these tests is a temperature scan of the dielectric losses and relative permittivity at a fixed frequency. The temperature scan is recorded for frequencies between 1 Hz and

1 MHz with a step size of one decade. Thus, the total number of temperature scans obtained per material equals seven.

3.5.4 Conduction current

In section 2.3 it is explained that also the electrical volume conductivity of a coating material can have an influence on the breakdown behaviour of a coated gas insulated system. The volume conductivity of a material can be evaluated with a conduction current measurement.

In a conduction current measurement a material specimen is placed between two parallel plane electrodes as shown in Figure 3.35. Between the electrodes a high DC voltage is applied which causes polarization processes to occur in the material. These polarization processes give rise to a small polarization current which decreases in amplitude and disappears over time when the material is fully polarized.

When the polarization current has disappeared a steady state conduction current remains which is directly related to the DC resistance and thus the volume conductivity of the material. The polarization and conduction current can be measured with an electrometer which is a very sensitive current meter capable of measuring currents in the order of 10^{-14} A.

The HVDC source is connected to the high voltage electrode through the resistor R_{dc} to protect the electrometer from overcurrents in case the material specimen breaks down during the measurement. The resistance of R_{dc} is 660 MW. To effectively measure the conductivity of the material specimen only the current through the specimen should be recorded. However, currents may flow between the high voltage and measuring electrode along the specimen surface. These currents are also measured by the electrometer resulting in an error in the measurement of the volume conductivity. Therefore, guarding electrodes are located around the measuring electrode to direct the surface currents to

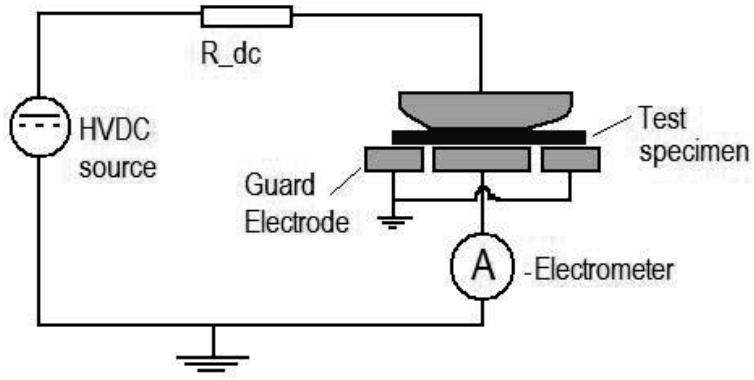

Figure 3.35: Schematic drawing of the conduction current setup.

ground instead of the measuring electrode. In this setup the HVDC source is a Heinzinger 40 kV/15 mA power supply and the electrometer is a Keithley 617.

The volume conductivity σ was calculated from the steady state conduction current density J_{ss} and applied electric field E_o with the equation below, which is Ohm's law.

$$\sigma = \frac{J_{ss}}{E_0} \tag{14}$$

The applied electric field E_0 was calculated by dividing the applied voltage by the thickness of the specimen. With the electrometer the steady state conduction current I_{ss} was measured. The conduction current density was then calculated by dividing the measured current by the surface area of the measuring electrode A_{el} as shown in the following equation.

$$J_{ss} = \frac{I_{ss}}{A_{el}} \tag{15}$$

The steady state conduction current can be seen when the polarization current has disappeared. When testing a material the time to reach steady state depends on the applied electric field and the temperature. The current is recorded from the time instant just before the voltage is applied up to 30 hours to observe the polarization current. The steady state conduction current is determined by fitting a curve to the measurement trace and extrapolating this curve to 100 hours. The current value at 100 hours is then taken as the steady state conduction current.

3.5.5 Coating breakdown tests

The final parameter of interest with respect to the breakdown of a coated gas insulated system is the breakdown strength of the coating materials. As explained in chapter 2, the electric field in the gas gap can be modified when a coating is applied on one of the electrodes. Ideally, the electric field in the gas is reduced with respect to the uncoated system because the gas is considered the weakest part of the gas-coating insulation. However, when the electric field in the gas is reduced, the electric field in the coating is enhanced.

When the enhanced electric field strength in the coating is relatively close to the breakdown electric field strength of the coating material, a breakdown might occur in the coating. Consequently, a full breakdown of the gas-coating insulation is very likely to occur due to the increased amount of ions in the gas caused by the breakdown of the coating.

The combination of both the breakdown strength of the coatings and the calculated electric field strength in the coatings can provide information on the location where the breakdown of the system starts (in the coating or in the gas). Therefore, the breakdown strength of the coating materials was evaluated with coating breakdown tests.

The coating breakdown tests are performed in the test setup depicted in Figure 3.36. The coating material sample, which is shown in grey, is placed on a grounded stainless steel plane electrode. For comparison reasons, it is favourable to apply lightning impulse voltage on the coating material samples. Unfortunately, this was not possible because a suitable small size impulse voltage generator was not available. Therefore, the breakdown tests are performed under power frequency AC voltage. The test voltage is applied to the test sample via a stainless steel sphere electrode depicted by the black circle. The electrodes and test sample are placed in a glass container which is filled with transformer oil. The oil is added to prevent partial discharges close to the high voltage electrode and discharges occurring on the surface of the test sample.

The breakdown tests are performed according to IEC 60243-1 [50]. The applied test procedure is the short-time (rapid-rise) test in which the applied voltage level is increased from zero at a uniform rate of rise until breakdown occurs. The rate of rise is selected to obtain a test duration between 10 and 20 seconds. The standard rates of rise are 100 V/s, 200 V/s, 500 V/s, 1 kV/s, 2 kV/s and 5 kV/s.

The short-time test is applied to ten samples of each material to obtain a good fit to a suitable distribution function. For the first sample of each material a low rate of rise was selected to make an estimation of the expected breakdown voltage. From this expected breakdown voltage the correct rate of rise for the remaining nine samples was calculated. According to the standard it is acceptable if the mean test duration of all ten samples is between 10 and 20 seconds. Therefore, the longer duration of the first test is within the test specifications.

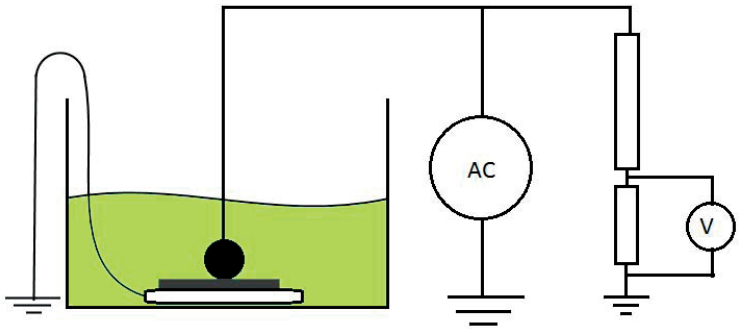

Figure 3.36: Schematic representation of the coating breakdown test setup.

4

Gas and gas-coating breakdown test results

This chapter presents the results of the gas and gas-coating breakdown experiments described in chapter 3. Section 4.1 describes the results of the different gas breakdown test procedures evaluated to determine the most suitable test procedure for the coated electrodes. The results of the breakdown tests on bare and coated small size electrodes are presented in section 4.2. In section 4.3, the difference is investigated between breakdown tests with a one minute and six minutes waiting time between impulse applications. Section 4.4 presents the breakdown test results on bare and coated medium and large size electrodes. Section 4.5 contains a discussion on the gas-coating breakdown test results including an evaluation of the improvement of the breakdown strength of the rod-plane arrangement due to the application of a coating on the rod electrode.

4.1 EVALUATION OF BREAKDOWN TEST PROCEDURES

As explained in section 3.4, an investigation was performed to determine the most suitable test procedure for the gas and gas-coating breakdown tests. For the uncoated rod electrodes the multiple level test, the 50% and 10% up-down test and the progressive stress test were compared with respect to the obtained 50% breakdown voltage U_{50} and the test duration.

From the results the value of U_{50} was calculated according to the standard [49]. Moreover, the 10% breakdown voltage U_{10} obtained from the 10% up-down test was compared with the U_{10} obtained from the 50% up-down test after fitting the results to a three parameter Weibull distribution. Deriving the U_{10} from the 50% up-down method with statistical calculations is allowed according to the standard [49].

Multiple level test (class 1)

The results of the multiple level test are displayed in Figure 4.1. In a multiple level test the number of disruptive discharges in each voltage level should be between 0 and 10

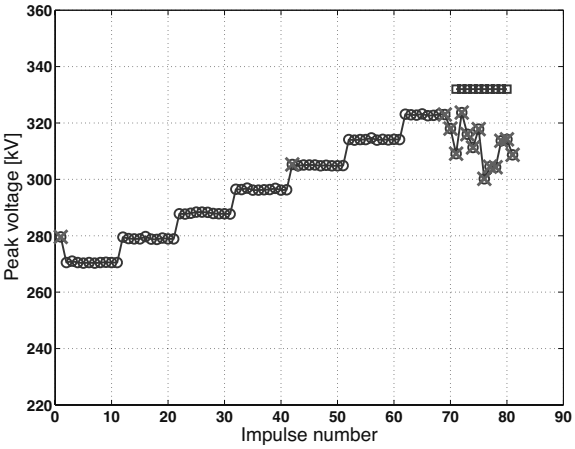

Figure 4.1: Multiple level test on small size bare electrode with a machined finish.

resulting in a disruptive discharge frequency between 0 and 1 for each level. Usually, the disruptive discharge frequency increases with the voltage level and the results should show a range of disruptive discharges frequencies between 0 and 1. The disruptive discharge frequencies per level are fitted to a suitable distribution function from which the desired values of the breakdown probability are derived.

The results show that there are no breakdowns in five of the eight applied voltage levels, one breakdown in one voltage level and three breakdowns in the seventh voltage level. Furthermore, in the highest voltage level all ten impulse applications resulted in a disruptive discharge.

In total, the multiple level test results contain the discharge frequencies listed in Table 4.1. Unfortunately, no suitable distribution function can be fitted to these test results. There-

Table 4.1: Disruptive discharge frequencies and voltage levels, multiple level test.

Voltage level [kV]	Disruptive discharge frequency
271	0
279	0
288	0
297	0
305	0.1
314	0
323	0.3
332	1

fore, the 50% breakdown voltage is not evaluated and this test procedure is rejected as a suitable candidate for the gas breakdown tests.

The aberrant breakdown behaviour in the multiple level test might be caused by conditioning of the gas due to the large amount of impulse applications and the short waiting between impulses of one minute. In the low voltage levels the consecutive impulse applications deplete the gas from ions and electrons as explained in section 3.4. Consequently, the lower six levels contain almost no disruptive discharges.

Moreover, in the 323 kV level a breakdown occurs after which all impulses result in a breakdown in both the 323 kV and 332 kV levels. This might be caused by the fact that, due to the first breakdown of the series, the gas conditioning has disappeared. Note that the applied voltage is already 10% higher than the predicted breakdown voltage. Furthermore, the first breakdown of the series results in a significant increase in the ion and electron concentrations in the gas gap reducing the breakdown strength of the gas.

This breakdown behaviour might be resolved by increasing the lightning impulse waiting time to six minutes. However, results in section 4.3 will show that at six minutes waiting time the multiple level test also shows the aberrant breakdown behaviour although less pronounced. Therefore, also at six minutes waiting time the multiple level test is unsuitable as a test procedure for the gas breakdown tests in this research. Further increasing the waiting time is considered to be unfeasible due to time constraints.

50% up-down (class 2) and progressive stress test (class 3)

In the 50% up-down and progressive stress test no aberrant breakdown behaviour was visible as shown in the examples in section 3.4. Thus, it was possible to compare the values of U_{50}. The comparison results are shown in Table 4.2.

Table 4.2: Comparison of 50% up-down and progressives stress tests

Test method	50% Breakdown voltage	Average test duration
50% Up-down	297 [kV]	30 min.
Progressive stress	295 [kV]	100 min.

The results in Table 4.2 show that the 50% breakdown voltage obtained in both test procedures shows a difference of 2 kV which is 0.7% of the expected breakdown voltage. Furthermore, this difference is significantly smaller than the voltage level step size DU of 3% applied in both test procedures. Therefore, the 50% breakdown voltage obtained by both test procedures is considered equal.

With respect to the time duration both tests are different. The duration of the 50% up-down test is on average 30 minutes which is 70 minutes shorter than the progressive

stress test. Therefore it was decided to select the 50% up-down test procedure for the gas breakdown experiments.

10% up-down test (class 2)

As explained, the 10% breakdown voltage can be determined with a 10% up-down test or a derivation from the statistical distribution fitted on the results of a 50% up-down test. The comparison results are listed in Table 4.3.

Table 4.3: Comparison of 10% and 50% up-down tests with respect to U_{10}

Test method	10% Breakdown voltage	Lower/Upper 95% confidence interval	Average test duration
10% Up-down	288 [kV]	-3.8 / +3.8 [kV]	90 min.
50% Up-down	288 [kV]	-5.5 / +6.9 [kV]	30 min.

The results in Table 4.3 show that there is no difference in 10% breakdown voltage between the two up-down tests. The 95% confidence bounds of the 10% breakdown voltage obtained from the 10% up-down test are somewhat smaller. However, the duration of a 10% up-down test is three times longer than the duration of a 50% up-down test. Therefore, in this research the 10% breakdown voltage was derived from the 50% up-down test results, saving the extra time of performing 10% up-down tests.

4.2 BREAKDOWN VOLTAGE – SMALL SIZE ELECTRODES

This section presents the results of the breakdown tests on the small size rod electrodes in dry air at 0.9 MPa. The results of the uncoated electrodes with a machined and a sand blasted finish are shown in section 4.2.1. The results of the thin coatings, double layer coatings and thick coatings are presented in sections 4.2.2, 4.2.3 and 4.2.4 respectively. In all cases the combined test procedure is applied.

4.2.1 Uncoated electrodes

As a reference, two breakdown tests were performed on bare electrodes with a machined finish and another two on bare electrodes with a sand blasted finish. The breakdown test results of a bare electrode with machined finish is shown in Figure 4.2 and the results of a bare electrode with sand blasted finish is displayed in Figure 4.3.

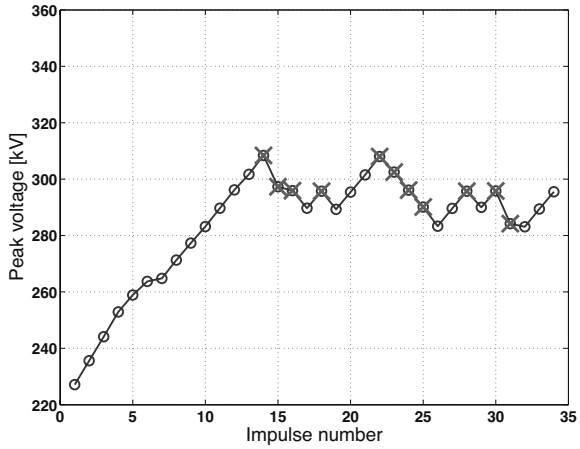

Figure 4.2: Breakdown test on a bare electrode with machined finish (m = 25).

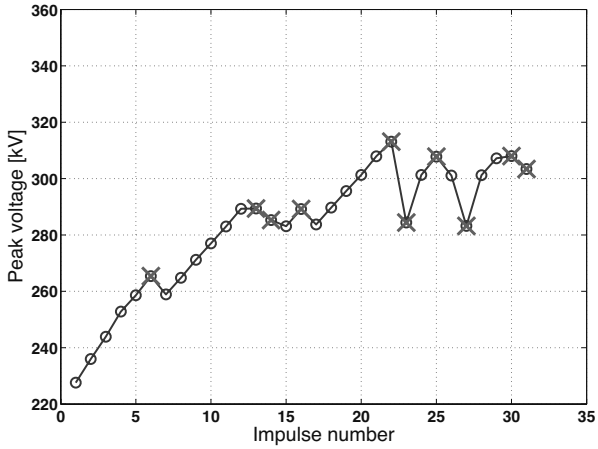

Figure 4.3: Breakdown test on a bare electrode with sand blasted finish (m = 25).

In the figures, impulse applications without breakdown are represented by the blue circles and impulse application resulting in a breakdown are represented by the red crosses. The results of the machined electrode show that the breakdown voltage remains at the same level after the first breakdown as is expected from an uncoated system.

In the case of the sand blasted electrode the breakdown behaviour is different as can be seen in Figure 4.3. The first breakdown occurs at significantly lower voltage than expected for an uncoated system. After the first breakdown it was possible to increase the voltage level of the applied impulses to a level comparable to the breakdown voltage of the machined electrodes.

As explained in section 2.4, the electrode surface roughness has a significant influence on the breakdown strength of a gas insulated system. Therefore, the low initial breakdown voltage might be caused by the relatively rough surface of the sand blasted electrodes. The surface roughness measurement results will be presented in section 5.1.

When the first breakdown occurs, the roughness peaks on the electrode surface might be evaporated or melted by the heat of the discharge plasma leaving a smoother electrode surface. Due to the smoother electrode surface the breakdown voltage might be increased to a value in the range of the machined electrodes as is the case in the test results.

The voltage of the 1st breakdown, the highest breakdown voltage and the 50% and 10% breakdown voltage of the tested electrodes are listed in Table 4.4. The 50% and 10% breakdown voltage are obtained by fitting a suitable probability distribution to the up-down part of the test results of each electrode. In almost all cases a three parameter Weibull distribution is applied. Furthermore, the mean values of the 50% and 10% breakdown voltage are obtained by performing a distribution fit on the combination of the breakdown data of the individual electrodes.

The mean first breakdown voltage of sand blasted electrodes is 11% lower than that of machined electrodes. Furthermore, the 50% breakdown voltage of sand blasted electrodes shows an increase of 3% with respect to the machined electrodes while the 10% breakdown voltage shows a reduction of 1,7 %. In both cases the difference is comparable to the voltage level step size DU in the up-down test and can therefore be considered to be insignificant.

Table 4.4: Breakdown test results of uncoated small size electrodes.

Test	1st Breakdown	Highest Breakdown	50% Breakdown	10% Breakdown
Bare, machined 1	308 [kV]	308 [kV]	299 [kV]	289 [kV]
Bare, machined 2	308 [kV]	308 [kV]	294 [kV]	285 [kV]
Mean Bare, machined	**308 [kV]**	**308 [kV]**	**297 [kV]**	**287 [kV]**
Bare, sand blasted 1	281 [kV]	321 [kV]	307 [kV]	282 [kV]
Bare, sand blasted 2	265 [kV]	313 [kV]	303 [kV]	281 [kV]
Mean Bare, sand blasted	**273 [kV]**	**317 [kV]**	**306 [kV]**	**281 [kV]**

The 50% and 10% breakdown voltages including the 95% confidence intervals are displayed in Figure 4.4 and Figure 4.5 respectively. Also from these figures it can be seen that the difference in 50% and 10% breakdown voltage between sand blasted and machined electrodes is insignificant.

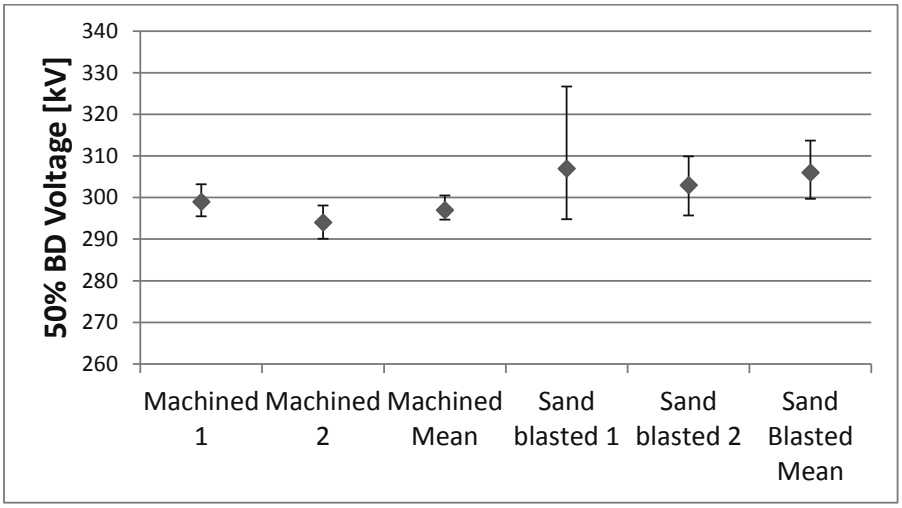

Figure 4.4: 50% Breakdown voltage of bare electrodes with machined and sand blasted finish. The 95% confidence intervals are represented by the error bars.

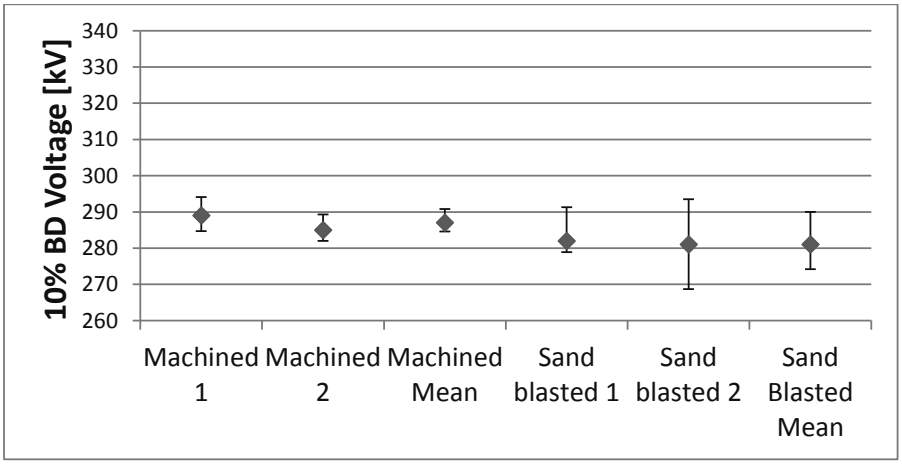

Figure 4.5: 10% Breakdown voltage of bare electrodes with machined and sand blasted finish. The 95% confidence intervals are represented by the error bars.

Moreover, the scatter in the breakdown test results is significantly larger for the sand blasted electrodes than for the machined electrodes. Thus, the 95% confidence intervals of the 50% and 10% breakdown voltage are wider for the sand blasted electrodes.

The large scatter in the test results of the sand blasted electrodes is caused by the lower first breakdown voltage. Furthermore, the large scatter might be caused by the

fact that after the first breakdown the surface roughness of the electrode tip shows a significant variation.

The unreliability plots of the three parameter Weibull distributions fitted to the breakdown test results of the machined and sand blasted bare electrodes are shown in Figure 4.6. The blue line represents the probability plot of the bare electrodes with a machined finish. The probability plot of the electrodes with a sand blasted finish is represented by the brown line. The 95% confidence intervals are represented by the dashed red lines.

The 95% confidence interval of the machined electrodes is smaller than that of the sand blasted electrodes over the entire probability range. Furthermore, the figure shows that the probability line of the machined electrode is significantly steeper which is related to the smaller scatter in the breakdown test results. In the probability range of 3% to 55% the confidence intervals of both electrode types overlap. Therefore, the difference in the breakdown voltage of both electrode types in this probability range is insignificant.

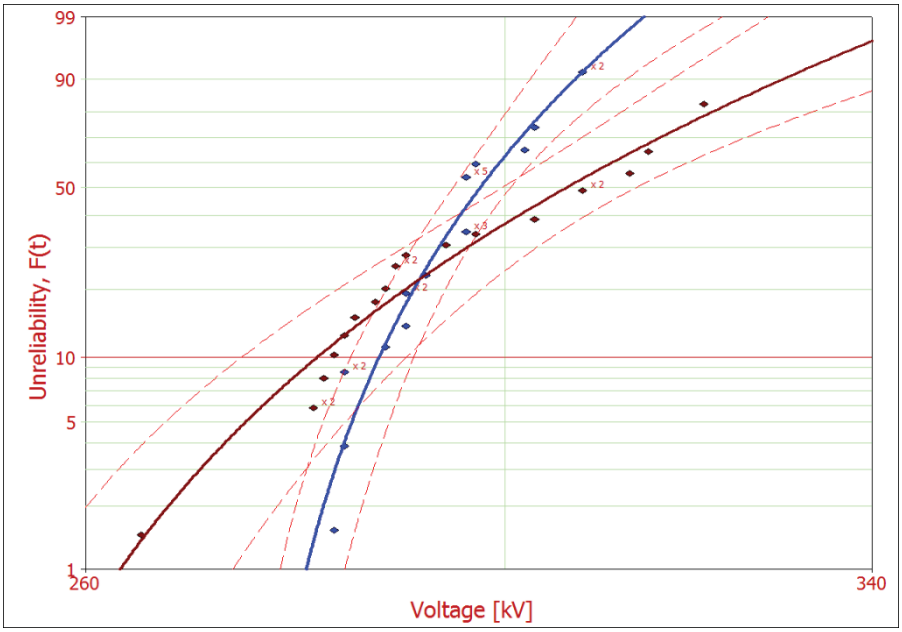

Figure 4.6: Three parameter Weibull unreliability plots of bare electrodes with machined (blue line) and sand blasted (brown line) finish. The 95% confidence bounds are represented by the red dashed lines.

4.2.2 Thin coatings

As an overview the tested thin dielectric coating materials and the corresponding thicknesses are listed in Table 4.5. In section 3.3 the coating materials are described in more

detail. The breakdown test results on the thin coatings are described per material type. At the end of this subsection an overview will be presented.

Table 4.5: Thin dielectric coating materials.

Coating	Thickness [µm]
EP-I	320
FP-I	420
FP-II	560
FP-III	25
FP-IV	40
PA11	250
Semiconductor A	450

EP-I

The breakdown test results of an EP-I coated electrode are shown in Figure 4.7. From the results it can be seen that after the first breakdown the breakdown strength of the system is reduced to a level below the breakdown strength of a bare electrode with a machined finish. This behaviour was observed for all tested electrode samples.

The fact that the breakdown strength is reduced to a level below that of the machined electrodes is caused by the fact that the coating is punctured by the discharge. The puncture is a small area of bare electrode surface. The latter might present a reduced breakdown voltage close to that of a bare electrode. Furthermore, the edges of the puncture could also contribute to an increased surface roughness resulting in a further reduction of the breakdown voltage.

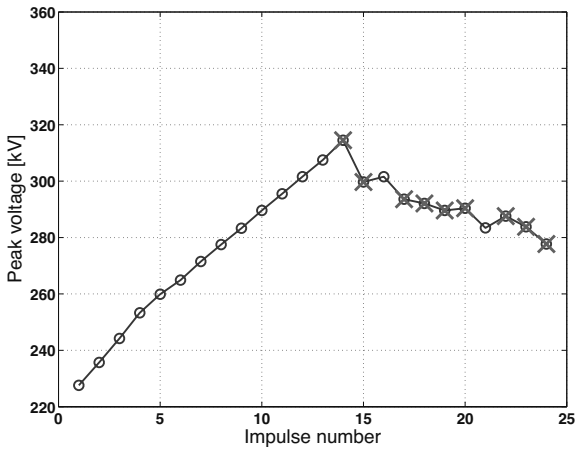

Figure 4.7: Breakdown test results of an EP-I coated electrode.

The values of the first and highest breakdown voltage of the individual EP-I coated electrodes are listed in Table 4.6. As explained and as can be seen from the table, the first breakdown is the highest breakdown voltage measured for each electrode. The 1st breakdown voltage for the EP-I coated electrodes ranges from 296 kV to 315 kV.

Table 4.6: 1st and highest breakdown voltage measured on EP-I coated electrodes

Electrode	1st Breakdown	Highest Breakdown
1	308 [kV]	308 [kV]
2	296 [kV]	296 [kV]
3	303 [kV]	303 [kV]
4	315 [kV]	315 [kV]
5	315 [kV]	315 [kV]
6	314 [kV]	314 [kV]

The results indicate that the EP-I coated electrodes are damaged after the first breakdown and are thus non-self-restoring. Therefore, the 1st breakdown voltages are fitted to a suitable probability distribution from which the 50% and 10% breakdown voltages are derived and compared with the results of the bare, machined electrodes. The 50% and 10% breakdown voltage of EP-I coated electrodes are shown in Figure 4.8 and Figure 4.9 respectively.

The 50% breakdown voltage of the EP-I coated electrodes shows a minor improvement of 4% with respect to bare electrodes. When the 10% breakdown voltage is compared with that of a bare electrode an improvement of 2.7% is found. However, the confidence intervals overlap which indicates that there is no improvement in the 10% breakdown voltage.

The third, fifth and seventh breakdowns of each electrode were also fitted to a probability distribution to evaluate the behaviour of EP-I coated electrodes after the first breakdown. The 50% and 10% values of the 3rd, 5th and 7th breakdown are also displayed in Figure 4.8 and Figure 4.9 respectively. As explained, the EP-I coating insulation is non-self-restoring which is shown by the fact that the 3rd, 5th and 7th 50% and 10% breakdown voltage are lower than the first breakdown voltage. Furthermore, both the 50% and 10% breakdown voltage show a decreasing trend with an increase in the breakdown number.

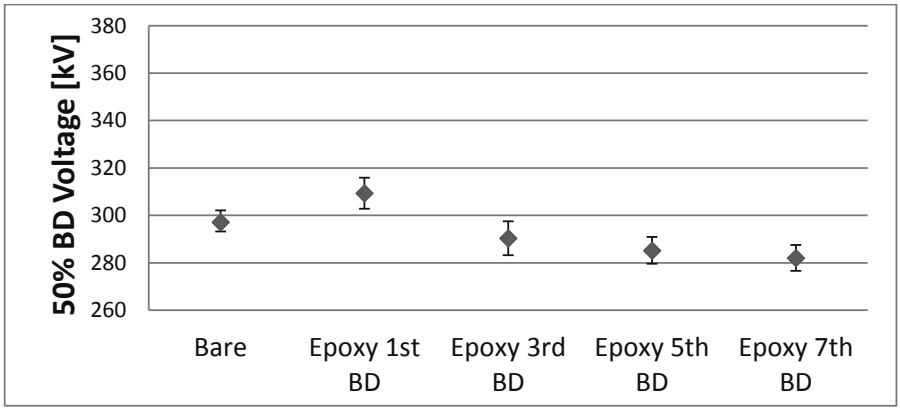

Figure 4.8: 50% Breakdown voltage of EP-I coated electrodes. The 95% confidence intervals are represented by the error bars.

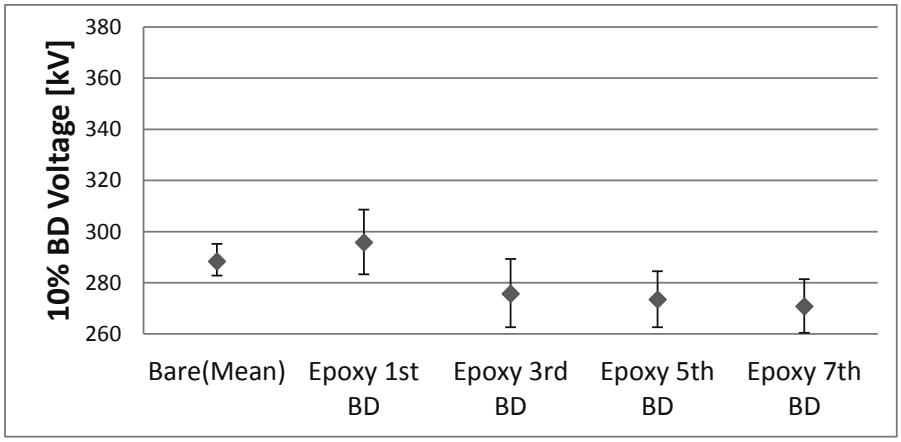

Figure 4.9: 10% Breakdown voltage of EP-I coated electrodes. The 95% confidence intervals are represented by the error bars.

FP-I

The breakdown test results of a FP-I coated electrode are shown in Figure 4.10. As with EP-I the breakdown strength of a FP-I coated electrode is reduced to a level below that of a bare electrode.

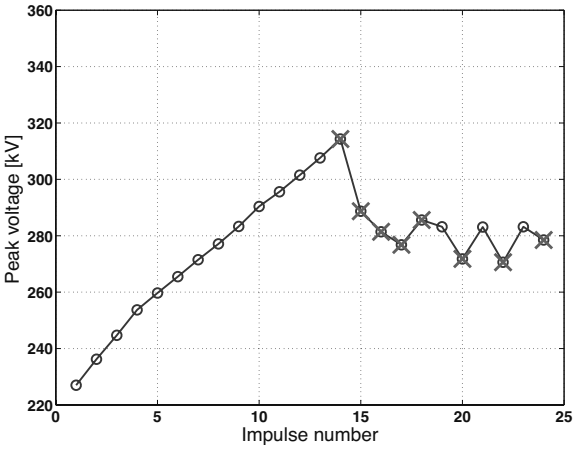

Figure 4.10: Breakdown test results of a FP-I coated electrode.

The 1st and highest breakdown voltage measured on the FP-I coated electrodes are displayed in Table 4.7. In almost all cases the highest breakdown voltage occurred at the first breakdown as shown in the example in Figure 4.10. However, in the case of electrode 3 the highest breakdown voltage occurred at the sixth breakdown. In the test results of this electrode it was observed that after the first four breakdowns it was possible to increase the impulse voltage to 318 kV before the next two breakdowns occurred. The test results of electrode 3 are presented in appendix A.

The 1st breakdown voltage of the FP-I coated electrodes ranges from 284 kV to 328 kV. The 1st breakdown voltage thus shows a scatter of 42 kV which is significantly larger than the scatter in the 1st breakdown voltage of the EP-I coated electrodes. The results of electrode 7, 8 and 9 are obtained with a waiting time between impulses of 6 minutes instead of 1 minute to observe the influence of the waiting time on the breakdown test

Table 4.7: 1st and highest breakdown voltage measured on FP-I coated electrodes.

Electrode	1st Breakdown	Highest Breakdown
1	314 [kV]	314 [kV]
2	315 [kV]	315 [kV]
3	302 [kV]	318 [kV]
4	284 [kV]	284 [kV]
5	293 [kV]	293 [kV]
6	308 [kV]	308 [kV]
7	297 [kV]	297 [kV]
8	310 [kV]	310 [kV]
9	328 [kV]	328 [kV]

results. The influence of the waiting time on the breakdown test results will be discussed in section 4.3.

Also for the FP-I electrodes the results show that the coating-gas insulation is non-self-restoring. The comparison between the bare and FP-I coated electrodes thus considers the 50% and 10% quantiles of the first breakdown voltage of the FP-I coated electrodes. The 50% and 10% quantiles of the 1st, 3rd, 5th and 7th breakdown voltage are depicted in Figure 4.11 and Figure 4.12 respectively.

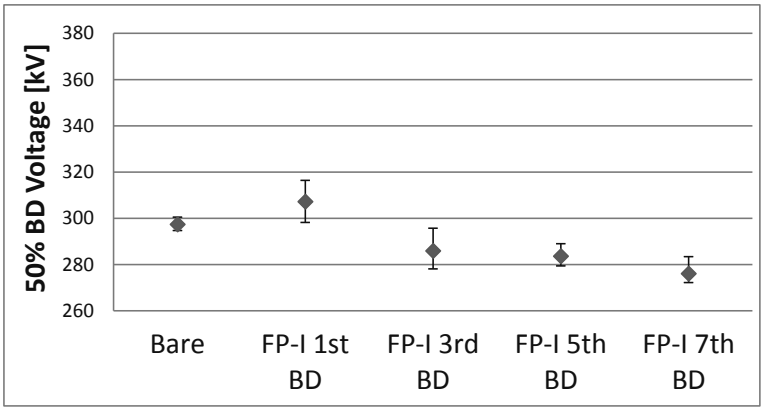

Figure 4.11: 50% Breakdown voltage of FP-I coated electrodes including 95% confidence intervals.

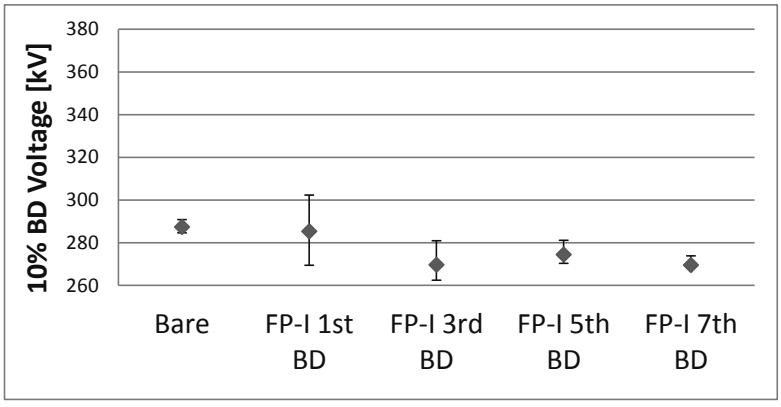

Figure 4.12: 10% Breakdown voltage of FP-I coated electrodes including 95% confidence intervals.

The 50% breakdown voltage seems to show a minor improvement of 3.4% with respect to a bare electrode. However, the 95% confidence intervals overlap which implies that the FP-I coated electrodes show no improvement with respect to bare electrodes. Also in this case the 50% breakdown voltage shows a downward trend when the breakdown

number is increased. Note that the 95% confidence intervals are wider than those of the EP-I coated electrodes due to the larger scatter in the measured breakdown voltages.

When observing the 10% quantile of the 1st breakdown voltage no significant difference can be found with respect to the bare electrodes. The corresponding 95% confidence interval is also significantly wider than that of the bare electrodes due to the larger scatter and the smaller amount of breakdown data available for distribution fitting. The difference between the 10% quantiles of the 3rd, 5th and 7th breakdown voltage is also insignificant.

The 50% and 10% breakdown voltages in Figure 4.11 and Figure 4.12 are based on the breakdown test results of all 9 FP-I coated electrodes listed in Table 4.7. As explained, the results of electrode 7, 8 and 9 are obtained in a test with a six minutes waiting time between impulses. It can be argued that it is unfavourable to include the results of electrode 7, 8 and 9 in the statistical analysis because of the difference in test parameters.

Therefore, the 10% and 50% first breakdown voltage was also calculated using only the results of the first six electrodes and compared with those obtained using all test results. The results of the comparison are shown in Figure 4.13. The 50% and 10% breakdown voltages at the left side of the figure are obtained with the results of only the first six electrodes and the values at the right side are obtained with the results of all electrodes.

As can be seen from the figure the difference between the 50% and 10% breakdown voltages obtained with a distribution fit on either the first six or on all electrodes is insignificant. Note that the 95% confidence intervals of the 50% and 10% breakdown voltage obtained with all electrodes are smaller which might be caused by the larger amount of breakdown test results used for distribution fitting.

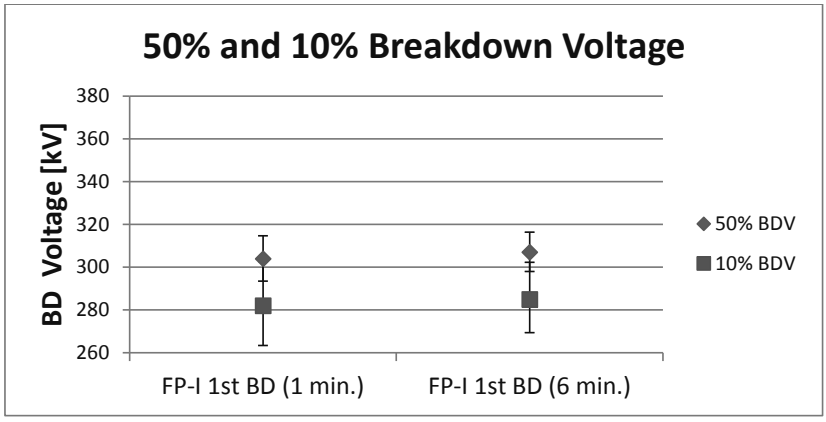

Figure 4.13: Comparison of 50% and 10% 1st Breakdown voltage of FP-I coated electrodes including 95% confidence intervals regarding addition of test results with 6 minutes waiting time between impulses.

FP-II

The breakdown test results of a FP-II coated electrode are shown in Figure 4.14. The breakdown behaviour of the FP-II coated electrodes is different compared to the FP-I and EP-I coated electrodes. In this case it was possible to increase the applied voltage after the first two to six breakdowns up to a maximum level which is significantly higher than the first breakdown voltage. The breakdown test results of all FP-II electrodes are displayed in appendix A.

The first and highest breakdown voltages measured on each sample are listed in Table 4.8. The table shows that the first breakdown voltage of the FP-II coated electrodes is relatively low with a value ranging from 283 kV to 308 kV. Whereas the highest breakdown voltage of each sample is significantly higher than the first breakdown voltage.

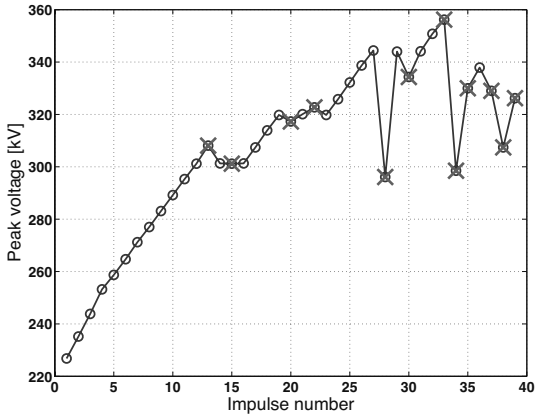

Figure 4.14: Breakdown test results of a FP-II coated electrode.

Table 4.8: 1st and highest breakdown voltage measured on FP-II coated electrodes

Electrode	1st Breakdown	Highest Breakdown	Difference
1	290 [kV]	314 [kV]	8.3%
2	296 [kV]	345 [kV]	17%
3	283 [kV]	301 [kV]	6.4%
4	300 [kV]	325 [kV]	8.3%
5	296 [kV]	317 [kV]	7.1%
6	308 [kV]	356 [kV]	16%
7	292 [kV]	340 [kV]	16%
8	285 [kV]	334 [kV]	17%
9	303 [kV]	339 [kV]	12%

The highest breakdown voltage ranges from 301 to 356 kV and the increase with respect to the corresponding first breakdown voltage ranges from 6.4% to 17%. The scatter in the first and highest breakdown voltage is 25 kV and 55 kV respectively.
As is the case with the FP-I samples, the breakdown tests on electrodes 7, 8 and 9 were performed with a 6 minutes waiting time between impulses to investigate the influence of the waiting time between impulses on the breakdown test results. The discussion on the influence of the waiting time between impulses on the breakdown test results is contained in section 4.3.

The 50% and 10% quantiles of the 1st, 3rd, 5th, 7th, 9th and highest breakdown voltages are shown in Figure 4.15 and Figure 4.16 respectively.

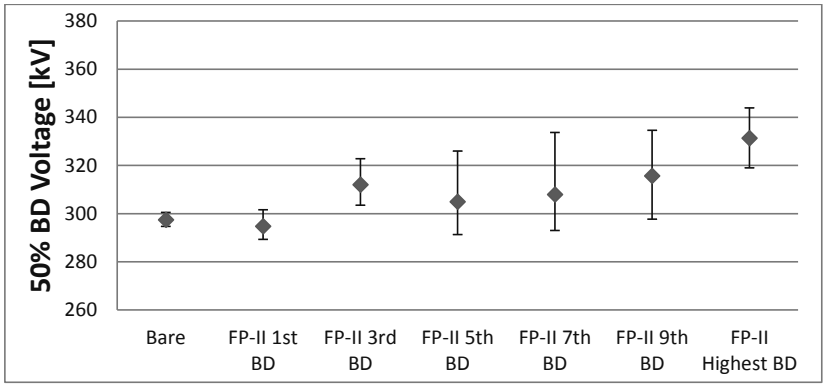

Figure 4.15: 50% Breakdown voltage of FP-II coated electrodes including 95% confidence intervals.

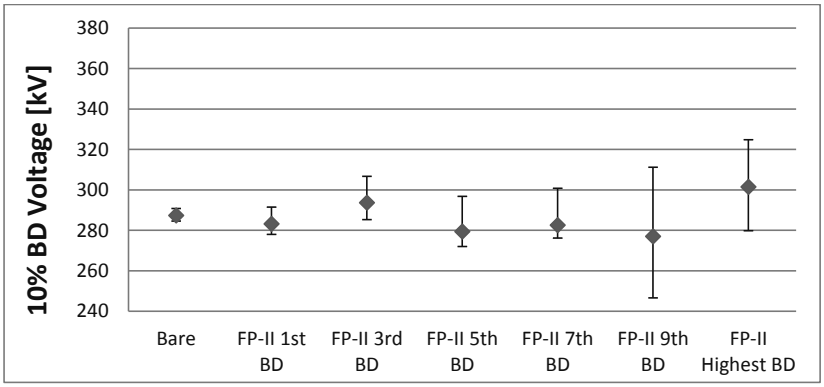

Figure 4.16: 10% Breakdown voltage of FP-II coated electrodes including 95% confidence intervals.

The difference between the 50% first breakdown voltage and the 50% breakdown voltage of bare electrodes is insignificant, although the value of the 50% first breakdown voltage is somewhat lower. Furthermore, the 50% breakdown voltage shows an increas-

ing trend with an increase in breakdown number as opposed to the FP-I and EP-I coated electrodes.

The 95% confidence interval of the 50% value of the higher breakdown numbers is relatively wide due to the large scatter in the corresponding breakdown voltages of the individual samples. The large scatter is caused by the fact that the number of breakdowns required to reach the highest breakdown voltage is different for each electrode. Due to the wide 95% confidence intervals the difference between the 50% 3rd, 5th, 7th, 9th and highest breakdown voltage is insignificant despite the visible upward trend. However, the 50% 3rd and highest breakdown voltages are significantly higher than the 50% 1st breakdown voltage and the 50% breakdown voltage of bare electrodes.

When observing the 10% quantiles of the breakdown voltage in Figure 4.16 it can be seen that the difference between the 10% 1st to 9th and highest breakdown voltages is insignificant. Furthermore, with respect to the 10% breakdown voltage of bare electrodes no significant difference is visible. Note that the 95% confidence intervals of the 10% 9th and highest breakdown voltages are significantly wider.

Also for FP-II the 50% and 10% breakdown voltages are obtained from the test results of all nine electrodes. Thus, also the results of electrodes 7, 8 and 9 are included which are obtained with a six minutes waiting time between impulses. Again it can be argued that it is unfavourable to include these electrodes in the statistical analysis because of the difference in test parameters.

Therefore, also in this case the 50% and 10% first breakdown voltages were calculated with only the results of the first six electrodes and compared with the values obtained with the results of all electrodes. The comparison is shown in Figure 4.17.

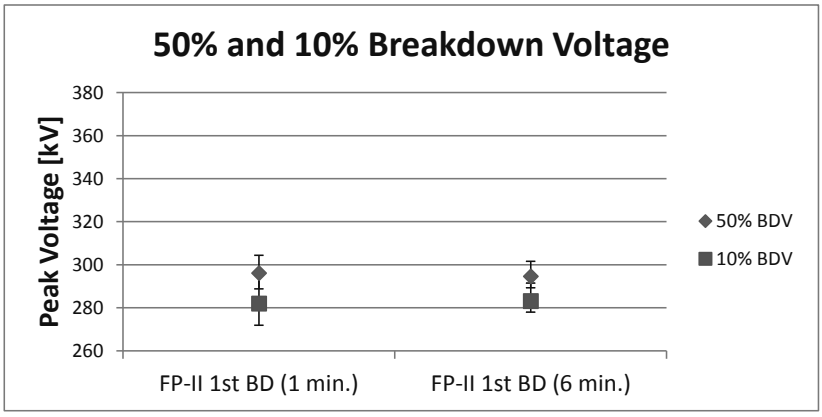

Figure 4.17: Comparison of 50% and 10% 1st Breakdown voltage of FP-II coated electrodes including 95% confidence intervals regarding addition of test results with 6 minutes waiting time between impulses.

The 50% and 10% 1st breakdown voltages on the left side of the figure are obtained with the results of only the first six electrodes and those on the right side are obtained with the results of all electrodes. The difference between the 50% and 10% 1st breakdown voltage obtained with a distribution fit on either the results of the first six electrodes or on the results of all electrodes is insignificant. Furthermore, the 95% confidence intervals of the 50% and 10% 1st breakdown voltage obtained with the results of all electrodes is somewhat smaller due to the larger amount of test results used for distribution fitting.

FP-II – Extra tests

As explained, the breakdown voltage of FP-II coated electrodes is increased after the first two to six breakdowns to a level which is significantly higher than the first breakdown voltage. This breakdown behaviour is different than is expected from a coated system. Therefore, several additional breakdown tests were performed.

First, three tested FP-II coated electrodes were selected to be retested with the same test procedure (combined test). The tested electrodes have remained in the test setup for a week after the initial test. The retest was performed on electrodes 2, 6 and 9 from Table 4.8. The main goal of these extra breakdown tests is to investigate if the increase in breakdown voltage is permanent or temporary in nature. As an example the results of the retest on electrode 6 are displayed in Figure 4.18.

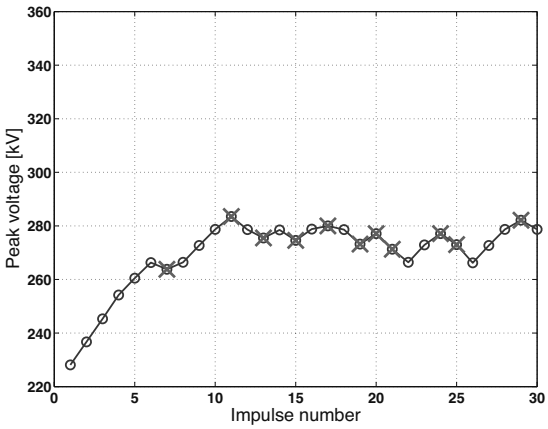

Figure 4.18: Breakdown results of the retest on FP-II coated electrode number 6.

Compared to the results of the initial test performed on electrode 6 shown in Figure 4.14 the breakdown behaviour has changed significantly. The results of the retests show that the increased breakdown voltage obtained in the initial test is temporary. The first

Table 4.9: First and highest breakdown voltages of the three retested FP-II coated electrodes.

Electrode	1st Breakdown	Highest Breakdown
2	250 [kV]	301 [kV]
6	264 [kV]	284 [kV]
9	273 [kV]	289 [kV]

and highest breakdown voltages obtained for the three tested electrodes are shown in Table 4.9.

Also in the retests the first breakdown voltage is lower than highest breakdown voltage. Furthermore, the value of the first and highest breakdown voltages are significantly lower when compared to the results of the corresponding initial tests.

The second type of test consists of a standard 50% up-down test on three unused FP-II coated electrodes. There is no progressive stress part in these test as opposed to the combined test procedure. The goal of this test is to evaluate the influence of the progressive stress part of the combined test on the breakdown behaviour of the FP-II coated electrodes. The breakdown test results of a 50% up-down test on an unused FP-II coated electrode are shown in Figure 4.19.

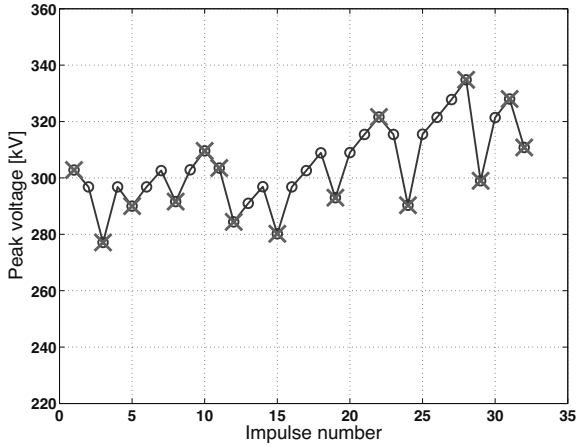

Figure 4.19: Breakdown results of a standard 50% up-down test on a FP-II coated electrode.

The results in the figure show an upward trend in the breakdown voltage with an increase in impulse number as was the case in the combined test procedure. However, this behaviour was not as pronounced as observed in the combined tests. Furthermore, the

upward trend was not observed in the results of all three tested samples. The results of the other samples are presented in appendix A.

The highest breakdown voltages of the three electrodes are listed in Table 4.10. Moreover, the 50% breakdown voltage was calculated from the test results of each electrode and shown in the table. The 50% breakdown voltages of the electrode samples are also shown in Figure 4.20 together with the 10% breakdown voltages. The 50% and 10% breakdown voltage obtained from all breakdown test results combined is also included in the figure.

Table 4.10: 50% and highest breakdown voltages of the three FP-II coated electrodes tested with a standard 50% up-down test.

Electrode	50% Breakdown	Highest Breakdown
1	302 [kV]	316 [kV]
2	313 [kV]	335 [kV]
3	300 [kV]	317 [kV]

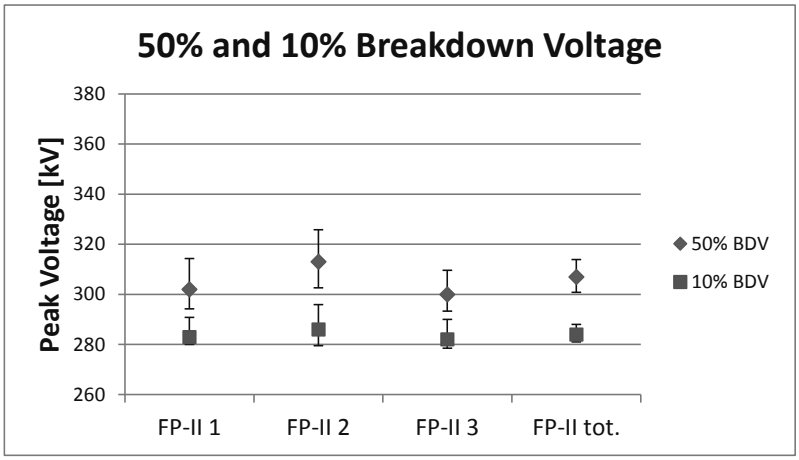

Figure 4.20: 50% and 10% breakdown voltage of FP-II coated electrodes including 95% confidence intervals obtained with standard 50% up-down tests.

The results in the table show that the highest breakdown voltage of these electrodes is in the same range as those obtained in the combined tests (Table 4.8). Furthermore, the 50% breakdown voltage obtained from the combined data of all three electrodes is somewhat higher than that of bare electrodes as was the case with the 50% 3rd breakdown voltage obtained in the combined test (Figure 4.15). The 10% breakdown voltages are in the same range as those obtained in the combined tests (Figure 4.16).

The results of the 50% up-down tests show that without the progressive stress part it is possible to obtain comparable values for the highest breakdown voltage. However, the increase in breakdown voltage with an increasing breakdown number is somewhat stronger in the combined tests. Higher values of the highest breakdown voltage were obtained for several samples tested with the combined test procedure.

FP-III

The breakdown test results of a FP-III coated electrode are shown in Figure 4.21. In most cases the breakdown voltage remains relatively constant after the first breakdown. The consecutive breakdown and withstand voltages vary around a mean value which is relatively close to the first breakdown voltage. However, in one test(electrode 1) the breakdown voltage was reduced to a level close to the 50% breakdown voltage of bare electrodes after the first breakdown which is comparable with the FP-I and EP-I breakdown test results. In another single case(electrode 4) the breakdown voltage increased after the first breakdown in a similar way as was found in the breakdown test results of the FP-II coated electrodes. The breakdown test results of all FP-III coated samples are presented in appendix A.

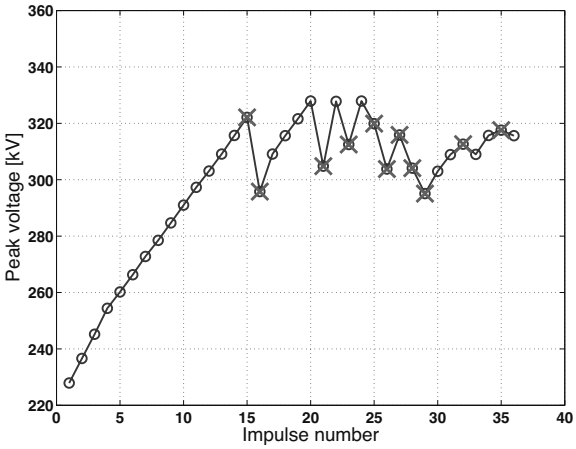

Figure 4.21: Breakdown test results of a FP-III coated electrode.

The first and highest breakdown voltages of the FP-III coated electrodes are displayed in Table 4.11. The first breakdown voltage ranges from 291 kV to 335 kV resulting in a scatter of 44 kV. For all electrodes the first breakdown voltage is also the highest breakdown voltage except for electrode 4 as explained above.

Table 4.11: First and highest breakdown voltages of FP-III coated electrodes.

Electrode	1st Breakdown	Highest Breakdown
1	328 [kV]	328 [kV]
2	292 [kV]	292 [kV]
3	322 [kV]	322 [kV]
4	309 [kV]	329 [kV]
5	291 [kV]	292 [kV]
6	335 [kV]	335 [kV]

The 50% and 10% quantiles of the 1st, 3rd, 5th and 7th breakdown voltages are shown in Figure 4.22 and Figure 4.23 respectively. Although the 50% quantile of the 1st breakdown is 6.5% higher than that of bare electrodes, the difference between both results is insignificant due to the barely overlapping 95% confidence bounds. When a lower confidence level such as the 68.2% confidence level is selected the difference is significant. The 95% confidence bounds of the 50% quantiles of all breakdown numbers are relatively wide due to the large scatter in the breakdown behaviour and the small amount of sample data available.

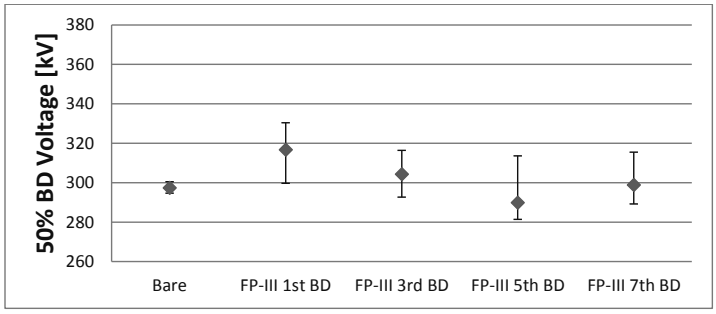

Figure 4.22: 50% Breakdown voltage of FP-III coated electrodes including 95% confidence intervals.

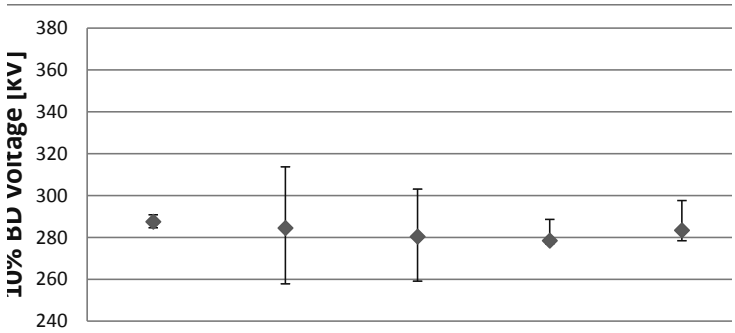

Figure 4.23: 10% Breakdown voltage of FP-III coated electrodes including 95% confidence intervals.

The large scatter in the breakdown behaviour is particularly visible when observing the test results of electrodes 2 and 5 (see appendix A). In Table 4.11 it can be seen that the first and highest breakdown voltages of electrode samples 2 and 5 are low compared to the results of the other electrodes.

Figure 4.23 shows that the 10% quantiles of all breakdown numbers show only a minor difference with respect to the 10% breakdown voltage of bare electrodes. Also for the 10% quantiles the 95% confidence intervals are wide due to the large scatter in breakdown test results and the small amount of test data available for distribution fitting. Therefore, the difference between the 10% quantiles is considered insignificant. Note that the difference between the 10% quantiles of the breakdown voltage would also be insignificant when the confidence bounds were small.

FP-IV

The breakdown test results of a FP-IV coated electrode are depicted in Figure 4.24. The figure shows that the applied voltage can be increased after the first breakdown as was the case with the FP-II coated electrodes.

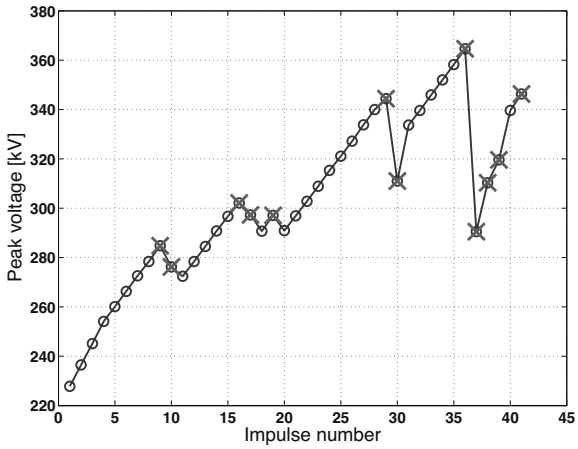

Figure 4.24: Breakdown test results of a FP-IV coated electrode.

This breakdown behaviour was observed in the test results of all FP-IV coated electrode samples. Furthermore, the number of breakdowns necessary to reach the maximum breakdown voltage in a breakdown test ranges between 2 and 26. The breakdown test results of the FP-IV coated samples are presented in appendix A.

The first and highest breakdown voltage of the FP-IV coated samples are listed in Table 4.12. From the table it can be seen that the first breakdown voltage of the FP-IV

Table 4.12: First and highest breakdown voltage of FP-IV coated electrodes.

Electrode	1st Breakdown	Highest Breakdown	Difference
1	273 [kV]	359 [kV]	32%
2	273 [kV]	299 [kV]	9.5%
3	293 [kV]	351 [kV]	20%
4	285 [kV]	365 [kV]	28%
5	285 [kV]	378 [kV]	33%
6	285 [kV]	328 [kV]	15%

coated electrodes is relatively low ranging from 273 to 293 kV with a corresponding scatter of 20 kV. The highest breakdown voltage of all electrodes is significantly higher than the corresponding first breakdown voltage. The highest breakdown voltage ranges from 299 kV to 378 kV with an improvement varying between 9.5% to 33% with respect to the corresponding first breakdown voltage. Moreover, the scatter in the highest breakdown voltage is relatively large with a value 79 kV.

The 50% and 10% quantiles of the 1st, 10th, 12th and highest breakdown voltages are shown in Figure 4.25 and Figure 4.26 respectively. The 50% first breakdown voltage is significantly lower than the 50% breakdown voltage of bare electrodes with a difference of 4.8%. The 95% confidence intervals of both values show no overlap. As opposed to the 50% first breakdown voltage, the 50% quantiles of the 10th, 12th and highest breakdown voltage are significantly higher than the 50% breakdown voltage of the bare electrodes as the 95% confidence intervals also show no overlap. Furthermore, the 50% breakdown voltage shows an increasing trend with an increase in breakdown number.

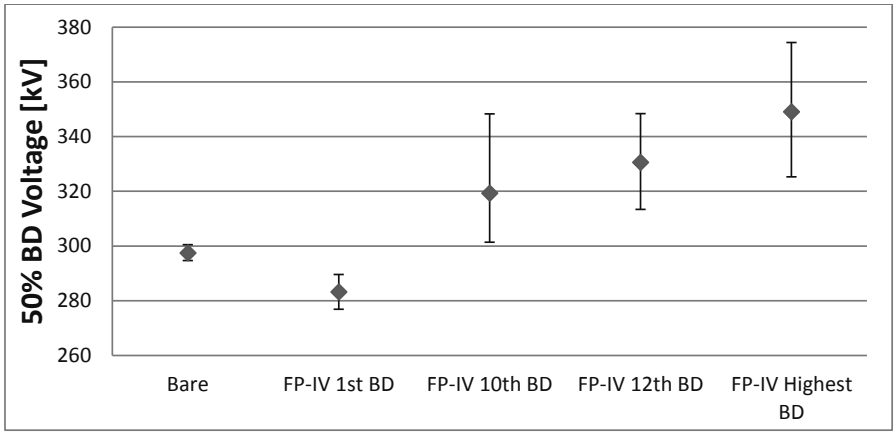

Figure 4.25: 50% Breakdown voltage of FP-IV coated electrodes including 95% confidence intervals.

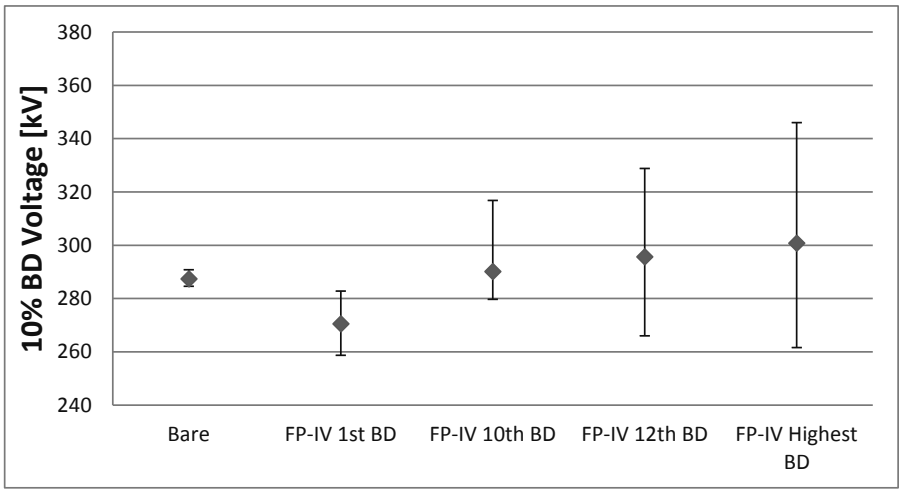

Figure 4.26: 10% Breakdown voltage of FP-IV coated electrodes including 95% confidence intervals.

The increase with respect to the 50% breakdown voltage of bare electrodes is 7.4%, 11% and 17% for the 10th, 12th and highest breakdown voltage respectively. Moreover, with respect to the 50% first breakdown voltage the 10th, 12th and highest breakdown voltage show an increase of 13%, 17% and 23% respectively.

Note that the confidence intervals of the 50% quantiles of the 10th and 12th breakdown voltage are particularly wide due to the fact that the maximum breakdown voltage is reached after a varying number of breakdowns. Furthermore, the 95% confidence intervals of the 50% highest breakdown voltage are wide due to the large scatter in the values of the highest breakdown voltage. Due to the wide confidence intervals the difference between the 50% 10th, 12th and highest breakdown voltage is insignificant. When the 68.2% confidence level is applied the difference between the 50% 10th and highest breakdown voltage is significant.

When observing the 10% breakdown voltages in Figure 4.26 a minor upward trend can be seen between the 1st, 10th, 12th and highest 10% breakdown voltages. However, the 95% confidence intervals are very wide and therefore the difference between these 10% quantiles is considered insignificant. The 10% first breakdown voltage is significantly lower than the 10% breakdown voltage of bare electrodes with a difference of 5.9%. Unfortunately, with a reduced confidence level of 68.2% the difference between the 10% highest breakdown voltage and the 10% breakdown voltage of bare electrodes is also insignificant. However, the difference between the 10% first breakdown voltage and the 10% 10th, 12th and highest breakdown voltage is in this case significant.

PA11

The breakdown test results of a PA11 coated electrode are shown in Figure 4.27. As can be seen from the figure the breakdown strength of the PA11 coated electrode is reduced to a level close to that of a bare electrode after the first breakdown. This behaviour is present in the breakdown test results of all PA11 coated electrode samples and is comparable with the breakdown behaviour of the EP-I and FP-I coated electrodes. The breakdown test results of the PA11 coated samples are presented in appendix A.

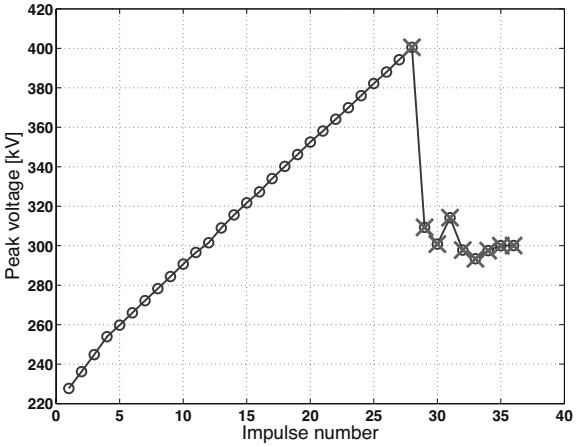

Figure 4.27: Breakdown test results of a PA11 coated electrode.

The first and highest breakdown voltage of the PA11 coated electrode samples are listed in Table 4.13. Note that twelve electrodes were tested instead of six due to the fact that in the first test series a decrease in breakdown voltage was observed between the first four electrodes. It was suspected that contamination of the tank with coating particles produced by the breakdowns caused a reduction in the gas breakdown strength and thus a reduction in the measured breakdown voltage. Therefore, the tank was cleaned and the coating particles removed before testing electrodes 5 and 6. The first breakdown voltage of these electrodes was higher than those of electrodes 2 to 4.

Consequently it was argued that another set of six PA11 coated electrodes should be tested because the test conditions were modified due to the cleaning of the tank before testing electrodes 5 and 6. Thus, electrode samples 7 to 12 were all tested without cleaning the tank. The breakdown test results of the final six electrodes show that the reduced first breakdown voltage of electrodes 2 to 4 might be only statistical in nature and therefore not related to contamination of the tank with coating particles.

Table 4.13: First and highest breakdown voltage of PA11 coated electrode samples.

Electrode	1st Breakdown	Highest Breakdown
1	401 [kV]	401 [kV]
2	320 [kV]	320 [kV]
3	316 [kV]	316 [kV]
4	303 [kV]	303 [kV]
5	346 [kV]	346 [kV]
6	364 [kV]	364 [kV]
7	356 [kV]	356 [kV]
8	356 [kV]	356 [kV]
9	318 [kV]	318 [kV]
10	380 [kV]	380 [kV]
11	343 [kV]	343 [kV]
12	343 [kV]	343 [kV]

The first breakdown voltage ranges from 303 to 401 kV resulting in a large scatter of 98 kV. Moreover, the highest breakdown voltage is in all cases equal to the first breakdown voltage as explained above. The PA11 coated electrodes in combination with the gas in the test tank present a non-self-restoring insulation.

The 50% and 10% quantiles of the 1st, 3rd, 5th and 7th breakdown voltage are depicted in Figure 4.28 and Figure 4.29 respectively. Figure 4.28 shows that the 50% first breakdown voltage is significantly higher than the 50% breakdown voltage of bare electrodes with a corresponding improvement of 15%. Furthermore, the 95% confidence intervals are

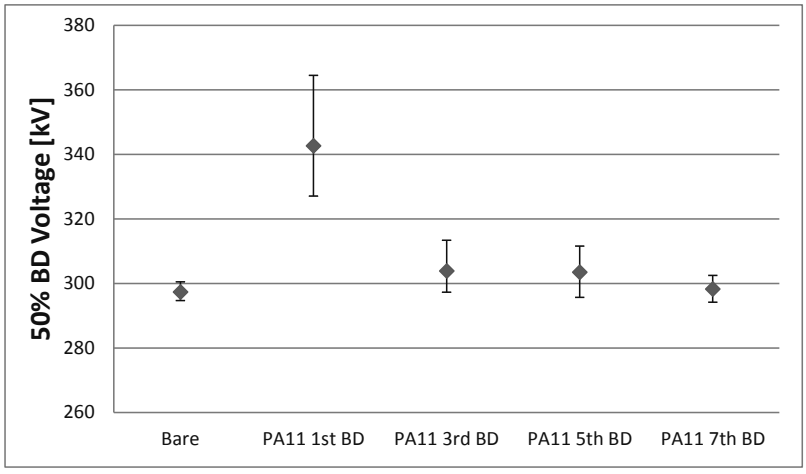

Figure 4.28: 50% Breakdown voltage of PA11 coated electrodes including 95% confidence intervals.

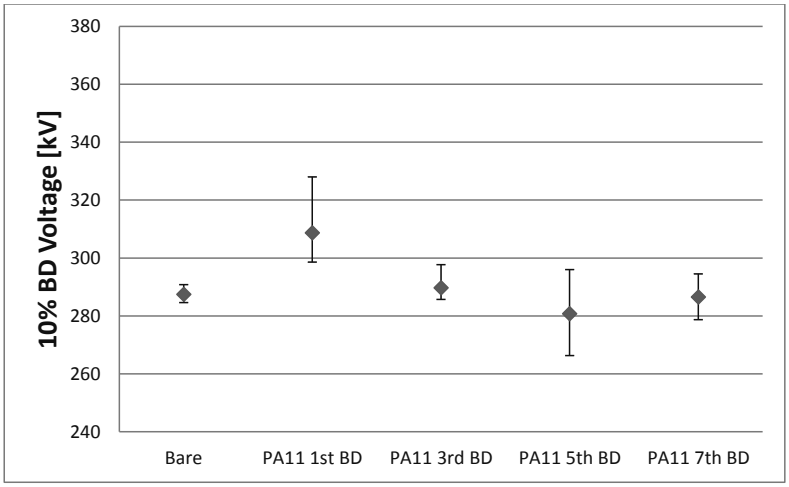

Figure 4.29: 10% Breakdown voltage of PA11 coated electrodes including 95% confidence intervals.

relatively wide due to the large scatter in the measured first breakdown voltage of the individual electrode samples.

The 50% 3rd, 5th and 7th breakdown voltages are comparable with the 50% breakdown voltage of bare electrodes. The breakdown strength of the PA11 coated electrodes is effectively reduced to a level comparable with the breakdown strength of bare electrodes.

Figure 4.29 shows that also for the 10% quantiles the first breakdown is significantly higher than the breakdown voltage of bare electrodes. The corresponding improvement is 7.7%. Moreover, the 10% 3rd, 5th and 7th breakdown voltages are comparable with the 10% breakdown voltage of bare electrodes which again indicates that the breakdown strength of PA11 coated electrodes is reduced to that of bare electrodes.

Semiconductor A

The breakdown test results of an electrode sample coated with semiconductor A are displayed in Figure 4.30. The figure shows that the breakdown and withstand voltages vary around a certain value after the first breakdown. With respect to the first breakdown voltage a minor increase is visible after several breakdowns.

This breakdown behaviour is observed in the results of most of the Semiconductor A coated electrode samples, although the minor increase in the breakdown voltage is in one case absent (electrode 6). However, in one case(electrode 5) the breakdown voltage is increased after the first breakdown voltage in a similar fashion as the FP-II and FP-IV coated electrodes. Furthermore, in another single case(electrode 4) the breakdown voltage decreased after the first breakdown to a level below the 50% breakdown voltage of

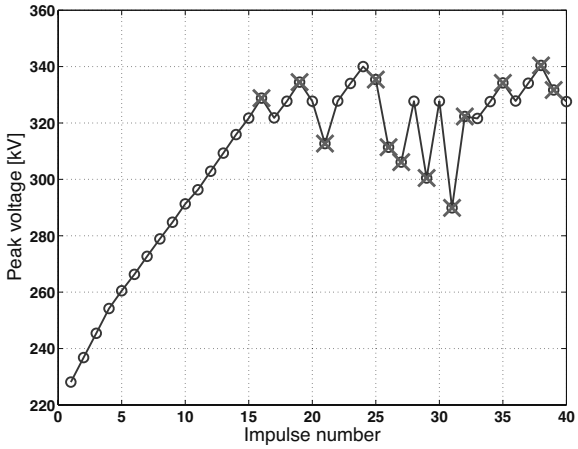

Figure 4.30: Breakdown test results of a semiconductor A coated electrode sample.

bare electrodes. The breakdown test results of all Semiconductor A coated electrodes are shown in appendix A.

The first and highest breakdown voltage of the Semiconductor A coated electrodes are listed in Table 4.14. In 4 out of 6 cases the highest breakdown voltage is higher than the first breakdown voltage with a difference ranging from 0.3% to 14%. Furthermore, the first breakdown voltage varies between 304 and 337 kV whereas the highest breakdown voltage ranges from 310 kV to 346 kV. The scatter in the first and highest breakdown voltage is 33 kV and 36 kV respectively.

Table 4.14: First and highest breakdown voltage of Semiconductor A coated electrodes.

Electrode	1st Breakdown	Highest Breakdown	Difference
1	329 [kV]	340 [kV]	3.3%
2	322 [kV]	331 [kV]	2.8%
3	337 [kV]	338 [kV]	0.3%
4	321 [kV]	321 [kV]	0%
5	304 [kV]	346 [kV]	14%
6	310 [kV]	310 [kV]	0%

The 50% and 10% quantiles of the 1st, 3rd, 5th, 7th, 9th and highest breakdown voltage are displayed in Figure 4.31 and Figure 4.32 respectively. The 50% first breakdown voltage is significantly higher than the 50% breakdown voltage of bare electrodes with a corresponding improvement of 7.7%.

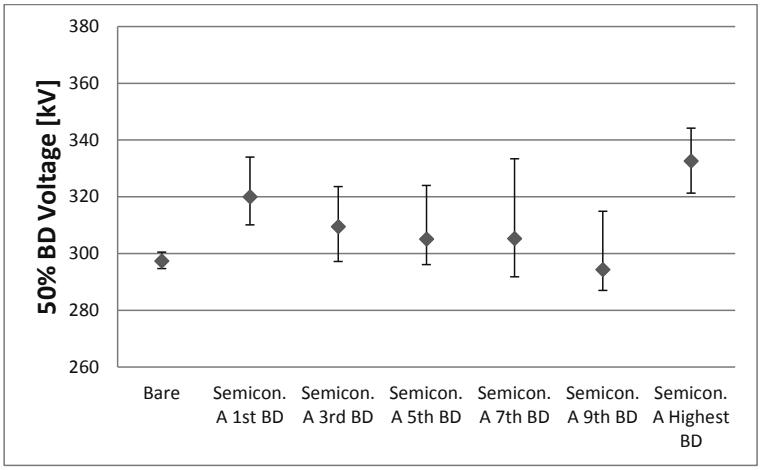

Figure 4.31: 50% Breakdown voltage of Semiconductor A coated electrodes including 95% confidence intervals.

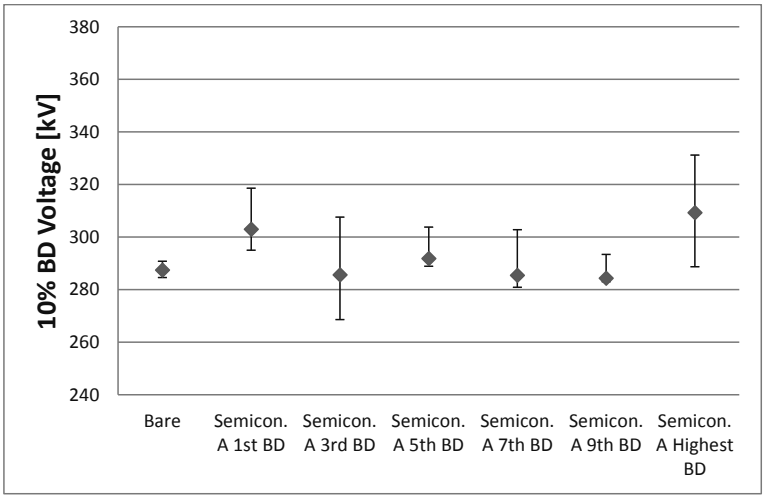

Figure 4.32: 10% Breakdown voltage of Semiconductor A coated electrodes including 95% confidence intervals.

Furthermore, the 50% highest breakdown voltage shows a larger improvement of 12% with respect to the 50% breakdown voltage of bare electrodes. The 50% 3rd, 5th, 7th and 9th breakdown voltages show a slightly decreasing trend although the 95% confidence intervals are relatively wide, especially on the upper side. Furthermore, the difference between the 50% breakdown voltage of bare electrodes and the 50% 3rd, 5th, 7th and 9th breakdown voltages is insignificant. When a lower confidence level of 68.2% is chosen

the 50% 3rd and 5th breakdown voltages show a significant difference with that of bare electrodes.

When observing the 10% quantiles of the breakdown voltage it can be seen that the 10% first breakdown voltage is significantly higher than the 10% breakdown voltage of bare electrodes with a difference of 5.4%. Furthermore, the 10% highest breakdown voltage shows an increase of 7.6% with respect to that of bare electrodes. Unfortunately, the 95% confidence intervals of both 10% quantiles overlap and thus the difference is insignificant. However, when a lower confidence level of 68.2% is selected the difference is significant. Meanwhile, the difference between the 10% breakdown voltage of bare electrodes and the 3rd, 5th, 7th and 9th breakdown voltage is insignificant regardless of the selected confidence level.

Summary

For comparison, the 50% and 10% quantiles of the 1st and highest breakdown voltage of all thin coating materials are summarized here. The 50% quantiles of the 1st and highest breakdown voltage are depicted in Figure 4.33 and Figure 4.34 respectively. Whereas the 10% quantiles of the 1st and highest breakdown voltage are shown in Figure 4.35 and Figure 4.36.

Regarding the 50% 1st breakdown voltage only the EP-I (Epoxy), PA11 and Semiconductor A coated electrodes show a significant increase over the 50% breakdown voltage of bare electrodes. The largest increase is obtained for the PA11 coated electrodes. Note that with a 68.2% confidence level the 50% 1st breakdown voltage of FP-III and FP-I coated electrodes would also show a significant increase with respect to the 50% breakdown

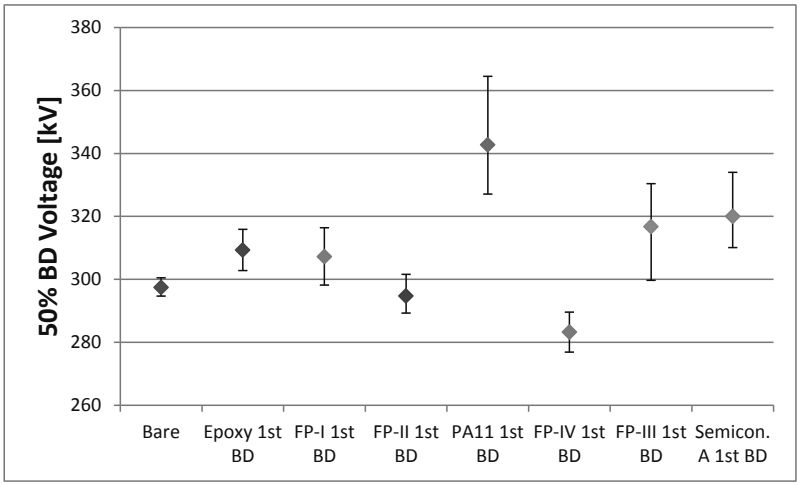

Figure 4.33: 50% 1st Breakdown voltage of the electrode samples coated with a thin coating including 95% confidence intervals.

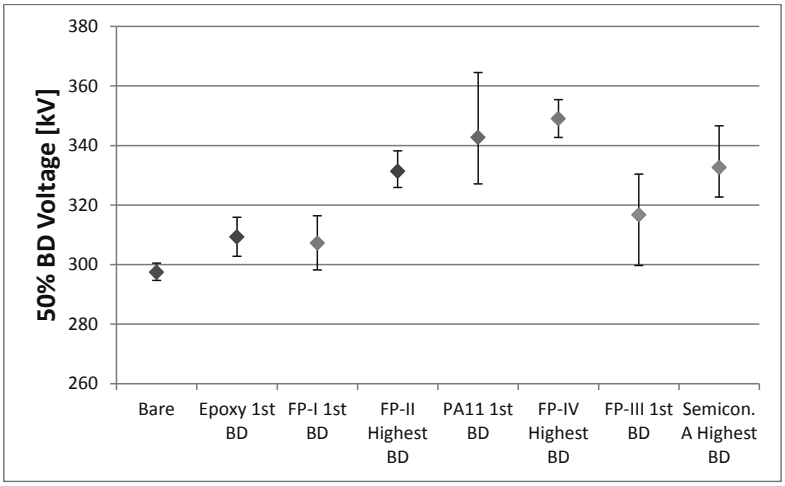

Figure 4.34: 50% Highest Breakdown voltage of the electrode samples coated with a thin coating including 95% confidence intervals.

voltage of bare electrodes. The 50% 1st breakdown voltage of the FP-IV coated electrodes is significantly lower than that of bare electrodes.

When observing the 50% Highest breakdown voltage it can be seen that in this case the EP-I, FP-II, PA11, FP-IV and Semiconductor A coated electrodes show a significant increase with respect to bare electrodes. Furthermore, the largest increase is in this case obtained for the FP-IV coated electrodes. When a 68.2% confidence level is applied all materials show a significant improvement in the 50% Highest breakdown voltage with respect to the 50% breakdown voltage of bare electrodes.

Figure 4.35 shows that only the 10% first breakdown voltage of the PA11 and Semiconductor A coated electrodes show a significant improvement over the 10% breakdown voltage of bare electrodes. In this case a reduction of the confidence level to 68.2% will not result in more materials with a significant improvement in the 10% first breakdown voltage. The 10% first breakdown voltage of the FP-IV coated electrodes show a significant reduction with respect to the 10% breakdown voltage bare electrodes.

In the case of the 10% highest breakdown voltage only PA11 shows a significant increase over the 10% breakdown voltage of bare electrodes. This is mainly caused by the wide 95% confidence intervals found for the other materials. The selection of a 68.2% confidence level results in a significant increase with respect to the 10% highest breakdown voltage of bare electrodes for more materials such as FP-II and Semiconductor A.

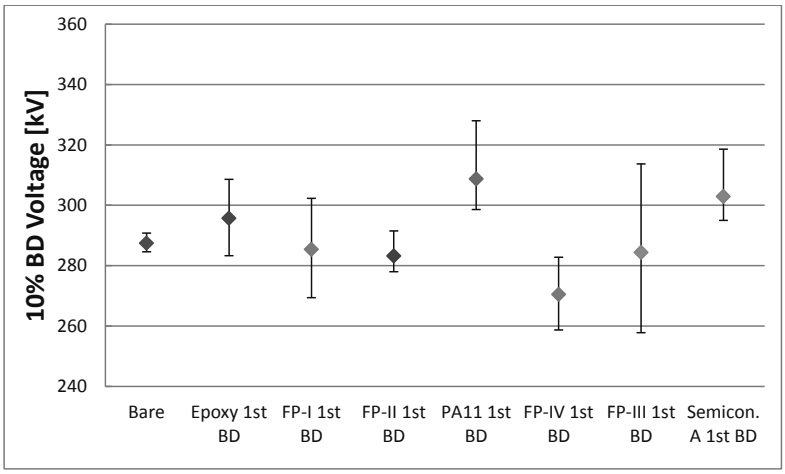

Figure 4.35: 10% 1st Breakdown voltage of the electrode samples coated with a thin coating including 95% confidence intervals.

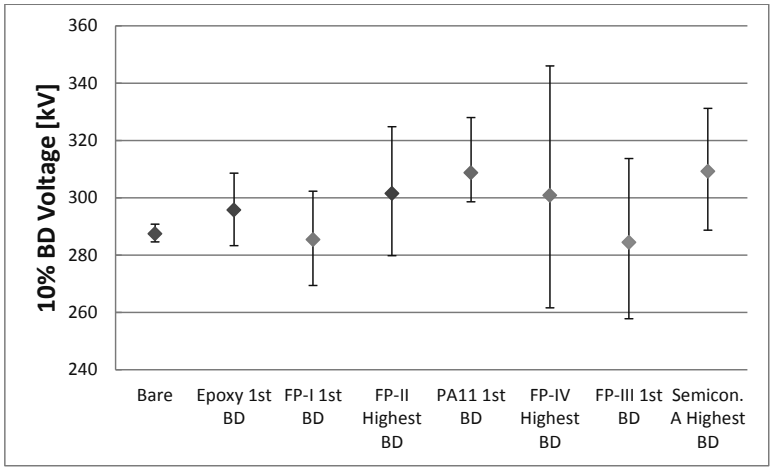

Figure 4.36: 10% Highest Breakdown voltage of the electrode sample coated with a thin coating including 95% confidence intervals

4.2.3 Double layer thin coatings

As an overview the tested double layer coating materials including the total layer thicknesses are listed in Table 4.15. More information on these coating materials can be found in section 3.3. Also for the double layer coatings the breakdown test results are described per material type.

Table 4.15: Thin double layer coating materials

Coating	Total thickness [µm]
FP-II – FP-I	590
FP-II – PA11	340

FP-II – FP-I

The breakdown test results of a FP-II – FP-I coated electrode sample are depicted in Figure 4.37. In almost all cases the breakdown voltage initially decreases after the first breakdown after which the breakdown voltage can be increased to either the initial level or to a slightly higher level.

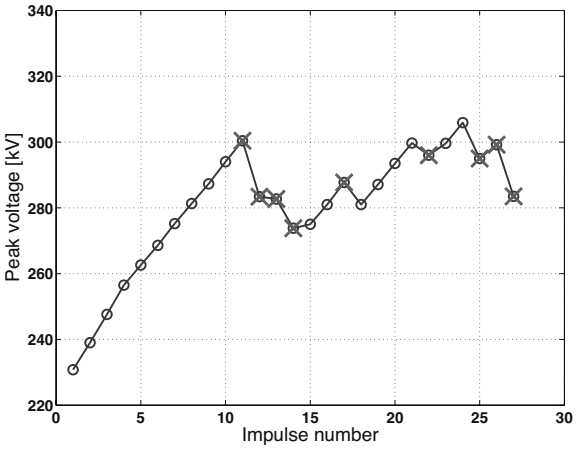

Figure 4.37: Breakdown test results of a FP-II – FP-I coated electrode.

Furthermore, in most cases the breakdown voltage drops again after the second increase. For one electrode sample(electrode 5) the breakdown voltage could be increased after the first breakdown in a similar fashion as observed for the single layer FP-II and FP-IV coated electrodes although the increase was in this case less pronounced. The breakdown test results of the other FP-II – FP-I coated electrodes are presented in appendix A.

The first and highest breakdown voltage of the FP-II – FP-I coated electrodes are displayed in Table 4.16. From the table it can be seen that for all electrodes except electrode 1 the highest breakdown voltage is slightly higher than the first breakdown voltage. Furthermore, the first breakdown voltage varies between 287 and 312 kV. Whereas the highest breakdown voltage has a range of 293 to 318 kV. The scatter of both the 1st

Table 4.16: 1st and highest breakdown voltage of FP-II – FP-I coated electrodes.

Electrode	1st Breakdown	Highest Breakdown	Difference
1	300 [kV]	300 [kV]	0%
2	287 [kV]	293 [kV]	2.1%
3	312 [kV]	318 [kV]	1.9%
4	293 [kV]	305 [kV]	4.1%
5	281 [kV]	306 [kV]	8.9%
6	312 [kV]	318 [kV]	1.9%

and highest breakdown voltage is 25 kV. Moreover, the difference between the highest breakdown voltage varies between 1.9% and 8.9%.

The 50% and 10% quantiles of the 1st, 3rd, 5th, 7th and highest breakdown voltage are depicted in Figure 4.38 and Figure 4.39 respectively. Figure 4.38 shows that the difference between the 50% 1st breakdown voltage and the 50% breakdown voltage of bare electrodes is insignificant. Furthermore, the 1st, 3rd, 5th, 7th and highest breakdown voltages show a slightly decreasing and consecutive upward trend.

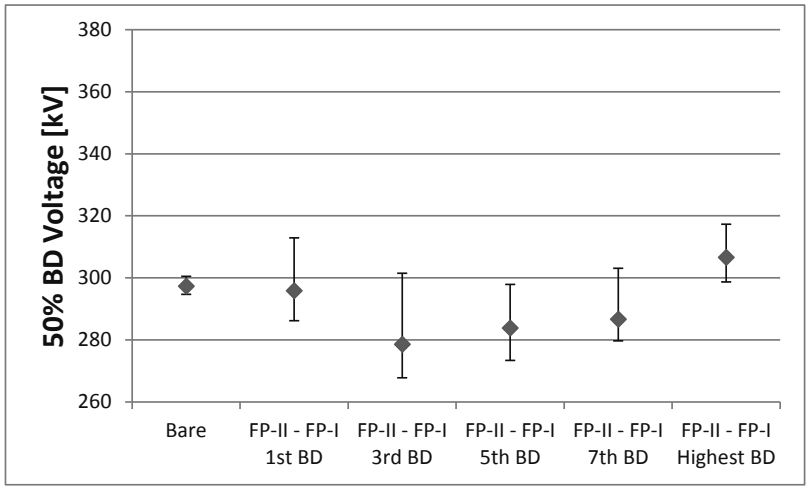

Figure 4.38: 50% Breakdown voltage of FP-II – FP-I coated electrodes including 95% confidence intervals.

However, due to the wide 95% confidence intervals the difference between these 50% quantiles is considered insignificant. With the 95% confidence intervals the difference between the 50% highest breakdown voltage and the 50% breakdown voltage of bare

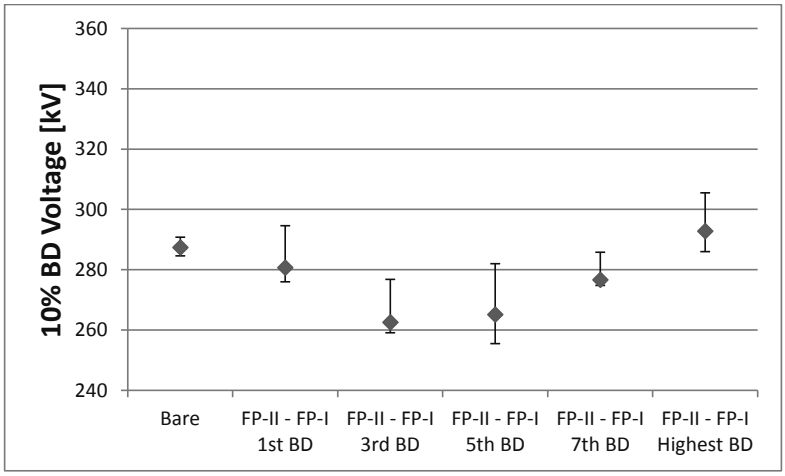

Figure 4.39: 10% Breakdown voltage of FP-II – FP-I coated electrodes including 95% confidence intervals.

electrodes is insignificant. However, when the confidence level is lowered to 68.2% this difference becomes significant with a small value of 3.1%.

From Figure 4.39 it can be seen that the 10% quantiles of the 1st to 7th breakdown voltage also show a decreasing and consecutive increasing trend. Moreover, the difference between the 10% breakdown voltage of bare electrodes and the 10% quantiles of the 1st and highest breakdown voltages is insignificant. The 10% quantiles of the 3rd and 5th breakdown voltage are significantly lower than the 10% breakdown voltage of bare electrodes.

FP-II – PA11

Figure 4.40 shows the breakdown test results of a FP-II – PA11 coated electrode. From the figure it can be derived that the breakdown voltage is reduced to a level below the 50% breakdown voltage of bare electrodes.

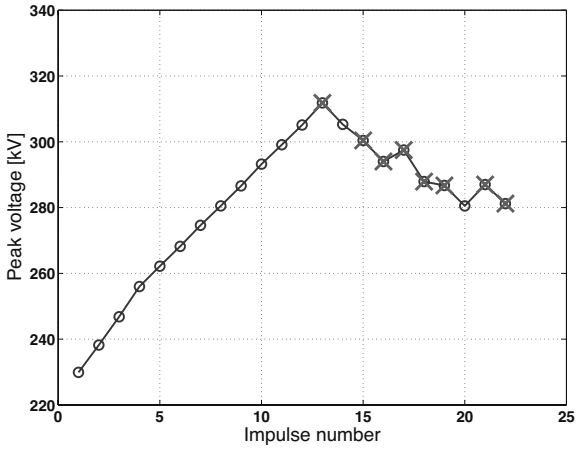

Figure 4.40: Breakdown test results of a FP-II – PA11 coated electrode.

The breakdown test results of all FP-II – PA11 coated electrodes show the same behaviour which is comparable with the breakdown behaviour of the single layer EP-I, FP-I and PA11 coated electrodes. The breakdown test results of all FP-II – PA11 coated electrodes are presented in appendix A.

The first and highest breakdown voltage of the FP-II – PA11 coated electrode samples are listed in Table 4.17. The table shows that the first breakdown voltage is equal to the highest breakdown voltage as was explained above. Furthermore, the first breakdown voltage ranges from 300 to 339 kV which gives a scatter of 39 kV.

Table 4.17: 1st and highest breakdown voltage of FP-II – PA11 coated electrodes.

Electrode	1st Breakdown	Highest Breakdown
1	312 [kV]	312 [kV]
2	305 [kV]	305 [kV]
3	300 [kV]	300 [kV]
4	339 [kV]	339 [kV]
5	306 [kV]	306 [kV]
6	312 [kV]	312 [kV]

The 50% and 10% quantiles of the 1st, 3rd, 5th and 7th breakdown voltage are depicted in Figure 4.41 and Figure 4.42 respectively. Figure 4.41 shows that the 50% first breakdown voltage of the FP-II – PA11 coated electrodes is significantly higher than the 50% breakdown voltage of bare electrodes. The corresponding difference is 3.9%. Furthermore, the 50% 3rd, 5th and 7th breakdown voltage are significantly lower than the 50% breakdown

voltage of bare electrodes. With respect to the 10% quantiles it can also be seen that the 1st breakdown voltage is significantly higher than the breakdown voltage of bare electrodes with a difference of 4.2%. Moreover, the 10% 5th and 7th breakdown voltages are significantly lower than the 10% breakdown voltage of bare electrodes.

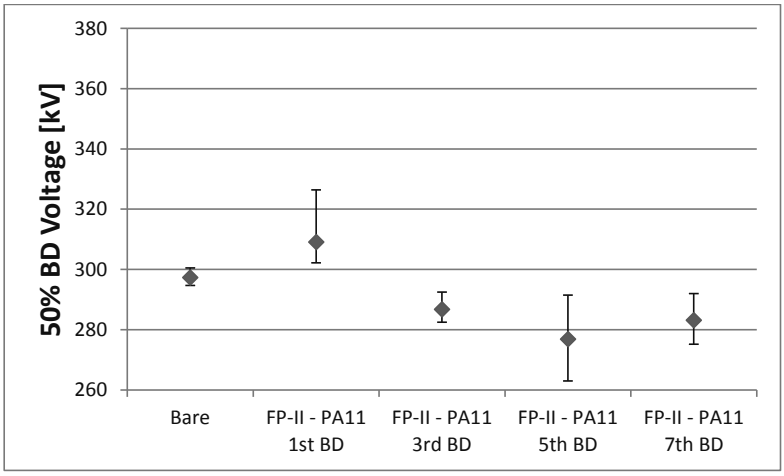

Figure 4.41: 50% Breakdown voltage of FP-II – PA11 coated electrodes including 95% confidence intervals.

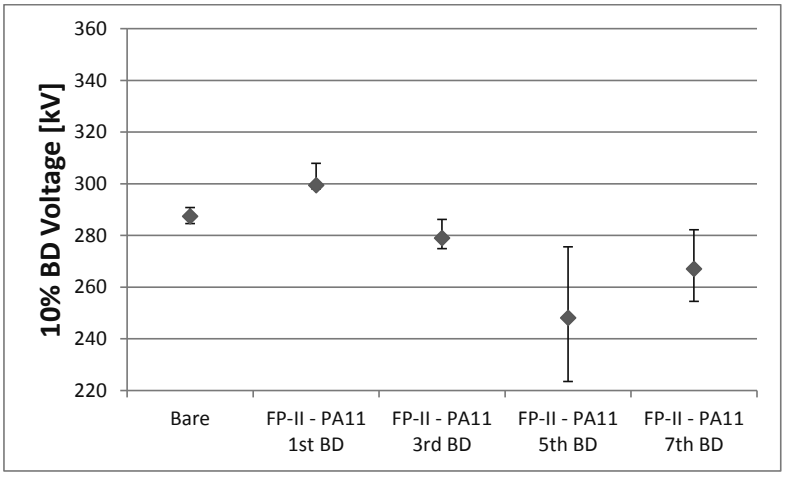

Figure 4.42: 10% Breakdown voltage of FP-II – PA11 coated electrodes including 95% confidence intervals.

Summary

For comparison the 50% and 10% quantiles of the first and highest breakdown voltages of the double layer coated electrode samples are summarized here. The 50% quantiles are depicted in Figure 4.43 and the 10% quantiles are shown in Figure 4.44.

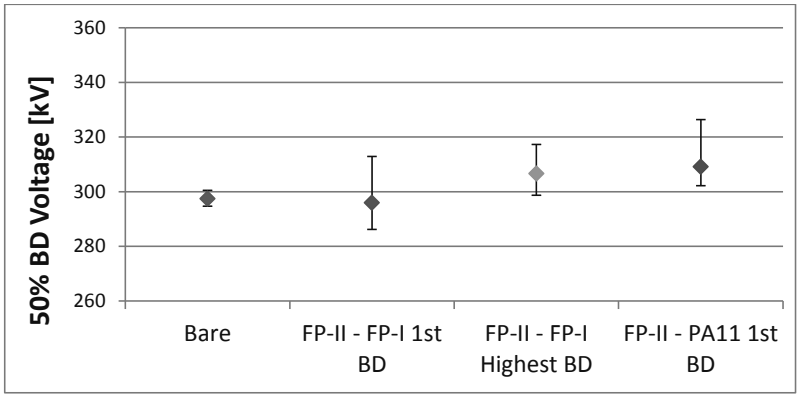

Figure 4.43: 50% Breakdown voltage of the electrodes on which a double layer coating is applied. Including 95% confidence intervals.

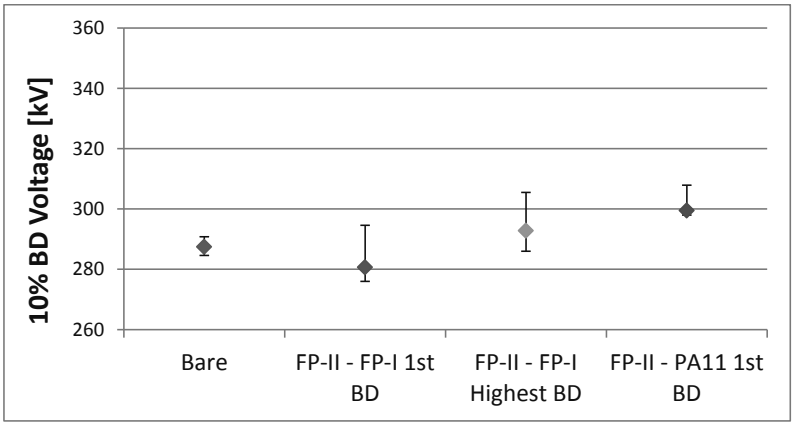

Figure 4.44: 10% Breakdown voltage of the electrodes on which a double layer coating is applied. Including 95% confidence intervals.

Figure 4.43 shows that only the FP-II – PA11 coated electrodes show a significant improvement in the 50% breakdown voltage. However, when the confidence level is reduced to 68.2% the 50% highest breakdown voltage of the FP-II – FP-I coated electrodes will also show a significant improvement. When observing the 10% quantiles it can be seen that also in this case only the FP-II – PA11 coated electrodes show a significant improvement.

4.2.4 Thick coatings

In this subsection the breakdown test results of the thick epoxy nanocomposite coatings are presented. As an overview the thick epoxy based coating materials are listed in Table 4.18. More information on these coating materials can be found in section 3.3. Note that the layer thickness of all thick coatings is 10 mm.

Table 4.18: Thick dielectric coating materials.

Coating	Filler	APS
Neat Epoxy	No Filler	-
Epoxy nanocomposite A	0.2 vol.% hBN	70 nm
Epoxy nanocomposite B	0.2 vol.% cBN	150 nm
Epoxy Nanocomposite C	0.6 vol.% hBN	70 nm

The breakdown test results of all electrode samples coated with either neat epoxy or one of the epoxy nanocomposites show similar behaviour. Therefore, the breakdown tests results of only one electrode sample are shown here. The breakdown test results of all neat epoxy and epoxy nanocomposite coated electrode samples are presented in appendix A.

The breakdown test results of a neat epoxy coated electrode are depicted in Figure 4.45. It can be seen from the figure that after the first breakdown the breakdown voltage is reduced to a level of roughly 360 kV.

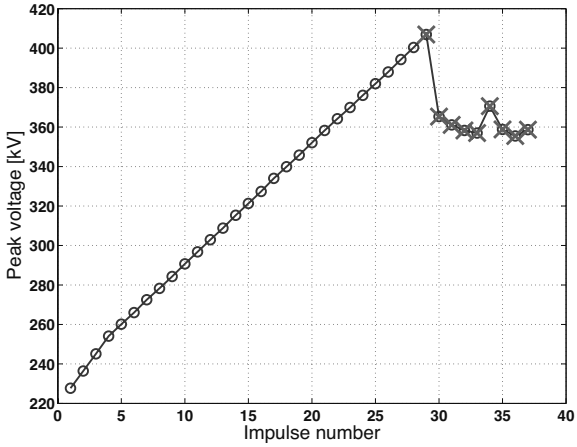

Figure 4.45: Breakdown test results of an electrode sample with a thick neat epoxy coating.

Almost all breakdown tests results of the electrodes with a thick coating show this reduction to a lower breakdown voltage level which varies between 350 and 380 kV. The breakdown voltage is therefore not reduced to that of a bare electrode which can be explained by the fact that in almost all cases breakdown occurred in the form of a surface flashover. The coating materials were not punctured by the electrical breakdown except for one electrode sample(electrode 2) from which a fragment broke off. In this case the breakdown voltage was reduced to a level which was significantly lower than the 50% breakdown voltage of bare electrodes.

The first breakdown voltages of the neat epoxy and nanocomposite coated electrodes are listed in Table 4.19. From the table it can be seen that the first breakdown voltage of the neat epoxy coated electrodes ranges from 374 to 453 kV resulting in a scatter of 79 kV. Moreover, the first breakdown voltage of the nanocomposite A coated electrodes varies between 365 and 427 kV giving a scatter of 62 kV. For nanocomposite B coated electrodes the first breakdown voltage ranges from 379 to 398 kV which presents a relatively small scatter of 19 kV. Finally, the first breakdown voltage of nanocomposite C coated electrodes varies between 342 and 403 kV resulting in a scatter of 61 kV.

Table 4.19: First breakdown voltage of neat epoxy and nanocomposite coated electrode samples.

Electrode	Neat Epoxy	Nano A	Nano B	Nano C
1	407 [kV]	420 [kV]	397 [kV]	403 [kV]
2	407 [kV]	396 [kV]	398 [kV]	342 [kV]
3	388 [kV]	365 [kV]	379 [kV]	390 [kV]
4	453 [kV]	427 [kV]	397 [kV]	385 [kV]
5	392 [kV]	383 [kV]	385 [kV]	385 [kV]
6	374 [kV]	396 [kV]	385 [kV]	N/A

The 50% and 10% quantiles of the first breakdown voltage are displayed in Figure 4.46 and Figure 4.47 respectively. From Figure 4.46 it can be seen that for all thick coating materials the 50% first breakdown voltage shows a significant improvement with respect the 50% breakdown voltage of bare electrodes.

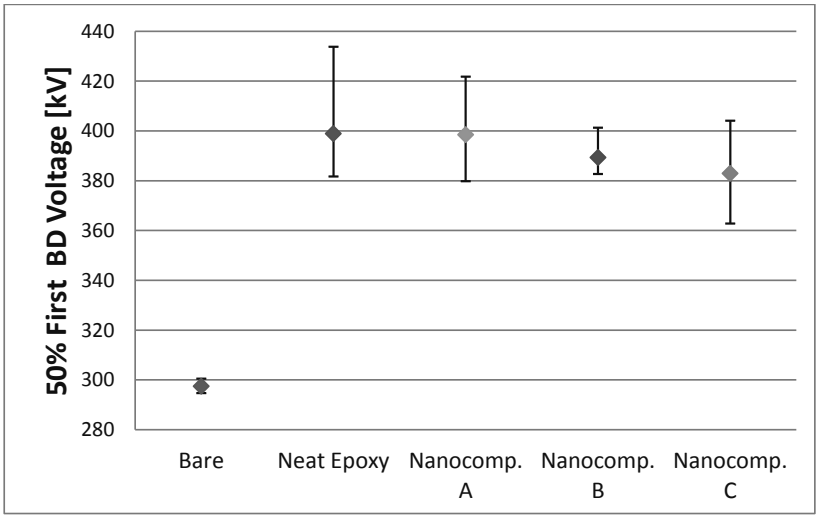

Figure 4.46: 50% First breakdown voltage of neat epoxy and nanocomposite coated electrodes.

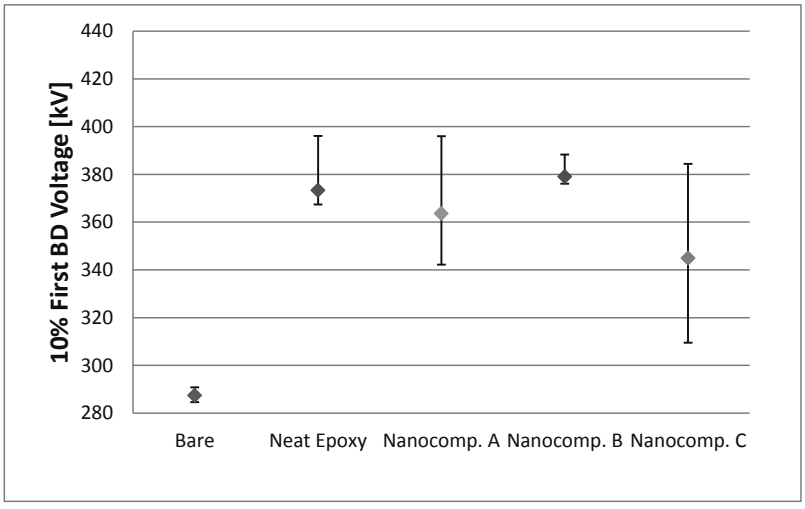

Figure 4.47: 10% First breakdown voltage of neat epoxy and nanocomposite coated electrodes.

The improvement in the 50% breakdown voltage is 34% for both neat epoxy and nanocomposite A. Whereas nanocomposites B and C show an improvement of 31% and 29% respectively. Note that the 95% confidence intervals of the nanocomposite B coated electrodes are small compared to the other nanocomposites and neat epoxy.

With respect to the 10% breakdown voltage of bare electrodes the 10% first breakdown voltage of the neat epoxy and nanocomposite coated electrodes also shows a significant

improvement. In this case the improvement in the 10% breakdown voltage is 30% for neat epoxy and 27%, 32% and 20% for nanocomposites A, B and C respectively. Note that also for the 10% breakdown voltage nanocomposite B has a small 95% confidence interval compared to the 10% first breakdown voltage of the other nanocomposites and neat epoxy.

Retests

As explained above the breakdown voltage of almost all electrode samples coated with a thick coating was reduced to a value between 350 and 380 kV after the first breakdown. To investigate if this decrease in the breakdown voltage is permanent or temporary the tested electrodes were retested using the same test procedure. Furthermore, the test results can also indicate if the reduced breakdown voltage is stable or that the breakdown voltage shows a further decrease with an increase in the number of breakdowns.

The breakdown test results of all neat epoxy and epoxy nanocomposite coated electrodes show roughly the same behaviour. Therefore, also for the retests the breakdown test results of only one electrode are presented here. The breakdown test results of a used epoxy nanocomposite A coated electrode are depicted in Figure 4.48. The results of the other neat epoxy and epoxy nanocomposite coated electrodes are presented in appendix A.

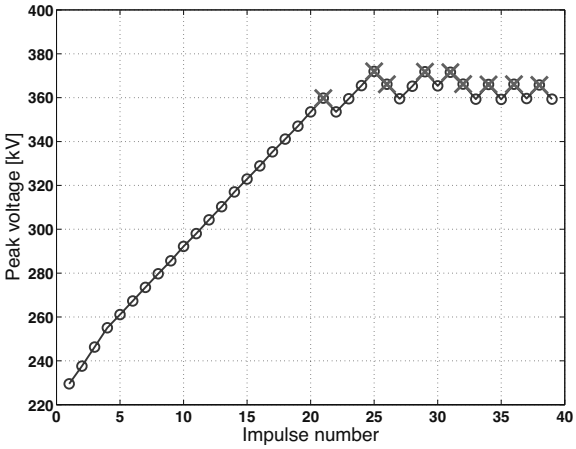

Figure 4.48: Breakdown test results of a used epoxy nanocomposite A coated electrode.

The figure shows that after the first breakdown the breakdown voltage is stabilized around a fixed value which ranges from 350 to 380 kV depending on the electrode sample. Because the breakdown voltage is stabilized after the first breakdown it is possible

to calculate the 50% and 10% breakdown voltage of each electrode sample according to the procedure used in a 50% up-down test. The 50% and 10% breakdown voltage of each electrode are shown in Table 4.20 and Table 4.21 respectively.

Table 4.20: 50% breakdown voltage of retested neat epoxy and epoxy nanocomposite coated electrode samples.

Electrode	Neat Epoxy	Nano A	Nano B	Nano C
1	355 [kV]	374 [kV]	365 [kV]	357 [kV]
2	352 [kV]	373 [kV]	Broken	361 [kV]
3	362 [kV]	371 [kV]	364 [kV]	375 [kV]
4	373 [kV]	368 [kV]	363 [kV]	373 [kV]
5	369 [kV]	378 [kV]	362 [kV]	369 [kV]
6	366 [kV]	366 [kV]	365 [kV]	N/A

Table 4.21: 10% breakdown voltage of retested neat epoxy and epoxy nanocomposite coated electrode samples.

Electrode	Neat Epoxy	Nano A	Nano B	Nano C
1	348 [kV]	361 [kV]	353 [kV]	343 [kV]
2	346 [kV]	365 [kV]	Broken	346 [kV]
3	354 [kV]	361 [kV]	354 [kV]	361 [kV]
4	364 [kV]	361 [kV]	352 [kV]	361 [kV]
5	361 [kV]	359 [kV]	355 [kV]	353 [kV]
6	358 [kV]	353 [kV]	355 [kV]	N/A

The 50% breakdown voltage of the neat epoxy coated electrodes ranges from 352 to 373 kV giving a scatter of 21 kV. In the case of nanocomposite A the 50% breakdown voltage varies between 366 and 378 kV presenting a scatter of 12 kV. Nanocomposite B presents a 50% breakdown voltage in the range of 362 to 365 kV which corresponds to a scatter of 3 kV. Note that the 50% breakdown voltage of nanocomposite B electrode 2 is missing due to the fact that a coating fragment broke off in the initial test as described above. Finally, the 50% breakdown voltage of nanocomposite C varies between 357 and 375 kV which presents a scatter of 18 kV. It can be seen that nanocomposite B shows the smallest scatter in the 50% breakdown voltage.

When observing the 10% breakdown voltages in Table 4.21 it can be seen that the 10% breakdown voltage of the neat epoxy coated electrodes varies between 346 and 364 kV which corresponds to a scatter of 18 kV. The 10% breakdown voltage of the nanocomposite A coated electrodes ranges from 353 to 365 kV giving a scatter of 12 kV. Nanocomposite B shows a 10% breakdown voltage ranging from 352 to 355 kV corresponding to a scatter of 3 kV. Finally, the 10% breakdown voltage of the nanocomposite

C coated electrodes varies between 343 and 361 kV presenting a scatter of 18 kV. Also in this case the nanocomposite B electrodes show the smallest scatter.

For each coating material the test results of all electrodes are combined after which a suitable probability distribution, in most cases a three parameter Weibull distribution, is fitted to the combined test results. The 50% and 10% quantiles of the breakdown voltage of each material are then derived from the obtained distributions.

The 50% and 10% breakdown voltage of the retested thick coating materials are shown in Figure 4.49 and Figure 4.50 respectively. From Figure 4.49 it can be derived that the 50% breakdown voltage of the retested coated electrodes is reduced with respect to the 50%

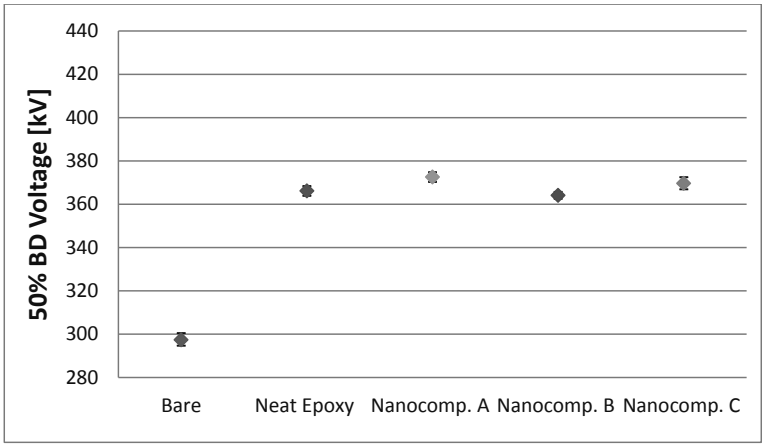

Figure 4.49: 50% Breakdown voltage of retested neat epoxy and epoxy nanocomposite coated electrode samples including 95% confidence intervals.

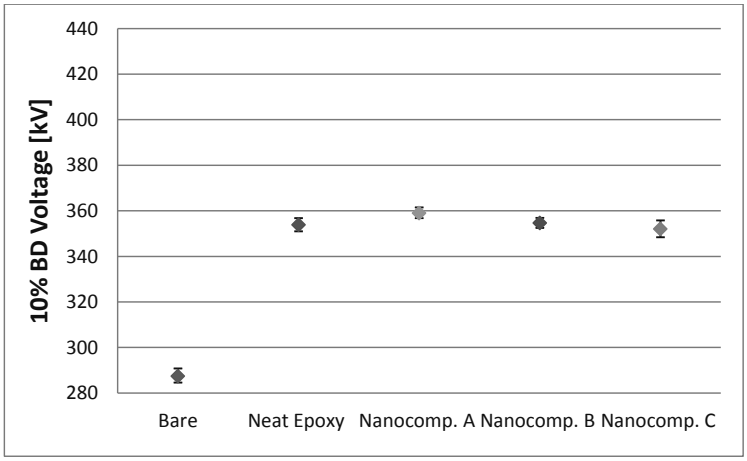

Figure 4.50: 10% Breakdown voltage of retested neat epoxy and epoxy nanocomposite coated electrode samples including 95% confidence intervals.

breakdown voltage obtained in the corresponding initial tests. Therefore, it seems that the reduction in the breakdown voltage of the neat epoxy and epoxy nanocomposite coated electrodes after the first breakdown in the initial tests remains unchanged. Note that a further decrease in the breakdown voltage is not observed.

The remaining improvement in the 50% breakdown voltages of the retested neat epoxy and nanocomposite B coated electrodes with respect to that of bare electrodes is 23%. Moreover, nanocomposites A and C show an improvement of 25% and 24% respectively. The remaining improvement with respect to bare electrodes has thus dropped with 11% for neat epoxy, 9% for nanocomposite A, 8% for nanocomposite B and 5% for nanocomposite C when compared to the improvement obtained in the initial tests. Note that the difference between the improvement of the nanocomposite C coated electrodes in the initial test and in the retests is insignificant due to the overlapping 95% confidence intervals. When the confidence level is reduced to 68.2% the difference remains insignificant.

The difference between the 50% breakdown voltages of the retested neat epoxy and epoxy nanocomposite coated electrodes is minor with a maximum difference of 2.3%. Moreover, the 95% confidence intervals are small due to the relatively small scatter in the breakdown and withstand data used for distribution fitting.

Figure 4.50 shows that the difference between the 10% breakdown voltages of the retested neat epoxy and epoxy nanocomposite coated electrodes is also minor with a maximum difference of 2.0%. Furthermore, the 95% confidence intervals are in this case also small due to the small scatter in the breakdown and withstand data used for distribution fitting.

The remaining improvement in the 10% breakdown voltage with respect to bare electrodes is 23% for neat epoxy and nanocomposite B, 25% for nanocomposite A and 22% for nanocomposite C. Moreover, the reduction in the improvement with respect to the initial tests is 7%, 2%, 9% and -2% (increase) for the neat epoxy and nanocomposite A, B and C coated electrodes respectively. However, the reduction in the improvement is insignificant for the nanocomposite A and C coated electrodes due to the overlapping 95% confidence intervals. Also for a confidence level of 68.2% the reduction is insignificant.

4.3 WAITING TIME IN LIGHTNING IMPULSE BREAKDOWN TESTS

As explained in section 3.4, the waiting time between the applied impulses in a lightning impulse breakdown test might have an influence on the breakdown behaviour. In this section the influence of the waiting time between impulses on the breakdown test results is described.

For the investigation two extra breakdown tests were performed on small size bare electrodes with a machined finish using the combined test procedure. The waiting time between the applied impulses in these tests is six minutes instead of one minute. The 50% and 10% breakdown voltage obtained in these tests is compared with those obtained in the breakdown tests with a 1 minute waiting time.

The 50% and 10% breakdown voltages of bare, machined electrodes tested with a one minute and six minutes waiting time between impulses are displayed in Figure 4.51 and Figure 4.52 respectively. The blue diamonds in the figures represent the breakdown voltages obtained with a six minutes waiting time whereas the red squares represent those obtained with a one minute waiting time.

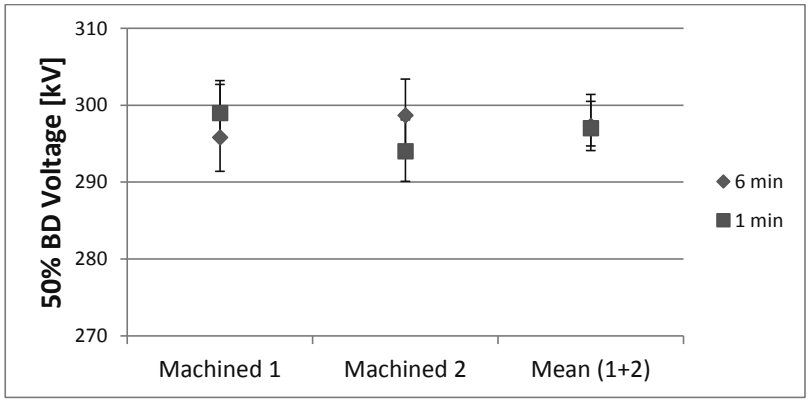

Figure 4.51: 50% Breakdown voltage of bare, machined electrodes tested with a one minute and a six minutes waiting time between impulses, including 95% confidence intervals.

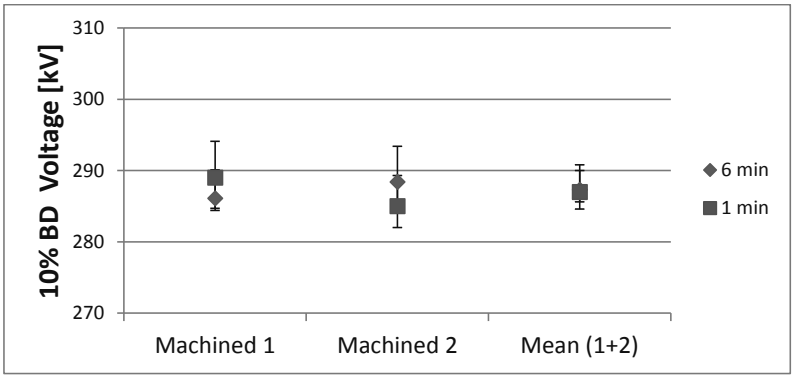

Figure 4.52: 10% Breakdown voltage of bare, machined electrodes tested with a one minute and six minutes waiting time between impulses, including 95% confidence intervals.

Figure 4.51 shows that the difference between the 50% breakdown voltages obtained with a waiting time of one minute and a waiting time of six minutes is insignificant. Furthermore, the test results in Figure 4.52 show that for the 10% breakdown voltage the difference between the results obtained with a waiting time of one minute and a waiting time of six minutes is also insignificant.

The difference between the breakdown test results of machined electrodes using a one minute or six minutes waiting time between impulses is considered to be insignificant. Therefore, for the lightning impulse breakdown tests a one minute waiting time is applied to minimize the test duration.

FP-I and FP-II coated electrodes

The influence of the waiting time between impulses on the breakdown behaviour of FP-I and FP-II coated electrodes was also investigated. For both FP-I and FP-II three extra samples were tested using the combined test procedure with a six minutes waiting time between impulses.

The breakdown test results of a FP-I coated electrode using a six minutes waiting time are depicted in Figure 4.53. From the figure it can be derived that also in this case the breakdown voltage is reduced to a level below that of a bare electrode after the first breakdown. The breakdown test results of the other FP-I coated electrodes are presented in appendix A.

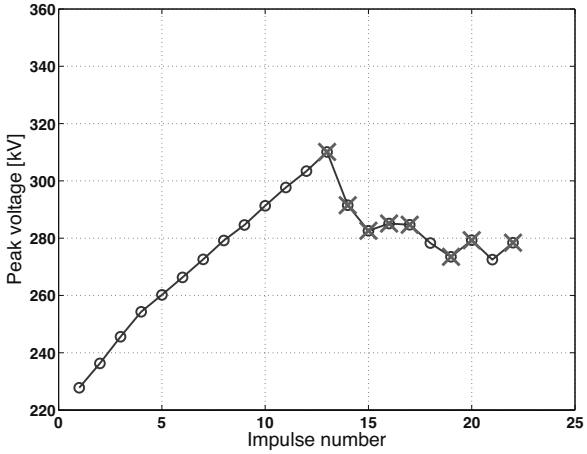

Figure 4.53: Breakdown test results of a FP-I coated electrode using a waiting time of 6 minutes.

Moreover, the first breakdown voltages range from 297 to 328 kV which is in the same range as the first breakdown voltages obtained in the tests with a one minute waiting time.

The breakdown test results of a FP-II coated electrode using a six minutes waiting time are shown in Figure 4.54. The figure shows that also for a six minutes waiting time the breakdown voltage increases with an increase in breakdown number. The breakdown test results of the other FP-II coated electrodes can be found in appendix A.

In this case, the first breakdown voltages range from 285 to 303 kV which is in the same range as the first breakdown voltage obtained in the tests with a one minute waiting time. Moreover, the highest breakdown voltage obtained in the tests with a six minutes waiting time varies between 334 and 340 kV which falls within the range of highest breakdown voltages obtained in the tests with a one minute waiting time. Furthermore, the corresponding improvement with respect to the 50% breakdown voltage of bare electrodes ranges from 12% to 16% which also falls within the range of improvements found for the tests with a one minute waiting time.

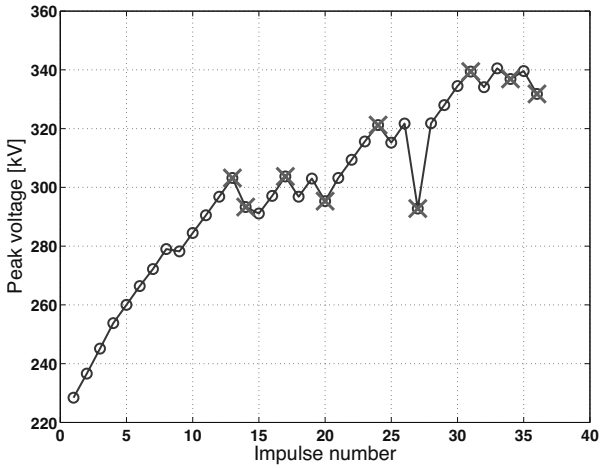

Figure 4.54: Breakdown test results of a FP-II coated electrode using a waiting time of six minutes.

In total, it can be concluded that the difference between the breakdown behaviour found in the lightning impulse breakdown tests with a one minute waiting time and the behaviour found in the tests with a six minutes waiting time is negligible. Note that it cannot be concluded that the waiting time in general has no influence on the lightning impulse breakdown behaviour of the gas and gas-coating insulation in the test setup. For example, it might be the case that the waiting time between impulses only has an influence on the breakdown test results in a larger time scale. In this case the waiting

time between impulses should be increased further to observe any significant influence on the breakdown behaviour which is unfeasible with respect to the time constraints.

Another possibility is the fact that the influence of the waiting time on the breakdown behaviour is only significant at a shorter time scale due to the relatively small gap distance of 22 mm. To observe any influence on the breakdown behaviour the waiting time between impulses should be reduced. However, the time required to charge the capacitors in the impulse voltage generator is too long to apply a significantly shorter waiting time.

4.4 BREAKDOWN VOLTAGE – MEDIUM AND LARGE SIZE ELECTRODES

As explained in section 3.2, three different electrode sizes are used in the breakdown tests. The lightning impulse breakdown tests are also performed on the medium and large size electrodes to investigate the influence of the electrode surface area and a more homogeneous electric field distribution on the breakdown behaviour, as explained in section 3.4.

For the breakdown tests on the medium and large size electrodes two coating materials were selected which showed the most favourable breakdown behaviour in the breakdown tests on the small size electrodes. One thin and one thick coating material were selected. The selected materials are PA11 and neat epoxy.

PA11 was selected because of the highest improvement in the 50% and 10% first breakdown voltage with respect to the 50% and 10% breakdown voltages of bare electrodes. Neat epoxy was chosen as the most suitable material for the large and medium size electrodes because of the fact that it was unfeasible to produce large quantities of epoxy nanocomposite material.

4.4.1 Medium size electrodes (48 mm diameter)

As a reference the breakdown tests were first performed on uncoated electrodes. The breakdown test results of the uncoated medium size electrodes are listed in Table 4.22. As was the case for the breakdown tests on the small size electrodes described in sections 4.1 to 4.3, the breakdown tests on the medium size electrodes are performed in dry air with a gas pressure of 0.9 MPa. Two bare electrodes were tested using the combined test procedure.

For each of the two electrodes the up-down part of the test results was fitted to three parameter Weibull distribution after which the 50% and 10% breakdown voltage were determined. The mean 50% and 10% breakdown voltages were determined by performing a distribution fit on the combination of the breakdown test results of both electrodes.

Table 4.22: Breakdown test results of uncoated medium size electrodes in dry air at 0.9 MPa.

Electrode	1st Breakdown	Highest Breakdown	50% Breakdown	10% Breakdown
1	387 [kV]	387 [kV]	366 kV]	350 [kV]
2	401 [kV]	401 [kV]	367 [kV]	353 [kV]
Mean	394 [kV]	394 [kV]	368 [kV]	351 [kV]

The results in the table show that the difference in the 50% and 10% breakdown voltage between the two electrodes is relatively small with a difference of 1 kV and 3 kV in the 50% and 10% breakdown voltages respectively. Moreover, the first breakdown voltage is higher than the 50% breakdown voltage with a mean difference of 7.1% and the 1st breakdown voltage is in both cases the highest breakdown voltage. This behaviour is comparable with the test results found for the uncoated small size electrodes. More information on the breakdown test results of the medium size uncoated electrodes can be found in appendix A.

The first breakdown voltages of the PA11 and neat epoxy coated electrodes are shown in Table 4.23. The results in the table show that the first breakdown voltage of the PA11 coated electrodes varies between 377 and 425 kV which corresponds to a scatter of 48 kV or 11%.

Table 4.23: First breakdown voltages of medium size PA11 and Neat Epoxy coated electrodes.

Electrode	PA11	Neat Epoxy
1	377 [kV]	376 [kV]
2	425 [kV]	383 [kV]
3	420 [kV]	356 [kV]
4	413 [kV]	369 [kV]
5	399 [kV]	383 [kV]
6	399 [kV]	376 [kV]
7	384 [kV]	363 [kV]
8	405 [kV]	363 [kV]

The first breakdown voltage of the neat epoxy coated electrodes ranges from 356 to 383 kV which corresponds to a scatter of 27 kV or 7%.

The 50% and 10% breakdown voltages of the bare, PA11 coated and neat epoxy coated electrodes are depicted in Figure 4.55 and Figure 4.56 respectively. Figure 4.55 shows that the 50% breakdown voltage of PA11 coated electrodes is significantly higher than the 50% breakdown voltage of bare electrodes with a corresponding improvement of 9.5%. Furthermore, the 50% breakdown voltage of the neat epoxy coated electrodes shows no

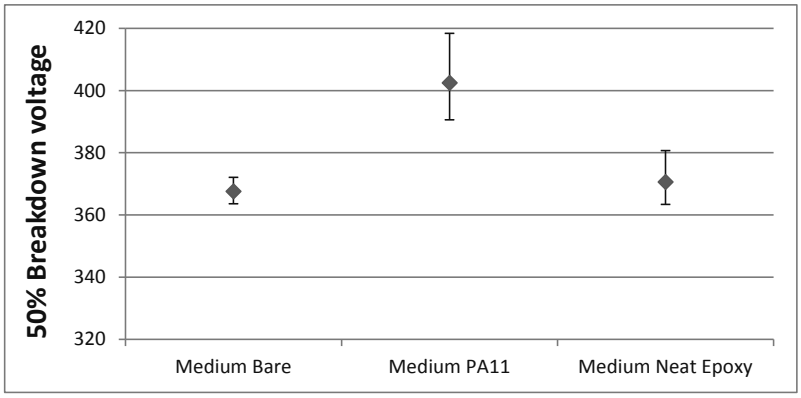

Figure 4.55: 50% Breakdown voltage of medium size bare, PA11 coated and neat epoxy coated electrodes including 95% confidence intervals.

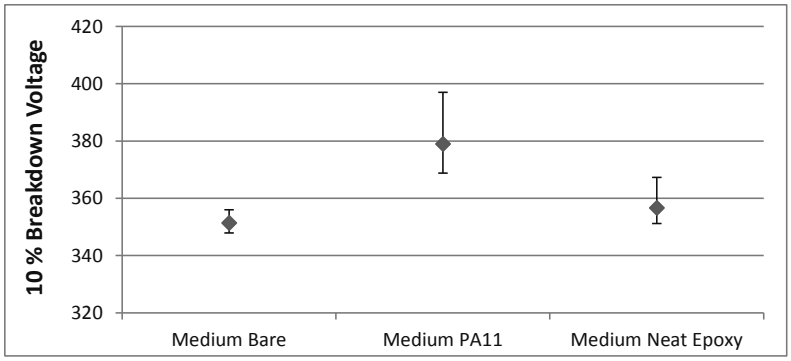

Figure 4.56: 10% Breakdown voltage of medium size bare, PA11 coated and Neat Epoxy coated electrodes including 95% confidence intervals.

significant improvement with respect to that of bare electrodes. When a confidence level of 68.2% is selected the improvement remains insignificant.

When observing the 10% breakdown voltages in Figure 4.56 it can be seen that also in this case the PA11 coated electrodes show a significant improvement with respect to bare electrodes. The corresponding improvement is 8%. The neat epoxy coated electrodes again show no significant improvement which is also the case when the confidence level is reduced to 68.2%. Compared to the results of the small electrodes it is observed that the improvement in the 50% breakdown voltage with respect to bare electrodes for PA11 coated electrodes is reduced from 15% to 9.5%.

However, the improvement in the 10% breakdown voltage shows a minor increase from 7.7% to 8%. Note that for both the 50% and 10% breakdown voltage the improvement remains significant. For the neat epoxy coated electrodes it is observed that the

improvement in the 50% breakdown voltage is reduced from 34% to an insignificant improvement. Furthermore, the improvement in the 10% breakdown voltage is reduced from 30% to an insignificant improvement. Next to the improvement, the 50% and 10% breakdown voltage of neat epoxy is also reduced from 399 and 373 kV to 371 and 357 kV respectively compared to the results of the small electrodes.

4.4.2 Large size electrodes (70 mm diameter)

Also for the large size electrodes breakdown tests were first performed on uncoated electrodes to obtain a reference. The breakdown test results of the uncoated electrodes are shown in Table 4.24.

Table 4.24: Breakdown test results of uncoated large size electrodes in dry air at 0.9 MPa.

Electrode	Highest Breakdown	50% Breakdown	10% Breakdown
1	446 [kV]	422 [kV]	417 [kV]
2	445 [kV]	436 [kV]	425 [kV]
Mean	446 [kV]	432 [kV]	416 [kV]

From the results in the table it can be seen that also for the large size electrodes the difference in the breakdown test results of the two bare electrodes is small. The difference between the highest, 50% and 10% breakdown voltages is 1 kV, 14 kV and 8 kV respectively. Note that in this case the applied test procedure was a standard 50% up-down to avoid the long step up sequence in the combined test. Therefore, the first breakdown voltage is not applicable and is in this case not included in the test results.

The first breakdown voltages obtained for the large size PA11 and neat epoxy coated electrodes are listed in Table 4.25. From the results it can be seen that the first breakdown voltage of the PA11 coated electrodes ranges from 430 to 479 kV which corresponds to a scatter of 49 kV or 10%. Moreover, the first breakdown voltage of the neat epoxy coated electrodes varies between 358 and 379 kV which represents a scatter of 21 kV or 5.5%.

The 50% and 10% quantiles of the breakdown voltage of the bare, PA11 coated and neat epoxy coated large size electrodes are depicted in Figure 4.57 and Figure 4.58 respectively. Figure 4.57 shows that also for the large size electrodes the 50% breakdown voltage of PA11 coated electrodes shows a significant improvement with the 50% breakdown voltage of bare electrodes. The corresponding improvement is 4.6%. The 50% breakdown voltage of neat epoxy coated electrodes shows a relatively large decrease of 15% with respect to large size bare electrodes.

Table 4.25: First breakdown voltage of large size PA11 and Neat Epoxy coated electrodes.

Electrode	PA11	Neat Epoxy
1	451 [kV]	358 [kV]
2	430 [kV]	363 [kV]
3	479 [kV]	363 [kV]
4	462 [kV]	364 [kV]
5	427 [kV]	379 [kV]
6	455 [kV]	379 [kV]
7	435 [kV]	363 [kV]
8	471 [kV]	371 [kV]

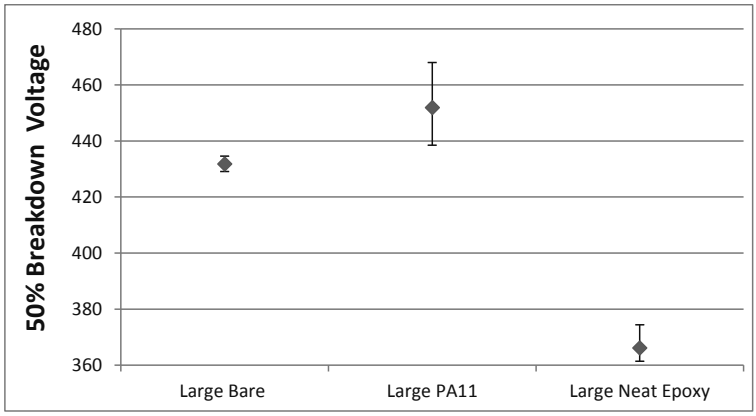

Figure 4.57: 50% Breakdown voltage of large size bare, PA11 coated and Neat Epoxy coated electrodes including 95% confidence intervals.

The results in Figure 4.58 show that the 10% breakdown voltage of PA11 coated electrodes shows no significant improvement with respect to the 10% breakdown voltage of bare electrodes. Unfortunately, also with a 68.2% confidence level the improvement is insignificant. The 10% breakdown voltage of the neat epoxy coated electrodes shows even a significant decrease of 14%.

The improvement in the 50% and 10% breakdown voltage of the PA11 coated electrodes shows a further reduction from 9.5% to 4.6% and 8% to no significant improvement respectively compared with the results of the medium size electrodes. In the case of the neat epoxy coated electrodes the insignificant improvement in the 50% and 10% breakdown voltage with respect to bare electrodes is decreased to a reduction of 15% and 14% respectively. Note that the 50% breakdown voltage of neat epoxy coated electrodes shows a decrease from 373 to 366 kV with respect to the results obtained for

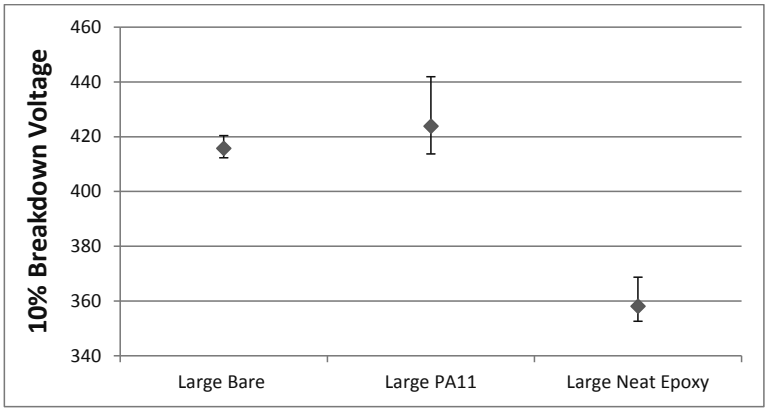

Figure 4.58: 10% Breakdown voltage of large size bare, PA11 coated and Neat Epoxy coated electrodes including 95% confidence intervals.

the medium size electrodes. Furthermore, the 10% breakdown voltage of large size neat epoxy coated electrodes is almost equal to that obtained for medium size electrodes with a difference of 1 kV.

4.5 DISCUSSION

In this section the gas and gas-coating breakdown test results presented in sections 4.1 through 4.4 are discussed. This section also includes an in-depth discussion on the applied breakdown test procedure and the influence of the waiting time between impulses on the breakdown test results.

4.5.1 Breakdown test procedure

As explained in sections 3.4 and 4.1, a range of breakdown test procedures exist in the standards to determine the dielectric withstand or breakdown voltage of solid, liquid and gaseous insulating media. Because this research consists of a relatively large amount of breakdown tests it was important to find the most efficient test procedure with respect to the time duration and the accuracy of the test results.

The preliminary investigation into the available test procedures for self-restoring insulation media, presented in section 4.1, showed that the 50% up-down (class 2, procedure D [49]) test has the shortest test duration which is up to 3.3 times shorter than the other evaluated procedures. The 50% and 10% breakdown voltages were in all cases obtained by statistical analysis of the breakdown test results. The difference in the breakdown voltages obtained from the different tests was negligible.

The test types or classes in the standards were defined to directly obtain the 50% or 10% breakdown voltage using simple calculations on the test results instead of using complex computational algorithms. Moreover, the standard deviation can also be obtained in some cases with a simple formula.

In this comparison, the breakdown test results obtained from the different test procedures are subjected to statistical analysis using distribution fitting software (Weibull++) instead of using the prescribed formulas. Both the 50% and 10% breakdown voltages are then derived from the obtained probability distributions. Because the acquired probability distributions are dependent on the breakdown and withstand data only, the 50% and 10% breakdown voltages obtained from each test should be comparable with minor differences caused by a varying number of breakdowns. This is confirmed by the fact that the 50% resp. 10% breakdown voltage obtained from each test show no significant difference.

The IEC 60060-1 standard does not take the availability of powerful distribution fitting software into account. With the use of distribution fitting software it is unnecessary to make use of different test procedures or test parameters to obtain breakdown voltages with different values of the breakdown probability. The only prerequisite is the availability of a sufficient amount of test data to acquire a reliable distribution fit from which the breakdown voltages and probabilities including confidence intervals can be extracted. Note that the distribution fitting requires a relatively small amount of time and combined with a fast test procedure results in a severe reduction of the total testing time. Furthermore, the amount of information obtained from the test data is much larger compared to the traditional procedures described in IEC 60060-1.

4.5.2 Waiting time between impulse applications

It was explained in section 3.4 that the waiting time between impulse applications in a lightning impulse breakdown test can have significant influence on the breakdown test results which was investigated in section 4.3 using the same rod-plane test setup (section 3.1) as used for the gas-coating breakdown tests.

The results of the investigation showed that for the 50% resp. 10% breakdown voltage no significant difference was found between a test with a six minutes waiting time and a test with a one minute waiting time, which is different from the observations obtained from literature[51] and as described in section 3.4. In section 4.3 two probable causes of this difference were discussed.

With respect to the results obtained in literature [51] several factors are different in this research. Firstly, in this research the gas gap distance is 2.2 cm which is roughly a factor ten smaller resulting in a different equilibrium ion concentration in the gas gap as explained on the next page. Secondly, the applied gas type and pressure is in this case dry air and 0.9 MPa while in literature SF_6 with a pressure of 0.4 MPa is applied. Thirdly, the

shape and surface area of the electrodes in the rod-plane test setup are different from those used in the coaxial setup in literature.

The equilibrium concentration of charge carriers in the gas gap of the rod-plane setup is likely to be smaller than found in the coaxial setup in literature due to the higher recombination rate of charge carriers, caused by the close presence of the electrode surfaces in the rod-plane gas gap. The equilibrium charge carrier concentration profile of the coaxial gas gap in literature has a plateau shape which falls to zero at a distance of 2 cm from the electrode surfaces due to the enhanced recombination of charge carriers near the electrode surfaces. The corresponding profile is shown on the left side of Figure 4.59. In the rod-plane gap it is more likely that the concentration profile has a hyperbolic shape and that a full equilibrium concentration is not reached due to the recombination processes at the electrode surfaces, which reduce the charge carrier concentration along the entire gas gap due to the small gap width[51]. The corresponding charge carrier concentration profile is shown on the right-hand side of Figure 4.59. Because of the lower predicted charge carrier concentration in the gas gap of the rod-plane gap it is expected that the time constant of reestablishment of equilibrium is also smaller compared to literature, which explains the fact that in this research no difference can be found between lightning impulse breakdown tests with a one minute and six minutes waiting time.

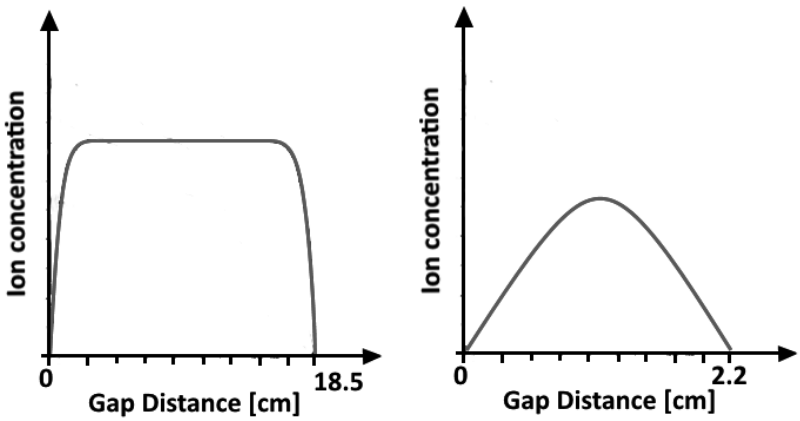

Figure 4.59: Sketch of charge carrier concentration profile of coaxial gap [51] (left) and rod-plane gap (right)

As explained above, SF_6 gas with a pressure of 0.4 MPa is used in literature, while in this investigation dry air is applied with a pressure of 0.9 MPa. According to theory, the effective ionization rate (ionization rate minus electron attachment rate) of dry air at 0.9 MPa is comparable to that of SF_6 at 0.34 MPa. Therefore, the equilibrium concentration of negative ions should be comparable resulting in a comparable equilibrium concentration of

charge carriers and consequently a comparable time constant for the reestablishment of the equilibrium concentration of charge carriers.

However, as opposed to the effective ionization rate, the impact ionization rate of both gases at the corresponding gas pressures is not equal, resulting in different equilibrium concentrations of positively charged species for both situations. This implies that there is a significant difference in the time constant related to the reestablishment of the equilibrium charge carrier concentration in the gas gap. The difference between the equilibrium concentration of charge carriers and the corresponding time constant in SF_6 and dry air has not been investigated. However, it is expected that the influence of the gas gap size and shape on the equilibrium charge carrier concentration and corresponding time constant is dominant in this case. Therefore, it is expected that the gas gap size and shape are the most significant parameters with respect to the influence of the waiting time between impulses in a lightning impulse breakdown test on the breakdown test results.

4.5.3 Gas-coating breakdown test results on small size electrodes

With the above mentioned considerations on the most efficient test procedure and the influence of the waiting time between impulses taken into account, the lightning impulse breakdown tests were performed on gas and gas-coating insulation using the rod-plane test setup. As explained in section 3.3, a wide range of dielectric coating materials were evaluated with respect to the breakdown voltage of the combined gas-coating insulation system and the corresponding possible improvement over the breakdown of an uncoated gas insulated system.

To facilitate the evaluation of a wide variety of coating materials, the size of the rod electrodes to which the coating materials are applied is kept relatively small as explained in section 3.2 (small size electrodes). The considerations on selecting the correct electrode dimensions and gas gap distance are also explained in section 3.2. The results of the gas and gas-coating breakdown tests on small size electrodes are presented in section 4.2.

The type of coatings applied to the electrode surfaces have been classified as either a thick or a thin coating in this research as described in chapter 2 and section 3.3. As explained in section 3.3, the layer thickness of the coatings is the main classification parameter. However, the two coating types also differ significantly with respect to the production process, application method and the physical mechanisms involved in the breakdown of the combined gas-coating insulation.

Consequently, the approach of improving an existing GIS design with a coating would be different for both coating types. Therefore, the evaluation results of the two coating types can be analysed independently. However, a comparison between the results of thin and thick coatings can facilitate the selection of either one or a combination of both types of coatings for improvement of a GIS design.

Thin coatings – 1st breakdown

The results have shown that the 50% 1st breakdown voltage of the coated samples was significantly higher than that of uncoated electrodes for three out of seven thin coating materials. These materials are EP-I (4% improvement), Semiconductor A (8% improvement) and PA11 (15% improvement).

To determine if the 50% 1st breakdown voltage of coated samples is significantly different from that of bare electrodes the 95% confidence intervals should not overlap as explained in section 4.2. When the confidence intervals do show overlap the difference is considered insignificant. This selection criterion is less strict when a lower confidence level of 68.2% is selected for the confidence intervals because the width of these intervals is reduced to half that of the 95% confidence intervals.

When a 68.2% confidence level is selected, the 50% 1st breakdown voltage of FP-I and FP-III also becomes significantly higher than that of bare electrodes with an improvement of 3% and 7% respectively. Thus, the total number of thin coating materials with a significant improvement in the 50% 1st breakdown voltage is increased to five. The two remaining thin coating materials show either no significant improvement or even a reduction of the 50% 1st breakdown voltage with respect to uncoated electrodes. FP-II shows no significant difference in the 50% 1st breakdown voltage and the 50% 1st breakdown voltage of FP-IV is significantly lower, with a reduction of 5%.

When observing the 10% 1st breakdown voltage it can be seen from the results that only PA11 and Semiconductor A show a significant improvement with respect to bare electrodes of 7% and 5% respectively. The other materials show either no significant improvement or even a reduction in the case of FP-IV.

Considering both the 50% and 10% 1st breakdown voltage it can be concluded that PA11 shows the largest improvement over uncoated electrodes followed by semiconductor A. EP-I, FP-I and FP-III show only an improvement in the 50% 1st breakdown voltage with the latter two only showing an improvement when the confidence level is reduced to 68.2%.

The reason why the coating materials show either an improvement, a reduction or no significant change in the 50% resp. 10% 1st breakdown voltage with respect to uncoated electrodes is related to the coating material and electrode characteristics. The coating material and electrode characteristics are evaluated in chapter 5. Moreover, in section 5.6 the correlation between the results of the gas-coating breakdown tests and the coating material characteristics is investigated.

Thin coatings – breakdown behaviour after the 1st breakdown

In most cases found in literature (chapter 2) and for four out of seven thin coating materials tested in this research, the breakdown voltage of a coated gas insulated system is reduced after the first breakdown to the level of an uncoated system. Mostly, the

breakdown voltage is reduced to a value below that of uncoated electrodes, due to the increased surface roughness near the location of the breakdown, as shown in section 4.2. For thin coatings, breakdowns always result in a puncture through the coating layer. Therefore, it can be stated that in these cases the gas-coating insulation is broken and that the improving quality of the coating is lost, provided that the coating improved the breakdown voltage in the first place.

However, for FP-II, FP-IV and to a lesser extent Semiconductor A, the breakdown behaviour after the first breakdown is different. For these materials the breakdown voltage either remains relatively constant or even increases after the first breakdown. In the latter case, the breakdown voltage increases further with an increase in the number of breakdowns up to a maximum level which is different for each electrode sample. Moreover, the highest breakdown voltage is reached after a varying number of breakdowns.

To quantify the above mentioned behaviour, the 50% and 10% highest breakdown voltage are derived with statistical analysis in the same way as performed for the 1st breakdown voltage. When the 50% highest breakdown voltage is observed it can be seen that in this case FP-II and FP-IV coated electrodes show a significant improvement with respect to uncoated electrodes of 11% and 17% respectively. The improvement of Semiconductor A has increased to 12% when the 50% highest breakdown voltage is selected instead of the 50% 1st breakdown voltage. Note that the 50% highest breakdown voltage of all other materials and the uncoated electrodes is the same as the 50% 1st breakdown voltage.

Regarding the 10% highest breakdown voltage, FP-II, FP-IV and Semiconductor A show no significant improvement due to the wide 95% confidence intervals. When compared to the 10% 1st breakdown voltage it can be seen that the 10% highest breakdown voltage of semiconductor A has reduced from 5% to an insignificant improvement. However, when a lower confidence level of 68.2% is selected, the improvement of FP-II and Semiconductor A becomes significant with values of 5% and 8% respectively. Again it should be noted that the 10% highest breakdown voltage of all other materials is the same as the 10% 1st breakdown voltage.

Because the breakdown behaviour of FP-II, FP-IV and Semiconductor A after the 1st breakdown was different than expected, two extra tests were conducted on FP-II as described in section 4.2.2. Firstly, a second breakdown test was performed on three already tested, FP-II samples. These tests were performed to determine if the increase in breakdown voltage observed in the initial tests is related to a permanent change in the composition of the coating material or if it is related to a temporary improvement of the gas-coating insulation.

Secondly, on three new FP-II samples a standard 50% up-down test was performed instead of the combined test procedure, which is used in all other breakdown tests on coated electrodes. These tests were performed to evaluate the influence of the progres-

sive stress part of the combined tests on the increase in breakdown voltage after the first breakdown.

Based on the results of the first test we conclude that the increase in the breakdown voltage of the FP-II coated electrodes after the first breakdown is temporary. The breakdown voltage of the used electrodes is reduced to the same level as the 1st breakdown of new, untested, FP-II coated electrodes. Therefore, the improvement in the breakdown voltage after the first breakdown is lost.

The results of the second test have shown that without the progressive stress part of the breakdown tests the breakdown voltage also shows a positive dependency on the number breakdowns after the first breakdown. However, the increase in the breakdown voltage is in this case less pronounced compared to the results obtained from the combined test procedure which includes the progressive stress part before the first breakdown.

In total, the results of the extra tests indicate that the above mentioned behaviour of FP-II electrodes after the first breakdown is related to a temporary change in either the gas composition, gas conditions, coating surface conditions or a combination of these factors. Moreover, pre-conditioning of the coating-gas insulation with a progressive stress sequence enhances this behaviour. Note that these extra tests were not performed on FP-IV and Semiconductor A coated electrodes.

More information on the underlying mechanism causing this behaviour can be obtained from the coating material and electrode characteristics which are evaluated in chapter 5. In section 5.6, the correlation between the breakdown behaviour and the material characteristics of the FP-II, FP-IV and Semiconductor A coated electrodes is discussed.

Thin coatings – double layer coatings

The seven thin coating materials, of which the breakdown test results are discussed above, all consist of a single layer. Before a thin coating layer is applied to the electrode surface the electrode surface is roughened with abrasive blasting as explained in section 3.3. It was hypothesised that electric field enhancements, caused by the rough electrode surface under the coating layer, reduce the breakdown strength of the gas-coating insulation. To overcome this reduction, it was suggested to apply a semi-conductive coating layer on the electrode surface on top of which the actual dielectric coating layer is applied. Consequently two double layer coatings were produced with FP-II as the base, semi-conductive, layer and either PA11 or FP-I as the topcoat. These two materials are described in section 3.3. Note that the double layer coatings are also classified as thin coatings.

The results of the breakdown tests on the double layer coatings have shown that only FP-II – PA11 shows a significant improvement of roughly 4% in both the 50% and

10% 1st breakdown voltage. The 50% and 10% 1st breakdown voltage of the FP-II – FP-I coated electrodes show no significant difference with respect to uncoated electrodes. The breakdown test results are described in more detail in section 4.2.3.

The breakdown test results of the FP-II – FP-I coated electrodes also show that the breakdown voltage is increased after the first breakdown as was the case for the single layer FP-II, FP-IV and semiconductor A coated electrodes. However, for FP-II – FP-I the increase in the breakdown voltage is less pronounced than in the case of the single layer materials. The 50% highest breakdown voltage of FP-II – FP-I shows a significant but small improvement of 1% with respect to uncoated electrodes when a 68.2% confidence interval is chosen. The difference between the 10% highest breakdown voltage of FP-II – FP-I and that of uncoated electrodes is insignificant.

We conclude that the double layer coatings show a severely reduced improvement in the 50% resp. 10% first and highest breakdown voltages with respect to the single layer PA11 and FP-I coated electrodes. This severe reduction is related to the observed loss of adhesion between the bottom layer and the topcoat in the double layer coatings as will be discussed in section 5.6 in combination with the observed breakdown damage in section 5.5.

Thick coatings

The breakdown test results of the thick coatings, described in section 4.2.4, show that the 50% 1st breakdown voltage of all thick coating materials show a significant improvement with respect to uncoated electrodes ranging from 29% to 34%. Regarding the 10% 1st breakdown voltage the thick coating materials show a significant improvement between 20% and 32%.

The difference between the four thick coating materials with respect to the 50% 1st breakdown voltage is relatively small. The most remarkable difference is the fact that the 95% confidence interval of the epoxy nanocomposite B coated electrodes is noticeably smaller than the 95% confidence intervals of the other thick coating materials for both the 50% and 10% 1st breakdown voltage.

For the thick coating materials breakdowns almost always occur in the form of surface discharges between the tip of the rod electrode and the holding plane of the rod electrodes. The breakdown voltage of the electrodes coated with a thick coating material is reduced after the first breakdown to a level which is still significantly higher than that of bare electrodes. Consequently, the breakdown voltage is stabilized at the reduced level which is confirmed by performing the same test a second time on all electrodes after the first tests. The results of these retests are described in section 4.2.4.

The results of the retests show that the improvement in the 50% resp. 10% breakdown voltages of the thick coatings after the first breakdown is reduced to values between 22% and 25% with respect to the 50% resp. 10% breakdown voltage of bare electrodes. This

reduction is related to a change in the surface state of the thick coatings after the first surface discharge. This change in the surface state is visible as surface discharge tracks as explained in section 5.5.

In section 5.6, the correlation between the material and electrode characteristics and the relatively small difference in breakdown tests results between the four different thick coating materials is discussed. The influence of the material characteristics and the surface discharge damage on the breakdown behaviour after the first breakdown is also discussed in section 5.6.

Comparison

When comparing the breakdown test results of the thin and thick coatings it can be seen that the thick coatings present an improvement in the breakdown voltage with respect to bare electrodes which is roughly twice as large as observed for the thin coating materials. Therefore, it can be stated that the thick coatings show the best performance with respect to the improvement of the breakdown voltage.

However, thick coatings also exhibit several disadvantages with respect to thin coatings. Firstly, it is unfeasible to apply thick coatings on large electrode surfaces due to the related production and application procedures which become less reliable when a large surface area and thus a large coating volume is required.

Secondly, the thermal conductivity of dielectric materials is relatively low. Applying a thick dielectric layer thus results in a severely reduced cooling capacity of the coated conductors. Consequently the amount of electrode surface covered by a thick coating is limited to small sections. Thirdly, the amount of resin necessary to coat an electrode is orders of magnitude larger compared to thin coatings which presents a severe increase in production costs.

In total, the comparison between thin and thick coating indicates that thick coatings are more suitable to be used in small areas with high electric fields due to the observed large improvement in combination with the limitations on the coating surface area. Whereas thin coatings are more suitable for larger electrode surfaces where a smaller improvement in the breakdown voltage is required.

4.5.4 Scaling up to larger dimensions

From the results of the breakdown tests on the small size electrodes two coating materials were selected which showed the largest improvement in the breakdown voltage with respect to uncoated electrodes. The selected materials are PA11 as a thin coating and Neat Epoxy as a thick coating.

These materials are applied to the medium and large size electrodes after which breakdown tests were performed on the coated medium and large size electrodes using the same test procedure as applied in the breakdown tests on the small size electrodes. The

dimensions of the medium and large size electrodes are shown in section 3.2 and the corresponding breakdown test results are described in section 4.4.

These breakdown tests are performed to investigate the influence of an increased electrode surface area and a less divergent electric field distribution on the improvement in the breakdown voltage of coated electrodes with respect to uncoated electrodes. For these tests only the best performing thin coating is selected to save valuable testing time. With respect to thick coatings the difference between the best performing materials was insignificant. Therefore, neat epoxy was used because for this research it was unfeasible to apply nanocomposite B to medium and large size electrodes due to the large amount of nanoparticles required.

The results of the breakdown tests on medium and large size electrodes show that for medium size electrodes the improvement in the 50% resp. 10% 1st breakdown voltage of PA11 coated electrodes with respect to uncoated electrodes remains significant with a value of 9.5% and 8% respectively. In the case of large size electrodes the PA11 coated electrodes also show a significant improvement in the 50% 1st breakdown voltage which is in this case 5%. Unfortunately, the 10% 1st breakdown voltage of large size PA11 coated electrodes shows no significant improvement.

Regarding the breakdown test results on medium and large size neat epoxy coated electrodes it can be seen that the improvement in the 50% resp. 10% 1st breakdown voltage of medium size neat epoxy coated electrodes is reduced to an insignificant difference with respect to uncoated electrodes. Moreover, the 50% resp. 10% 1st breakdown voltage of large size neat epoxy coated electrodes even shows a reduction of 15% and 14% respectively, compared to uncoated electrodes.

The fact that the improvement in the 50% resp. 10% 1st breakdown voltage of PA11 coated electrodes is reduced when the electrode size is increased is caused by two main factors. Firstly, the increase in electrode surface area and thus the increase in coating volume results in an increased probability of production errors such as the inclusion of particles and air bubbles. Secondly, the electric field in the gas gap is less divergent which reduces the influence of the rod electrode on ionization phenomena in the gas. The influence of electron field emission from the rod electrode becomes less pronounced which presents less room for improvement with the application of a thin coating on the electrode surface.

The strong reduction of the improvement in the 50% resp. 10% breakdown voltage of Neat epoxy coated electrodes is related to the change in the electric field strength in the gas gap when the electrode size is increased. Because for thick coatings the electric field in the gas gap is directly related to the permittivity of the coating materials, the cause of the reduction of the improvement in the 50% resp. 10% 1st breakdown voltage is discussed in section 5.6.

4.6 SUMMARY

In total, the results of the breakdown tests presented in this chapter led to the following observations. Firstly, of all thin coating materials PA11 shows the highest improvement in the 1st breakdown voltage. This improvement is also present when the electrode surface area is increased and the electric field is less divergent.

Secondly, in several cases the breakdown voltage of electrodes coated with a thin coating is not reduced after the first breakdown. Initially, in most of these special cases the breakdown voltage even increases with an increase in the number of breakdowns. Unfortunately, the observed increase in the breakdown voltage is lost after a certain amount of time. Note that in all of these cases the coating is punctured after breakdown.

Thirdly, applying a semi-conductive layer beneath a coating layer did not result in a higher improvement of the 50% resp. 10% 1st breakdown voltage when compared to the improvement found for the corresponding single layer coatings. Fourthly, the improvement in the 50% resp. 10% 1st breakdown voltage is twice as large for thick coatings as it is for thin coatings. However, the application of thick coating layers on electrodes in GIS is more limited compared to thin coatings. Therefore, a suitable combination of thin and thick coatings should be determined for the improvement of each GIS design.

Finally, reducing the divergence of the electric field in the gas gap significantly reduces the improvement in the 50% resp. 10% 1st breakdown voltage for electrodes coated with thick neat epoxy. This reduction even results in a decrease of the 50% resp. 10% 1st breakdown voltage compared to uncoated electrodes when the largest electrode size is used.

5

Coating material characterisation

In this chapter the coating material characteristics are evaluated using the experiments described in section 3.5. Section 5.1 presents the results of the surface roughness measurements on bare and coated electrodes. In section 5.2, the dielectric response of the coating materials is evaluated with frequency and temperature scans of the relative permittivity and dielectric losses. The electrical conductivity results of the coating materials are presented in section 5.3. Section 5.4 contains the results of the AC breakdown tests on the flat coating material samples. In section 5.5 the damage of the coating layers caused by the electrical breakdowns is presented. Finally, section 5.6 contains a discussion on the coating material characteristics including a discussion on the possible relation between the coating material characteristics and the breakdown behaviour of the gas-coating system described in chapter 4.

5.1 SURFACE ROUGHNESS

In section 2.4 it was explained that the roughness of the electrode surfaces can have a significant influence on the breakdown voltage of a gas insulated system. Therefore, the surface roughness of the bare electrodes was evaluated according to the method described in section 3.5.1. Furthermore, the surface of the coated electrodes might not be smooth as indicated by the visibly rough surface of several coating materials. Thus, the surface roughness of the coated electrodes is also evaluated.

The results of the surface roughness measurements are listed in Table 5.1. The surface roughness is evaluated with the roughness parameters R_z and R_y which represent the ten-point average roughness and the maximum height respectively. More information on surface roughness parameters is presented in section 3.5.1.

As can be seen from the table the coating surfaces are generally smoother than the surface of a bare, machined electrode with values of R_z ranging from 0.48 to 4.79 µm and R_y varying between 0.79 and 6.9 µm, excluding the surface roughness of the FP-III

Table 5.1: Surface roughness parameters of the uncoated electrodes and coating materials.

Material	R_z [µm]	R_y [µm]
Bare, machined	6.37	7.53
Bare, sand blasted	18.5	28.5
Neat epoxy	2.19	3.10
Nanocomposite B	2.34	3.65
Nanocomposite C	2.14	3.17
Semiconductor A	0.60	0.87
EP-I	2.88	3.69
FP-II	2.91	4.37
FP-I	1.45	1.86
FP-III	8.91	13.9
FP-IV	1.82	2.71
PA11 small	0.57	0.79
PA11 medium	0.48	0.82
PA11 large	1.05	1.61
FP-II – FP-I	4.79	6.90
FP-II – PA11	2.19	2.77

coated electrodes which is exceptionally larger than that of bare, machined electrodes. Especially the value of R_y is significantly larger than that of bare, machined electrodes. The large roughness of the FP-III coated electrodes is most likely caused by the relatively small average layer thickness of 25 µm which is in the same range as the R_y of the sand blasted electrodes.

All thin coatings have been applied on the rod electrodes after sand blasting. Therefore, it might be the case that the FP-III material shows no full smoothing of the electrode surface roughness resulting in a relatively rough coating surface. Furthermore, it might also be the case that the highest peaks on the aluminium surface remain uncovered.

Two materials which are also interesting are PA11 and Semiconductor A which both show a relatively smooth surface. The R_z of both materials varies between 0.48 and 0.60 µm, whereas R_y ranges from 0.79 to 0.87 µm. Note that in these cases the roughness is always smaller than 1 µm. An exception is found for the large size electrodes coated with PA11. In this case the coating surface is rougher with an R_z and R_y of 1.05 and 1.61 µm respectively, which might be caused by variations in the production process.

Finally, both double layer coatings show a larger surface roughness than the corresponding single layer versions of the topcoats. For example, the FP-II – PA11 coated electrodes have an R_z and R_y which are almost four times larger than that of PA11 coated electrodes.

5.2 DIELECTRIC RESPONSE

As explained in section 2.3, the relative permittivity of a coating material can have a significant influence on the breakdown behaviour of a coated gas insulated system. Therefore, the dielectric response of the coating materials was measured using dielectric spectroscopy. From the dielectric response the relative permittivity can be derived. The measurement method and procedures are described in detail in section 3.5.3.

5.2.1 EP-I

The frequency spectra of the relative permittivity of the EP-I samples at temperatures of -40 °C, -20 °C, 0 °C, 20 °C, 40 °C and 60 °C are depicted in Figure 5.1, whereas the frequency spectra obtained at 80 °C, 100 °C and 120 °C are depicted in Figure 5.2. For comparison, the value of the relative permittivity is selected at a frequency of 100 kHz because the main frequency of a lightning impulse is in the same range.

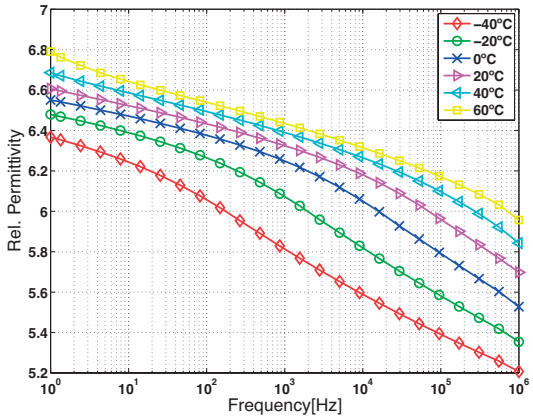

Figure 5.1: Relative permittivity of EP-I material samples as a function of frequency at temperatures between -40°C and 60°C. The frequency range is 1 Hz to 1 MHz.

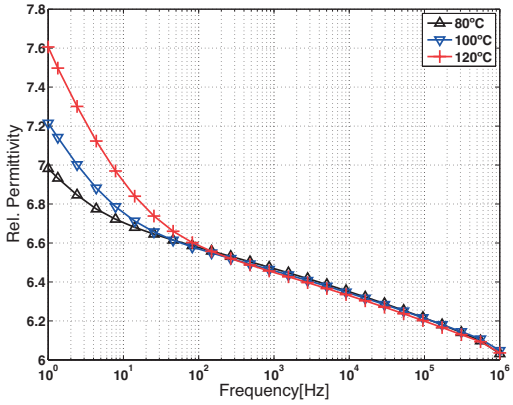

Figure 5.2: Relative permittivity of EP-I material samples as a function of frequency at temperatures between 80 °C and 120 °C. The frequency range is 1 Hz to 1 MHz.

Therefore, it is derived from the figures that the relative permittivity of the EP-I samples at 100 kHz ranges from 5.40 to 6.22 for temperatures between -40 °C and 120 °C. Note that the relative permittivity of the EP-I samples is higher than expected from an epoxy resin based material. Epoxy resins usually show a relative permittivity in the range of 3.5 to 5 at power frequency.

Epoxy resin based materials are prone to absorb water from the environment. Because the EP-I samples were not dried before performing the dielectric spectroscopy measurements, absorbed water in the coating material is not removed. In [48] and [53] it is shown that water ingress in epoxy resins increases the relative permittivity over the entire frequency range which clarifies the higher than expected relative permittivity. Unfortunately, no dielectric spectroscopy measurements were performed on dried EP-I

Table 5.2: Relative permittivity of EP-I at 100 kHz

Temperature	Relative permittivity
120 °C	6.20
100 °C	6.22
80 °C	6.22
60 °C	6.18
40 °C	6.10
20 °C	5.97
0 °C	5.80
-20 °C	5.59
-40 °C	5.40

samples for a direct comparison. The values of the relative permittivity at 100 kHz are listed in Table 5.2.

In Figure 5.1 it can be seen that for all isothermals there is a slight change in the slope of the frequency spectrum. The location of this change moves to higher frequencies when the temperature is increased. This change is caused by beta relaxation processes which are related to movement of small polymer chain segments or side chains[54]. Furthermore, in Figure 5.2 it can be seen that the permittivity shows a steeper increase with a decrease in frequency for the low frequency range. This behaviour is caused by Maxwell-Wagner polarization [54] which is related to charge accumulating at internal dielectric boundaries formed by the absorbed water as discussed below.

The beta relaxation processes, which are slightly visible in the relative permittivity plots, are clearly visible in the dielectric loss (ε") plots as wide peaks which extend along several frequency decades, as depicted in Figure 5.3. The loss peaks are present in the loss plots at -40 ºC to 20 ºC and shift to a higher frequency with an increase in temperature. Beta relaxation processes show an Arrhenius type temperature dependency. Therefore, the activation energy can be calculated by fitting the frequency locations of the relaxation peaks for each isothermal to an Arrhenius equation. The activation energy of the beta relaxation processes is in this case 0.81 eV.

The dielectric relaxation processes found in materials can be characterised by a range of functions which describe the complex permittivity as a function of frequency and temperature [54]. The most widely applied functions include the Debye function, the

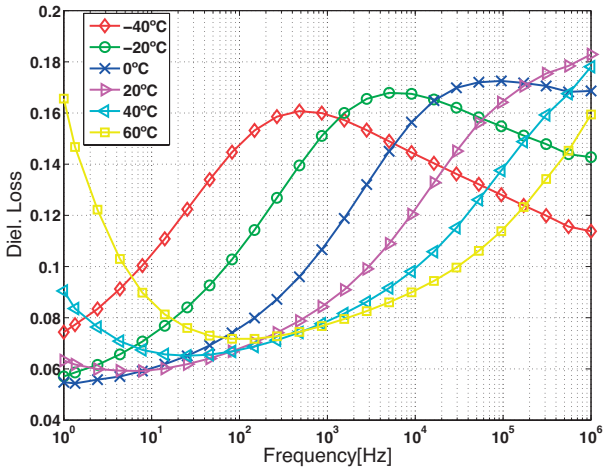

Figure 5.3: Dielectric losses of EP-I material samples as a function of frequency at temperatures between -40 ºC and 60 ºC. The frequency range is 1 Hz to 1 MHz.

Cole-Cole function, the Cole-Davidson function and the HN-function (derived by Havriliak and Negami) [54]. For polymers, the HN-function is most suitable because of the presence of alpha and beta relaxation. The HN-function is described below.

$$\varepsilon_{HN}(\omega, T) = \varepsilon_{\infty} + \frac{\varepsilon_s - \varepsilon_{\infty}}{(1 + (i\omega\tau_{HN})^{\beta})^{\alpha}} \qquad (16)$$

In the HN-function the term ε_s - ε_∞ is the dielectric relaxation intensity and τ_{HN} is the relaxation time constant. The parameter ε_s represents the permittivity for $\omega \rightarrow 0$ and ε_∞ represents the permittivity for $\omega \rightarrow \infty$. The beta relaxation processes are represented by the exponent β. Next to the beta relaxation processes, also alpha relaxation processes are included in the HN-function, which are related to the movement of large polymer chain sections at temperatures in the range of the glass transition. Alpha relaxation is not visible in the dielectric loss plots of EP-I in the applied frequency and temperature range. In the next section, on the dielectric response of FP-I, alpha relaxation is described in more detail.

At 40 ºC and 60 ºC the dielectric losses show a steep increase when the frequency is reduced below 10 Hz and 100 Hz respectively. This increase in losses is caused by an increased DC conductivity of the material due to the increased temperature. Moreover, the contribution of Maxwell-Wagner polarization, caused by the absorbed water, becomes significant from temperatures of 40 ºC and higher. The fact that the dielectric loss increase at low frequencies is not purely ohmic in nature can be seen from the slope of this increase. When plotted in a double logarithmic plot the slope of the corresponding isothermals is smaller than 1, indicating the presence of charge separation phenomena such as Maxwell-Wagner. The most simple model with which Maxwell-Wagner polarization can be described, is a two-layer structure containing two materials with different permittivity (ε_1, ε_2) and conductivity (σ_1, σ_2). The complex permittivity is in this case determined by the equations displayed below.

$$\varepsilon(\omega) = \varepsilon_{\infty} + \frac{\Delta\varepsilon}{1 + i\omega\tau_{MW}} \qquad (17)$$

$$\Delta\varepsilon = \frac{\varepsilon_2\sigma_1 + \varepsilon_1\sigma_2}{(\sigma_1 + \sigma_1)^2(\varepsilon_1 + \varepsilon_2)} \qquad (18)$$

$$\Delta\varepsilon = \frac{\varepsilon_2\sigma_1 + \varepsilon_1\sigma_2}{(\sigma_1 + \sigma_1)^2(\varepsilon_1 + \varepsilon_2)} \qquad (19)$$

The relaxation time constant τ_{MW} is now dependent on the relative permittivity and the conductivity of both materials. The most significant feature of this, is the fact that the time constant is inversely dependent on the conductivity of the two materials. When the materials have a relatively high conductivity, the effect of Maxwell-Wagner polarization is more pronounced in the applied frequency range. More generally, it can be stated that Maxwell-Wagner polarization effects are more pronounced for conductive materials.

When observing the dielectric losses at temperatures of 80 ºC, 100 ºC and 120 ºC shown in Figure 5.4 it can be seen that the losses are dominated by the steep increase at frequencies below 100 Hz. The combination of the increase in losses and the increase in relative permittivity in the low frequency range again indicate the presence of Maxwell-Wagner polarization as described above.

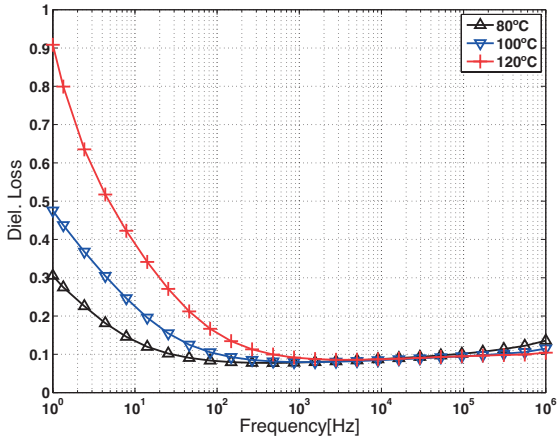

Figure 5.4: Dielectric losses of EP-I material samples as a function of frequency at temperatures between 80 ºC and 120 ºC. The frequency range is 1 Hz to 1 MHz.

Note that DC conductivity is also present in this temperature range although the presence is masked by the Maxwell-Wagner polarization. Moreover, electrode polarization is not present because the increase in the relative permittivity at low frequencies is very small compared to cases where electrode polarization is present[54]. When electrode polarization occurs, the relative permittivity at low frequencies shows an increase of several orders of magnitude which is not the case here. Furthermore, electrode polarization mostly occurs in measurements on highly conductive materials[54].

5.2.2 FP-I

The frequency spectrums of the relative permittivity of FP-I at temperatures ranging from -40 ºC to 120 ºC are depicted in Figure 5.5. Also in this case the permittivity is relatively high for ECTFE based materials of which the relative permittivity generally is in the order of 2.5. Furthermore, it can be seen in the figure that also for FP-I, beta relaxation processes are present which are related to side chain movement. As opposed to the EP-I samples the permittivity increase with a frequency decrease shows no steeper slope at the low frequency range. Therefore, charge separation effects such as Maxwell-Wagner and electrode polarization[54] are not present.

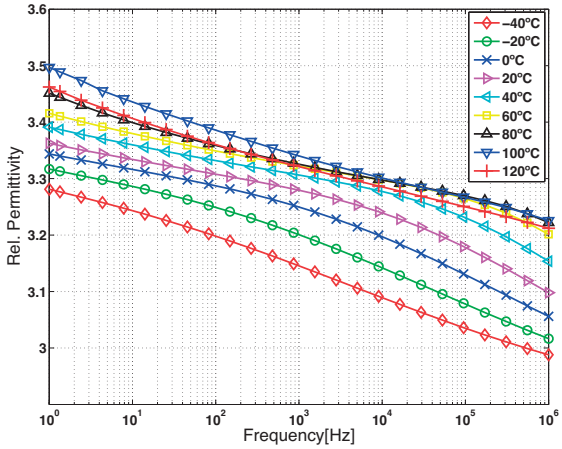

Figure 5.5: Relative permittivity of FP-I material samples as a function of frequency at temperatures between -40ºC and 120ºC. The frequency range is 1 Hz to 1 MHz.

The values of the relative permittivity at 100 kHz are presented in Table 5.3. From the table it can be seen that the relative permittivity of FP-I ranges between 3.04 and 3.27 for temperatures in the range of -40 ºC to 120 ºC. The temperature dependency of the relative permittivity is significantly smaller than for the EP-I coated electrodes.
In Figure 5.6 the frequency spectra of the dielectric losses between -40 ºC and 60 ºC are shown. The evidence of beta relaxation processes found in the frequency spectra of the relative permittivity are clearly visible as wide peaks in the dielectric loss spectra. Also in this case the loss peaks shift to higher frequencies with an increase in temperature. The amplitude of the loss peaks also increases with an increase in temperature. The activation energy of the beta relaxation processes is 0.42 eV.

The frequency spectra of the dielectric losses(ε") at temperatures of 80ºC, 100ºC and 120ºC are depicted in Figure 5.7. These dielectric loss spectra show an increase for decreasing frequencies in the range below 10 kHz. This increase is not visible in the relative

Table 5.3: Relative permittivity of FP-I at 100 kHz

Temperature	Relative permittivity
120 ºC	3.25
100 ºC	3.27
80 ºC	3.27
60 ºC	3.27
40 ºC	3.23
20 ºC	3.18
0 ºC	3.13
-20 ºC	3.08
-40 ºC	3.04

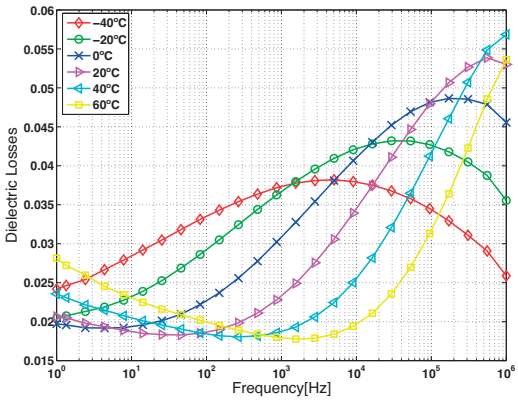

Figure 5.6: Dielectric losses of FP-I material samples as a function of frequency at temperatures between -40 ºC and 60 ºC. The frequency range is 1 Hz to 1 MHz.

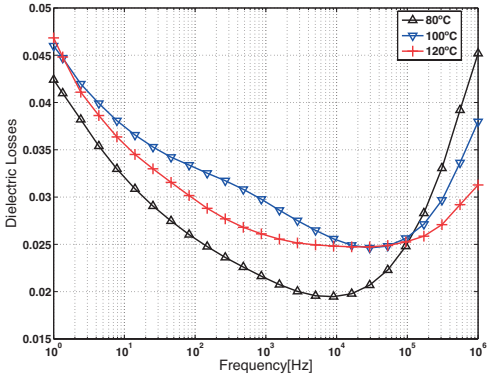

Figure 5.7: Dielectric losses of FP-I material samples as a function of frequency at temperatures between 80 ºC and 120 ºC. The frequency range is 1 Hz to 1 MHz.

permittivity spectra indicating that the losses are the result of DC conductivity which increases with an increase in temperature.

To obtain more insight into the temperature behaviour of the dielectric losses and relative permittivity of FP-I, temperature ramp tests were performed according to the procedure described in section 3.5. The temperature scans obtained from the ramp tests are shown in Figure 5.8 and Figure 5.9.

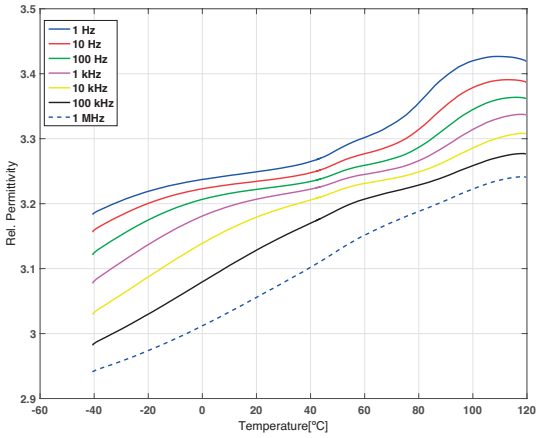

Figure 5.8: Relative permittivity of FP-I material samples as a function of temperature for frequencies between 1 Hz and 1 MHz. The temperature range is -40 °C to 120 °C.

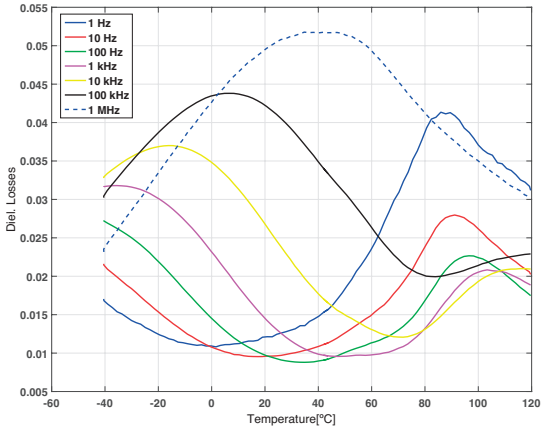

Figure 5.9: Dielectric losses of FP-I material samples as a function of temperature for frequencies between 1 Hz and 1 MHz. The temperature range is -40 °C to 120 °C.

In Figure 5.8 the temperature scans of the relative permittivity are displayed. The beta relaxation processes are visible in the low temperature range of the plots in the form of a change in the slope of the plots. Moreover, in the high temperature range another slope change and subsequent bump can be seen which is caused by alpha relaxation processes related to the glass transition[54].
The temperature scans of the dielectric losses(ε") are depicted in Figure 5.9. In the left hand side of the figure the wide loss peaks related to the beta relaxation processes are visible for frequencies between 100 Hz and 1 MHz. These loss peaks shift to higher temperatures when the frequency is increased.

On the right hand side of the figure, in the high temperature range, a narrow loss peak is visible for frequencies between 1 Hz and 10 kHz. These loss peak are caused by alpha relaxation processes related to movement of large chain sections which occur when the temperature is in the range of the glass transition. The glass transition temperature of ECTFE materials is around 85ºC as determined by dynamic mechanical analysis (DMA).

5.2.3 FP-IV

The frequency spectra of the relative permittivity of FP-IV at temperatures ranging from -40 ºC to 60 ºC are displayed in Figure 5.10, whereas the spectra at temperatures between 80 ºC and 120 ºC are displayed in Figure 5.11. From the figures it can be seen that the permittivity increase at low frequencies is dominant for temperatures of 0 ºC and higher which is caused by Maxwell-Wagner polarization. As explained in section 3.3, this mate-

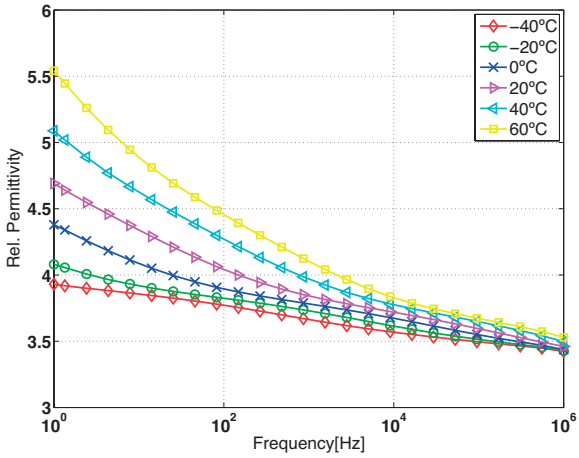

Figure 5.10: Relative permittivity of FP-IV material samples as a function of frequency at temperatures between -40ºC and 60ºC. The frequency range is 1 Hz to 1 MHz.

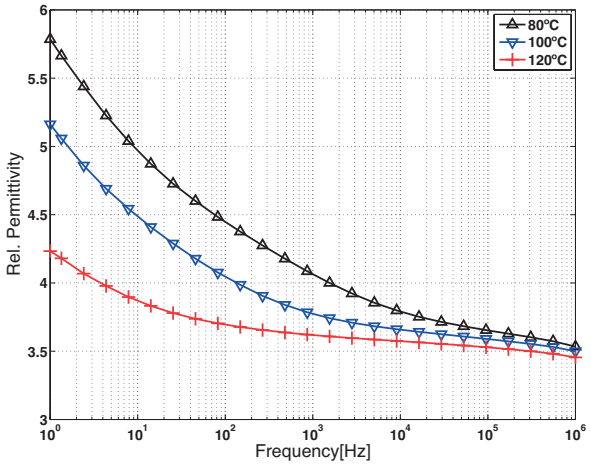

Figure 5.11: Relative permittivity of FP-IV material samples as a function of frequency at temperatures between 80°C and 120°C. The frequency range is 1 Hz to 1 MHz.

rial contains mica particles which introduce dielectric boundaries within the material which can give rise to charge accumulation.

When Figure 5.10 is observed carefully it can be seen that there is beta relaxation visible in the spectra at temperatures between -40 °C and 20 °C. For higher temperatures the relaxation shifts outside the frequency range and Maxwell-Wagner polarization masks the relaxation behaviour. The beta relaxation is best visible in the spectrum at -40°C which is located between 100 Hz and 10 kHz.

The beta relaxation processes are more clearly visible in the dielectric loss(ε″) spectra depicted in Figure 5.12. The corresponding loss peaks are visible in the loss spectra up to 20 °C shifting up in frequency with an increase in temperature. The corresponding activation energy is 0.60 eV. Note that the amplitude of the loss peaks seems to be relatively small which is also observed in the relative permittivity by a relatively minor slope change. However, with respect to the EP-I and FP-I materials the amplitude of the loss peaks is comparable. The scale of the figures is significantly larger in the case of FP-IV reducing the visibility of the loss peaks.

In the low frequency range the dielectric losses increase when the frequency is reduced for temperatures of -20°C and higher. This increase coincides with the increase in relative permittivity which again indicates the presence of Maxwell-Wagner polarization at the boundaries between the polymer matrix and the mica particles. Moreover, the slope of the dielectric loss plots at low frequencies is smaller than 1 when plotted in a log-log plot which is another indication of Maxwell-Wagner polarization.

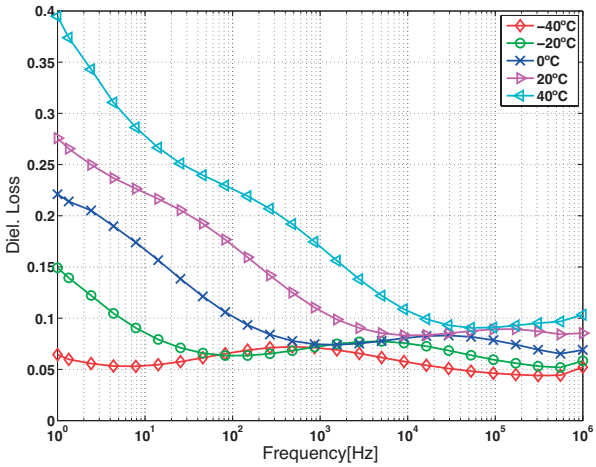

Figure 5.12: Dielectric losses of FP-IV material samples as a function of frequency at temperatures between -40°C and 40°C. The frequency range is 1 Hz to 1 MHz.

In the low frequency range a bump can also be seen in the frequency spectra at temperatures of 0°C and higher. This bump is another loss peak related to beta relaxation which is obscured by the presence of Maxwell-Wagner polarization. The obscured loss peak is also observed in the dielectric loss spectra at 60 °C and 80 °C as shown in Figure 5.13. At 100 °C and 120 °C the obscured loss peak is not observed. The activation energy of the beta relaxation processes related to these loss peaks is 0.56 eV.

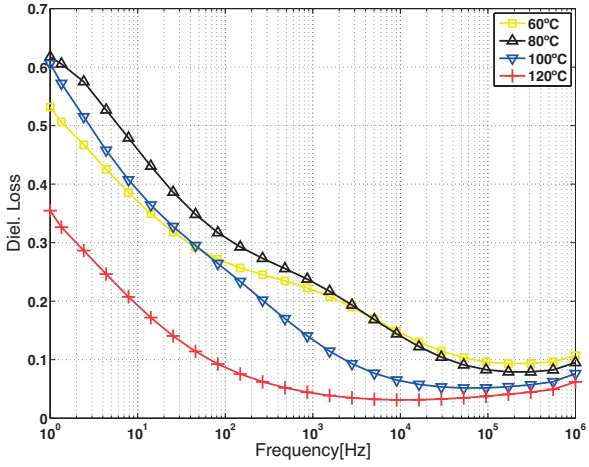

Figure 5.13: Dielectric losses of FP-IV material samples as a function of frequency at temperatures between 60 °C and 120 °C.

In Figure 5.13 it can also be seen that the dielectric losses show a decreasing trend with an increase in temperature for temperatures of 80ºC and higher. Moreover, the relative permittivity shows the same trend in the same temperature range as shown in Figure 5.11. This behaviour can be caused by alpha relaxation processes which are related to the glass transition. Therefore, the dielectric loss data is plotted as a function of temperature in Figure 5.14 and Figure 5.15.

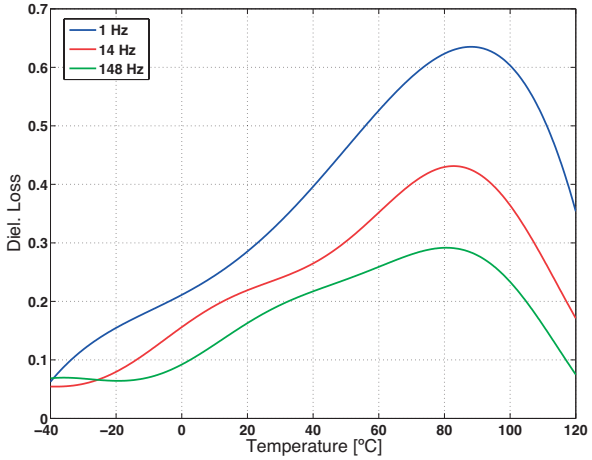

Figure 5.14: Dielectric losses of FP-IV material samples as a function of temperature for frequencies between 1 Hz and 148 Hz. The temperature range is -40 ºC to 120 ºC.

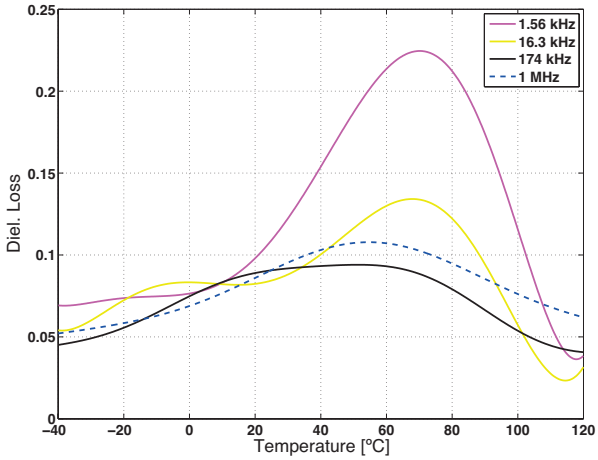

Figure 5.15: Dielectric losses of FP-IV material samples as a function of temperature for frequencies between 1.56 kHz and 1 MHz. The temperature range is -40 ºC to 120 ºC.

The temperature plots of the dielectric losses are obtained by plotting the data of the corresponding frequency spectra as a function of temperature. Consequently, the temperature plots for each frequency consist of only nine date points on which a function is fitted. The temperature plots are thus approximations based on nine temperature points each and are less accurate than the results obtained in a temperature ramp test as applied for the FP-I samples.

In the temperature plots of the dielectric losses a large loss peak can be seen around 80 °C for frequencies between 1 Hz and 16.3 kHz. This loss peak is present near the glass transition temperature of the FP-IV material and can thus be classified as alpha relaxation. Therefore, the decreasing trend in the relative permittivity and the dielectric losses as a function of temperature for temperatures of 80 °C and higher is caused by alpha relaxation processes.

The beta relaxation loss peak found in the high frequency low temperature range of the frequency spectra in Figure 5.12 can also be found in the temperature plots in Figure 5.15. In the 1.56 kHz graph this beta relaxation peak is represented by the small bump between -40 °C and -20°C which actually is a peak obscured by the alpha relaxation. Moreover, a similar bump is found in the 16.3 kHz graph between -20 °C and 0 °C. For the 174 kHz graph the beta relaxation peak and the alpha relaxation peak are comparable in size resulting in a relatively wide and flat peak between 0 °C and 80 °C. Finally, the peak in the 1 MHz graph is mainly caused by the beta relaxation as the influence of the alpha relaxation is minor at this frequency.

The obscured loss peak found in the low frequency region of the frequency spectra of the dielectric losses at temperatures between 0 °C and 80 °C can also be seen in the temperature plots in Figure 5.14 as a bump at the low temperature region. This bump shifts from 0°C to 20°C and 40°C when the frequency is increased from 1 Hz to 14 Hz and 148 Hz. Note that these beta relaxation processes are also present at 1.56 kHz although no loss peak is visible in the corresponding temperature plot due to the strong influence of the alpha relaxation processes in that temperature range.

The values of the relative permittivity at 100 kHz are listed in Table 5.4. From the table it can be seen that the relative permittivity shows a relatively small variation between 3.50 and 3.68. Furthermore, the permittivity shows an increase up to 60 °C. The permittivity decreases when the temperature is increased further. As explained above, this behaviour is caused by the alpha relaxation processes present at temperatures above 60 °C.

Table 5.4: Relative permittivity of FP-IV at 100 kHz

Temperature	Relative permittivity
120 °C	3.53
100 °C	3.58
80 °C	3.66
60 °C	3.68
40 °C	3.65
20 °C	3.60
0 °C	3.55
-20 °C	3.50
-40 °C	3.50

5.2.4 PA11

The frequency spectra of the relative permittivity of the PA11 samples at temperatures between -40 °C and 40 °C are depicted in Figure 5.16 and the spectra at temperatures between 60 °C and 120 °C are displayed in Figure 5.17. Up to 20°C the frequency spectra of the relative permittivity shows an increasing trend with a decrease in frequency of which the slope shows a minor change. Because the slope change is barely visible, relaxation phenomena are also difficult to observe in the frequency spectra of the relative permittivity.

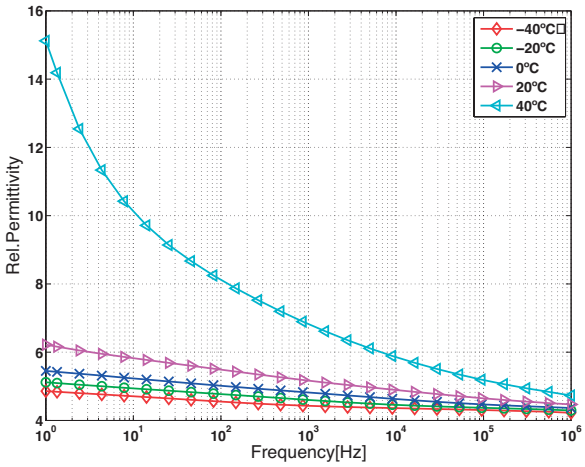

Figure 5.16: Relative permittivity of PA11 material samples as a function of frequency at temperatures between -40 °C and 40 °C. The frequency range is 1 Hz to 1 MHz.

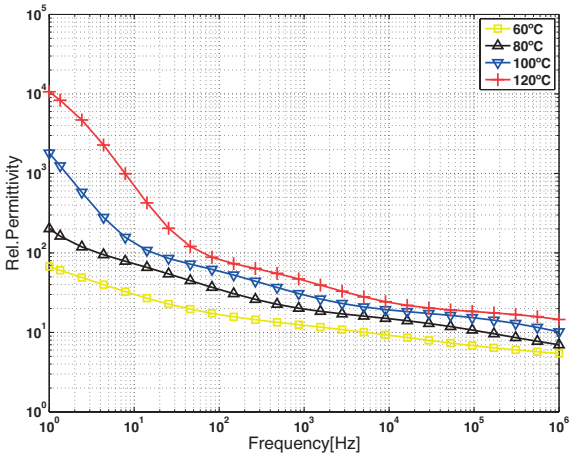

Figure 5.17: Relative permittivity of PA11 material samples as a function of frequency at temperatures between 60 °C and 120 °C. The frequency range is 1 Hz to 1 MHz.

For temperatures of 40 °C and higher the relative permittivity shows a very steep increase for a decrease in frequency. Especially at temperatures above 40 °C the relative permittivity reaches very high values of up to 10^4 at 1 Hz for the 120 °C spectrum.

Beta relaxation processes are visible in the dielectric loss(ε″) spectra at temperatures of 20°C and lower as shown in Figure 5.18. The loss peak shifts from 20 Hz to 2 kHz when

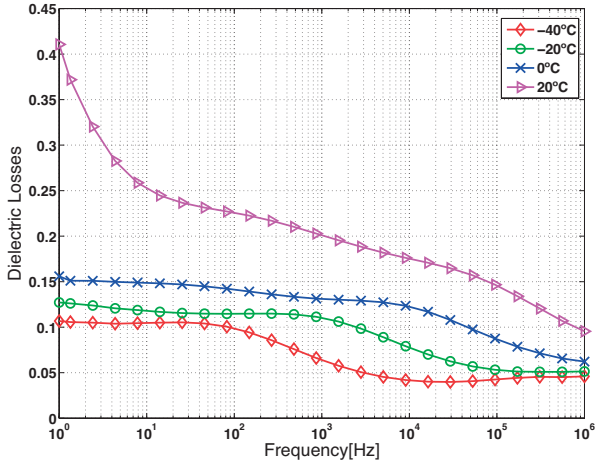

Figure 5.18: Dielectric losses of PA11 material samples as a function of frequency at temperatures between -40 °C and 20 °C. The frequency range is 1 Hz to 1 MHz.

the temperature is increased from -40 ºC to 0 ºC. The corresponding activation energy is 0.7 eV.

Note that on the low frequency side of the dielectric loss spectra at temperatures between -40 ºC and 0 ºC the above mentioned loss peaks are partially obscured. Furthermore, the dielectric loss spectrum at 20 ºC shows a significant increase for frequencies below 50 kHz. The slope of this increase is steeper for frequencies below 10 Hz.

For temperatures of 40 ºC and higher the dielectric loss spectra show significantly different behaviour as depicted in Figure 5.19. At these temperatures the dielectric losses show a steep increase to very high values reaching up to $6x10^4$ when the frequency is reduced to 1 Hz.

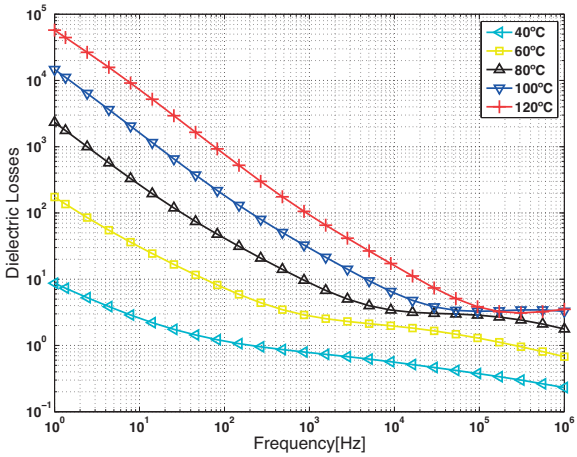

Figure 5.19: Dielectric losses of PA11 material samples as a function of frequency at temperatures between 40 ºC and 120 ºC

In literature it is found that polyamide 11 type materials show a glass transition temperature in the range of 40 ºC to 70 ºC[55], [56]. Moreover, polyamide 11 exhibits ionic conduction which gives rise to a significant contribution to the dielectric losses in the low frequency range[55], [56].

The ionic transport in the material is visible as the obscuring of the loss peaks between -40 ºC and 0 ºC followed by the steep increase in the dielectric losses found for temperatures of 20 ºC and higher. Ionic transport in the material increases with an increase in temperature as can be seen from the dielectric loss figures. For temperatures above the glass transition the ionic conduction in the material is increased strongly with respect to the conduction at temperatures below the glass transition.

Regarding ionic conduction, several observations in the relative permittivity and dielectric loss figures can be explained. Firstly, at low frequencies enough time is available for ions to accumulate at the electrode interfaces due to ionic transport. This charge accumulation is electrode polarization which is clearly visible as the steep increase to very high values in the relative permittivity plots in the low frequency range at temperatures of 40 ºC and higher. Below 40 ºC the ionic transport is too weak to cause significant electrode polarization. Secondly, when the frequency is increased there is only enough time available for ions to accumulate at the boundaries of charged species within the material and at the end of conducting paths. This change in the ion accumulation process is known as conductivity relaxation [4-5]. The conductivity relaxation is not visible in the relative permittivity plots due to the presence of electrode polarization. However, the slope of the dielectric loss plots at high temperatures and at low frequencies is smaller than 1 and is changing with temperature indicating that the conductivity contribution is not DC (ohmic).

Due to the presence of electrode polarization and a significant conductivity contribution it is difficult to observe any relaxation process. However, because the dielectric spectroscopy measurements are conducted below and above the glass transition it is expected that alpha relaxations are present. Therefore, temperature ramp tests were conducted according to the method described in section 3.5 to obtain the temperature scans of the dielectric losses as depicted in Figure 5.20.

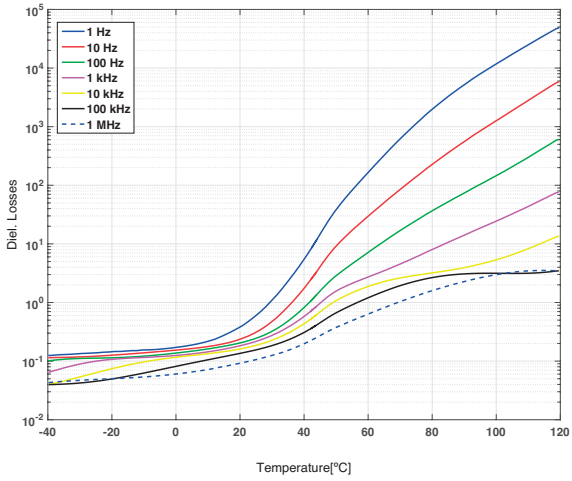

Figure 5.20: Dielectric losses of PA11 material samples as a function of temperature for frequencies between 1 Hz and 1 MHz. The temperature range is -40 ºC to 120 ºC.

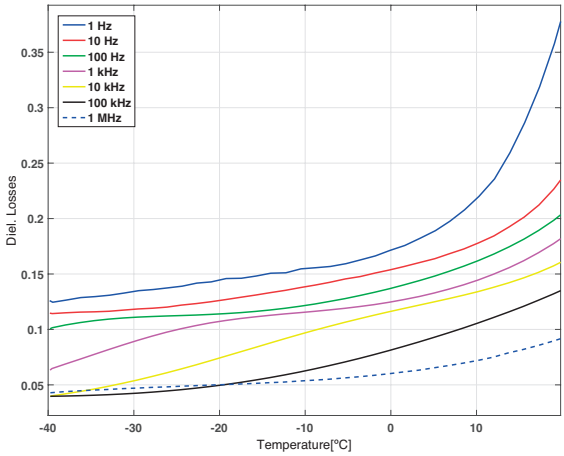

Figure 5.21: Detail of the dielectric losses as a function of temperature for frequencies between 1 Hz and 1 MHz. The temperature range is -40ºC and 20ºC.

From the figure it can be seen that the around 50 ºC a bump is present in the temperature scans of all frequencies. This bump represents the alpha relaxation peak which is obscured by the conductivity and the electrode polarization of the material sample.

The temperature scans of the dielectric losses are observed in more detail in Figure 5.21. In this figure the temperature scans are displayed in the temperature range between -40 ºC and 20 ºC. The loss peaks related to beta relaxation processes found in the frequency spectra in Figure 5.18 are also visible in the detailed view of the temperature scans. These loss peaks are in this case represented by the bumps found in the 100 Hz, 1 kHz and 10 kHz scans at a temperature of roughly -35 ºC, -20 ºC and -5 ºC respectively. Note that these loss peaks are obscured by the alpha relaxation and conductivity contributions.

The values of the relative permittivity of PA11 at 100 kHz are listed in Table 5.5. As can be seen from the table the relative permittivity ranges from 4.31 at -40 ºC to 18.4 at 120 ºC. Moreover, between -40 ºC and 20 ºC the relative permittivity shows a relatively small increase, whereas between 40 ºC and 120 ºC the permittivity shows a relatively large increase. This difference is directly related to the glass transition temperature of roughly 50 ºC above which ionic conduction in the material is strongly increased.

Table 5.5: Relative permittivity of PA11 at 100 kHz

Temperature	Relative permittivity
120 °C	18.4
100 °C	15.4
80 °C	10.7
60 °C	6.85
40 °C	5.19
20 °C	4.65
0 °C	4.47
-20 °C	4.37
-40 °C	4.31

5.2.5 FP-II and FP-III

For FP-III and FP-II the dielectric spectroscopy results have shown that these materials exhibit the behaviour of a resistive material with a relatively high conductivity. In both cases the strong conductivity contribution masks the dielectric relaxation behaviour of the materials.

The behaviour of these materials can be seen in the dielectric loss(ε″) spectra displayed in Figure 5.22 and Figure 5.23 for FP-III and FP-II respectively. In the case of FP-III the dielectric losses show a steep increase with a decrease in frequency over the entire recorded frequency range. At 1 MHz the losses are in the order of 10^2 while at 1 Hz the losses have increased to the order of 10^8. The slope of the dielectric loss increase is 1 which indicates a significant DC (ohmic) conductivity contribution. For FP-II the steep

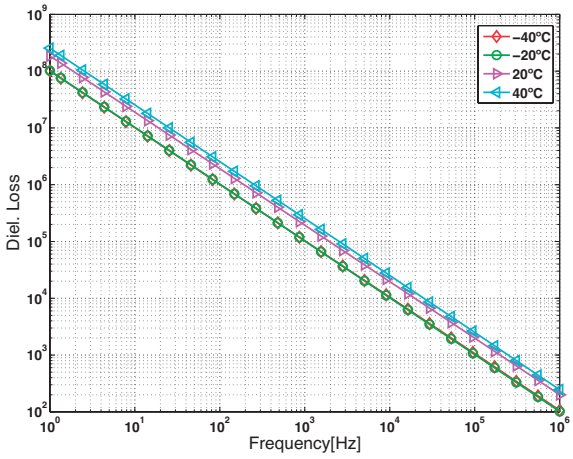

Figure 5.22: Dielectric losses of FP-III material samples as a function of frequency at temperatures between -40 °C and 40°C. The frequency range is 1 Hz to 1 MHz.

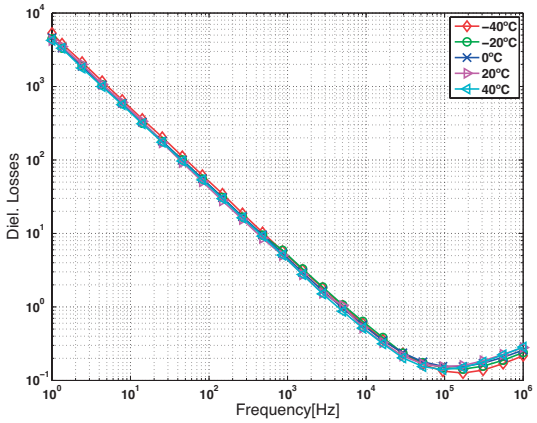

Figure 5.23: Dielectric losses of FP-II material samples as a function of frequency at temperatures between -40 °C and 40 °C. The frequency range is 1 Hz to 1 MHz.

increase in dielectric losses for decreasing frequency is present below 100 kHz starting at the order of 10^{-1} and finishing at the order of 10^{3}. Also in this case the slope is 1, indicating a significant DC (ohmic) conductivity contribution.

Above 100 kHz, no conductivity contribution is visible in the dielectric loss plots of FP-II. Therefore, in this frequency region the relaxation behaviour of FP-II can be assessed. The frequency spectra of the relative permittivity of FP-II are depicted in Figure 5.24.

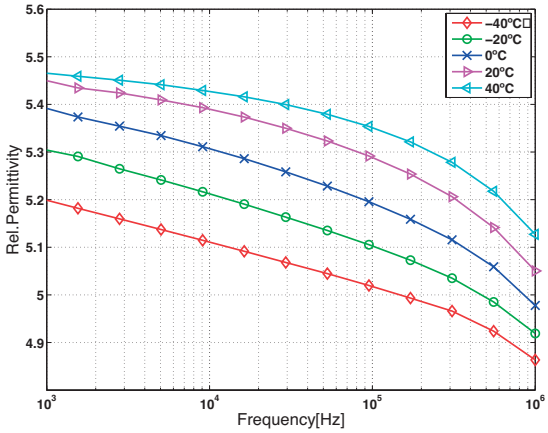

Figure 5.24: Relative permittivity of FP-II material samples as a function of frequency at temperatures between -40 °C and 40 °C. The frequency range is 1 kHz to 1 MHz.

Below 1 kHz the influence of electrode polarization effects becomes visible in the relative permittivity spectra indicating that between 1 kHz and 100 kHz the steep slope in the dielectric losses is only caused by DC conductivity. In the relative permittivity spectra the onset of beta relaxation can be seen which is also present in the form of increasing dielectric losses for an increase in frequency in the frequency range above 100 kHz. The corresponding dielectric loss peak is located at a frequency above 1 MHz.

The values of the relative permittivity of FP-II at 100 kHz are listed in Table 5.6. As can be seen from the table the value of the relative permittivity ranges from 5.02 at -40 ºC to 5.35 at 40ºC. The increase in relative permittivity between -40 ºC and 40 ºC is 0.33 which is in the same range as observed for FP-I.

Table 5.6: Relative permittivity of FP-II at 100 kHz

Temperature	Relative permittivity
40 ºC	5.35
20 ºC	5.29
0 ºC	5.20
-20 ºC	5.11
-40 ºC	5.02

Complex conductivity

Because both FP-III and FP-II exhibit conductive behaviour, more information on the dielectric behaviour can be found in the complex conductivity spectra of these materials. The frequency spectra of the real part of the complex conductivity of FP-III are depicted in Figure 5.25.

As can be seen from the figure, the frequency spectra of the real part of the complex conductivity are relatively flat. There is no upward slope visible for an increase in frequency as is the case with most dielectric materials[54]. This indicates that the material behaves like a resistor and that electrode polarization obscures any dielectric relaxation behaviour over the entire measured frequency and temperature range.

At 1 Hz the real part of the complex conductivity ranges from 5.6×10^{-7} to 6.9×10^{-6} S/m for temperatures ranging from -40 ºC to 120 ºC. When the real part of the complex permittivity is extrapolated to a frequency close to 0 Hz the DC conductivity is obtained. For FP-III at 20 ºC the approximated DC conductivity is 9.6×10^{-7} S/m which represents a highly conductive semiconductor. The frequency spectra of the real part of the complex conductivity of FP-II are displayed in Figure 5.26 and Figure 5.27 for the lower and upper temperature range respectively.

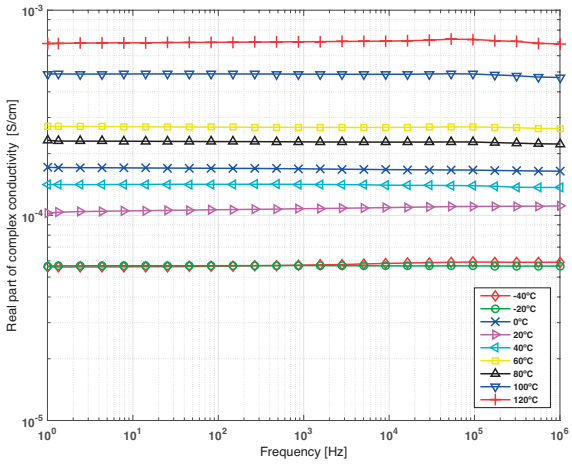

Figure 5.25: Real part of the complex conductivity of FP-III as a function of frequency at temperatures between -40 ºC and 120 ºC. The frequency range is 1 Hz to 1 MHz.

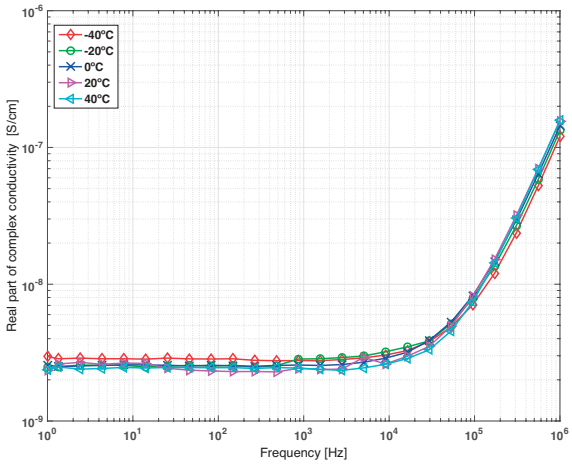

Figure 5.26: Real part of the complex conductivity of FP-II as a function of frequency at temperatures between -40 ºC and 40 ºC. The frequency range is 1 Hz to 1 MHz.

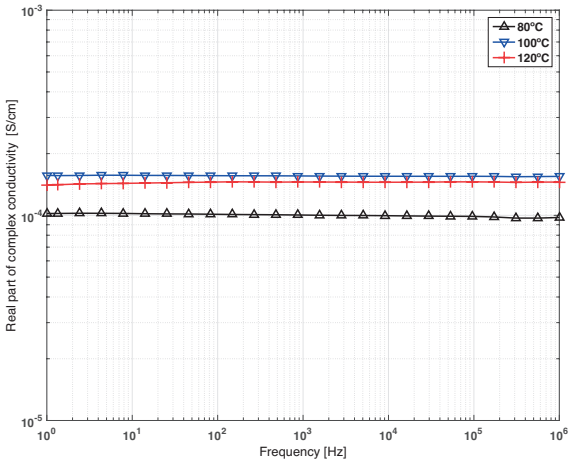

Figure 5.27: Real part of the complex conductivity of FP-II as a function of frequency at temperatures between 80 °C and 120 °C.

In Figure 5.26 it can be seen that at temperatures between -40 °C and 40 °C FP-II shows an upward slope in the real part of the complex conductivity for increasing frequency above 10 kHz. This behaviour is expected from a dielectric material. Moreover, below 10 kHz the real part of the complex conductivity forms a plateau which indicates that in this range the DC conductivity of the material becomes dominant. At 1 Hz the value of the real part of the complex conductivity varies between 2.36×10^{-11} and 2.96×10^{-11} S/m. When the real part of the complex conductivity at 20°C is extrapolated to a frequency very close to 0 Hz a value of 2.30×10^{-11} S/m is obtained for the DC conductivity which is in the range of an intrinsic semiconductor.

For temperatures above the glass transition of FP-II the dielectric response of the material is significantly different as can be seen in Figure 5.27. In this temperature range the real part of the complex conductivity of FP-II shows the same behaviour as was observed for FP-III. Thus, in this case FP-II behaves like a resistive material with the real part of the complex conductivity varying between 1.0×10^{-6} and 1.6×10^{-6} S/m at 1 Hz.

5.2.6 Thick epoxy nanocomposites

To investigate the influence of the different nanoparticle shapes and volume concentrations on the dielectric response of the thick epoxy materials dielectric spectroscopy measurements were performed. The main parameter of interest is in this case the relative permittivity of which the frequency spectra at 20 °C are depicted in Figure 5.28.

As can be seen from the figure the frequency spectra of all thick nanocomposite materials show the same shape. The addition of the different types of nanoparticles in

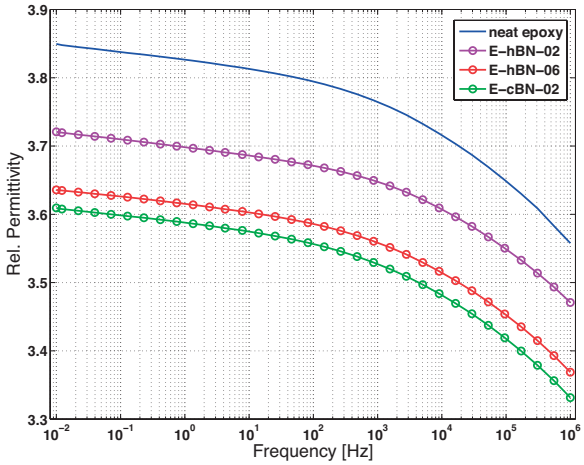

Figure 5.28: Relative permittivity of thick epoxy nanocomposites as a function of frequency at a temperature of 20 °C. The frequency range is 10 mHz to 1 MHz.

different concentrations merely shifts the frequency spectra of the relative permittivity to lower values with respect to neat epoxy.

The values of the relative permittivity at 100 kHz are listed in Table 5.7. As can be seen from the table, the introduction of 0.2 vol.% of hBN results in a reduction of the relative permittivity with 0.1. Moreover, when the concentration of hBN is increased to 0.6 vol.% another reduction of 0.1 is found. Note that a further increase of the volume concentration of hBN will not result in a further decrease of the relative permittivity[48].

The lowest value of the relative permittivity is obtained for nanocomposite B which is filled with 0.2 vol.% cBN. The relative permittivity is 0.03 lower than that of nanocomposite C and 0.23 lower than that of neat epoxy. Unfortunately, increasing the volume concentration of cBN to 0.6% and higher will not result in a further decrease of the relative permittivity[48].

Table 5.7: Relative permittivity of thick epoxy nanocomposites at 100 kHz and 20 °C

Material	Relative permittivity
Neat Epoxy	3.65
Nanocomposite A (0.2 vol.% hBN)	3.55
Nanocomposite B (0.2 vol.% cBN)	3.42
Nanocomposite C (0.6 vol.% hBN)	3.45

5.3 COATING CHARACTERISTICS – ELECTRICAL CONDUCTIVITY

Apart from the surface roughness and the relative permittivity, the volume conductivity can also have an influence on the breakdown strength of a coated gas insulated system as explained in sections 2.3 and 2.4. Therefore, the volume conductivity of the coating materials is evaluated using conduction current measurements of which the equipment and procedure has been described in section 3.5. Note that the term DC conductivity used in section 5.2 also refers to the volume conductivity of a material.

The volume conductivities of the coating materials are listed in Table 5.8. From the table it can be seen that the epoxy nanocomposites and EP-I have a conductivity in the order of 10^{-16} [S/m] which is in the range of an electrical insulator. Moreover, the lowest volume conductivity is found for FP-I which is in the order of 10^{-17} [S/m].
The conductivity of FP-II, PA11, FP-IV and FP-III is significantly higher than that of an electrical insulator. With respect to the volume conductivity these materials can be classified as a lossy insulator. FP-III shows the highest volume conductivity of $1x10^{-6}$ [S/m] which is in the same range as resistor materials. PA11 and FP-IV both show a volume conductivity in the order of 10^{-13} [S/m], whereas FP-II has a volume conductivity in the order of 10^{-11} [S/m]. Moreover, the conductivity of PA11 is three times higher than that of FP-IV.

When observing the volume conductivity of the epoxy nanocomposites it can be seen that the conductivity is increased significantly when the nanoparticles are introduced into the polymer matrix. Furthermore, the conductivity shows a slight increase when the volume concentration of hBN is increased from 0.2% to 0.6%. Increasing the volume concentration to 1% results in a further increase of the conductivity. However, when the volume concentration of hBN is raised to 5% the conductivity is reduced to a value below that of the nanocomposites with a 0.2% volume concentration of hBN [48]. The highest conductivity is obtained with the introduction of 0.2 vol.% cBN (nanocomposite

Table 5.8: Volume conductivity of the coating materials at room temperature.

Material	Volume conductivity [S/m]
EP-I	$\sim 1x10^{-16}$
FP-I	$\sim 1x10^{-17}$
FP-II	$2x10^{-11}$
PA11	$9x10^{-13}$
FP-IV	$3x10^{-13}$
FP-III	$1x10^{-6}$
Neat Epoxy	$3.1x10^{-16}$
Nanocomposite A (0.2 vol.% hBN)	$5.5x10^{-16}$
Nanocomposite B (0.2 vol.% cBN)	$7.0x10^{-16}$
Nanocomposite C (0.6 vol.% hBN)	$5.9x10^{-16}$

B). Increasing the volume concentration of cBN to 0.6%, 1% and 5% results in a reduction of the conductivity [48].

Note that the volume conductivities of FP-II and FP-III in Table 5.8 are obtained from the dielectric spectroscopy results. In the case of FP-III the combination of the very small layer thickness of 25 µm and the available voltage settings of the high voltage DC source resulted in a relatively high applied electric field strength. The resulting conduction current was out of the range of the electrometer. Therefore, the conductivity of FP-III could not be measured with the conduction current measurement setup.

In the case of FP-II observation of the measured current trace showed that the polarization current vanished within 20 seconds. The remaining steady state conduction current was below the noise level of $1x10^{-14}$ A. This observation implies that at a high DC voltage and at steady state the material behaves as an insulator which is contradictory to the behaviour observed in the dielectric spectroscopy results.

It is hypothesised that the behaviour of FP-II observed in the conduction current measurements is caused by electrode polarization which is different from the electrode polarization observed in the dielectric spectroscopy measurements due to the difference in the applied voltage level. When hetero-charge is present at the electrode boundaries the electric field inside the material is reduced. Consequently, the conduction current flowing through the material is also reduced. In the hypothesis it is considered that the conduction current is reduced to a value below the noise level of the electrometer.

To prove the above mentioned hypothesis, space charge measurements were performed on flat samples of both FP-I and FP-II coating materials using the pulsed electro-acoustic method (PEA)[57], [58]. In these measurements the applied electric field strengths were comparable with the electric field strengths applied in the conduction current measurements.

In Figure 5.29 the raw space charge profile of a FP-I sample is shown after the voltage is turned off. The measurement signal was not processed and calibrated to obtain the space charge density due to the fact that the sample thickness was too small to perform these processes. Therefore, the Y-axis represents the measured signal voltage from the output of the space charge measurement cell and amplifier. The X-axis merely represents the number of the corresponding point in the space charge profile and therefore has no unit, although it is directly related to the travel time of acoustic waves between the location in the sample and the measurement cell.

Due to the small sample thickness the space charge in the bulk of the material is not clearly visible in the measurement results. Fortunately, the mirror charges present at the electrode-sample interfaces, after the voltage is turned off, give a good indication of the accumulated charge in the material. Note that the FP-I and FP-II samples were polarized for 2 hours with a DC electric field of 14 kV/mm before voltage was turned off.

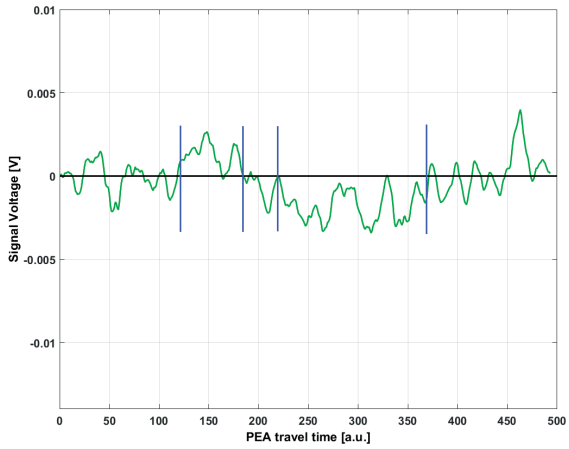

Figure 5.29: Raw space charge profile of a FP-I sample, voltage off (E = 14 kV/mm polarization field)

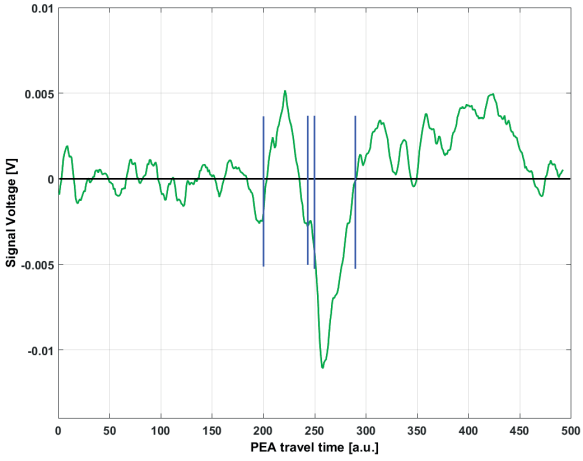

Figure 5.30: Raw space charge profile of a FP-II, voltage off. (E = 14 kV/mm polarization field)

In the raw FP-I space charge profile the bounds of the electrode interfaces are indicated by the blue lines. The mirror charges at the electrode interfaces have the same polarity as the electrode charges when the voltage was turned on. This indicates that close to the electrodes hetero-charge is present. However, the amplitude of the signal is relatively small which indicates that the accumulated amount of space charge is also relatively small. This is consistent with the dielectric spectroscopy results presented in section 4.6.

The raw space charge profile of a FP-II sample is depicted in Figure 5.30. In this case the results show that a relatively large amount of hetero-charge accumulation is present

in the material. The amplitude of the signal at the location of the mirror charges is 2 to 4 times higher than observed for FP-I.

The results of the space charge measurements indicate that the hypothesis of heterochare accumulation near the electrodes causing a severe reduction of the conduction current is likely.

5.4 AC BREAKDOWN STRENGTH

As explained in section 3.5, breakdown of gas-coating insulations can start in either the gas or the coating material. Therefore, the breakdown strength of the coating materials was evaluated with breakdown tests using the breakdown test setup and procedure described in section 3.5.

Note that the breakdown tests are performed under AC voltage as was described in section 3.5. Ideally, the coating material samples should be tested under lightning impulse voltage to obtain a direct comparison with the gas-coating breakdown tests in which lightning impulse voltage is applied in all cases. Unfortunately, no means of applying lightning impulses of the required voltage levels were available. The main impulse voltage generator of the high voltage laboratory has a minimum peak voltage of 25 kV while the required peak voltage level is in the range of 1 to 15 kV.

5.4.1 Thin coating materials

The 50% and 10% AC breakdown strength of the thin coating materials are depicted in Figure 5.31 and Figure 5.32 respectively. As can be seen from Figure 5.31 the 50% breakdown strengths of FP-I, EP-I, PA11 and FP-IV are comparable with values of 43, 40, 46 and 48 kV/mm respectively. Moreover, the 95% confidence bounds of the 50% breakdown strength of these materials all overlap which indicates that the difference between these materials is insignificant. However, when a confidence level of 68.2% is chosen the 50% breakdown strength of both PA11 and FP-IV are significantly higher than that of FP-I and EP-I. The difference in breakdown strength between FP-I and EP-I and between PA11 and FP-IV remains insignificant.

The lowest 50% breakdown strength of 15 kV/mm is found for FP-II. The breakdown strength of FP-II is roughly three times lower than that of the other thin coating materials which is a relatively large difference.

When observing the 10% breakdown strength it can be seen that the values obtained for FP-I, PA11, EP-I and FP-IV are also in this case relatively comparable. The 10% breakdown strength of FP-I, PA11, EP-I and FP-IV are 35, 40, 34 and 35 kV/mm respectively. Due to the wide and overlapping 95% confidence intervals, the difference in 10% breakdown

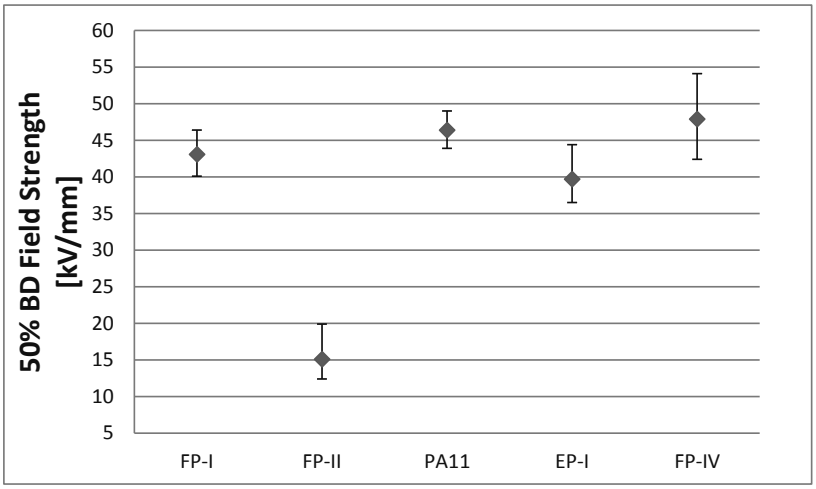

Figure 5.31: 50% Breakdown strength of thin coating materials. Including 95% confidence intervals.

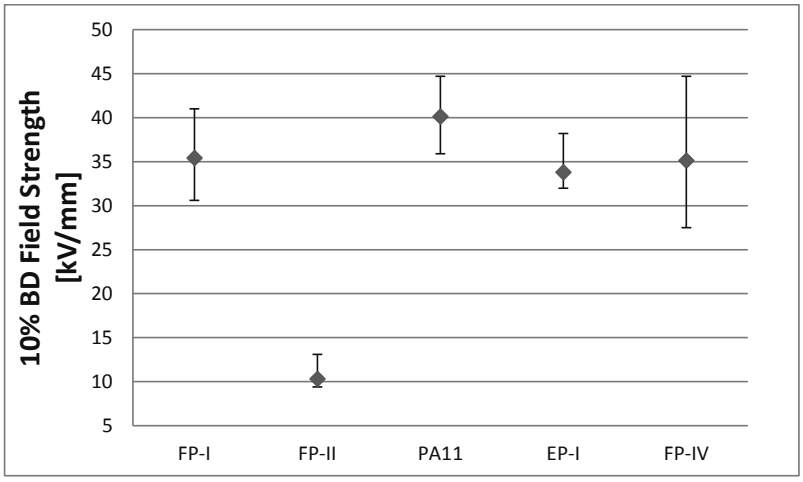

Figure 5.32: 10% Breakdown strength of thin coating materials. Including 95% confidence intervals.

strength between these four materials is considered insignificant. However, when the confidence level is reduced to 68.2% the 10% breakdown strength of PA11 becomes significantly larger than that of EP-I.

The 10% breakdown strength of FP-II is 10 kV/mm which is 3.5 to 4 times lower than the 10% breakdown strength of the four other thin coating materials. Thus, also for the 10% breakdown strength FP-II shows a relatively large difference with respect to the other thin coating materials.

Note that the AC breakdown strength of FP-III is not included in the results due to the fact that it was not possible to cause a breakdown in the sample using this test setup.

As described in sections 3.3 and 5.3, the conductivity of FP-III is in the order of 10^{-6} [S/m] and the layer thickness is 25 µm. When for example a voltage is applied of 1 kV the corresponding electric field strength in the sample will become 40 kV/mm. The resulting leakage current through the material is in that case approximately 3 mA which is larger than the discharge current detection threshold. During the measurements it was observed that the system detected a discharge while there was no evidence of a discharge found on the sample which is thus caused by the relatively large leakage current.

5.4.2 Thick coating materials

The AC breakdown strength of the thick epoxy nanocomposite coatings was obtained using the same test setup and procedure as used for the thin coatings[48]. However, in this case the test results were analysed according to the method contained in the IEC 62539 standard[59]. The standard recommends using the 90% confidence bounds for the comparison of the breakdown test results of different sample types instead of the 95% confidence bounds used for all the other breakdown tests in this thesis.

The 50% and 10% breakdown strength of the epoxy nanocomposite coatings are depicted in Figure 5.33 and Figure 5.34 respectively. From Figure 5.33 it can be seen that the introduction of 0.6 vol.% of hBN or 0.2 vol.% of cBN results in a significant increase of the 50% AC breakdown strength with respect to neat epoxy. For nanocomposites B (0.2 vol.% cBN) and C (0.6 vol.% hBN) the 50% breakdown strength has increased from a value of 40 kV/mm to 49 and 50 kV/mm respectively.

The 50% breakdown strength of nanocomposite A (0.2 vol.% hBN) is 43 kV/mm which is 3 kV/mm higher than that of neat epoxy. Unfortunately, the difference in 50% breakdown strength between neat epoxy and nanocomposite A is insignificant due to the overlapping 90% confidence intervals. Moreover, the 50% breakdown strength of both nanocomposites B and C is significantly larger than that of nanocomposite A.

When the volume concentration of hBN is increased above 0.6% to 1% and 5% the 50% breakdown strength is reduced to a level which is ultimately below that of neat epoxy in the case of 5 vol.% hBN[48]. Furthermore, when the volume concentration of cBN is increased above 0.2% to values of 0.6%, 1% and 5% the 50% breakdown strength is also reduced to a level below that of neat epoxy in the case of 5 vol.% cBN[48].
Figure 5.34 shows that the 10% breakdown strength of nanocomposites B and C is also significantly higher than that of neat epoxy. The 10% breakdown strength of neat epoxy and nanocomposites B and C is 35, 43 and 45 kV/mm respectively. Furthermore, also for the 10% breakdown strength the value obtained for nanocomposite A (38 kV/mm) shows no significant increase with respect to neat epoxy.

Also in the case of the 10% breakdown strength the value is reduced when the volume concentration of both hBN and cBN is increased above 0.6% and 0.2% respectively[48]. Moreover, the 10% breakdown strength is reduced to a level below that of neat epoxy

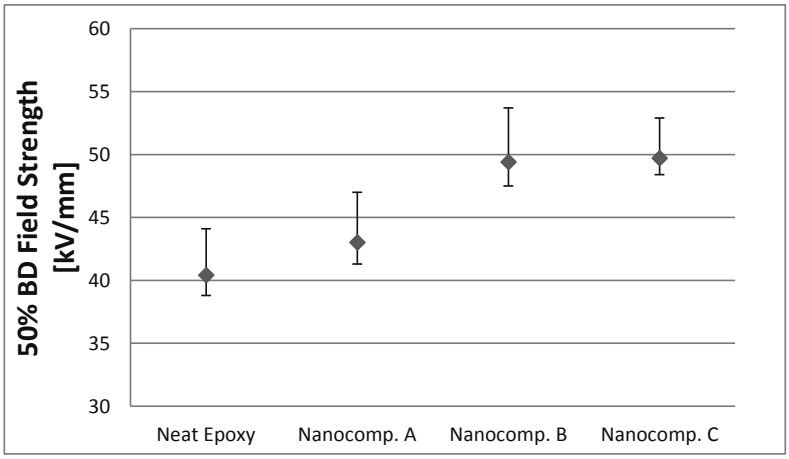

Figure 5.33: 50% Breakdown strength of epoxy nanocomposites. Including 90% confidence intervals.

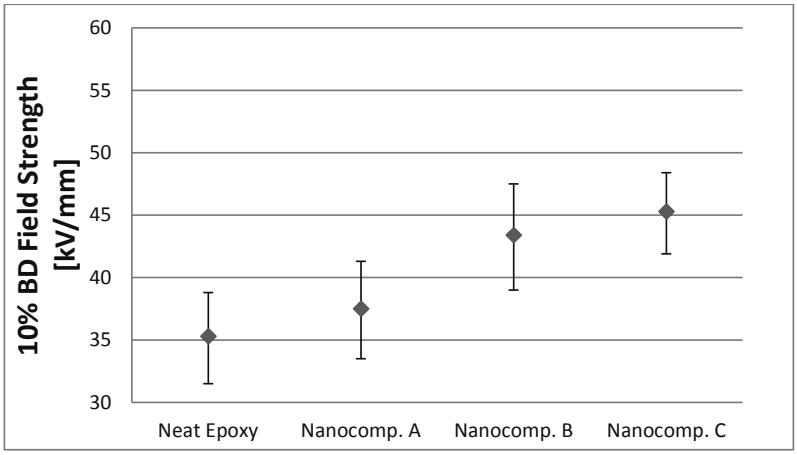

Figure 5.34: 10% Breakdown strength of epoxy nanocomposites. Including 90% confidence intervals.

when the volume concentration of either hBN or cBN is increased to 5% as was the case with the 50% breakdown strength.

5.5 BREAKDOWN DAMAGE

In sections 5.1 to 5.4 several different coating material characteristics were evaluated including the surface roughness, relative permittivity, dielectric losses, volume electrical conductivity and the AC breakdown strength. These parameters are all dependent on the molecular structure and the application process of the material and are evaluated when

the material is in an undamaged condition. However, it is also interesting to inspect the damage inflicted to each coating material by an electrical breakdown in the coating-gas insulation. For each material the shape and size of the resulting damage is different as will be explained in this section with the help of images taken via an optical microscope.

EP-I

Figure 5.35 contains a microscopic view of the surface of an EP-I coated electrode including breakdown marks. In the figure five distinct punctures can be seen of which two are relatively large, two are small and one has an intermediate size. The two large punctures seem to be caused by multiple breakdowns occurring from the same location resulting in an increased removal of coating and electrode material. The edges of the three smaller punctures are quite rough, whereas the edges of the large punctures seem to be smoother due to the melting of coating material caused by the occurrence of multiple discharges.

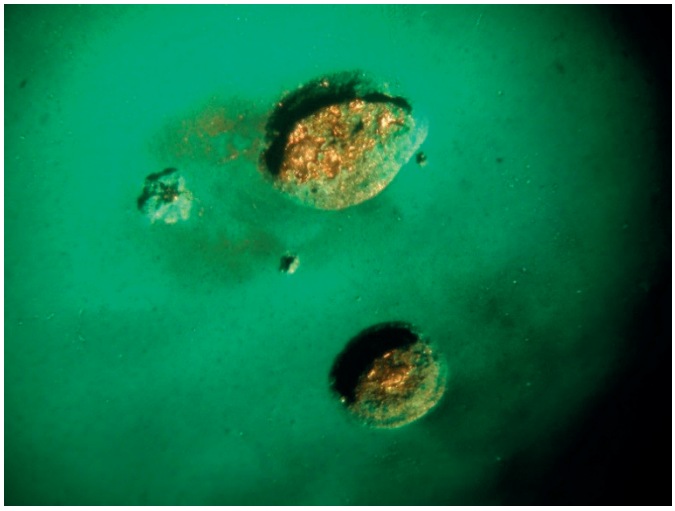

Figure 5.35: Microscopic view of the surface of an EP-I coated electrode after a breakdown test.

Next to the punctures four more features can be found on the coating surface. Firstly, near the two large punctures superficial brown coloured burn marks can be found which are most likely caused by the series of discharges occurring at these punctures. Secondly, microscopic metallic particles can be seen on the coating surface which originate from the bare electrode surfaces of the punctures due to the occurrence of the discharges. Thirdly, the coating surface shows some waviness which is not visible on the surface roughness scans due to the fact that the wavelength of this unevenness is longer than the threshold of 0.8 mm for the surface roughness measurement.

Fourthly, when observing the areas around the punctures more closely it can be seen that circumference of the punctures is not constant over the coating thickness. For example, the medium sized puncture on the left is wider on the surface than on the bottom of the puncture. It seems that on top a larger part of the coating surface has been removed by the discharges.

FP-I

In Figure 5.36 a microscopic view of the surface of a FP-I coated electrode is shown including a breakdown mark. As opposed to the EP-I case only one minor puncture can be seen in the figure. Thus, all discharges seem to have originated from the location of the puncture. Moreover, the puncture is relatively small considered that all discharges started at that location.

When observing the coating surface in more detail several features can be seen. Firstly, vague brownish discoloration can be seen on the lower right hand side of the puncture which are most likely burn marks caused by the multitude of discharges. Secondly, the edge of the puncture is relatively smooth compared to the EP-I case and it seems to slightly bulge out from the coating surface. Thirdly, the coating surface has a smooth appearance with some scratches visible on the left hand side of the figure which is confirmed by the surface roughness measurements. Finally, the material is slightly transparent with small islands of pigment visible. It seems that the colouring of the material is not homogeneously distributed over the material volume.

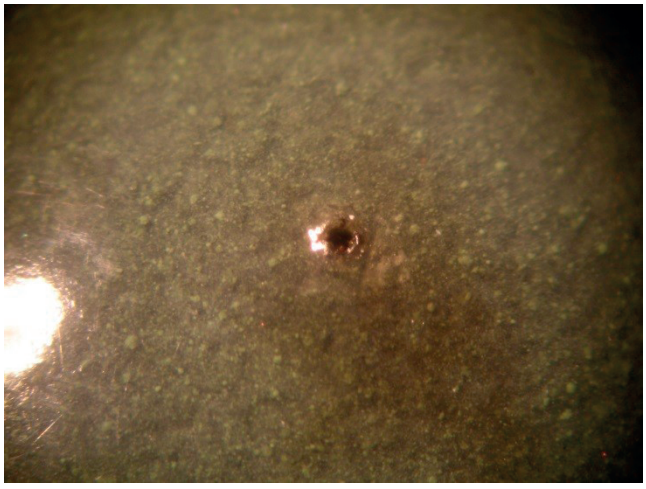

Figure 5.36: Microscopic view of the surface of a FP-I coated electrode after a breakdown test.

FP-II

Figure 5.37 shows a microscopic view of the surface of a FP-II coated electrode after a breakdown test. In the figure five breakdown punctures of varying sizes can be found. The larger punctures are seemingly locations where multiple discharges have originated. Furthermore, the punctures are similar in shape with respect to the single puncture found for FP-I. However, the edge of the punctures show a significantly larger protrusion than observed for FP-I. The punctures have the appearance of a crater of which the height of the edge is positively dependent on the size of the puncture.
Next to the punctures it is observed that the surface of the coating is rough compared to FP-I and EP-I which is confirmed by the results of the surface roughness measurements. Moreover, microscopic metallic particles are visible on the coating surface and on the edges of the punctures which are created by the melting of the aluminium electrode due to the discharges.

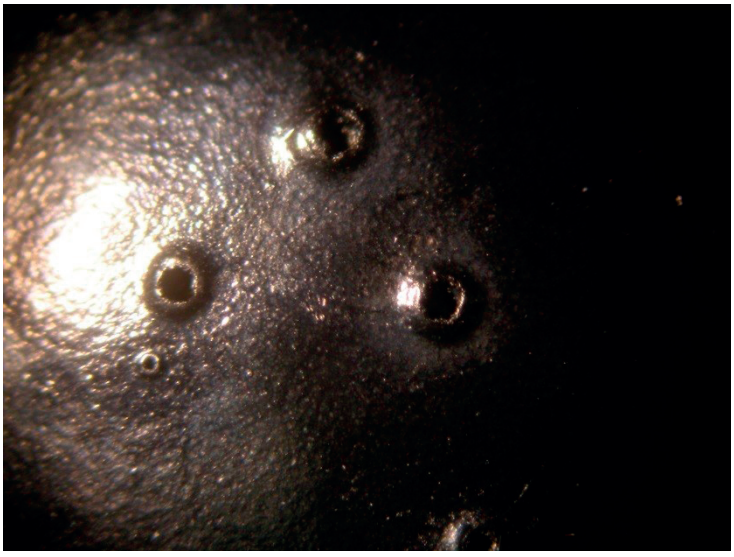

Figure 5.37: Microscopic view of the surface of a FP-II coated electrode after a breakdown test.

PA11

In Figure 5.38 and Figure 5.39 microscopic views of the surface of two different PA11 coated electrodes are displayed. In Figure 5.38, five distinct breakdown punctures can be seen which have varying sizes and shapes. The two smallest punctures seem to be caused by only a single or a few discharges, whereas the largest puncture was the starting point of multiple discharges. Furthermore, the shape of the punctures becomes rounder when the number of subsequent discharges is increased.

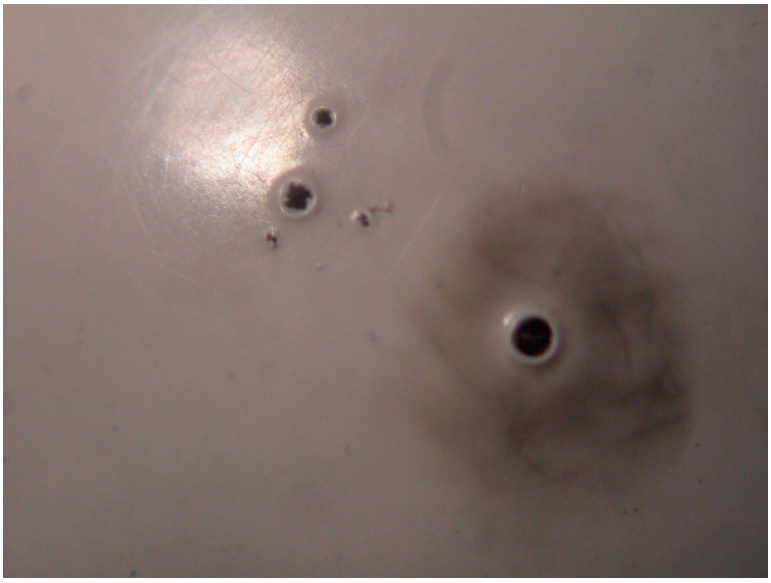

Figure 5.38: Microscopic view of the surface of a PA11 coated electrode after a breakdown test.

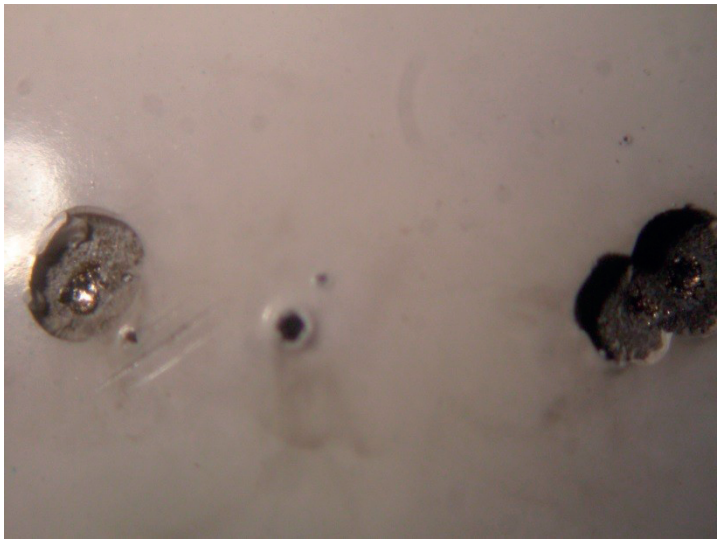

Figure 5.39: Microscopic view of the surface of a PA11 coated electrode after a breakdown test. Including more extensive breakdown damage.

Also for PA11 the edges of the punctures protrude from the surface as was the case with FP-I and FP-II. The height of the protrusions is in this case comparable to those found for FP-I and is positively dependent on puncture size. Next to the punctures, it can be

seen from Figure 5.38 that a distinct burn mark is present around the largest puncture which is the result of more intense discharge activity.
As can be seen in Figure 5.39, there are cases in which the breakdown damage found on the PA11 coating surface is more extensive. In this case the punctures are significantly larger as shown on the left and on the far right of the figure.

It seems that a larger section of the coating material around the breakdown point was removed. Small pieces of PA11 material were found in the tank after testing, indicating that the adhesion of the coating material to the electrode surface was weaker for larger portions of the coating material. Moreover, within these large punctures a melting spot of the aluminium electrode can be seen around which undamaged electrode surface is present. This also indicates that the removed portion of the coating surface is larger than the surface area of the discharge location.

When observing the undamaged part of the PA11 coating surface in both figures it can be seen that the surface is apparently very smooth. This observation is supported by the surface roughness measurement results which show that PA11 has the smoothest surface of all materials tested in this thesis.

FP-IV

Figure 5.40 shows a microscopic view of the surface of a FP-IV coated electrode after a breakdown test was performed. On the undamaged region of the coating surface, glitter like particles can be seen which are the mica particles contained in the coating material.

When observing the breakdown damage it can be seen that only one puncture is present which has a relatively large size. Moreover, the coating material is applied on top

Figure 5.40: Microscopic view of the surface of a FP-IV coated electrode after a breakdown test.

of an adhesion layer as explained in section 3.3. This coating layer can be seen in the form of the black part at the edge of the puncture.

The entire surface area of the bare aluminium electrode in the puncture is damaged by the discharges which indicates that no parts of the coating material broke off outside of the discharge region. Furthermore, a faint superficial burn mark can be seen close to the puncture which is caused by the repetitive exposure of that region to radiation and heat originating from the discharges.

Note that the thickness of the FP-IV coating layers is on average 40 µm, which is significantly smaller than the thickness of FP-I, FP-II, PA11 and EP-I. Due the small thickness it is more likely that the material evaporates during a discharge instead of breaking off.

FP-III

In Figure 5.41 a microscopic view of the surface of a FP-III coated electrode is depicted including breakdown damage. When taking a closer look at the undamaged coating surface it can be seen that the surface is relatively rough. Moreover, it seems that dents and scratches in the underlying aluminium electrode surface are visible through the coating. The surface roughness measurement results show that the coating surface is significantly rougher than the other coating materials. Furthermore, the very small coating thickness of 25 µm is in the same range as the surface roughness of the underlying electrode which indicates that it is possible for an unevenness at the electrode surface to be present at the coating surface.

The breakdown damage consists of four punctures in the coating surface around which two relatively large burn marks are present. These burn marks are caused by the heat and

Figure 5.41: Microscopic view of the surface of a FP-III coated electrode after a breakdown test.

radiation emitted by the discharges. The relatively large size is most likely caused by the fact that the material has a small layer thickness.

As was the case for FP-IV, the entire surface area of the bare aluminium parts in the punctures is damaged by the discharges again indicating that no part of the coating material was removed outside of the discharge region. Moreover, the edges of the puncture have a characteristic shape which indicates that the coating was evaporated during the discharges.

Semiconductor A

Figure 5.42 contains a microscopic view of the surface of a semiconductor A coated electrode including breakdown damage. On the coating surface two large and one small puncture can be seen. The shape of the large punctures is not uniform and the edges are sharp and rough.

The coating material seems to be relatively brittle which is demonstrated by the fact that in the tank a large amount of small coating particles was found after a breakdown test. Furthermore, the punctures are larger than the corresponding discharge spots on the electrode surface leaving a rough surface of remaining coating material around these locations. An extra indication is the partially detached coating particle at the lower edge of the centre puncture in the figure.

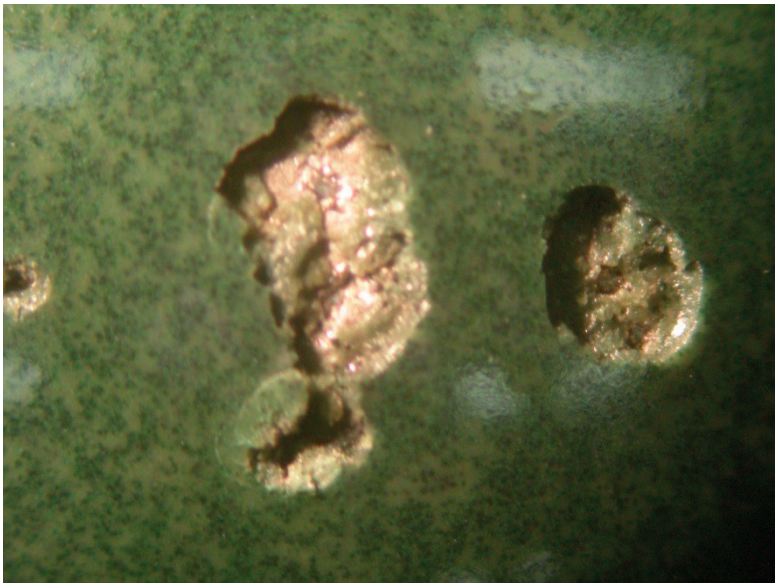

Figure 5.42: Microscopic view of the surface of a semiconductor A coated electrode after a breakdown test.

Regarding the undamaged coating surface it is observed that the surface is relatively smooth which is supported by the surface roughness measurements which show that this coating material has a smoothness very close to that of PA11. Moreover, dark green particles can be seen in the coating of which the resin has an olive green colour. These particles seem to be the microparticle fillers mixed into the base material.

FP-II – FP-I

A microscopic view of the surface of a double layer FP-II – FP-I coated electrode including breakdown marks is depicted in Figure 5.43. In the figure multiple punctures can be seen of which the two in the centre are clearly visible. The shape and size of the punctures is comparable to the punctures found on the FP-I coated electrodes including the height of the protruding edges.

With respect to the undamaged coating surface it can be seen that the surface contains a large amount of small scratches which vary in length. The results of the surface roughness measurements show that this coating material has the second largest roughness behind FP-III which coincides with the visually observed roughness.

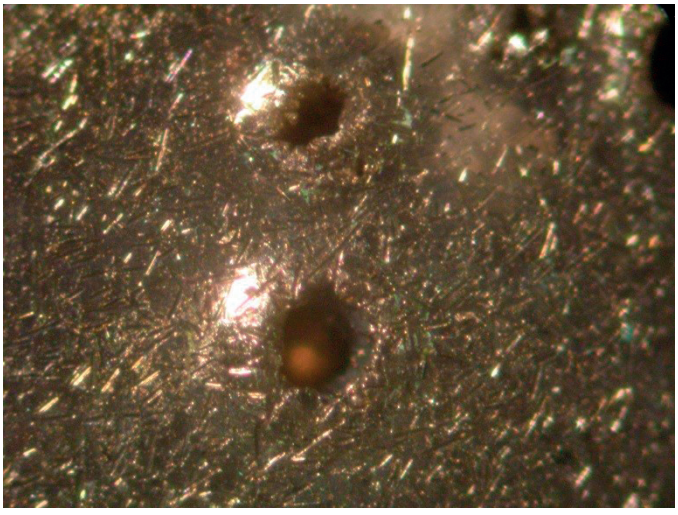

Figure 5.43: Microscopic view of the surface of a double layer FP-II – FP-I coated electrode after a breakdown test.

FP-II – PA11

In Figure 5.44 a microscopic view of the surface of a FP-II – PA11 coated electrode is displayed including extensive breakdown damage. The majority of the figure is occupied by the bottom FP-II coating layer being exposed by the removal of the top PA11 coating

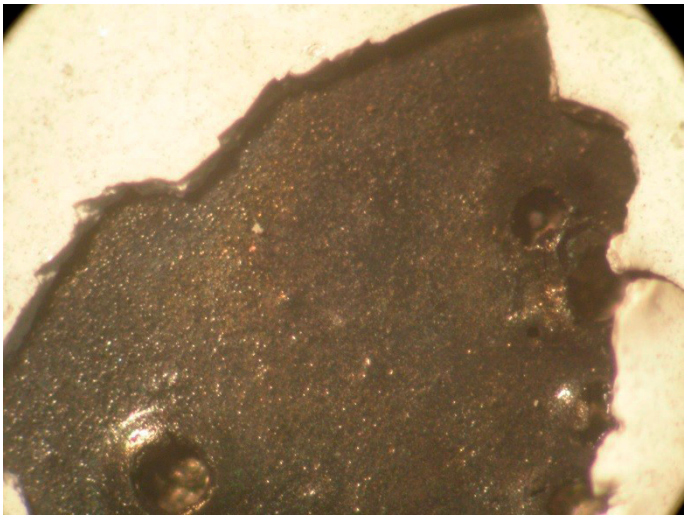

Figure 5.44: Microscopic view of the surface of a double layer FP-II – PA11 coated electrode after a breakdown test.

layer due to the repetitive discharging which occurred in this region. The exposed region is larger than what is shown in this figure.
The exposed FP-II layer indicates that the adhesion between the top PA11 layer and the bottom FP-II layer was insufficient. Moreover, on the far right hand side of the figure it can be seen that the PA11 layer is still attached to the rest of the PA11 topcoat at that location. However, the adhesion with the FP-II layer is already lost. Also, the beginning of a crack in the PA11 material is visible there.

In the exposed FP-II region several punctures can be seen which differ in size. The shape and size of these punctures including the protruding crater like edges are comparable with those found on the surface of the single layer FP-II coated electrodes. On the coating surface and on the edges of the punctures small metallic particles, originating from the bare aluminium electrode surfaces, can be seen as was the case for the EP-I and FP-II coated electrodes.

Note that the PA11 coating surface has a somewhat different appearance with respect to the single layer PA11 coated electrodes. In this case, microscopic black speckles can be seen on the PA11 coating surface which were not present on the single layer PA11 coating surface. Furthermore, the PA11 surface seems to be rougher with respect to the single layer PA11 surface which is confirmed by the surface roughness measurement results.

Thick nanocomposite coatings

Figure 5.45 contains a microscopic view of the surface of an electrode coated with thick epoxy nanocomposite A. Because the surface of all nanocomposite coatings show comparable damage after performing a breakdown test only the damage of one nanocomposite coating type is discussed here.

As explained in sections 4.2.4 and 4.4, breakdown of the thick epoxy nanocomposite coatings occurred in the form of surface flashovers in all cases except for one case in which a large portion of the coating broke off after several consecutive breakdowns. The damage caused by the surface flashovers can be seen in Figure 5.45 as a faint blackening of the coating surface. The blackening of the surface occurs as traces between the tip of the electrode and the side of the electrode where the grounded electrode holding plane is located.

On the surface of the neat epoxy coated electrodes the traces were not as clearly visible as observed for the nanocomposites. Only with a very bright light source and from the correct angle the traces could be seen which are not distinctly black in colour as opposed to the traces observed on the surface of the nanocomposites. Unfortunately, the traces on the neat epoxy surface could not be captured with a camera.

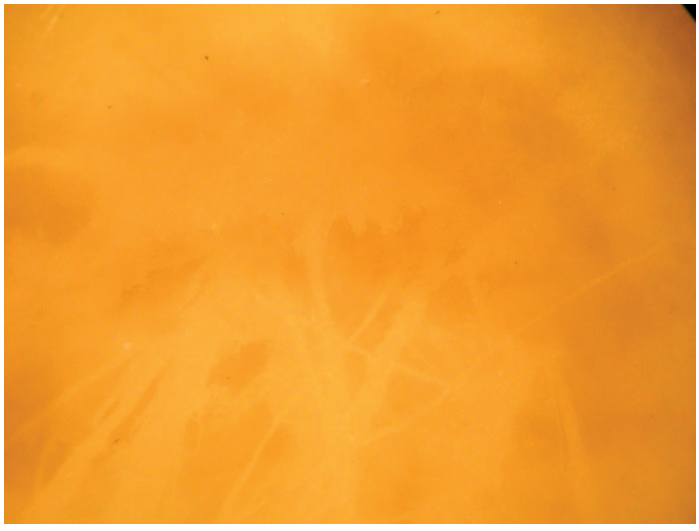

Figure 5.45: Microscopic view of the surface of a thick nanocomposite coated electrode after a breakdown test.

5.6 DISCUSSION

In sections 5.1 through 5.5 the material characterisation test results are discussed. This section starts with a short overview of the most significant material parameters.

Subsequently, the correlation between the results of the gas-coating breakdown tests presented in chapter 4 and the above mentioned parameters is discussed.

5.6.1 Overview of material parameters

For the comparison of the materials with respect to the surface roughness, the parameter R_y is selected which represents the maximum height in the roughness profile as explained in sections 5.1 and 3.5.1. The values of R_y are depicted in the graph in Figure 5.46.

As already explained in section 5.1, all coating materials have an R_y smaller than that of bare, machined electrodes, which is 7.5 µm. The only exception is FP-III with an R_y of 13.9 µm which is caused by the fact that the coating layer thickness is only 25 µm while the underlying electrode surface has an R_y of 28.5 µm due to abrasive blasting. PA11 and Semiconductor A show the smoothest surface with an R_y of 0.79 and 0.87 µm respectively.

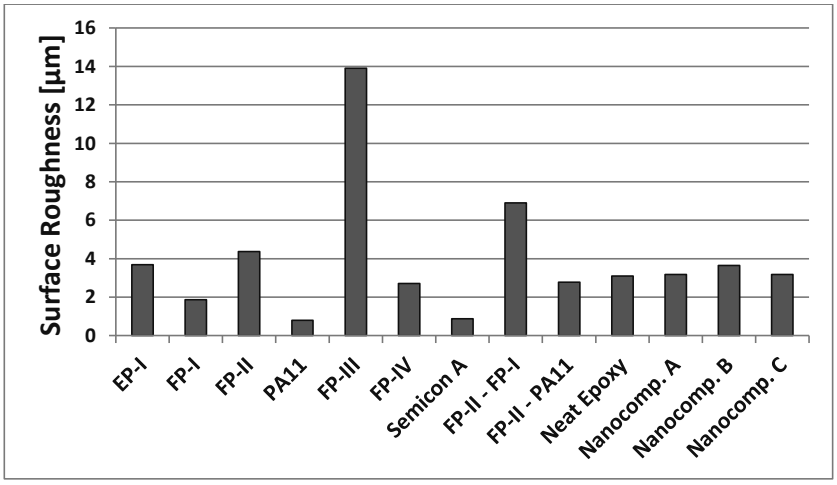

Figure 5.46: Surface roughness parameter Ry of all coating materials applied on small size electrodes.

The dielectric response of the coating materials is discussed in detail in section 5.2. To quantify the dielectric response of the materials in relation with the gas-coating breakdown test results, two main parameters were selected for comparison. These parameters are the relative permittivity and the dielectric losses at both 50 Hz and 100 kHz. The relative permittivity of a selection of the materials at 50 Hz and 100 kHz is displayed in Figure 5.47.

As can be seen from the figure, the relative permittivity of the thick coating materials is comparable. Moreover, the relative permittivity of PA11, FP-II and EP-I is high compared to the other coating materials.

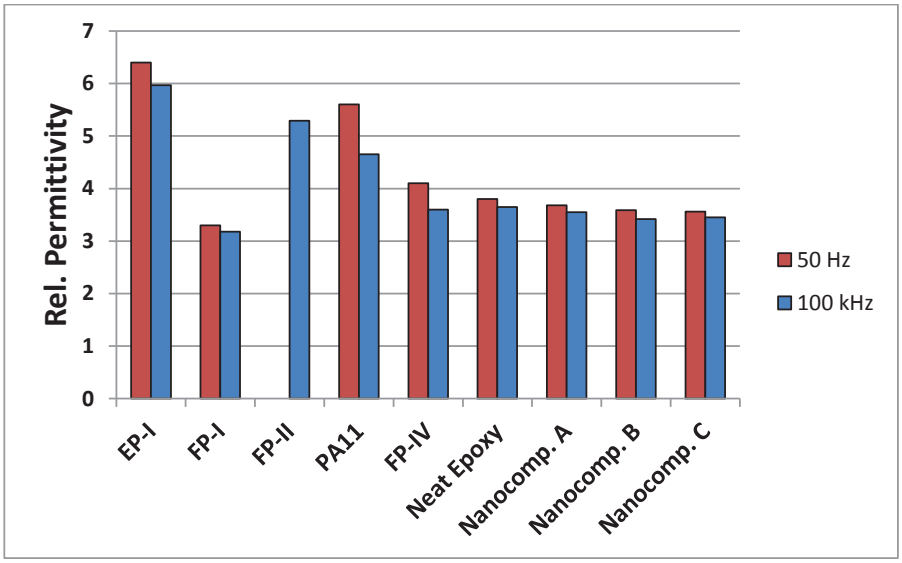

Figure 5.47: Relative permittivity of the coating materials at 50 Hz and 100 kHz.

The dielectric losses of the materials at 50 Hz and 100 kHz are shown in Figure 5.48. The figure shows that the dielectric losses of FP-III are very high compared to all other coating materials, especially at 50 Hz. For FP-II the dielectric losses are also relatively high at 50 Hz as opposed to the dielectric losses at 100 kHz which are comparable with PA11, FP-IV and EP-I. The dielectric losses of the thick coating materials and FP-I are comparable.

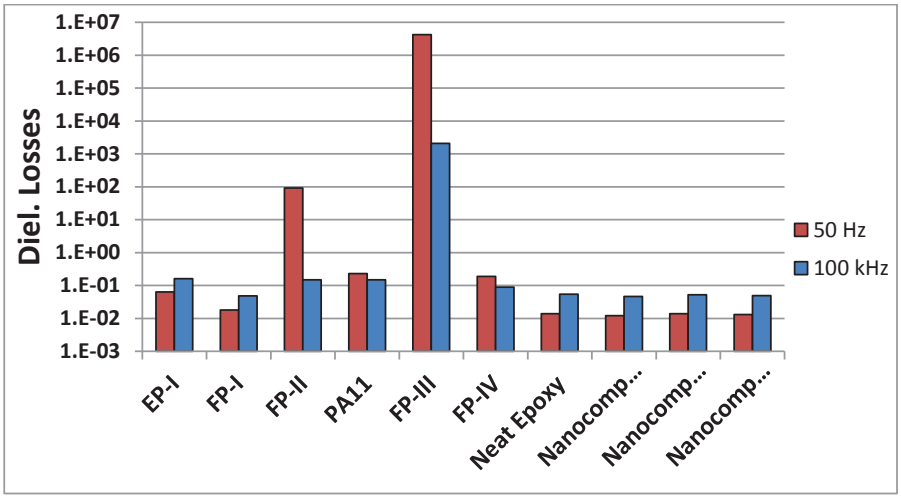

Figure 5.48: Dielectric losses of the coating materials at 50 Hz and 100 kHz.

In section 5.2, beta relaxation processes were observed in the dielectric response of several coating materials. Because the frequency position of the relaxation peaks, related to the beta relaxation processes, show an Arrhenius type dependency on the temperature, the activation energies of the beta relaxation processes were determined. The activation energies of the beta relaxation processes found in the dielectric response of EP-I, FP-I, PA11 and FP-IV are depicted in Figure 5.49.

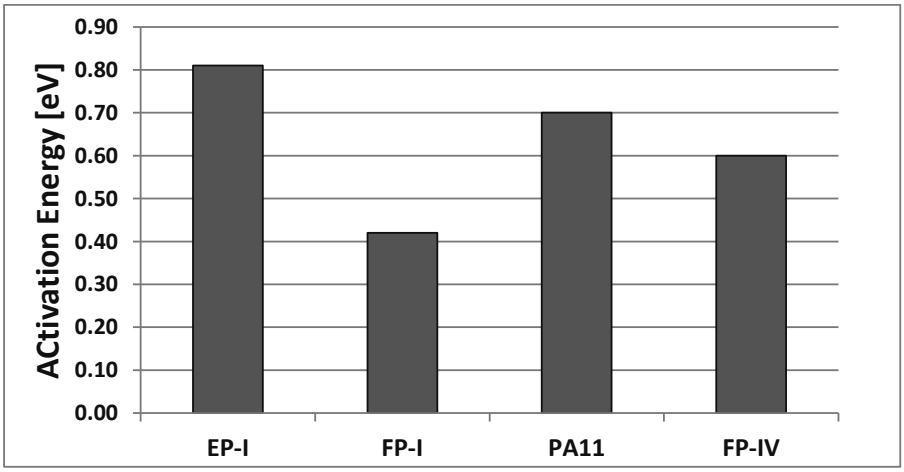

Figure 5.49: Activation energy of beta relaxation processes observed in four thin coating materials.

The figure shows that the beta relaxation process in EP-I has the highest activation energy of 0.81 eV, whereas the activation energy of FP-I is the lowest with 0.42 eV. The activation energy of PA11 and FP-IV is 0.70 and 0.60 eV respectively.

The electrical conductivity of the coating materials is discussed in depth in section 5.3. In Figure 5.50, the values of the electrical conductivity of the materials are compared. As explained in section 5.3, FP-III has the highest conductivity in the order of 10^{-6} [S/m] which is comparable to resistor material. Regarding the conductivity, neat epoxy, the epoxy nanocomposites, EP-I and FP-I can be classified as a lossless insulator. FP-II, PA11 and FP-IV are classified as a lossy insulator due to the relatively high conductivity in the order of 10^{-13} up to 10^{-11} [S/m].

In section 5.4, the AC breakdown strength of the coating samples was investigated. The 50% and 10% breakdown voltage of the coating materials are displayed in Figure 5.51. Note that for the sake of simplicity the 95% confidence bounds are not included in this case.

The figure shows that FP-II is the weakest coating material with a breakdown strength which is three to four times smaller compared to the other coating materials. The break-

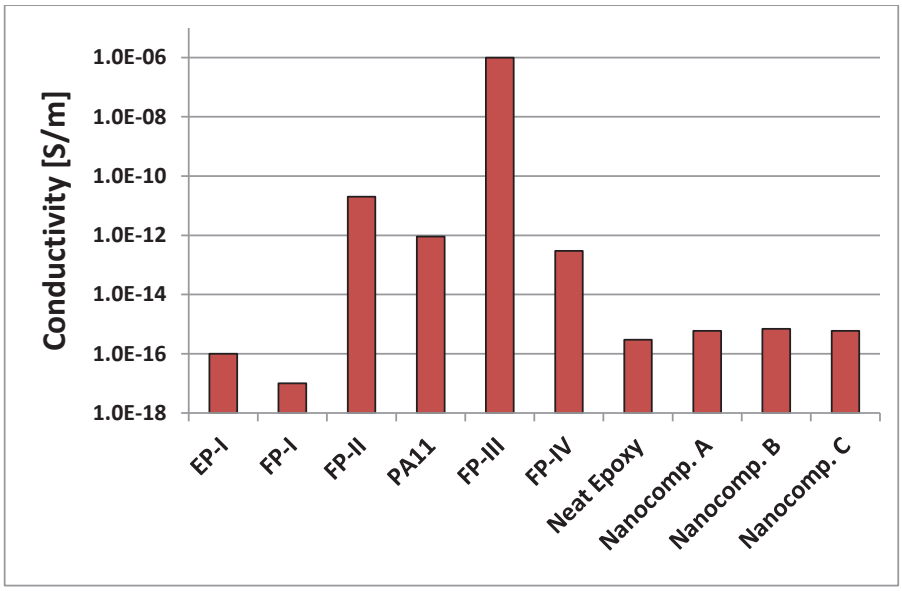

Figure 5.50: Electrical conductivity of the coating materials.

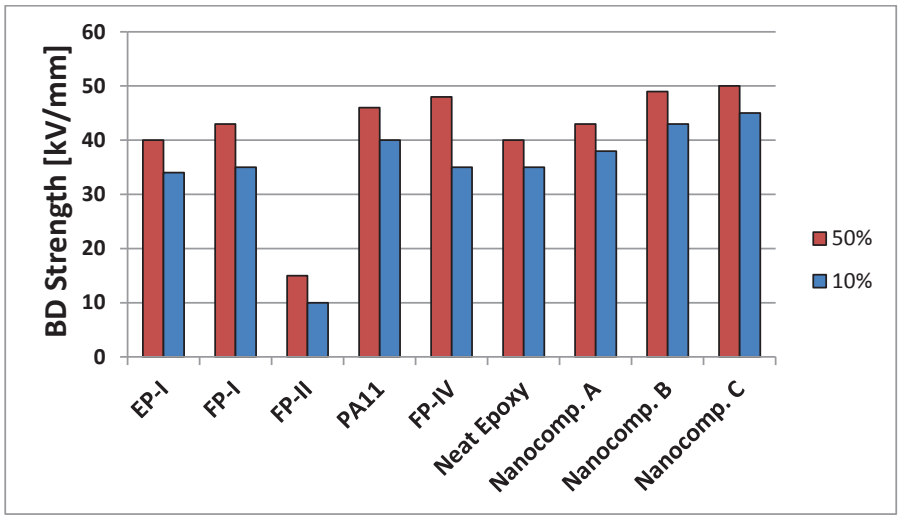

Figure 5.51: 50% and 10% Breakdown strength of the coating samples.

down strength of all other materials is comparable, having a maximum difference of 10 kV/mm. The highest breakdown strength is observed for Nanocomposite C with a 50% breakdown strength of 50 kV/mm and a 10% breakdown strength of 45 kV/mm.

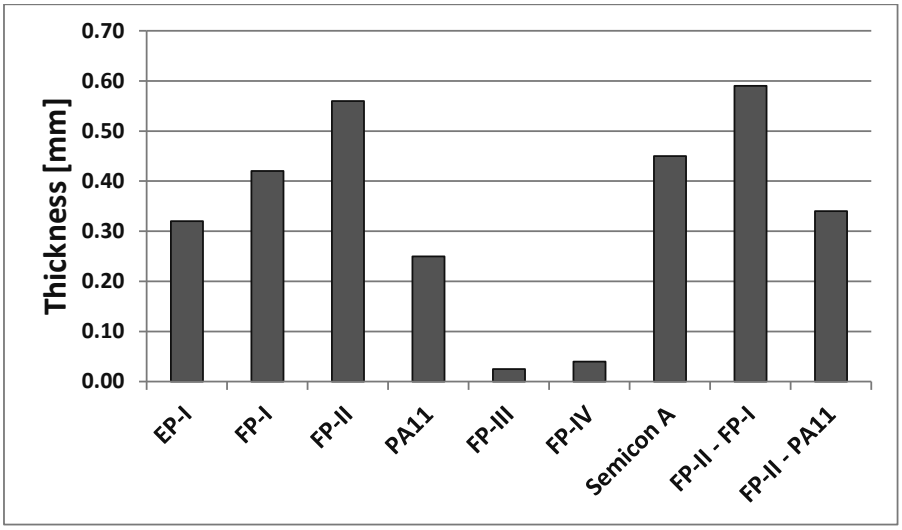

Figure 5.52: Layer thickness of thin coating materials.

Finally, the thickness of the thin coating materials can have an influence on the gas-coating breakdown test results. For the sake of convenience the thicknesses of the thin coating materials are also presented here in Figure 5.52. More information on the coating materials and the application processes is described in section 3.3.

From the figure it can be seen that FP-III and FP-IV are very thin compared to the other thin coating materials with a thickness of 25 and 40 µm respectively. The thickest single layer coating is FP-II with a thickness of 560 µm and the thickest coating overall is FP-II – FP-I with a thickness of 590 µm. As explained in section 3.3 the thick coating materials all have a thickness of 10 mm.

5.6.2 Correlation between gas-coating breakdown test results and material characteristics

In this subsection it is investigated whether or not there is a link between the material characteristics and the gas-coating breakdown test results described in chapter 4. This subsection has the same structure as the discussion in section 4.5.3 and can be considered as a follow-up on that section.

1st breakdown of thin single layer coatings

In section 4.5.3 it was discussed that the 1st breakdown voltage of electrodes coated with a thin coating either shows an improvement, a reduction or no significant difference with respect to uncoated electrodes. Furthermore, it was explained that the reason for this behaviour can be found in the material characteristics of the coatings.

It was observed in chapter 4 that PA11 shows the highest improvement in both the 50% and 10% 1st breakdown voltage with values of 15.3% and 7.4% respectively. The coating with the second highest improvement is semiconductor A with an improvement of 7.6% and 5.4% for the 50% resp. 10% 1st breakdown voltage. The third coating with an improvement is EP-I with a value of 4% for the 50% 1st breakdown voltage only.

FP-I, FP-II and FP-III showed no significant change in both the 50% and 10% 1st breakdown voltage with respect to uncoated electrodes. Finally, FP-IV showed a significant decrease of 4.8% and 5.9% in the 50% resp. 10% 1st breakdown voltage.

1st breakdown voltage of thin single layer coatings versus coating surface roughness

The first material parameter of interest is the coating surface roughness. In section 2.4 it was explained that the breakdown voltage of a gas gap is reduced when the electrode surface roughness is increased. Although the influence of the electrode surface roughness on the breakdown voltage of a gas insulated system was investigated for uncoated electrodes, the same is theoretically true for coated electrodes.

When observing the results of the coating surface roughness measurements it can be seen that both Semiconductor A and PA11 show a significantly smoother surface compared to all other coating materials. Therefore, it can be stated that the smoothest coatings show the highest improvement, which indicates that the smoothness of a coating can have a significant positive influence on the breakdown strength of a gas-coating insulation.

However, a further correlation between the breakdown test results and the electrode surface roughness is unclear. For example, the first breakdown voltage of FP-III is not the lowest 1st breakdown voltage of all thin coatings while the surface is significantly rougher than the surface of other thin coating materials. Moreover, the surface of FP-I coated electrodes is relatively smooth with an R_y of 1.86 while the 1st breakdown voltage is lower than that of EP-I which has a roughness of 3.69.

The observations described above suggest that the correlation between material characteristics and the 1st breakdown voltage of thin coatings should be sought in combinations of multiple material parameters.

1st breakdown voltage of thin single layer coatings versus dielectric response and electrical conductivity

In sections 2.3 it was explained that the accumulation of hetero-charges on the coating surface can decrease the electric field in the gas gap resulting in an increase in the breakdown voltage of the gas-coating insulation system. In that section it was also explained that, in theory, this effect is maximized when the relative permittivity of the coating is as close as possible to one and the electrical conductivity is as low as possible.

However, in section 2.4 it was explained that the breakdown voltage of the gas-coating system can be improved if the field emission of electrons into the gas gap is reduced. To minimize electron field emission, the electric field strength at the electrode surface should be minimized. To accomplish this, the relative permittivity of the coating should be as high as possible which opposes the requirement stated for surface charge accumulation. Furthermore, in a resistive electric field distribution the electric field is pushed into regions with low conductivity.

Therefore, the conductivity of the coating material should also be as high as reasonably possible which again opposes the requirements for electric field reduction in the gas gap due to hetero-charge accumulation. Note that with a relatively high coating conductivity the surface charge accumulation would consist of homo-charges reducing the electric field in the coating and thus at the electrode surface.

In total, the influence of the material relative permittivity and electrical conductivity on the breakdown strength of a coated GIS is contradictory regarding both the reduction of the electric field in the gas gap and the reduction of electron field emission. This contradiction is visible in the 1st breakdown test results of the thin coating materials. There is no clear correlation between the relative permittivity and electrical conductivity of the materials and the corresponding 1st breakdown voltage. Unfortunately, the activation energy of the beta relaxation processes in the coating materials also show no correlation with the 1st breakdown voltage.

1st breakdown voltage of thin single layer coatings versus breakdown strength and layer thickness

Above it is explained that the accumulation of hetero-charges reduces the electric field in the gas gap. Consequently, the accumulation of hetero-charges at the coating surface also increases the electric field in the coating material significantly. It is stated in literature that the coating materials have a significantly higher breakdown strength than the gas and that with the accumulation of surface charges this advantage can be exploited.

However, the breakdown strength of dry air at 0.9 MPa is roughly 27 kV/mm, while the breakdown strength of most coating materials ranges from 40 to 48 kV/mm. When hetero-charge accumulates at the coating surface, the electric field in the coating can easily be enhanced to a value which is significantly higher than the breakdown strength of the coating, due to the relatively small thickness of the coating layer. Consequently, breakdown of the gas-coating insulation starts in the coating layer instead of the gas gap.

An important example is FP-II, which has a very low breakdown strength of 15 kV/mm. In this case, the probability that the 1st breakdown starts in the coating layer is relatively high, which is reflected by the fact that the 1st breakdown voltage of these coating materials is somewhat lower than that of bare electrodes.

Unfortunately, the 1st breakdown voltage of FP-IV is significantly lower than that of uncoated electrodes while the breakdown strength of the coating material is the highest among the thin coating materials. However, there are several aspects which can clarify this behaviour. Firstly, the relative permittivity of this coating is 3.6, whereas the relative permittivity of FP-II is 5.3 which suggests that the electric field strength, without charge accumulation, in the FP-IV coating is significantly higher.

Secondly, the thickness of the FP-IV coating is 40 µm, whereas the thickness of the FP-II coating is 560 µm. When the amount of accumulated hetero-charge at both coating surface is comparable, the electric field in the FP-IV layer is enhanced significantly more than in the case of FP-II. Furthermore, the surface roughness of the underlying electrode has a larger influence on the electric field strength in the coating material when the thickness is smaller.

Thirdly, the electrical conductivity of FP-IV is significantly lower than that of FP-II. Therefore, the combination of both the lower electrical conductivity and relative permittivity results in a higher electric field strength in the FP-IV layer compared to FP-II as explained above. In total, these three factors indicate that it is possible that the breakdown of the FP-IV coated electrodes is initiated in the FP-IV layer instead of the gas gap as is the case for FP-II.

1st breakdown voltage of thin single layer coatings – evaluation

The results discussed above indicate that, due to the small layer thickness of the thin coatings, it is unlikely that hetero-charge accumulation can cause a significant reduction of the electric field strength in the gas gap. Therefore, it is most likely that the reduction of electron field emission is the main cause of the improvement of the 1st breakdown voltage for coated electrodes. Moreover, the cases in which a reduction of the 1st breakdown voltage is observed are caused by a breakdown in the coating material instead of the gas gap.

Overall we conclude that the best thin coating materials should have the following properties. Firstly, the coating should have a high relative permittivity and a relatively high conductivity to minimize electric field strength in the coating and thus minimize electron field emission. Secondly, the probability of a breakdown of the system starting in the coating should be minimized by selecting a material with a high breakdown strength. Thirdly, the thickness of the coating layer should be large enough to reduce the electric field in the coating and minimize the influence of the roughness of the underlying electrode surface. Note that the thickness of the coating should remain within the range of a thin coating to prevent other physical effects from becoming significant, which is the case for thick coatings.

The reason why PA11 shows the highest improvement in both the 50% and 10% 1st breakdown voltage is the fact that this material has all of the above mentioned qualities.

PA11 has a very smooth surface, a high relative permittivity, a relatively high conductivity due to the observed ionic conduction, a relatively high breakdown strength and a sufficient layer thickness.

All the other materials miss one or more of these qualities resulting in either a small improvement, no improvement or even a reduction in the 1st breakdown voltage with respect to uncoated electrodes. An interesting example of this fact is FP-III, which has a very small layer thickness of 25 µm and consequently a very rough surface with an R_y of 13.9 µm. Both parameters suggest that the coating should show poor performance with respect to the 1st breakdown voltage. However, the results show that the 50% 1st breakdown voltage of FP-III is 6.5% higher than that of uncoated electrodes. Unfortunately, this improvement is considered insignificant due to relatively large scatter in the results which cause an overlap with the 95% confidence intervals of uncoated electrodes.

When the layer thickness of FP-III is doubled to 50 µm, the disadvantage of a small layer thickness and a rough surface would be less pronounced. Combined with the fact that the material has a very high breakdown strength of 67 [kV/mm] according to the datasheet and a high conductivity in the order of 10^{-6} [S/m] might result in a coating with favourable performance. Preliminary experiments on FP-III coated electrodes, with a layer thickness of 40 µm, have shown that with this material an improvement of roughly 32% in the 50% 1st breakdown voltage can be achieved [60].

Breakdown behaviour of thin single layer coatings after the 1st breakdown

In section 4.5.3 it was also discussed that several thin coating materials show an increase in the breakdown voltage after the first breakdown. The breakdown voltage further increases with the number of breakdowns. The materials which show this behaviour are FP-II, FP-IV and to a lesser extent Semiconductor A.

As explained above, both FP-II and FP-IV show a 1st breakdown voltage which is either somewhat lower or significantly lower than the 1st breakdown voltage of bare electrodes. Moreover, both materials mainly consist of a fluoropolymer, which is ECTFE in the case of FP-II and FEP in the case of FP-IV, as described in section 3.3.

The extra tests on FP-II samples described in section 4.2 and discussed in section 4.5.3 have shown that the increased breakdown voltage is present for a limited amount of time. Furthermore, the presence of the progressive stress part in the test procedure enhances the increase in breakdown voltage after the first breakdown. The latter suggests that either preconditioning of the coating or the lower first breakdown voltage enhances the breakdown voltage increase.

The temporary nature suggests that the composition or physical structure of the coating material has no influence on the breakdown voltage after the first breakdown. Moreover, the increase only occurs after breakdowns, which suggests that either the generation of charge carriers or the evaporation of the coating causes the increase

in breakdown voltage. Therefore, the increase in the breakdown voltage after the first breakdown is caused by an external factor.

The accumulation of hetero-charges on the surface would not increase the breakdown voltage of the system because the presence of these charge near the punctures in the coating would present significant field enhancements which decrease the breakdown voltage. Homo-charge accumulation on the coating surface, which is present when the coating conductivity is higher than the gas conductivity, can decrease electron field emission as discussed above. From the results of the 1st breakdown voltage it can be seen that the accumulation of homo-charges on the coating surface is insufficient to reduce the electric field strength to a level below the breakdown strength of the coating. Hence, the 1st breakdown voltage of these coatings is lower than that of bare electrodes.

The presence of punctures in the coating material, shown in section 5.5, can provide a faster transport of homo-charges from the electrode to the coating surface, thereby increasing the amount of accumulated homo-charge. This results in an increase in the breakdown voltage due to the shielding of the punctures and the stronger inhibition of electron field emission.

The breakdown damage on the coating surface of both FP-IV and FP-II, presented in section 5.5, has shown that the punctures are small and that the coating material has evaporated. This observation is supported by the fact that no coating particles were found in the tank after testing.

As already explained, both coatings contain fluorine which is released from the material during breakdown. The free fluorine atoms can increase the breakdown strength of the gas due to their strong electronegativity. However, the total evaporated coating volume is very small and it is questionable if such a small amount of fluorine atoms can significantly enhance the electronegativity of the gas.

Breakdown behaviour of double layer thin coatings

As discussed in section 4.5.3, two double layer materials were produced in which FP-II is applied as a base layer to smooth out the roughness of the electrode surface before applying the topcoat which either consists of FP-I or PA11. The goal was to further improve the breakdown voltage of single layer FP-I and PA11 coated electrodes.

The results showed that in both cases the breakdown voltage has decreased significantly with respect to the single layer versions, which is the opposite of what was expected. Two main causes of this behaviour can be identified. Firstly, microscopic images of the coating surface after breakdown, presented in section 5.5, show that the adhesion between the FP-II and PA11 layer was insufficient. It is very likely that air was trapped between the layers which presented a field enhancement, causing the reduction in the breakdown voltage. Secondly, at a frequency of 100 kHz, which is the base frequency of a standard lightning impulse, the dielectric response of FP-II is more comparable to an

insulator than a resistive material. Because of this, the smoothening effect of the FP-II layer is not present.

Breakdown behaviour of thick coatings

It was discussed in section 4.5.3 that the difference in the breakdown test results of the electrodes coated with the different thick coating materials was insignificant. In section 2.3 it was explained that with thick coatings it is possible to modify the capacitive electric field distribution of a gas-coating insulation in such a way that the electric field strength in the gas gap is significantly reduced. The maximum reduction is obtained when the permittivity is as close as possible to one. Note that hetero-charge accumulation and inhibition of electron field emission can also be present in gas-coating insulation systems with thick coatings.

The reason that the difference in the 50% 1st breakdown voltage of the different thick coatings is insignificant can be found in the material parameters. Firstly, it was the intention to reduce the relative permittivity of neat epoxy by introducing nanoparticles as explained in section 5.2. The relative permittivity was reduced from 3.65 down to 3.42 for nanocomposite B which is a reduction of 6%. It can be seen that the reduction is relatively small which explains why the difference in the 50% 1st breakdown voltage is insignificant.

Secondly, the dielectric losses, electrical conductivity and surface roughness of the thick coating materials are also comparable, whereas the coating thickness is in all cases 10 mm. The only material parameter which shows a significant difference of up to 20% is the breakdown strength. However, the breakdown strength of the thick coating materials has a negligible influence on the breakdown strength of the gas-coating system because all breakdowns occur in the form of surface flashovers.

As discussed in section 4.5.3, the breakdown voltage of the thick coatings is reduced after the first breakdown. The reduced breakdown voltage is still significantly higher than that of bare electrodes. This reduction is related to the flashover traces formed on the coating surfaces due to the breakdowns as shown in section 5.5. These traces present a path along which a surface flashover can propagate faster than on the undamaged coating surface, thus explaining the reduced breakdown voltage which is still larger than that of bare electrodes.

The fact that the surface flashover traces present a reduced breakdown voltage is caused by two main factors. Firstly, the coating surface at the discharge tracks is smoothened due to the local evaporation of coating material, reducing the path length of the propagating surface discharge. Secondly, it is observed that the traces contain carbon black, which can increase the surface conductivity, resulting in a lower surface flashover voltage.

Scaling up to larger dimensions

In section 4.5.4 it was discussed that the improvement in the 1st breakdown voltage of medium and large size PA11 coated electrodes with respect to uncoated electrodes is reduced. Fortunately, the improvement remains significant. This reduction can be explained with several facts. Firstly, electron field emission plays a less significant role in the breakdown of medium and large size electrodes due to the more homogeneous electric field distribution. Secondly, the increased surface area of the rod electrodes introduces a larger probability of the presence of material defects such as rough spots, thin spots and inclusions.

The 1st breakdown voltage of medium and large size neat epoxy coated electrodes shows a severe reduction in the improvement with respect to bare electrodes as explained in section 4.5.4. For medium size electrodes, the 50% 1st breakdown voltage shows no significant difference with respect to bare electrodes. For large size electrodes, the 50% 1st breakdown voltage is even 15% lower than that of bare electrodes. The main cause of this behaviour can be found in the capacitive electric field distribution in the gas gap.

The capacitive electric field distribution in the rod-plane gap with either a small, medium or large size electrode is depicted in Figure 5.53, Figure 5.54 and Figure 5.55 respectively. The blue, dashed lines represent the electric field distribution in the gap with an uncoated electrode, whereas the red lines represent the electric field in the gap with a neat epoxy coated electrode.

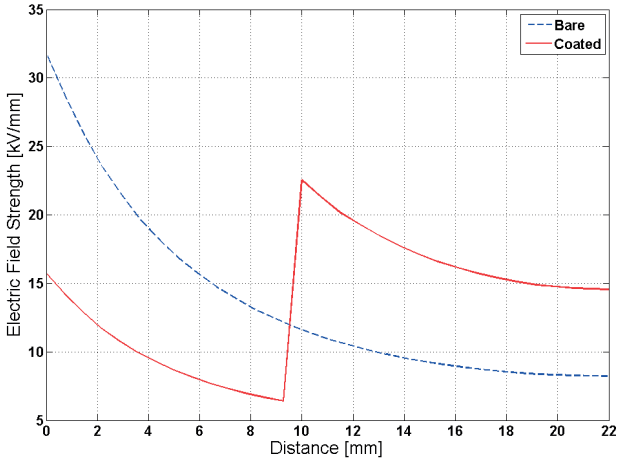

Figure 5.53: Electric field distribution in the rod plane gap with a bare (blue, dashed) and a neat epoxy coated (red) small size electrode.

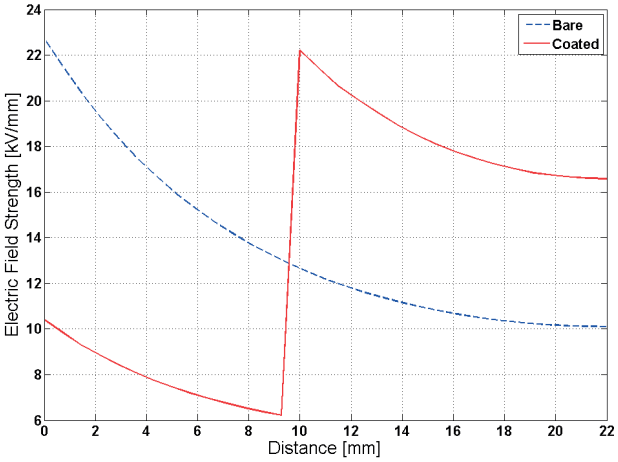

Figure 5.54: Electric field distribution in the rod plane gap with a bare (blue, dashed) and a neat epoxy coated (red) medium size electrode.

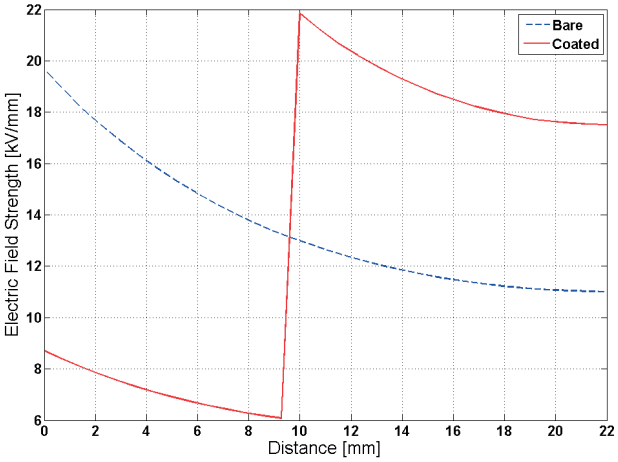

Figure 5.55: Electric field distribution in the rod plane gap with a bare (blue, dashed) and a neat epoxy coated (red) large size electrode.

As explained in section 2.3 and as can be seen in Figure 5.53, the maximum electric field strength in the gas gap is significantly reduced when a small size electrode is coated with a thick layer of neat epoxy. This reduction explains the relatively large improvement in the 1st breakdown voltage. When a medium size electrode is used, the results are different. Figure 5.54 shows that for medium size electrodes the reduction in the maximum electric field strength is insignificant when a neat epoxy coating is applied which coincides with the insignificant difference in the 1st breakdown voltage.

In the case of large size electrodes the maximum electric field strength in the gas is even significantly enhanced when a neat epoxy coating is applied, as can be seen in Figure 5.55. This electric field enhancement coincides with the fact that the 1st breakdown voltage of large size neat epoxy coated electrodes shows a significant reduction with respect to bare electrodes.

The results presented above also indicate that the modification of the capacitive electric field distribution is dominant with respect to the breakdown voltage of thick neat epoxy coated electrodes. Therefore, it can be stated that both the reduction of electron field emission and accumulation of hetero-charge on the coating surface play an insignificant role in the breakdown voltage of thick neat epoxy coated electrodes.

6

Model of electrical breakdown in SF_6 and dry air

In this chapter a mathematical model is presented which predicts the breakdown voltage and breakdown location in a gas insulated system filled with either SF_6 or dry air at normal conditions. In section 6.1 the breakdown model is described including the theoretical background and the applied software and methods. The verification of the breakdown model is described in section 6.2 which includes verification measurements in the rod-plane test setup and verification of the model with breakdown test results found in literature.

6.1 THE MODEL

This section starts with a brief introduction of the background theory of electrical breakdown in dry air and SF_6 followed by a detailed description of the implementation of the different varieties of the breakdown model.

6.1.1 Starting conditions of breakdown

Consider the gas gap in the rod-plane test setup used in this research. When no voltage is applied on the setup, the electric field in the gas gap is zero and the gas in the gas gap is in equilibrium. In an equilibrium state, electrons and ions are generated in the gas by photo-ionization of gas molecules due to background radiation [39], [61]–[63]. The charge carriers generated by photo-ionization are subsequently neutralized by recombination processes. Because both the ionization rate and recombination rate in the gas are equal in equilibrium the concentration of charge carriers in the gas remains constant and thus the net ionization rate is zero.

When an electric field is applied on the gas gap, electrons and ions are accelerated due to electrostatic forces. Consequently, the electrons and ions gain kinetic energy. Because electrons have a significantly smaller size than ions, they are accelerated to significantly higher velocities and thus electrons gain significantly more kinetic energy compared to

ions. Therefore, electrons play a major role in the initiation of an electrical breakdown [39], [61]–[63].

Due to the gain in the kinetic energy of electrons, gas molecules can be ionized through collisions with electrons, which is also known as impact ionization. The impact ionization presents a relatively large contribution to the ionization rate in the gas. Consequently, the ionization rate in the gas becomes larger than the recombination rate resulting in a positive net ionization rate. The net ionization rate a is defined as the number of newly generated ions per unit of distance in the direction of the electric field and is dependent on the gas type, gas pressure and the applied electric field [39].

The above mentioned ionization rate is present in all types of gases. However, dry air and SF_6 are electronegative. In electronegative gases free electrons are removed from the gas due to attachment to neutral gas molecules resulting in the creation of negative gas ions. Therefore, the electron attachment rate h opposes the net ionization rate, is defined as the number of electrons removed from the gas per unit of distance in the direction of the electric field and is also dependent on gas type, gas pressure and the applied electric field [62].

Because the net ionization rate a and the attachment rate h oppose each other it can be stated that a net production of electrons and positive ions in the gas occurs when the difference between both rates is larger than zero. The difference between the ionization rate a and the attachment rate h is also known as the effective ionization rate and is depicted in the equation below [64], [65].

$$\bar{\alpha} = \alpha - \eta \qquad (20)$$

The effective ionization rate is also dependent on gas type, gas pressure and electric field strength. Therefore, there is a minimum electric field strength above which the effective ionization rate is larger than zero and net ionization is effectively present. This minimum electric field strength is known as the critical field strength E_{crit} which is dependent on gas type and gas pressure.

In the gas gap of the rod-plane test setup the electric field distribution is inhomogeneous. The highest electric field strength can be found near the tip of the rod electrode. When the applied voltage is high enough, the electric field strength at the tip of the rod electrode reaches the value of the critical field strength. In this case a small region is created in the gas gap, near the tip of the rod electrode, in which the electric field strength is equal to or larger than the critical field strength. This region is called the critical region and is depicted in the sketch of the rod-plane gap in Figure 6.1.

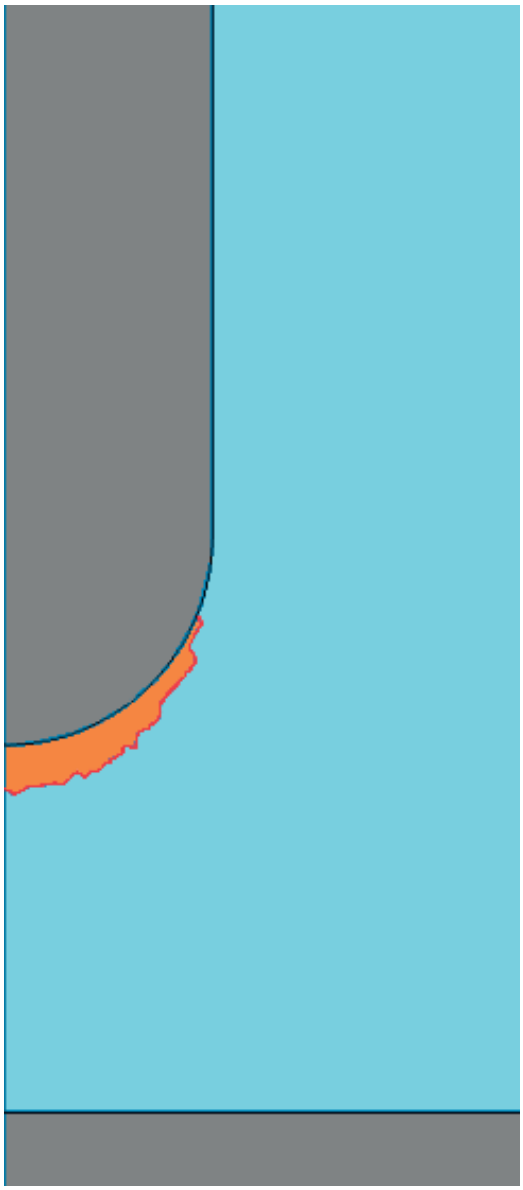

Figure 6.1: Sketch of rod-plane gap with critical region (orange) at the tip of the rod electrode bound by the red contour.

In the critical region significant ionization can be present which causes an exponential increase in the number of generated electrons resulting in the formation of an electron avalanche [39]. The formation of an avalanche can result in the initiation of an electrical breakdown in the gas gap.

The above mentioned processes can only occur if a starting electron is present within the critical region. Therefore, the main prerequisite for the occurrence of an electrical breakdown in the gas gap is the presence of a free moving starting electron or negative ion in the critical region.

As explained in section 2.4 there are several sources of starting electrons which can occur in the critical region. Firstly, electrons generated in the gas gap due to background radiation can move to the critical region. Secondly, electrons can be generated in the critical region by detachment from a negative ion entering the critical region [51]. Thirdly, if the rod electrode has negative polarity, electrons can be emitted from the rod electrode directly into the critical region due to electron field emission which is dependent on the electric field strength at the electrode surface. Other charge carrier generation processes such as thermionic emission, photo-electric effect and thermal ionization play an insignificant role in the breakdown of GIS.

6.1.2 Streamer breakdown

Regarding the applied gas pressure and gap length in the rod-plane test setup it can be stated that breakdown in this system will occur in the form of a streamer discharge [39], [51], [62]–[65]. Therefore, breakdown mechanisms such as the Townsend mechanism and the leader mechanism are not covered in this research.

In the previous section it was explained that a breakdown starts with the formation of an electron avalanche. The formation of an electron avalanche is the starting point of all breakdown mechanisms. An electron avalanche leaves a positive space charge in the gas gap because the mobility of positive ions is orders of magnitude smaller than that of electrons [39]. Most of these positive ions are located in the head of the streamer [39].

The main criterion for the initiation of a streamer is the amount of space charge accumulated in the avalanche head. When the number of ions in the avalanche head exceeds 10^8 ions, a streamer discharge is initiated [39], [51], [62]–[65]. The reason for this is the fact that the large amount of space charge presents a significant field enhancement near the head of the streamer which causes a significant increase in the generation rate of photons and thus the photo-ionization rate in that region. Consequently, new electron avalanches are formed near the streamer head, which marks the start of a streamer discharge.

The above mentioned criterion is formulated in literature as an integral which is referred to as the streamer criterion or the streamer integral. The integral is presented in the equation below [64], [65].

$$\int_0^{x_c} \bar{\alpha}(E,p)\,dx \geq K \qquad (21)$$

The streamer integral states that a streamer breakdown is initiated when the integral of the effective ionization function along a certain path is equal to or larger than the constant K. The critical length x_c is the distance x at which the streamer integral exceeds the constant K. For a streamer to successfully initiate, the integral should reach K at a position before the anode surface.

As already explained, the effective ionization function is dependent on the gas type. For both SF_6 and dry air several different effective ionization functions can be found in literature [64]–[71]. However, the difference in the results obtained from these different ionization functions is minimal. In the next section it is explained which effective ionization functions we selected.

Next to the effective ionization function, the value of the constant K also differs among the available literature sources. For SF_6 either a value of 18.4 or 10.5 is chosen [64], [65], [70]. For dry air a value of 9.15 has been found in literature [70].

6.1.3 Implementation

In this research we developed four breakdown models of increasing complexity which are based on the theory presented in sections 6.1.2 and 2.3.1.

Model 1 (uncoated)

The first model consists of a 2D rotational symmetric electric field calculation in a simplified geometric model of the gas gap of the rod-plane test setup using COMSOL Multiphysics. In Figure 6.2 a section of the 2D electric field calculation results in the rod-plane gap is shown. After the field calculations, the electric field is obtained along the purple line between the tip of the rod electrode and the plane electrode as shown in Figure 6.2. The purple line represents the expected breakdown path, which is selected by hand.

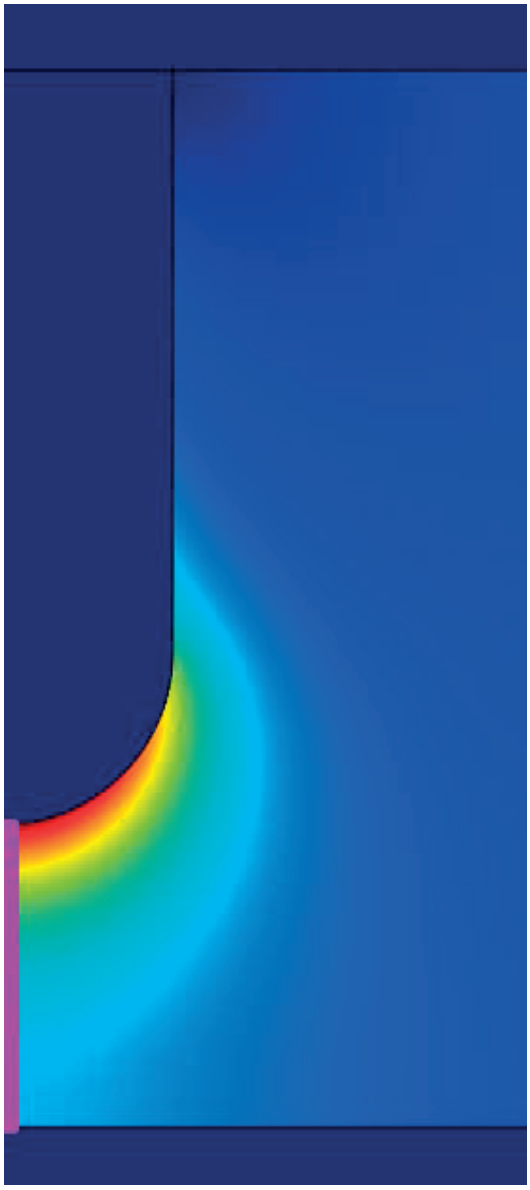

Figure 6.2: 2D rotational symmetric electric field calculation in rod-plane gap. The purple line represents the evaluation line.

The electric field data along the purple line is exported to MATLAB after which the streamer integral is calculated using the obtained electric field data in combination with the applied gas pressure. If the integral remains smaller than the value of K over the entire gap length, the applied voltage is increased and the integral recalculated. If, for a distance smaller than the gap length, the integral reaches the value K it is assumed that a streamer breakdown occurs and the model returns the applied voltage which represents the predicted 50% breakdown voltage. Therefore, the model continues recalculating the streamer integral until a streamer breakdown is expected.

For the calculation of the streamer integral a value of 10.5 and 9.15 is selected for the constant K in the case of SF_6 and dry air respectively. The effective ionization function for SF_6 is taken from [64], [65] and is presented in the equation below.

$$\bar{\alpha}\,[\mathrm{mm}]^{-1} = 27.7\,[\mathrm{kV}]^{-1} \cdot E\ - 246\ \cdot p\,[\mathrm{bar}\cdot\mathrm{mm}]^{-1} \qquad \textbf{(22)}$$

The electric field E and the pressure p are entered in the formula in units of [kV/mm] and [bar] respectively.

The effective ionization function for dry air is taken from [66] and is shown in the equation below.

$$\bar{\alpha} = \alpha - \eta_s - \eta_u \qquad \textbf{(23)}$$

The coefficients a, h_s and h_u represent the ionization, stable attachment and unstable attachment functions respectively. The ionization, stable attachment and unstable attachment functions are presented in equations 20 to 30 [66].

Ionization function for dry air

$$\alpha = p \cdot e^{\left(\frac{E}{p} - 58.2\right)/4.95} \quad \textit{for } E/p \leq 31 \textit{ [V/cm torr]} \qquad \textbf{(24)}$$

$$\alpha = 3.8553 \cdot p \cdot e^{\frac{-213 \cdot p}{E}} \quad \textit{for } 31 < E/p \leq 45 \textit{ [V/cm torr]} \qquad \textbf{(25)}$$

$$\alpha = p \cdot \exp(-64.927 + 5.2642 \cdot u - 0.20238 \cdot u^2 + 0.45178 \cdot 10^{-2} \cdot u^3 - 0.63081 \cdot 10^{-4} \cdot u^4 + 0.56724 \cdot 10^{-6} \cdot u^5 - 0.3278 \cdot 10^{-8} \cdot u^6 + 0.11739 \cdot 10^{-10} \cdot u^7 - 0.23661 \cdot 10^{-13} \cdot u^8 + 0.20479 \cdot 10^{-16} \cdot u^9)$$

with u = E/p and 45 < E/p ≤ 250 [V/cm torr] **(26)**

$$\alpha = 14.5 \cdot p \cdot e^{\frac{-356 \cdot p}{E}} \quad \textit{for } E/p > 250 \textit{ [V/cm torr]} \qquad \textbf{(27)}$$

Stable attachment function for dry air

$$\eta_s = 3.64 \cdot 10^{-3} \cdot p^{1.94} \quad \textit{for } E/p \leq 0.6 \text{ [V/cm torr]} \tag{28}$$

$$\eta_s = 1.426 \cdot 10^{-3} \cdot p^{1.94} \cdot \left(\frac{E}{p}\right)^{-1.834} \quad \textit{for } 0.6 < E/p \leq 10 \text{ [V/cm torr]} \tag{29}$$

$$\eta_s = 3.94 \cdot 10^{-3} \cdot p^{1.94} \cdot \left(\frac{E}{p}\right)^{-2.277} \quad \textit{for } E/p > 10 \text{ [V/cm torr]} \tag{30}$$

Unstable attachment function for dry air

$$\eta_u = 0 \quad \textit{for } E/p < 3 \text{ [V/cm torr]} \tag{31}$$

$$\eta_u = 1.95 \cdot p \cdot e^{\frac{-60 \cdot p}{E}} \cdot \frac{p}{E} \quad \textit{for } 3 \leq E/p < 25 \text{ [V/cm torr]} \tag{32}$$

$$\eta_u = 2 \cdot 10^{-4} \cdot E + 2 \cdot 10^{-3} \cdot p \quad \textit{for } 25 \leq E/p < 35 \text{ [V/cm torr]} \tag{33}$$

$$\eta_s = 8 \cdot 10^{-3} \cdot p \tag{34}$$

As can be seen from the equations, the ionization, stable attachment and unstable attachment functions for dry air are more complex and consist of three or four different formulae which are selected for specific electric field and pressure conditions.

Model 2: Particle tracing module (uncoated)

In model 1 the expected breakdown path is specified manually, which is in that case a straight line from the tip of the rod electrode to the plane electrode. Because the expected breakdown path is specified by hand it is not possible to predict the location of the breakdown and it is difficult to apply the model to other geometries.

To overcome the above mentioned deficiency it would be favourable to calculate the streamer integral along the electric field lines in the gas gap to predict the breakdown path. With version 4.3 and newer versions of COMSOL Multiphysics we can calculate integrals along electric field lines with the use of the particle tracing module [71].

Our model (2) predicts the 50% breakdown voltage and the breakdown location using only COMSOL as opposed to model 1 which also uses MATLAB. The model starts with the

calculation of the electric field in any arbitrary gas gap. Next, the particle tracing module is set to calculate the trajectories of massless particles which have their starting points at the surface of the high voltage electrodes. The particle velocity vectors are set to follow the electric field lines and the particles are set to freeze upon contact with the ground electrodes to ignore any particle collision effects.

The particle tracing module is also set to calculate the streamer integral along the calculated trajectory of each particle. Therefore, the model effectively calculates the streamer integral along each electric field line.

The results graphically show the particle trajectories, or field lines, along which the streamer integral has reached the value of K. If there are no field lines along which the streamer integral has reached the value K no breakdown is expected. To find the expected 50% breakdown voltage, the above mentioned procedure is automatically repeated within a specified range of applied voltages and with a specified voltage increment (parametric sweep). The lowest applied voltage resulting in at least one particle trajectory along which the streamer integral has reached the value of K is the expected 50% breakdown voltage. The corresponding particle trajectory is the expected breakdown path.

In Figure 6.3 a sketch of the rod-plane gap is shown in which a single particle trajectory is shown along which the streamer integral is larger than K. The applied voltage is 294 kV, which is the expected 50% breakdown voltage of the rod-plane gap filled with SF_6 at a pressure of 0.34 MPa. The rod electrode is a small size electrode (ø = 25 mm). The critical region is indicated by the red coloured boundary near the tip of the rod electrode.

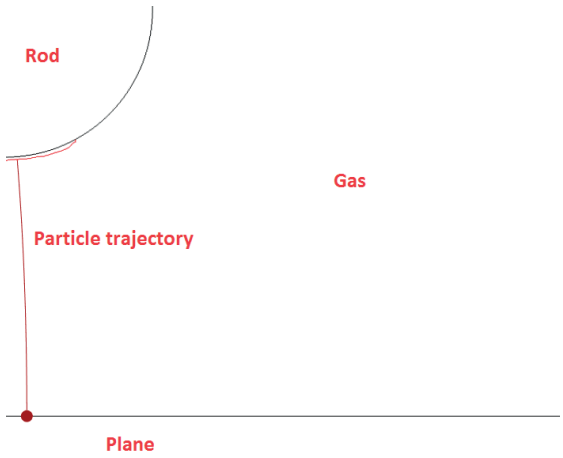

Figure 6.3: Sketch of the gas gap of the rod-plane test setup including critical region (bound by red contour) and particle trajectory along which the streamer integral is larger than K. (V = 294 kV)

When for the same conditions the applied voltage in the model is increased to 400 kV, more particle trajectories will be shown along which the streamer integral is larger than K as depicted in Figure 6.4. Also the size of the critical region is increased. The colour of the trajectories represents the maximum value of the streamer integral along each trajectory, with red and blue representing the highest and lowest maximum values respectively.
In model 2 the same values for K and the same effective ionization functions are used as applied in model 1.

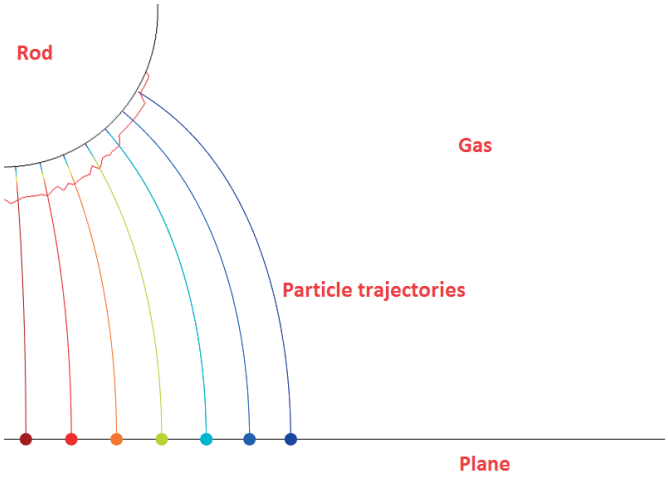

Figure 6.4: Sketch of the gas gap of the rod-plane test setup including critical region (bound by red contour) and particle trajectories along which the streamer integral is larger than K. (V = 400 kV)

Model 3: Electrode surface roughness (SF_6, uncoated)

In the verification results of model 2, which will be presented in section 6.2.3, it was observed that the predicted breakdown voltage was significantly higher than the measured breakdown voltage for SF_6 gas with a pressure of 0.5 MPa and higher. For lower SF_6 pressures and for dry air this discrepancy was not present.

As explained in section 2.4.2, the roughness of the electrode surface can have a significant negative influence on the breakdown voltage of a gas insulated system. In literature it is shown that the negative influence of the electrode surface roughness is significantly stronger in electronegative gases at a high gas pressure [38]. This effect is caused by the fact that in inhomogeneous electric fields at high gas pressures, ionization processes occur very close to the electrode surface due to the short attachment length. Consequently, the microscopic field enhancements at the electrode surface are located relatively close to the region in which ionization occurs, resulting in an apparent reduction of the critical electric field strength E_{cr} [38]. If the gas pressure is lower, the ionization

processes occur at a greater distance from the electrode surface and thus the influence of the electrode surface roughness is less pronounced.

In [38] a relationship was found between the reduction of the critical electric field strength and the product of the electrode surface roughness and gas pressure for SF_6. This relation is shown in Figure 6.5. Note that this figure was also shown in section 2.4.2.

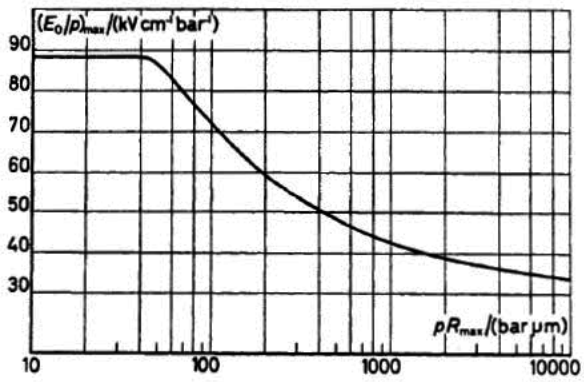

Figure 6.5: Critical electric field strength as a function of the product of the gas pressure and electrode surface roughness [38].

To correct the discrepancy between the model and the verification measurement results for SF_6 gas at pressures of 0.5 MPa and higher, we implemented the above mentioned relation in breakdown model 3. To accomplish this, the curve in Figure 6.5 was entered manually in MATLAB after which a function was fitted to the curve. Subsequently, the effective ionization function of SF_6 was modified using the fitted function. The modified effective ionization function is presented in equation 16. The parameters p, R and E represent the gas pressure in [bar], the electrode surface roughness in [µm] and the electric field strength in [kV/mm] respectively.

$$\begin{aligned} \bar{\alpha} &= \frac{p \cdot R + 159.5}{3.29 \cdot p \cdot R + 1565} \cdot 246 \cdot E - 246 \cdot p \text{ for } p \cdot R > 65 \text{ [µm·bar]} \\ \bar{\alpha} &= 27.7 \cdot E - 246 \cdot p \text{ for } p \cdot R \leq 65 \text{ [µm·bar]} \end{aligned} \quad \textbf{(35)}$$

Model limitations

In all three models it is assumed that a full streamer breakdown of the gas gap occurs when a streamer is initiated and thus when the streamer criterion is fulfilled. The models do not take the influence of streamer propagation into account, which can result in an underestimation of the breakdown voltage for larger and more complex gas gaps [72].

Because the gas gap in the rod-plane test setup is relatively short, it is expected that the influence of streamer propagation on the breakdown can be neglected in this case.

Another limitation of the models is the fact that the voltage polarity is not taken into account. The model assumes the worst-case situation which is in this case a negative polarity voltage on the rod electrode due to the fact that starting electrons are directly emitted from the rod electrode into the critical region because of electron field emission.

When a positive polarity voltage is applied to the rod electrode, the only source of starting electrons are negative ions and free electrons in the gas gap which have to travel to the critical region. Consequently, the waiting time between voltage application and streamer initiation is longer and is statistical in nature. In literature, this waiting time is referred to as the statistical time lag [73], [74]. The result of this is the fact that at positive polarity the 50% breakdown voltage is significantly higher than at negative polarity. Moreover, because of the statistical time lag, the scatter in the breakdown test results is also larger which results in a wider distribution function [5].

Model 4: Thick coatings in dry air

As explained in section 5.6.2, the breakdown behaviour of electrodes coated with thick coatings in the rod-plane arrangement is mainly related to the capacitive electric field distribution in the gas gap. Therefore, it was possible to develop a model for the prediction of the breakdown voltage of the rod-plane gap, coated with a thick coating layer.

This model is based on model 2, with the addition of a 10 mm thick coating layer in the COMSOL geometry. In the model, the relative permittivity of the coating layer is specified as a material parameter. The values of the relative permittivity were selected at 100 kHz and are presented in section 5.6.1. The starting point of the particle trajectories is in this case the coating surface instead of the electrode surface. Thus, the model incorporates the modification of the capacitive electric field distribution in the gas gap due to the presence of the coating layer, as explained in section 2.3.1. Charge accumulation at the coating surface and inhibition of electron field emission are not included in this model.

The model has been verified for thick coatings in dry air because the breakdown tests on thick coatings in the rod-plane arrangement were only performed in dry air at 0.9 MPa. The verification of this model is presented in section 6.2.6.

6.2 MODEL VERIFICATION

In this section the results of the verification breakdown tests are presented, followed by the verification of the four models including an extra verification of model 3 on alternative geometries.

6.2.1 Verification measurements

The verification measurements were performed on the rod-plane electrode arrangement using uncoated small, medium and large size electrodes. The applied gas pressures are 0.8 and 0.9 MPa for dry air and 0.34, 0.4, 0.5 and 0.6 MPa for SF_6. The applied test procedure is the standard 50% up-down test from IEC 60060-1 (test procedure D, class2 test) [49] and for each combination of gas pressure and electrode size, two or three separate 50% up-down tests are performed on two or three unused electrodes.

The results of the verification measurements of small, medium and large size electrodes are shown in Table 6.1, Table 6.2 and Table 6.3 respectively. As can be seen from the tables, the 95% confidence intervals of the 50% breakdown voltages are small with a maximum width of +/- 2%. Moreover, it can be observed in the tables that the increase in the breakdown voltage with an increase in the gas pressure is reduced when the gas pressure is increased above 4.0 bar for SF_6. This behaviour is different from the theory,

Table 6.1: Verification measurement results of small size electrodes in SF_6

Gas pressure	50% Breakdown voltage	95% confidence intervals
0.34 [MPa]	319 [kV]	+/- 3 [kV]
0.40 [MPa]	355 [kV]	+/- 4 [kV]
0.50 [MPa]	426 [kV]	+/- 8 [kV]
0.60 [MPa]	452 [kV]	+/- 4 [kV]

Table 6.2: Verification measurement results of medium size electrodes in SF_6 and dry air

Gas	50% Breakdown voltage	95% confidence intervals
0.8 [MPa] dry air	343 [kV]	+/- 5 [kV]
0.9 [MPa] dry air	368 [kV]	+/- 4 [kV]
0.34 [MPa] SF_6	409 [kV]	+/- 4 [kV]
0.40 [MPa] SF_6	476 [kV]	+/- 4 [kV]
0.50 [MPa] SF_6	504 [kV]	+/- 4 [kV]
0.60 [MPa] SF_6	587 [kV]	+/- 5 [kV]

Table 6.3: Verification measurement results of large size electrodes in SF_6 and dry air

Gas	50% Breakdown voltage	95% confidence intervals
0.8 [MPa] dry air	397 [kV]	+/- 3 [kV]
0.9 [MPa] dry air	432 [kV]	+/- 3 [kV]
0.34 [MPa] SF_6	492 [kV]	+/- 4 [kV]
0.40 [MPa] SF_6	560 [kV]	+/- 5 [kV]
0.50 [MPa] SF_6	599 [kV]	+/- 8 [kV]
0.60 [MPa] SF_6	685 [kV]	+/- 7 [kV]

which suggests that the relation between gas pressure and breakdown voltage should be linear, as explained in section 6.1.3 regarding breakdown model 1.

This difference is caused by the negative influence of the electrode surface roughness on the critical electric field strength for electronegative gases at a relatively high pressure. The influence of electrode surface roughness on the breakdown voltage is included in model 3 as explained in section 6.1.3.

6.2.2 Verification of model 1

For the verification of model 1, the verification measurement results are compared with the breakdown voltage predicted by the model as shown in Table 6.4, Table 6.5 and Table 6.6 for the small, medium and large size electrodes respectively. The model is considered to be adequate if the difference between the predicted breakdown voltage and the measured 50% breakdown voltage is smaller than +/-10%. Thus, the inaccuracy of the model should be smaller than 10%.

The comparison in Table 6.4 shows that for dry air at 0.9 MPa and SF_6 between 0.34 and 0.5 MPa the inaccuracy of the model varies between 0.3% and 6.2%, which is within the inaccuracy limits. However, at 0.6 MPa the difference between the predicted and measured 50% breakdown voltage is 15%, which exceeds our inaccuracy limits.

As shown in Table 6.5 and Table 6.6, the inaccuracy of the model varies between 1% and 7.9% for medium and large size electrodes in dry air at 0.9 and 0.8 MPa and in SF_6 at 0.34 and 0.4 MPa. Therefore, this model is adequate for medium and large size electrodes in dry air at 0.8 and 0.9 MPa and in SF_6 at pressures up to 0.5 MPa. Unfortunately, this model is not adequate for medium and large size electrodes in SF_6 at pressures of 0.5 MPa and higher with an inaccuracy varying between 19% and 27%.

Table 6.4: Comparison between predicted breakdown voltage and measured 50% breakdown voltage. Small size electrodes, Model 1

Gas	50% Breakdown voltage	Predicted breakdown voltage	Difference
0.9 [MPa] dry air	297 [kV]	298 [kV]	+0.3%
0.34 [MPa] SF_6	319 [kV]	299 [kV]	-6.2%
0.40 [MPa] SF_6	355 [kV]	350 [kV]	-1.4%
0.50 [MPa] SF_6	426 [kV]	435 [kV]	+2.1%
0.60 [MPa] SF_6	452 [kV]	520 [kV]	+15%

Table 6.5: Comparison between predicted breakdown voltage and measured 50% breakdown voltage. Medium size electrodes, Model 1

Gas	50% Breakdown voltage	Predicted breakdown voltage	Difference
0.8 [MPa] dry air	343 [kV]	356 [kV]	+3.8%
0.9 [MPa] dry air	368 [kV]	397 [kV]	+7.9%
0.34 [MPa] SF_6	409 [kV]	412 [kV]	+0.7%
0.40 [MPa] SF_6	476 [kV]	483 [kV]	+1.5%
0.50 [MPa] SF_6	504 [kV]	601 [kV]	+19%
0.60 [MPa] SF_6	587 [kV]	719 [kV]	+22%

Table 6.6: Comparison between predicted breakdown voltage and measured 50% breakdown voltage. Large size electrodes, Model 1

Gas	50% Breakdown voltage	Predicted breakdown voltage	Difference
0.8 [MPa] dry air	397 [kV]	416 [kV]	+4.8%
0.9 [MPa] dry air	432 [kV]	466 [kV]	+7.9%
0.34 [MPa] SF_6	492 [kV]	497 [kV]	+1.0%
0.40 [MPa] SF_6	560 [kV]	583 [kV]	+4.1%
0.50 [MPa] SF_6	599 [kV]	726 [kV]	+21%
0.60 [MPa] SF_6	685 [kV]	869 [kV]	+27%

6.2.3 Verification of model 2

For model 2, the comparison between the predicted and the measured 50% breakdown voltages of small, medium and large size electrodes are presented in Table 6.7, Table 6.8 and Table 6.9 respectively. The comparison for the small electrodes shows that the inaccuracy of the model varies between 0.3% and 8.5% for SF_6 gas pressures up to 0.6 MPa, which is within the inaccuracy limits. At 0.6 MPa the inaccuracy of the model is 23%, which exceeds the inaccuracy limits. For dry air at 0.9 MPa, the difference between the predicted and measured 50% breakdown voltage is 1.0%.

The comparisons for the medium and large size electrodes show that the inaccuracy of the model varies between 0% and 5.4% for dry air at 0.8 MPa and 0.9 MPa and for SF_6 at pressures up to 0.5 MPa. Therefore, this breakdown model is adequate for SF_6 gas pressures up to 0.5 MPa and dry air at pressures of 0.8 and 0.9 MPa. Unfortunately, the model exceeds the inaccuracy limits for SF_6 gas pressures of 0.5 and 0.6 MPa with values ranging from 17% to 25%.

Table 6.7: Comparison between predicted breakdown voltage and measured 50% breakdown voltage. Small size electrodes, Model 2

Gas	50% Breakdown voltage	Predicted breakdown voltage	Difference
0.9 [MPa] Dry Air	297 [kV]	300 [kV]	+1.0%
0.34 [MPa] SF_6	319 [kV]	318 [kV]	-0.3%
0.40 [MPa] SF_6	355 [kV]	370 [kV]	+4.2%
0.50 [MPa] SF_6	426 [kV]	462 [kV]	+8.5%
0.60 [MPa] SF_6	452 [kV]	554 [kV]	+23%

Table 6.8: Comparison between predicted breakdown voltage and measured 50% breakdown voltage. Medium size electrodes, Model 2

Gas	50% Breakdown voltage	Predicted breakdown voltage	Difference
0.8 [MPa] Dry Air	343 [kV]	346 [kV]	+0.9%
0.9 [MPa] Dry Air	368 [kV]	388 [kV]	+5.4%
0.34 [MPa] SF_6	409 [kV]	422 [kV]	+3.2%
0.40 [MPa] SF_6	476 [kV]	494 [kV]	+3.8%
0.50 [MPa] SF_6	504 [kV]	616 [kV]	+22%
0.60 [MPa] SF_6	587 [kV]	736 [kV]	+25%

Table 6.9: Comparison between predicted breakdown voltage and measured 50% breakdown voltage. Large size electrodes, Model 2

Gas	50% Breakdown voltage	Predicted breakdown voltage	Difference
0.8 [MPa] Dry Air	397 [kV]	386 [kV]	-2.8%
0.9 [MPa] Dry Air	432 [kV]	432 [kV]	0%
0.34 [MPa] SF_6	492 [kV]	478 [kV]	-2.8%
0.40 [MPa] SF_6	560 [kV]	562 [kV]	+0.4%
0.50 [MPa] SF_6	599 [kV]	700 [kV]	+17%
0.60 [MPa] SF_6	685 [kV]	836 [kV]	+22%

The results of model 2 show that for SF_6 the predicted breakdown voltage is in all cases higher than the predicted breakdown voltage of model 1. This difference is caused by two factors. Firstly, in model 2 no particle trajectory starts from the exact centre of the rod electrode tip, resulting in the fact that the streamer integral is not calculated on the exact same line as applied in model 1. Secondly, the rod electrode holding plane, which is shown in the topside of Figure 6.2, is not included in the electric field calculations of model 1, while it is included in the electric field calculations of model 2. Consequently, the electric field strength in the gas gap is slightly reduced, resulting in a higher predicted breakdown voltage compared to model 1.

The above mentioned difference in the prediction between models 1 and 2 is not present for dry air. In the case of dry air, model 2 predicts a lower predicted voltage and with a better accuracy compared to model 1.

Both model 1 and model 2 are not adequate for the prediction of the breakdown voltage in SF_6 at gas pressures of 0.5 MPa and higher as shown by the relatively high inaccuracy varying between 15% and 27%. Note that in this case the model always predicts a higher breakdown voltage than was measured. Therefore, the inaccuracy of the model can be considered as a bias. This bias is caused by the fact that the surface roughness of the electrodes is not taken into account in the model, as explained in section 6.1.3.

Therefore, we developed model 3 which consists of model 2 including a correction for the electrode surface roughness in SF_6. The correction has been described in section 6.1.3.

6.2.4 Verification of model 3 (SF_6)

As explained in the previous section, model 3 consists of model 2 with a correction for the electrode surface roughness in SF_6. The comparison between the predicted breakdown voltage and the measured 50% breakdown voltage is presented in Table 6.10, Table 6.11 and

Table 6.12 for small, medium and large size electrodes respectively. As can be seen in the tables, the accuracy of this breakdown model varies between 0.3% and 6.3% for the full range of applied gas pressure and for all electrode sizes. Thus, the correction of breakdown model 2 for the electrode surface roughness has significantly improved the accuracy.

In total, it can be stated that breakdown model 3 is adequate for the rod-plane test setup with a rod electrode size ranging from 25 to 70 mm, while filled with SF_6 at gas pressures of 0.34 up to and including 0.6 MPa.

Table 6.10: Comparison between predicted breakdown voltage and measured 50% breakdown voltage. Small size electrodes, Model 3

Gas	50% Breakdown voltage	Predicted breakdown voltage	Difference
0.34 [MPa] SF_6	319 [kV]	318 [kV]	-0.3%
0.40 [MPa] SF_6	355 [kV]	370 [kV]	+4.2%
0.50 [MPa] SF_6	426 [kV]	402 [kV]	-5.6%
0.60 [MPa] SF_6	452 [kV]	462 [kV]	+2.2%

Table 6.11: Comparison between predicted breakdown voltage and measured 50% breakdown voltage. Medium size electrodes, Model 3

Gas	50% Breakdown voltage	Predicted breakdown voltage	Difference
0.34 [MPa] SF_6	409 [kV]	422 [kV]	+3.2%
0.40 [MPa] SF_6	476 [kV]	494 [kV]	+3.8%
0.50 [MPa] SF_6	504 [kV]	536 [kV]	+6.3%
0.60 [MPa] SF_6	587 [kV]	618 [kV]	+5.3%

Table 6.12: Comparison between predicted breakdown voltage and measured 50% breakdown voltage. Large size electrodes, Model 3

Gas	50% Breakdown voltage	Predicted breakdown voltage	Difference
0.34 [MPa] SF_6	492 [kV]	478 [kV]	-2.8%
0.40 [MPa] SF_6	560 [kV]	562 [kV]	+0.4%
0.50 [MPa] SF_6	599 [kV]	608 [kV]	+1.5%
0.60 [MPa] SF_6	685 [kV]	702 [kV]	+2.5%

6.2.5 Verification of model 3 on alternative geometries

Up to this point, model 3 has only been verified in the rod-plane electrode arrangement with varying electrode sizes and gas types and pressures. To evaluate the applicability of the model to other configurations, the model was also verified using the results of lightning impulse breakdown tests on simplified and full disconnector configurations found in the PhD thesis of Philipp Simka [75].

Disconnector geometries from Simka's PhD thesis

The lightning impulse breakdown tests were performed by Simka on the simplified disconnector configurations depicted in Figure 6.6 and Figure 6.7 and on the full disconnector configurations displayed in Figure 6.8. Note that these figures are a 2D rotational symmetric representation of the configurations in which the vertical dashed line represents the symmetry axis. The simplified configurations A, B, C and D consist of parts of the fixed side contacts and a plane electrode. Configuration A includes only the fixed side arcing contact with a diameter of 22 mm, while configuration B includes only the fixed side main contact with an inner diameter of 134 mm and an outer diameter of 170 mm. Configurations C and D include both fixed side arcing and main contacts.

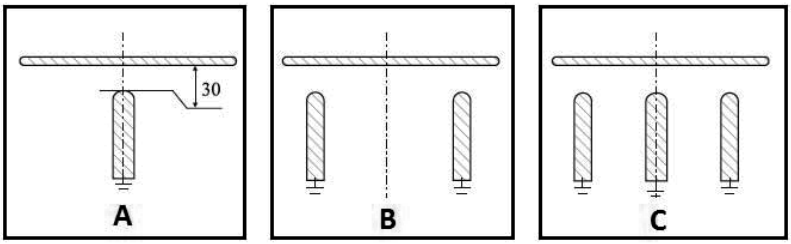

Figure 6.6: Simplified disconnector configurations A, B and C from [73].

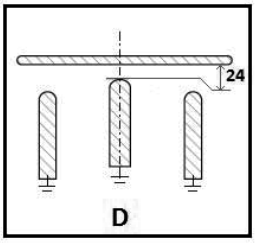

Figure 6.7: Simplified disconnector configuration D from [73]

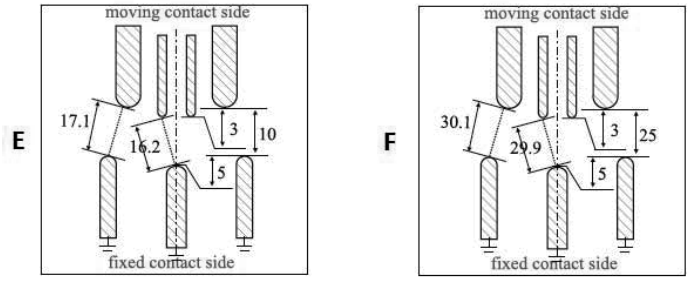

Figure 6.8: Full disconnector configurations E and F from [73]

The gap distance between the plane electrode and the contacts is 30 mm in the case of configurations A, B and C. In the case of configuration D, the gap distance between the arcing contact and the plane electrode is reduced to 24 mm, while the gap distance between the main contact and the plane electrode remains 30 mm. The electric field strength at the tip of the arcing contact in configuration D is the same as in configuration A.

The full disconnector configurations E and F consist of both the fixed side and mobile side main and arcing contacts. The mobile side arcing contact has an outer diameter of 42 mm and an inner diameter of 22 mm, while the mobile side main contact has an inner diameter of 79 mm and an outer diameter of 134 mm. The main contact separation is 10 mm for configuration E and 25 mm for configuration F.

Verification

The lightning impulse breakdown tests in [75] are performed in SF_6 at a gas pressure of 0.6 MPa. Moreover, both positive and negative polarity lightning impulses are applied to the plane electrode or the moving contact side. The fixed contact side is in all cases grounded. For the verification of the model only the measurement results are used in which the polarity of the fixed contact side is negative, which is in all cases the worst-case polarity with respect to the breakdown voltage. Thus, the applied voltage is in all cases a positive lightning impulse on the plane electrode or the moving contact side, as is the case for the breakdown tests performed in the rod-plane test setup in this research.

The comparison between the measured 50% breakdown voltage and the predicted breakdown voltage is presented in Table 6.13 and Table 6.14 for the simplified and full disconnector configurations respectively. As can be seen from Table 6.13 the inaccuracy of breakdown model 3 varies between 0.6% and 5.5% for configurations A, B and C. Therefore, for these configurations the model is adequate. Unfortunately, for configuration D the inaccuracy of the model is 12.7% which exceeds the inaccuracy limits for the model. In this case the model predicts a significantly lower breakdown voltage than obtained in the breakdown tests.

Table 6.13: Comparison between predicted and measured 50% breakdown voltage. Simplified disconnector configurations A to D, model 3.

Configuration	50% Breakdown voltage	Predicted breakdown voltage	Difference
A	485 [kV]	482 [kV]	-0.6%
B	724 [kV]	764 [kV]	+5.5%
C	587 [kV]	570 [kV]	-2.9%
D	557 [kV]	486 [kV]	-12.7%

The comparison results in Table 6.14 show that the model predicts the breakdown voltage of full disconnector configuration F (25 mm main contact opening) with an inaccuracy of 6.1%, which is within the inaccuracy limits of the model. Unfortunately, the inaccuracy of the model is 12.2% in the case of full disconnector arrangement E which has a main contact separation of 10 mm. As was the case for simplified disconnector configura-

tion D, the predicted breakdown voltage is significantly lower than the measured 50% breakdown voltage in the case of configuration E.

Table 6.14: Comparison between predicted and measured 50% breakdown voltage. Full disconnector configurations E and F

Configuration	50% Breakdown voltage	Predicted breakdown voltage	Difference
E	426 [kV]	374 [kV]	-12.2%
F	635 [kV]	596 [kV]	-6.1%

In total, the verification of breakdown model 3 on the simplified and full disconnector geometries from [75] has shown that the model adequately predicts the breakdown voltage of simplified disconnector configurations A through C and full disconnector configuration F. The model is not suitable for the prediction of the breakdown voltage of simplified disconnector configuration D and full disconnector configuration E.

The large inaccuracy of the model in the case of configurations D and E is most likely caused by the fact that streamer propagation is not included in this model, which can cause a severe underestimation of the breakdown voltage as explained in the final part of section 6.1.3 which covers the limitations of this model.

For example, in configuration D the electric field near the tip of the arcing contact is the same as found in configuration A. Consequently, in both configurations the streamer integral is fulfilled at a comparable applied voltage which results in a comparable predicted breakdown voltage, as can be seen from Table 6.13. However, the results show that the 50% breakdown voltage of configuration D is significantly higher than that of configuration A. This difference is related to streamer propagation because the initiation conditions are equal in both configurations.

6.2.6 Verification of model 4 (thick coatings in dry air)

The comparison between the predicted and measured 50% breakdown voltage of small size rod electrodes coated with the thick coatings in the rod-plane setup filled with dry air at 0.9 MPa is presented in Table 6.15. The comparison shows that the inaccuracy of the model ranges from 0.3% to 4.8% which is well within the inaccuracy limits. Note that the difference in the predicted breakdown voltage of the different coatings is also relative small as is the case for the measured breakdown voltages and as discussed in section 5.6.2. Therefore, the breakdown model confirms the explanation of the small difference in the breakdown voltage being caused by the small difference in material parameters and in particular the relative permittivity.

Table 6.15: Comparison between predicted and measured 50% breakdown voltage. Thick coatings on small size rod electrodes in dry air at 0.9 MPa.

Size	50% Breakdown voltage	Predicted breakdown voltage	Difference
Neat Epoxy	399 [kV]	380 [kV]	-4.8%
Nanocomp. A	399 [kV]	384 [kV]	-3.8%
Nanocomp. B	389 [kV]	388 [kV]	-0.3%
Nanocomp. C	383 [kV]	386 [kV]	+0.8%

In Table 6.16 the comparison between the predicted and measured 50% breakdown voltage is shown for small, medium and large size electrodes coated with neat epoxy in dry air at 0.9 MPa. In this case the inaccuracy of the model varies between 1.3% and 4.8%. In Table 6.16 the comparison results of small, medium and large size bare electrodes in dry air at 0.9 MPa, taken from Table 6.7, Table 6.8 and Table 6.9 respectively, are also displayed.

The prediction results confirm the breakdown behaviour of medium and large size electrodes discussed in section 5.6.2. For example, the model also predicts a strong reduction in the breakdown voltage of large size rod electrodes coated with a thick layer of neat epoxy, compared to the breakdown voltage of large size bare electrodes. Therefore, the model also confirms the fact that the breakdown behaviour of electrodes coated with a thick coating is governed by the modification of the capacitive electric field distribution in the gas gap.

Table 6.16: Comparison between predicted and measured 50% breakdown voltage. Bare and thick neat epoxy coated rod electrodes in dry air at 0.9 MPa.

Size	50% Breakdown voltage	Predicted breakdown voltage	Difference
Small Bare	297 [kV]	300 [kV]	+1.0%
Small Epoxy	399 [kV]	380 [kV]	-4.8%
Medium Bare	368 [kV]	388 [kV]	+5.4%
Medium Epoxy	371 [kV]	376 [kV]	+1.3%
Large Bare	432 [kV]	432 [kV]	0%
Large Epoxy	366 [kV]	378 [kV]	+3.3%

6.2.7 Summary

In this chapter four electrical breakdown models, of which one includes and three exclude the presence of a coating, were presented which can predict the 50% breakdown voltage of a range of GIS configurations filled with SF_6 or dry air. Three of the four models can also predict the corresponding breakdown path. One of the four electrical breakdown models can predict the 50% breakdown voltage of the rod-plane test setup filled with dry air in which the rod electrode is coated with a thick coating.

In the beginning of the chapter the theory of electrical breakdown initiation and streamer breakdown in SF_6 and dry air was briefly explained. This explanation was followed by a description of the implementation of the above mentioned theory in the three uncoated breakdown models. Additionally, the implementation of the breakdown model which incorporates thick coatings is explained. Finally, the four models were verified with the 50% breakdown voltage obtained from lightning impulse breakdown tests performed in this research and with results found in literature [75].

The verification of the four models showed that each model has several limitations with respect to the breakdown theory which result in a limited range of applications. Model one has two main limitations. Firstly, the model can only predict the 50% breakdown voltage and not the breakdown path, which limits the applicability of the model to relatively simple GIS configurations, such as the rod-plane gap. Secondly, the model does not include the electrode surface roughness which limits the applicability of the model to a maximum SF_6 gas pressure of 0.4 MPa.

Model two includes the prediction of the breakdown path which increases the range of applicable GIS configurations with respect to model one. However, model two has two main limitations. Firstly, this model also excludes the electrode surface roughness limiting the maximum applicable SF_6 gas pressure to 0.4 MPa. Secondly, the model excludes streamer propagation, which can result in a significant underestimation of the breakdown voltage of more complex GIS configurations in which the electrode separation varies significantly and the average gap distance is relatively small.

Note that for dry air models one and two are verified with breakdown test results at 0.8 MPa and 0.9 MPa. Therefore, the models are not verified for gas pressures outside of that range. However, it is expected that the models are also adequate for gas pressures below 0.8 MPa when considering GIS configurations comparable to the rod-plane setup.

Model three consists of model two, supplemented with the influence of the electrode surface roughness for SF_6. Therefore, the applicable range of SF_6 gas pressures is increased to a maximum of 0.6 MPa. Although for the verification of the model a maximum SF_6 gas pressure of 0.6 MPa is used, it is expected that the model is also suitable for higher gas pressures. The main limitation of this model is that it also excludes streamer propagation which results in the same underestimation of the breakdown voltage as explained for model two.

It can be stated that the most suitable breakdown model for SF_6 is model three which can be used with gas pressures up to at least 0.6 MPa. For simple configurations and for several more complex configurations the model is adequate. However, this model and model 2 can underestimate the breakdown voltage of more complex configurations in which the electrode separation varies significantly and the average gap distance is relatively small. To overcome this deficiency, both models should be extended with a routine which implements streamer propagation.

For dry air, up to and including 0.9 MPa gas pressure, the most suitable model is model 2. Up to 0.9 MPa pressure it was not necessary to correct the model for the electrode surface roughness. Note that breakdown model 3 is specifically developed for SF_6 and is therefore not suitable for dry air.

It is expected that a correction for the electrode surface roughness is necessary for dry air at pressures of 1.2 MPa and higher. However, such high gas pressures are outside of the normal pressure range of GIS and should thus only be considered for high pressure GIS, which is not commonly in use.

Finally, model 4 can predict the breakdown voltage of the rod-plane setup in which the rod electrode is covered with a thick coating. However, this model is currently limited to dry air because of the fact that the model was not verified in SF_6. Moreover, surface charge accumulation and inhibition of electron field emission are not included in the model.

7

Conclusions and Recommendations

In this thesis the electrical breakdown behaviour of gas-coating insulation was investigated in relation with the characteristics of the gases and coating materials. In addition, several predictive models of electrical breakdown in gas insulated systems, filled with SF_6 or dry air, were developed. In section 7.1 the results of the above mentioned investigations and the performance of the breakdown model are summarized in several conclusions. The recommendations for further research and the potential application of coatings in GIS are presented in section 7.2.

7.1 CONCLUSIONS

As explained above, the main topic of this thesis is the electrical breakdown behaviour of coated electrodes, which was investigated with negative polarity lightning impulse breakdown measurements. Therefore, it was important to apply an efficient measurement and analysis procedure which was found with an evaluation of the available breakdown test procedures in the standards. The evaluation has shown that by performing statistical analysis on the breakdown test results, using statistical distribution fitting software, the breakdown test procedure has no significant influence on the obtained 50% and 10% breakdown voltage. Consequently, the fastest breakdown test procedure is selected, which resulted in a significantly reduced testing time.

Next to the breakdown test procedure, it was also investigated if the waiting time between impulse applications in a lightning impulse breakdown test in the rod-plane test setup has an influence on the acquired 50% and 10% breakdown voltage. We conclude that the waiting time between impulses has no significant influence on the acquired 50% and 10% breakdown voltage when negative polarity impulses are applied in the rod-plane test setup. Note that for configurations with a significantly larger gap distance or for positive polarity impulse voltage, the waiting time between impulses can have a significant influence on the acquired 50% and 10% breakdown voltage.

Electrical breakdown behaviour of GIS coated with thin coatings

The investigation into the electrical breakdown behaviour of gas insulated systems filled with dry air and coated with thin coating materials has shown that the 1st breakdown voltage can be significantly improved with respect to uncoated systems. The highest improvement in the 1st breakdown voltage of the rod-plane gap has been achieved with the application of PA11 on small size rod electrodes. This improvement is 15% for the 50% 1st breakdown voltage and 7% for the 10% 1st breakdown voltage. The second and third highest improvement has been observed for Semiconductor A and EP-I.

The 1st breakdown voltage is not in all cases improved with the application of a thin coating layer on the small size rod electrodes. In two cases the 1st breakdown voltage was even significantly reduced.

From the combination of the above mentioned investigation and the results of the coating material characterisation we conclude that a suitable thin coating material should meet several requirements with respect to the material properties to obtain a significant improvement in the 1st breakdown voltage. Firstly, the coating surface should be as smooth as possible to minimize electric field enhancements in the gas near the coating surface. Secondly, the coating material should have a relative permittivity as high as reasonably possible, to minimize the electric field at the electrode-coating interface and to consequently minimize electron field emission. Thirdly, the electrical conductivity of the coating material should be as high as reasonably possible to maximize the concentration of homo-charges at the coating surface and to consequently minimize electron field emission. Fourthly, the coating should have a sufficiently high electrical breakdown strength and a sufficient layer thickness to prevent a breakdown from starting in the coating layer instead of the gas.

PA11 is the only coating material which meets all of the above mentioned requirements. According to our suitability requirements, this coating shows the largest significant improvement in the 1st breakdown voltage.

The reduction of the 1st breakdown voltage observed for two of the thin coating materials is directly related to the fact that the breakdown of the gas-coating insulation has started with the breakdown of the coating layer. In these cases the breakdown strength of the coating material or the thickness of the coating layer was insufficient. Note that the relative permittivity and the electrical conductivity also have a direct influence on the electric field strength inside the coating layer. Therefore, an improper selection of these parameters can also result in a breakdown starting in the coating layer.

From the above mentioned observations we can also conclude that for thin coatings the inhibition of electron field emission is the main cause of an improvement in the breakdown voltage of a gas insulated system. Therefore, the accumulation of hetero-charges on the coating surface, which reduces and homogenizes the electric field in the gas, is in most cases not present. Consequently, if the polarity of the rod electrode in the

rod-plane setup would have been positive, there would be no significant improvement in the breakdown voltage. In some cases, it is very likely that the accumulation of hetero-charges causes a breakdown in the coating layer and subsequently a breakdown of the entire insulation system.

The investigation of the breakdown behaviour of gas insulated systems coated with a thin coating also led to the observation that it is not always the case that the breakdown voltage of the coated system is directly reduced after the first breakdown. For two thin coating materials, FP-II and FP-IV, it was observed that the breakdown voltage is increased after the first breakdown. Moreover, the breakdown voltage increased further with the number of breakdowns after which the breakdown voltage was stabilized at a voltage which was significantly higher than the first breakdown.

From further investigations we conclude that the increased breakdown voltage is a temporary effect which is related to external factors and not the composition and physical structure of the coating material. These external factors can be the improvement of the gas in the gap due to the emission of fluorine atoms from the coating during breakdown, caused by evaporation of the material, or the increased accumulation of homo-charges at the coating surface originating from the punctures. Up to now, it cannot be concluded which of these two factors is dominant.

Summarizing the above mentioned observations on the breakdown behaviour of gas-coating insulation after the first breakdown, we conclude that gas-coating insulation systems can show temporary self-restoring behaviour.

Addition of a resistive layer beneath a thin coating

To increase the improvement in the 1st breakdown voltage of PA11 and FP-I coated electrodes with respect to uncoated electrodes, a resistive layer was added below these coating materials. The goal of the resistive base layer was to smoothen the electrode surface before applying the coating layer, since this would reduce the corresponding electric field enhancements in the coating and in the gas. Consequently, the breakdown voltage would be increased.

However,. from the results of the negative lightning impulse breakdown tests on these thin double layer coatings we can conclude that the addition of the semi-conductive layer results in a reduction of the improvement in the 1st breakdown voltage with respect to uncoated electrodes. This reduction is mainly caused by insufficient adhesion between the two layers. Moreover, the base layer, which is FP-II, is not resistive at frequencies above 1 kHz.

Electrical breakdown behaviour of GIS coated with thick coatings

The investigation into the breakdown behaviour of gas insulated systems filled with dry air and coated with a thick coating layer has shown that the 1st breakdown voltage can

be improved significantly with respect to uncoated systems. The improvement in the 50% 1st breakdown voltage, which varies between 29% and 34%, is roughly twice as large as found for electrodes coated with a thin layer of PA11. The improvement in the 10% 1st breakdown voltage ranges from 20% to 32%, which is approximately 3 to 4 times larger than found for PA11. Therefore, we conclude that with thick coatings a significantly larger improvement in the 1st breakdown voltage can be achieved compared to thin coatings.

The difference between the different thick coatings with respect to the improvement in the 1st breakdown voltage is relatively small, which is caused by the small difference in the material characteristics. Moreover, we can conclude that the breakdown strength of the coating materials is of less importance because of the fact that almost all breakdowns occur in the form of surface flashovers. Therefore, we also conclude that the surface conditions and the electric field at the coating surface are the main factors in the performance of thick coatings.

The investigation into the breakdown behaviour of thick coatings also led to the observation that after the first breakdown the breakdown voltage is reduced to a level which is still significantly higher than that of uncoated electrodes. The remaining improvement is 22% to 25%. This is different from thin coatings, for which in most cases the breakdown voltage is reduced to a level comparable to or below that of bare electrodes. From the investigation we can conclude that the reduced breakdown voltage is caused by the formation of discharge tracks on the coating surface which results in a reduction of the coating surface roughness and an increase of the surface conductivity.

Scaling up to larger dimensions

The lightning impulse breakdown tests were also performed on the medium and large size electrodes to investigate the influence of the electrode surface area and a less inhomogeneous electric field distribution on the breakdown behaviour of a coated gas insulated system filled with dry air. For this investigation PA11 and Neat Epoxy were selected as a thin and thick coating respectively.

From the results of this investigation we have drawn three conclusions. Firstly, we conclude that the improvement in the 1st breakdown voltage for PA11 is reduced when the electrode size is increased. This is caused by a reduced influence of electron field emission and an increased probability of the presence of defects in the coating layer. Note that the improvement remains significant.

Secondly, we conclude that the improvement in the 1st breakdown voltage of neat epoxy coated electrodes is reduced to an insignificant difference and even a significant reduction with respect to uncoated electrodes, when the electrode size is increased from small to medium and to large respectively. Thirdly, we can conclude that the breakdown behaviour of thick neat epoxy coated electrodes is governed by the modification of the capacitive electric field distribution in the gas gap. Other physical phenomena, such as

the accumulation of hetero-charges on the coating surface and inhibition of electron field emission, play an insignificant role in this case. Therefore, we also conclude that for the selection of a suitable thick coating the relative permittivity should be as close as possible to one.

Coating material characteristics

From the results of the material characterisation measurements, presented in chapter 5, we conclude that the coating materials show a relatively large variation in the material parameters. The highest coating surface roughness parameter R_y was obtained for FP-III with a value of 13.9 µm, while the lowest surface roughness was measured for PA11 with a value of 0.79 µm.

For the relative permittivity the lowest measured value at a frequency of 100 kHz and a temperature of 20°C was 3.18 for FP-I, while the highest measured value was 5.97 for EP-I. The dielectric losses of the materials at 100 kHz and 20°C vary from 0.046 for nanocomposite A to 2086 for FP-III. At 50 Hz the variation is significantly larger with a minimum of 0.012 and a maximum of 4.17×10^6 for Nanocomposite A and FP-III respectively. The activation energy of the beta relaxation processes, which was determined for EP-I, FP-I, PA11 and FP-IV, ranges from 0.42 eV for FP-I to 0.81 eV for EP-I.

The lowest electrical conductivity was found for FP-I with a value smaller than 10^{-17} S/m, while the highest electrical conductivity was found for FP-III with a value in the order of 10^{-6} S/m. The difference in the electrical conductivity is thus very large. The weakest coating with respect to the 50% resp. 10% AC breakdown strength is FP-II with a value of only 15 kV/mm and 10 kV/mm respectively. The strongest coating is Nanocomposite C with a 50% resp. 10% AC breakdown strength of 50 kV/mm and 45 kV/mm.

Finally, the thickness of the thin coatings ranges from a minimum of 25 µm for FP-III to a maximum of 560 µm for FP-I. For the double layer coatings the thickness ranges from 340µm to 590 µm. The thick coatings all have a thickness of 10 mm.

For thin coatings it has been shown that the coating surface roughness, layer thickness, relative permittivity, conductivity and breakdown strength should meet certain requirements to obtain an effective coating with respect to the improvement in the breakdown voltage of the gas-coating insulation, compared to uncoated gas insulation. However, a clear direct relation between these material parameters and the breakdown voltage has not been found. As an exception, the breakdown voltage of the gas-coating insulation shows a positive dependency with respect to the coating surface roughness.

For thick coatings a direct relation is present between the relative permittivity and the breakdown voltage of the gas-coating system as explained above and in section 2.3.1. The breakdown voltage of the gas-coating insulation shows a negative dependency with respect to the relative permittivity of the thick coating layer.

For the dielectric losses at 50 Hz and 100 kHz and for the activation energy of the beta relaxation processes also no direct relation has been found with the breakdown voltage of the gas-coating insulation. Moreover, for these material parameters no requirements could be formulated for obtaining an effective coating with respect to the improvement in the breakdown voltage compared to uncoated gas insulation.

Electrical breakdown models

In this research we developed four models with which the 50% breakdown voltage of an SF_6 or dry air filled GIS can be predicted. Three out of four models consider only uncoated GIS whereas one model includes thick coatings. With three of the four models the breakdown path and locations can also be predicted.

Our best model for uncoated SF_6 filled GIS configurations is valid for gas pressures up to and including 0.6 MPa and can be used for relatively simple electrode configurations such as rod-plane (with varying rod electrode sizes) and a limited amount of simple and full disconnector arrangements [75]. This model includes streamer breakdown and the influence of the electrode surface roughness. For the above mentioned applications the inaccuracy of the model varies between 0.3% and 6.3%. Next to the breakdown voltage, this model also predicts the breakdown path.

Our best model for uncoated dry air filled GIS configurations is valid for gas pressures up to and including 0.9 MPa. This model is verified in rod-plane configurations with varying electrode sizes and includes streamer breakdown. The surface roughness of the electrodes has no influence on the breakdown voltage in this pressure range. The inaccuracy of this model varies between 0% and 5.4% and this model also predicts the breakdown path.

We also developed a model with which the 50% breakdown voltage of rod-plane arrangements, in which a thick coating is applied on the rod electrode, can be predicted. This model includes rod electrodes with varying sizes, can also predict the breakdown path and is verified in dry air at 0.9 MPa. The inaccuracy of this model ranges from 0.3% to 4.8%.

7.2 RECOMMENDATIONS

Thick coatings show a significantly higher improvement in the 1st breakdown compared to thin coatings. However, the application of thick coatings is limited to a relative small electrode surface area. Therefore, we recommend to apply thick coatings at locations, with a small electrode surface area, inside GIS where the highest electric field strength is found. The coating material should have a relative permittivity as close as possible to one. Moreover, the coating thickness should be tailored to the size and geometry of the

gas gap to obtain the highest possible reduction in the capacitive electric field strength in the gas gap.

Thin coatings are suitable for application on larger electrode surfaces at locations where the electric field strength is less strong and where a smaller improvement in the breakdown voltage is required. In this case the coating material should meet the following requirements.

- The coating surface roughness should be as low as possible.
- The relative permittivity and the electrical conductivity of the coating material should be as high as reasonably possible.
- The coating layer thickness should be as large as possible within the limits of the application process (i.e. electrostatic spraying, dipping)
- The electrical breakdown strength of the coating should be as high as possible.

During the investigations into the breakdown behaviour of coated electrodes it was observed that the quality of the coating layer was not in all cases sufficient. Therefore, we recommend to inspect coated electrodes carefully before installation in GIS. If production errors are present in the coating layer the improvement in the breakdown voltage can be diminished or become negative.

With respect to the improvement of the breakdown strength of GIS by applying a coating, it should be noted that the investigation presented in this thesis is performed with negative lightning impulse breakdown tests. The conclusions and recommendations with respect to the application of a coating are therefore based on lightning impulse breakdown at the critical polarity. Consequently, if a gas insulated system is designed with a coating, we recommend to focus on the improvement of the lightning impulse breakdown voltage for the critical polarity. Another design approach we recommend is to maintain the same lightning impulse breakdown voltage while reducing the GIS dimensions or replacing the insulation gas with an alternative gas such as dry air. Note that, if the critical polarity of lightning impulse breakdown for a GIS design is positive, thin coatings might not provide an adequate solution.

Although it seems that the application of coatings in GIS is favourable with respect to the breakdown voltage, it should be noted that the application of a coating layer inside GIS also introduces an extra failure mode. It should be taken into account that breakdown of a coated GIS can be triggered by a breakdown in the coating layer. Moreover, when a breakdown occurs in a coated system, the original improvement in the breakdown voltage with respect to an uncoated system is lost. Therefore, we recommend to thoroughly test a coated GIS design to minimize the probability of a breakdown puncturing the coating or causing tracks on the coating surface. Furthermore, a repair plan should be developed in which the restoration procedure of a coated system, after the occurrence of a breakdown, is described.

The research presented in this thesis considers the improvement in the negative lightning impulse breakdown voltage of coated rod electrodes with various sizes in a rod-plane electrode arrangement. For the next step in the investigation of the feasibility of improving GIS with coatings we recommend to evaluate the breakdown behaviour of larger configurations such as a coaxial bus or a disconnector. For a coaxial bus, a thin coating, such as PA11, should be applied on the centre conductor and for a disconnector, a thick (neat epoxy or nanocomposite B) or thin (PA11) coating would be applied at a location close to the main contacts.

The temperature of the conductors inside GIS can reach values up to approximately 105 °C under maximum load. Therefore, we recommend to investigate the influence of the conductor temperature on the electrical breakdown behaviour of gas insulated systems with coated electrodes. Note that the electrical properties of coating materials can change dramatically when the temperature is increased as was shown in the results of the dielectric response measurements.

The conductor temperature is also important with respect to the mechanical properties of coating materials. Firstly, the physical structure of the coating material can change when the temperature is increased, which is related to the glass transition temperature. Ultimately, coating materials in the glassy state might lose the initial shape and thermoplastic coatings might become liquid. Secondly, it is expected that the, mostly aluminium, conductor has a larger linear thermal expansion coefficient than the coating material which might induce stress cracking at high temperatures. Therefore, we recommend to perform an investigation into the thermo-mechanical properties of coating materials as a function of temperature and to perform thermal expansion measurements combined with temperature cycling tests.

Note that it is also interesting to investigate the thermal conductivity of coating materials in relation with the electrical breakdown behaviour of coated GIS. Coating materials with a high thermal conductivity can provide more efficient heat transfer from the conductor to the gas resulting in a reduced conductor and coating temperature.

With respect to double layer coatings we recommend to perform an investigation into the feasibility of functionalizing the surface of the base layer to improve the adhesion between the base layer and the topcoat. Functionalization of the base layer can, for example, consist of the application of a specifically designed adhesion primer on the base layer surface before applying the topcoat.

Up to now only the electrical, mechanical and thermal properties of newly manufactured coatings were discussed. We recommend to perform an investigation into the ageing mechanisms for coated GIS. The expected lifetime of coated GIS also needs investigation. The presence of a coating can result in a significant change of the lifetime of a gas insulated system with respect to uncoated systems.

As a next step, we recommend to perform most of the above mentioned studies and experiments to get more insight into the viability of the application of coatings in GIS. Without further knowledge and insight on the electrical, mechanical, thermal and ageing behaviour of coatings in GIS, the correct operation of GIS with coatings cannot be guaranteed during its expected lifetime.

Electrical breakdown model

With respect to the modelling of electrical breakdown in coated and uncoated GIS we recommend to incorporate the following physical processes to come closer to a more unified model.

- The statistical and formative time lag of breakdown should be included in the model to take the difference between impulse and continuous voltages into account and to discriminate between positive and negative polarity voltages.
- Streamer propagation should be included in the model to increase the validity of the model to a wider range of simplified and complex configurations. The current models can severely underestimate the breakdown voltage of such configurations due to the lack of streamer propagation.
- We recommend to implement leader breakdown in the model to predict the breakdown voltage for systems with large electrode clearances. In practice, the electrode clearance would be at least ten times larger than considered in this thesis.
- For coated systems more research is necessary to find a clear correlation between material parameters of thin coatings and the breakdown voltage. Such research would consist of more breakdown measurements and the focus would be on keeping several material parameters constant while varying one or several material parameters of interest. In this way the influence of each material parameters can be identified.
- In this thesis, the range of the relative permittivity and electrical conductivity of the tested thick coating materials was relatively small and the layer thickness of these materials was kept constant. Therefore, for thick coatings we recommend to perform more breakdown tests using coating materials with a larger variation in the relative permittivity, electrical conductivity and layer thickness.

Appendix A

Lightning impulse breakdown test results

This appendix contains the figures of the results of the lightning impulse breakdown tests on coated and uncoated rod electrodes, discussed in chapter 4. The breakdown test results are divided in test series and batches. Each batch represents one set of electrodes which are placed at the same time in the rod-plane test setup and each test series represents a set of batches with comparable electrode and coating types. The electrode numbers coincide with the numbering of the electrode positions in the test setup.

A.1

Series 1 and 3 – Small size electrodes: bare and with a thin single and double layer coating

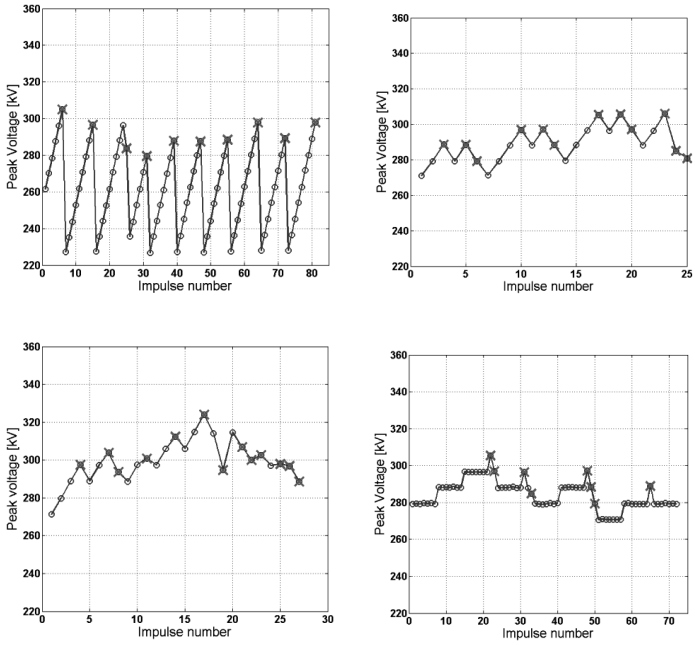

Figure A.1: Bare electrodes - Top left: series 1, batch 1, electrode 1 (progressive stress test), Top right: series 1, batch 1, electrode 1 (50% up-down test), Bottom left: series 1, batch 1, electrode 2 (50% Up-down test), Bottom right: series 1, batch 1, electrode 2 (multiple level test)

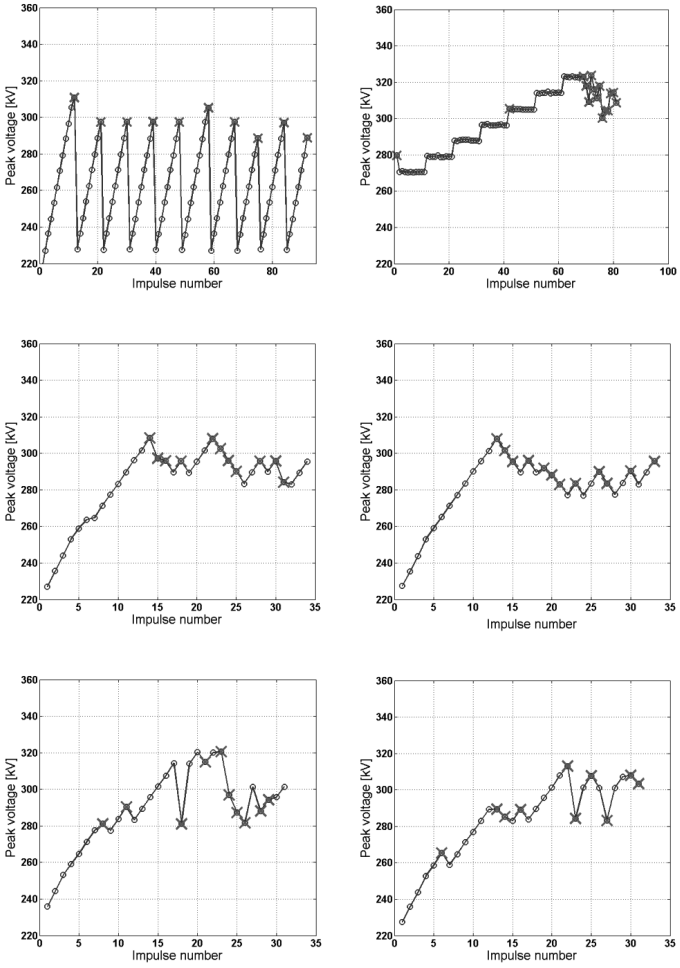

Figure A.2: Bare electrodes – Top left: series 1, batch 1, electrode 2 (progressive stress), Top right: series 1, batch 1, electrode 3 (multiple level), Middle left: series 1, batch 1, electrode 3 (combined test), Middle right: series 1, batch 1, electrode 4 (combined test), Bottom left: series 1, batch 1, electrode 5 (sand blasted, combined test), Bottom right: Series 1, batch 1, electrode 6 (sand blasted, combined test)

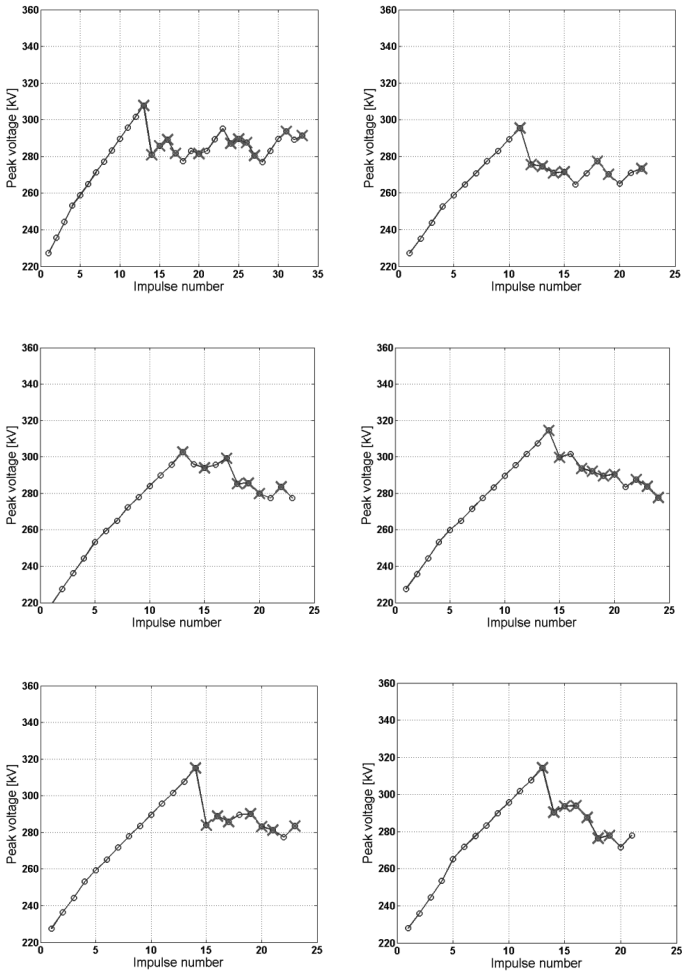

Figure A.3: EP-I coated – Top left: series 1, batch 1, electrode 7, Top right: series 1, batch 1, electrode 8, Middle left: series 1, batch 1, electrode 9, Middle right: series 1, batch 1, electrode 10, Bottom left: series 1, batch 1, electrode 11, Bottom right: series 1, batch 1, electrode 12

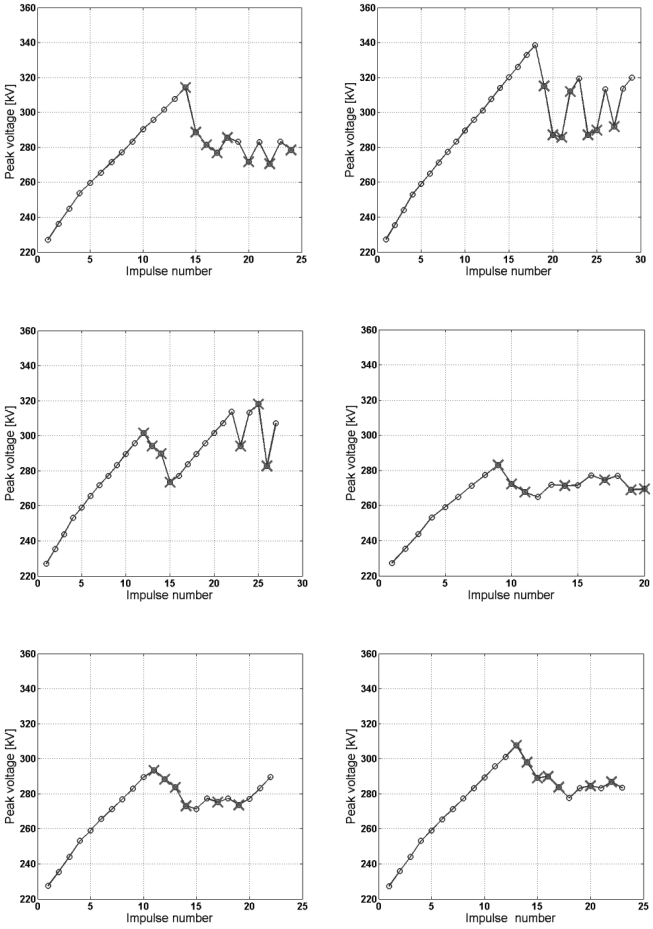

Figure A.4: FP-I coated – Top left: series 1, batch 2, electrode 1, Top right: series 1, batch 2, electrode 2, Middle left: series 1, batch 2, electrode 3, Middle right: series 1, batch 2, electrode 4, Bottom left: series 1, batch 2, electrode 5, Bottom right: series 1, batch 2, electrode 6

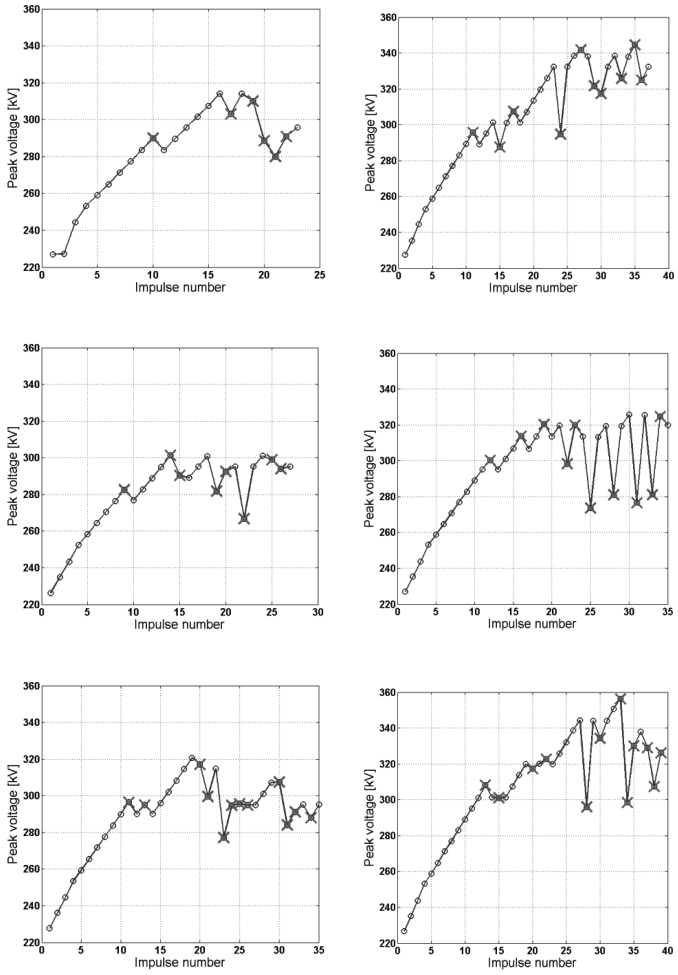

Figure A.5: FP-II coated - Top left: series 1, batch 2, electrode 7, Top right: series 1, batch 2, electrode 8, Middle left: series 1, batch 2, electrode 9, Middle right: series 1, batch 2, electrode 10, Bottom left: series 1, batch 2, electrode 11, Bottom right: series 1, batch 2, electrode 12

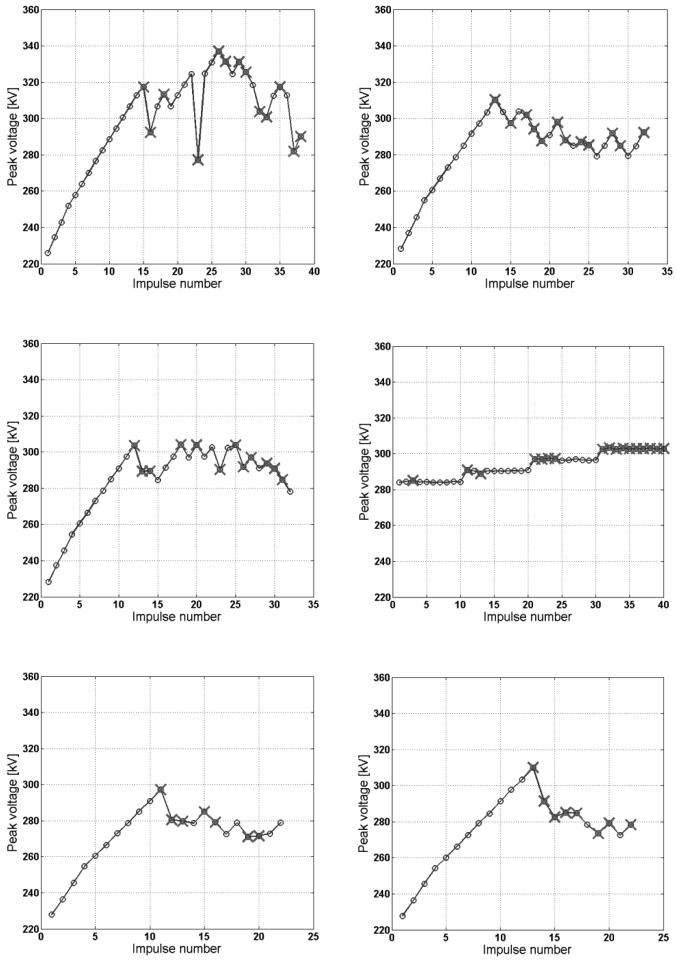

Figure A.6: Tests with 6 minutes waiting time – Top left: series 1, batch 3, electrode 1 (bare), Top right: series 1, batch 3, electrode 2 (bare), Middle left: series 1, batch 3, electrode 3 (bare), Middle right: series 1, batch 3, electrode 3 (bare, multiple level test), Bottom left: series 1, batch 3, electrode 4 (FP-I), Bottom right: series 1, batch 3, electrode 5 (FP-I)

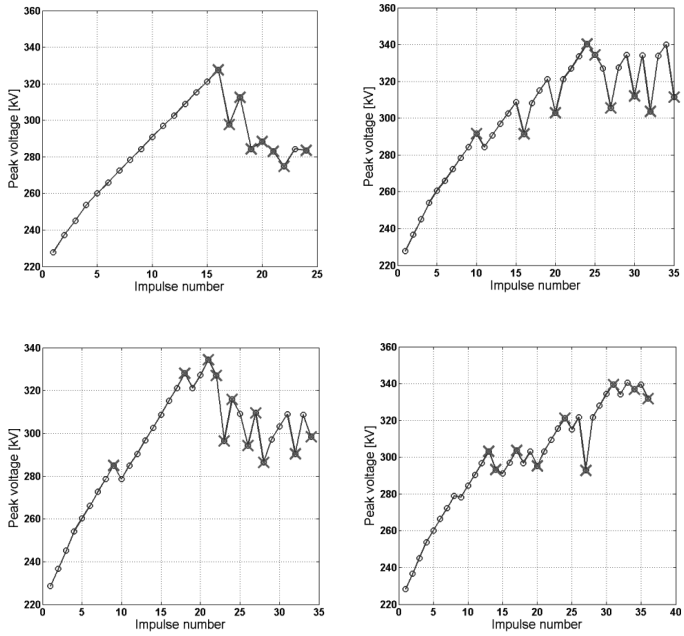

Figure A.7: Tests with 6 minutes waiting time – Top left: series 1, batch 3, electrode 6 (FP-I), Top right: series 1, batch 3, electrode 7 (FP-II), Bottom left: series 1, batch 3, electrode 8 (FP-II), Bottom right: series 1, batch 3, electrode 9 (FP-II)

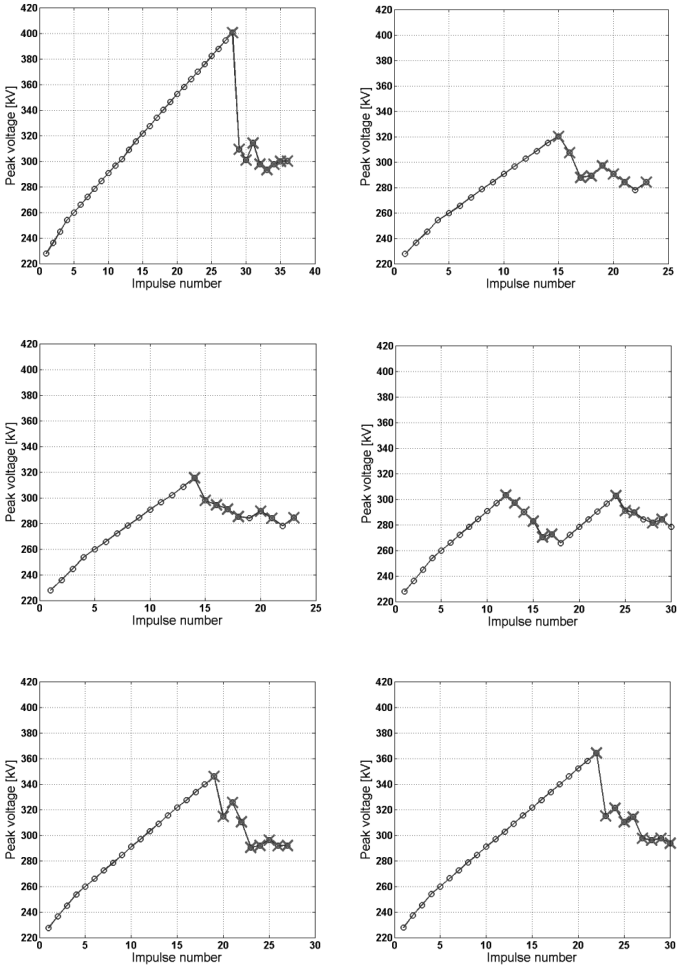

Figure A.8: PA11 - Top left: series 1, batch 4, electrode 1, Top right: series 1, batch 4, electrode 2, Middle left: series 1, batch 4, electrode 3, Middle right: series 1, batch 4, electrode 4, Bottom left: series 1, batch 4, electrode 5, Bottom right: series 1, batch 4, electrode 6

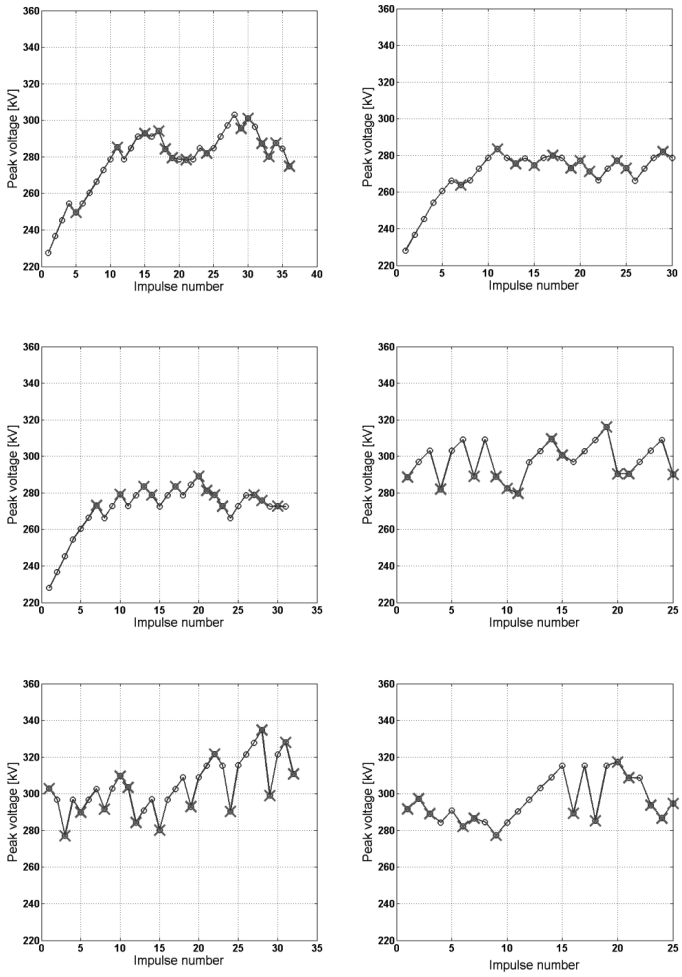

Figure A.9: FP-II extra tests - Top left: series 1, batch 5, electrode 1 (used electrode), Top right: series 1, batch 5, electrode 2 (used electrode), Middle left: series 1, batch 5, electrode 3 (used electrode), Middle right: series 1, batch 5, electrode 4 (new, 50% up-down), Bottom left: series 1, batch 5, electrode 5 (new, 50% up-down), Bottom right: series 1, batch 5, electrode 6 (new, 50% up-down)

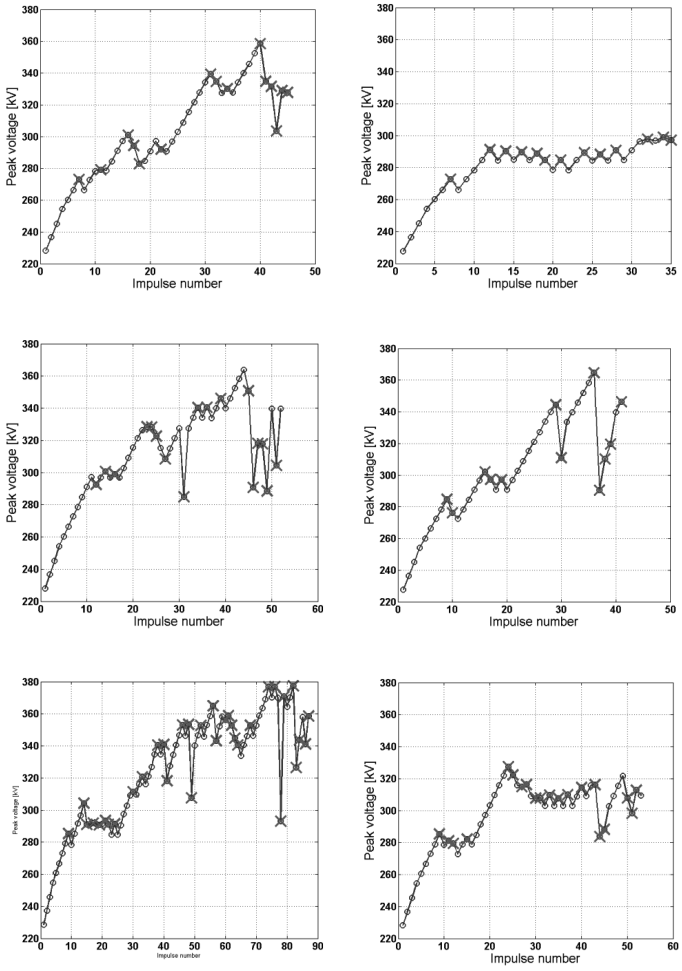

Figure A.10: FP-IV - Top left: series 1, batch 5, electrode 7, Top right: series 1, batch 5, electrode 8, Middle left: series 1, batch 5, electrode 9, Middle right: series 1, batch 5, electrode 10, Bottom left: series 1, batch 5, electrode 11, Bottom right: series 1, batch 5, electrode 12

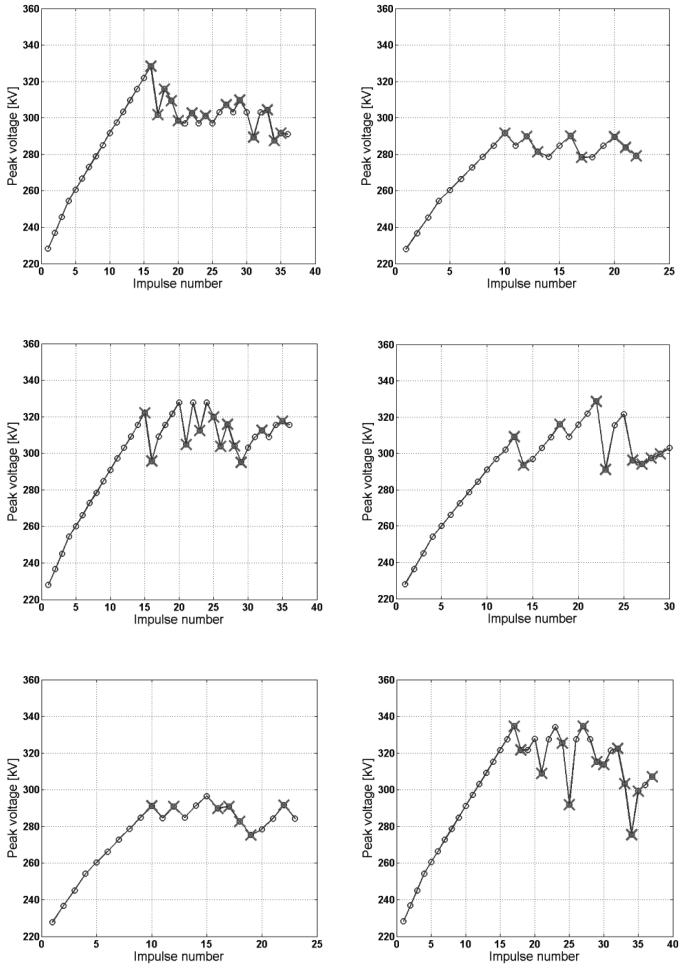

Figure A.11: FP-III - Top left: series 1, batch 6, electrode 1, Top right: series 1, batch 6, electrode 2, Middle left: series 1, batch 6, electrode 3, Middle right: series 1, batch 6, electrode 4, Bottom left: series 1, batch 6, electrode 5, Bottom right: series 1, batch 6, electrode 6

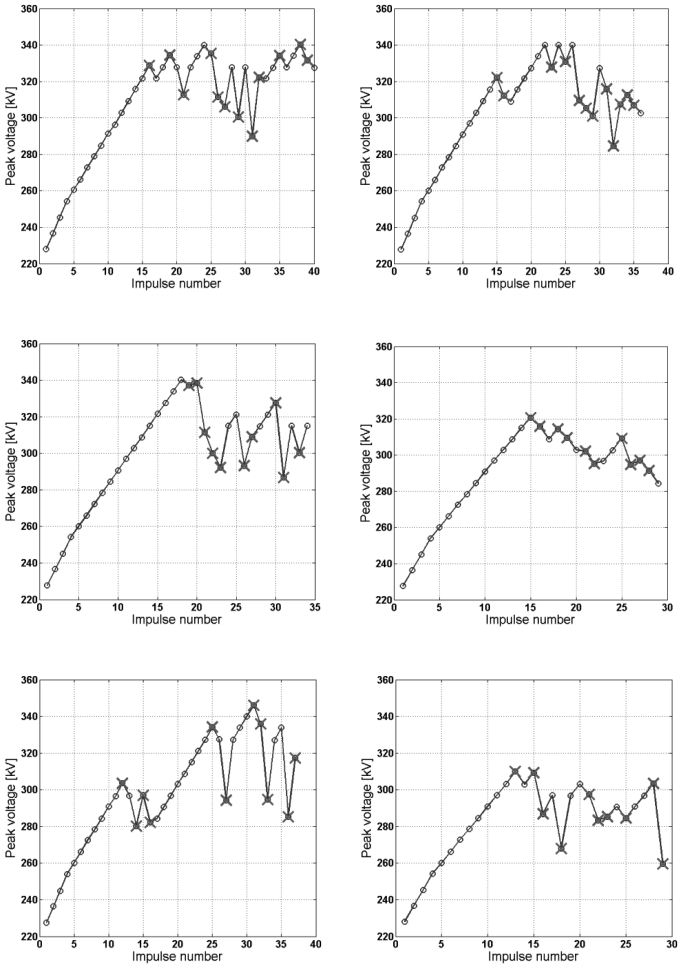

Figure A.12: Semiconductor A - Top left: series 1, batch 6, electrode 7, Top right: series 1, batch 6, electrode 8, Middle left: series 1, batch 6, electrode 9, Middle right: series 1, batch 6, electrode 10, Bottom left: series 1, batch 6, electrode 11, Bottom right: series 1, batch 6, electrode 12

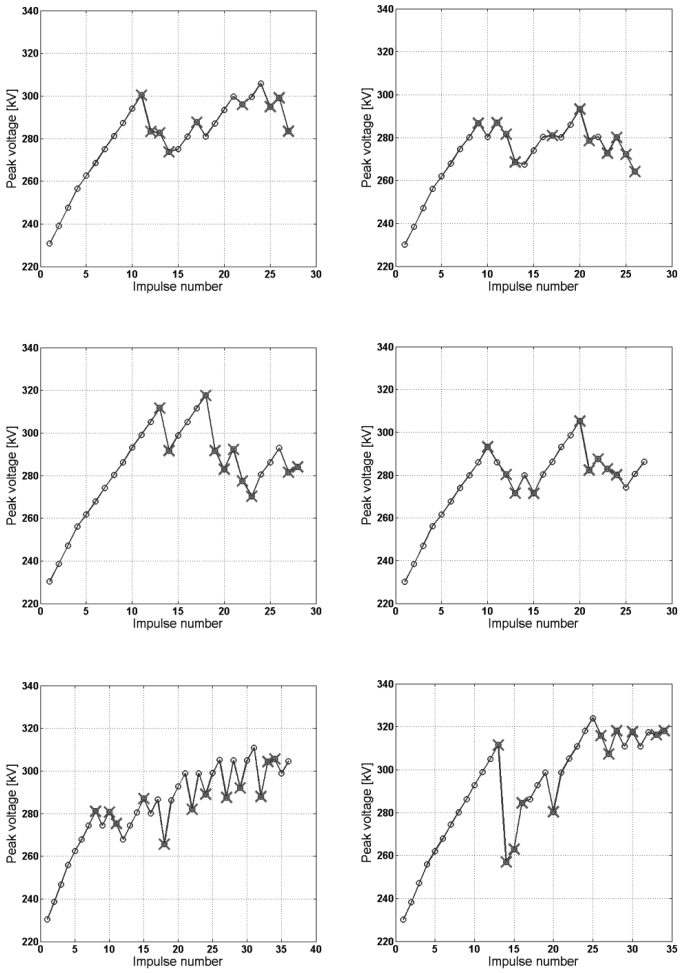

Figure A.13: FP-II – FP-I - Top left: series 3, batch 1, electrode 1, Top right: series 3, batch 1, electrode 2, Middle left: series 3, batch 1, electrode 3, Middle right: series 3, batch 1, electrode 4, Bottom left: series 3, batch 1, electrode 5, Bottom right: series 3, batch 1, electrode 6

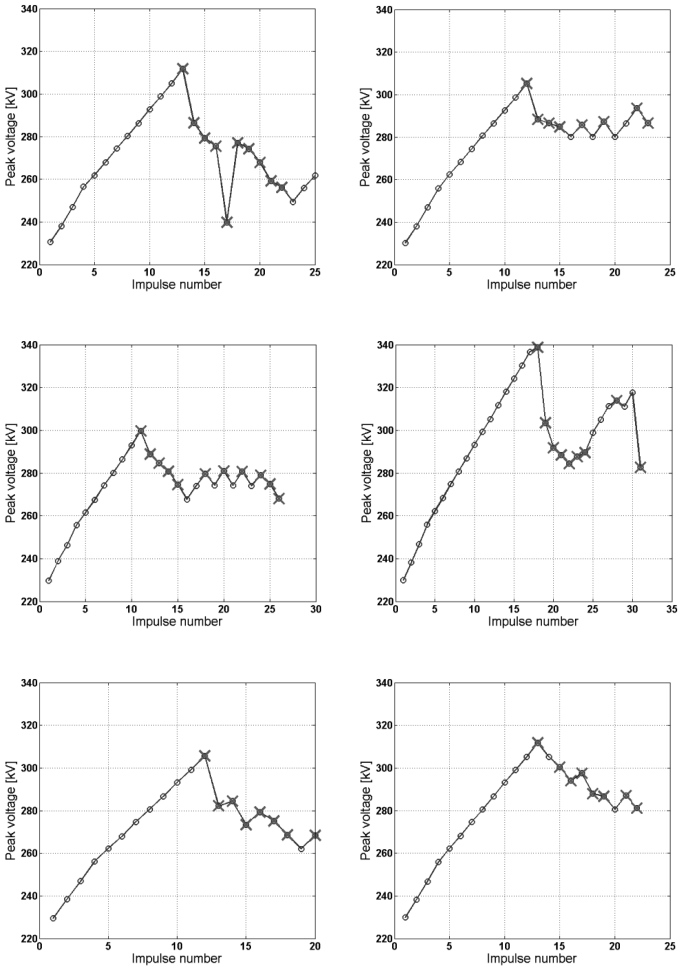

Figure A.14: FP-II – PA11 - Top left: series 3, batch 1, electrode 7, Top right: series 3, batch 1, electrode 8, Middle left: series 3, batch 1, electrode 9, Middle right: series 3, batch 1, electrode 10, Bottom left: series 3, batch 1, electrode 11, Bottom right: series 3, batch 1, electrode 12

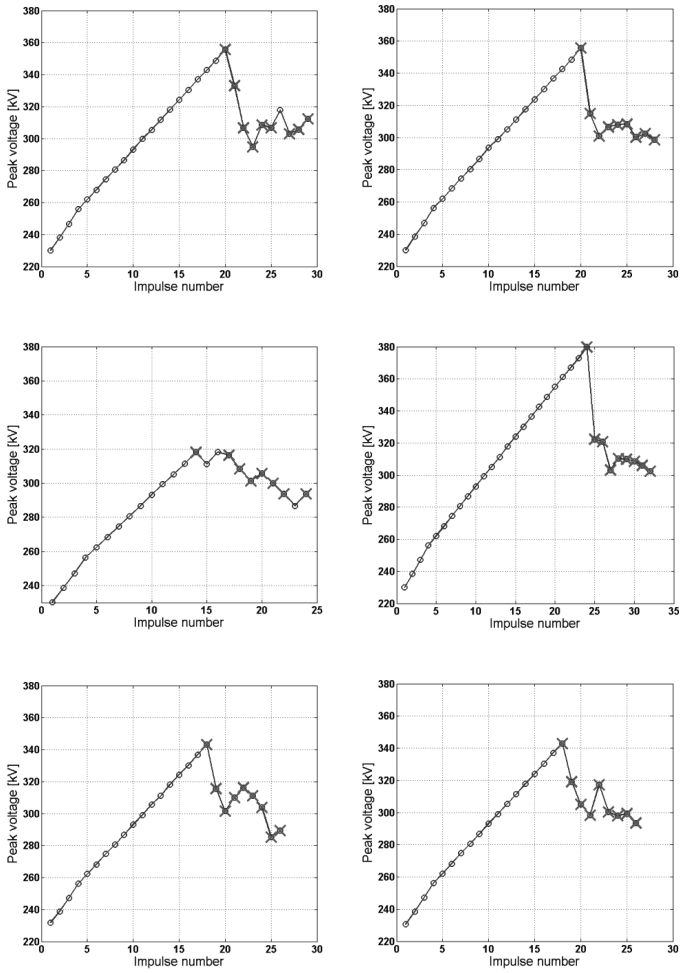

Figure A.15: PA11 - Top left: series 3, batch 2, electrode 1, Top right: series 3, batch 2, electrode 2, Middle left: series 3, batch 2, electrode 3, Middle right: series 3, batch 2, electrode 4, Bottom left: series 3, batch 2, electrode 5, Bottom right: series 3, batch 2, electrode 6

A.2

Series 2 and 4 – small size electrodes with thick coatings

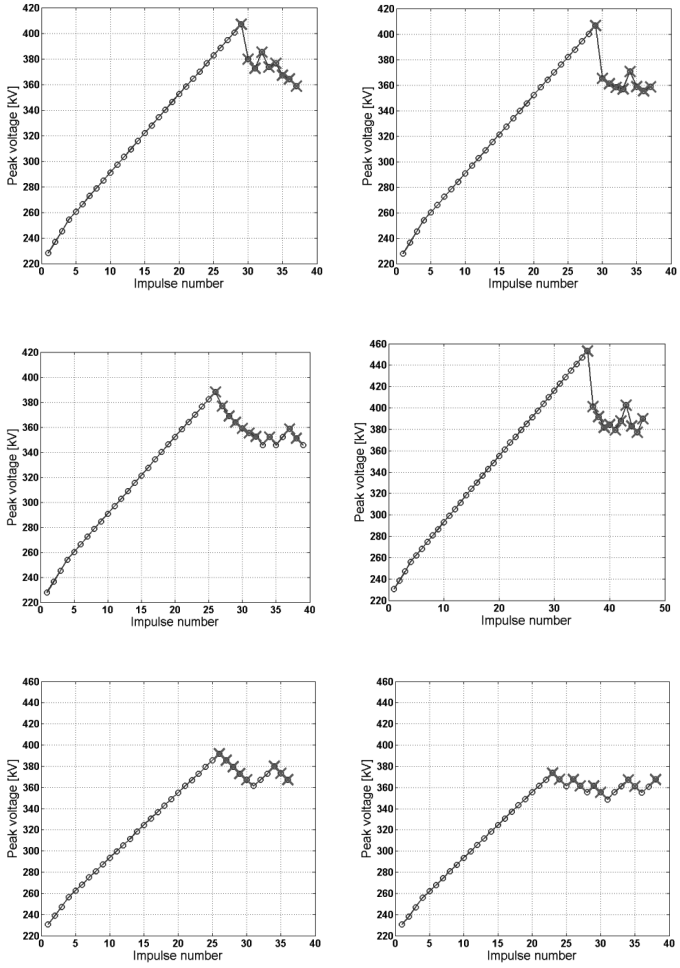

Figure A.16: Thick epoxy - Top left: series 2, batch 1, electrode 1, Top right: series 2, batch 1, electrode 2, Middle left: series 2, batch 1, electrode 3, Middle right: series 2, batch 5, electrode 1, Bottom left: series 2, batch 5, electrode 2, Bottom right: series 2, batch 5, electrode 3

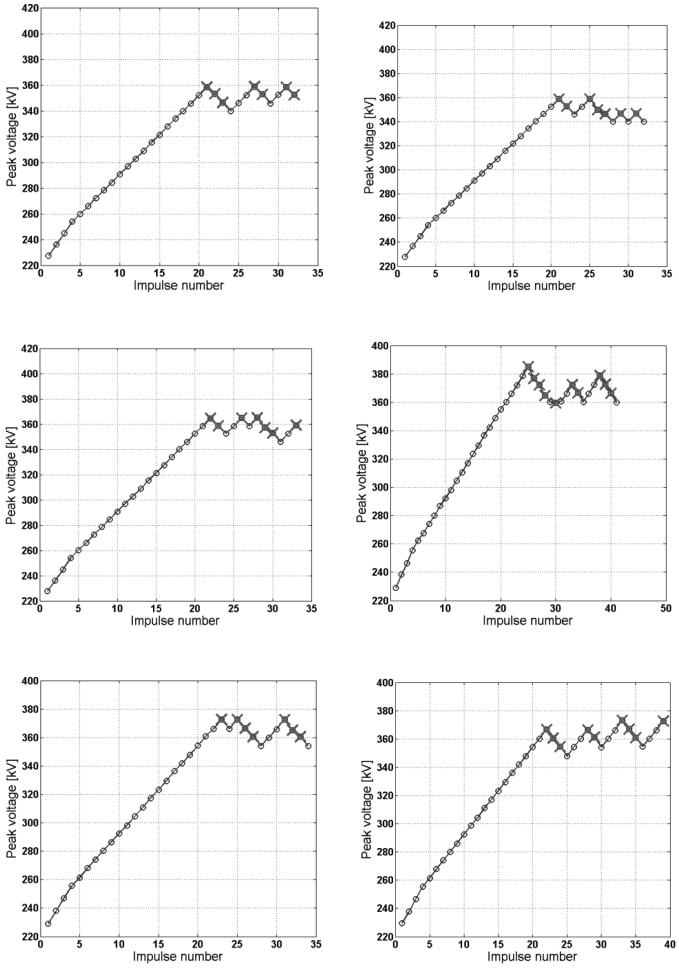

Figure A.17: Thick epoxy retests - Top left: series 2, batch 2, electrode 1, Top right: series 2, batch 2, electrode 2, Middle left: series 2, batch 2, electrode 3, Middle right: series 2, batch 6, electrode 1, Bottom left: series 2, batch 6, electrode 2, Bottom right: series 2, batch 6, electrode 3

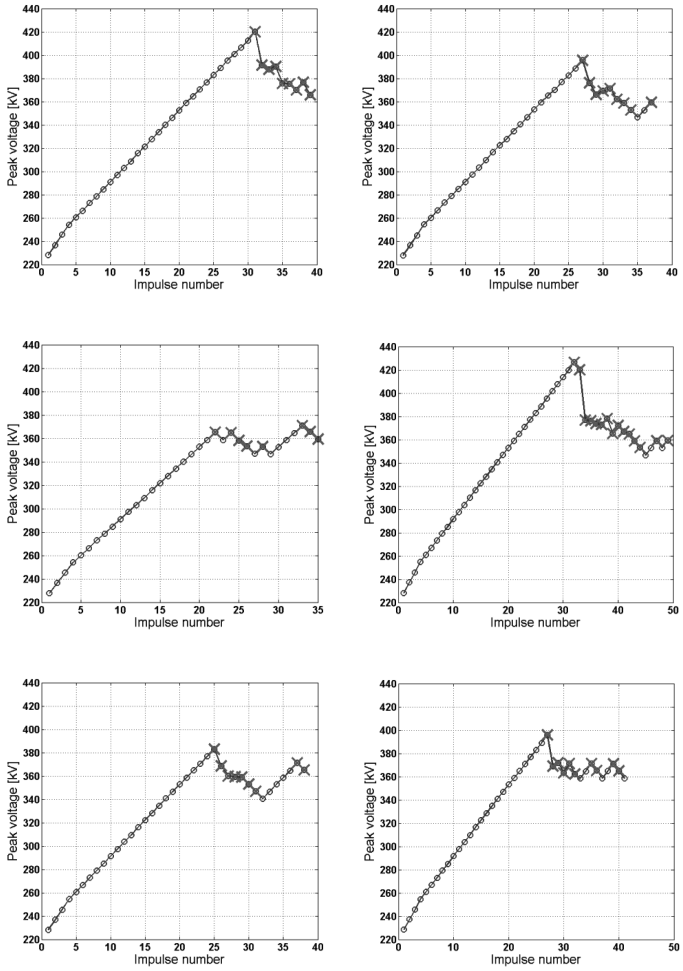

Figure A.18: Nanocomposite A - Top left: series 2, batch 3, electrode 1, Top right: series 2, batch 3, electrode 2, Middle left: series 2, batch 3, electrode 3, Middle right: series 2, batch 7, electrode 1, Bottom left: series 2, batch 7, electrode 2, Bottom right: series 2, batch 7, electrode 3

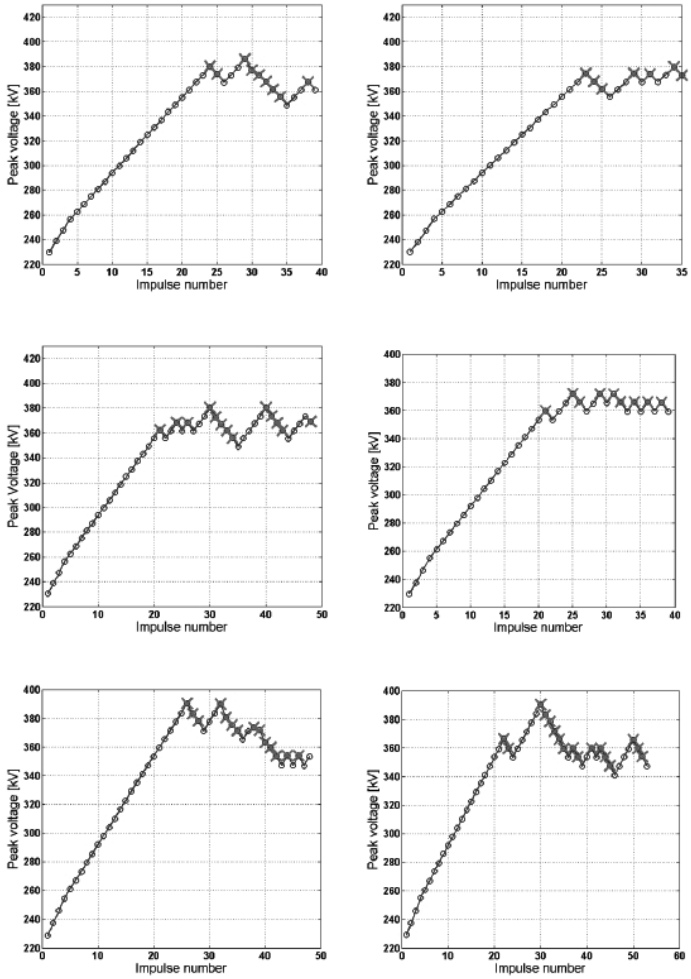

Figure A.19: Nanocomposite A retests - Top left: series 2, batch 4, electrode 1, Top right: series 2, batch 4, electrode 2, Middle left: series 2, batch 4, electrode 3, Middle right: series 2, batch 8, electrode 1, Bottom left: series 2, batch 8, electrode 2, Bottom right: series 2, batch 8, electrode 3

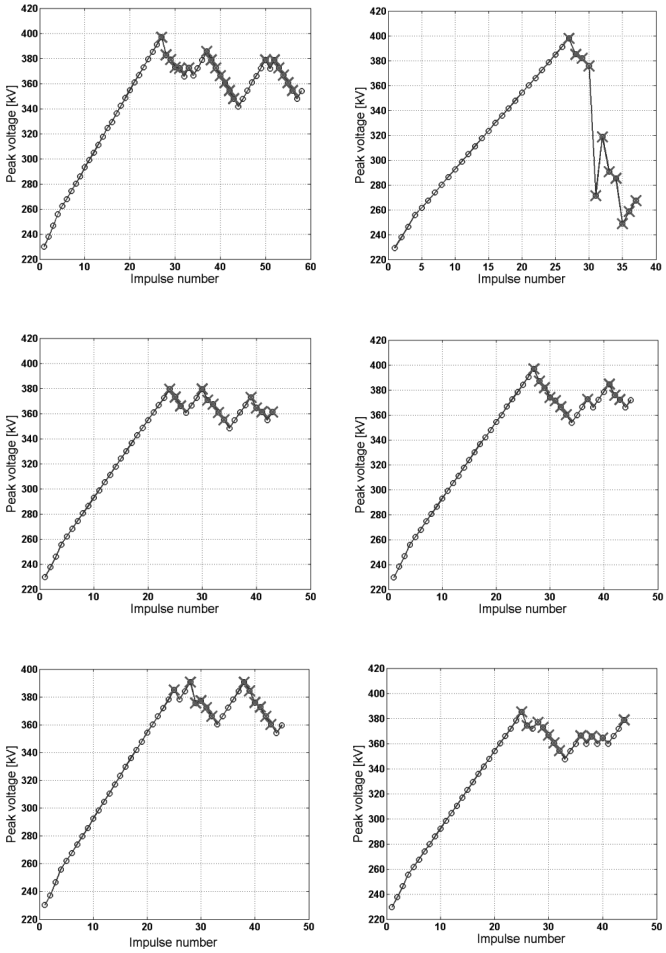

Figure A.20: Nanocomposite B - Top left: series 4, batch 1, electrode 1, Top right: series 4, batch 1, electrode 2, Middle left: series 4, batch 1, electrode 3, Middle right: series 4, batch 1, electrode 4, Bottom left: series 4, batch 1, electrode 5, Bottom right: series 4, batch 1, electrode 6

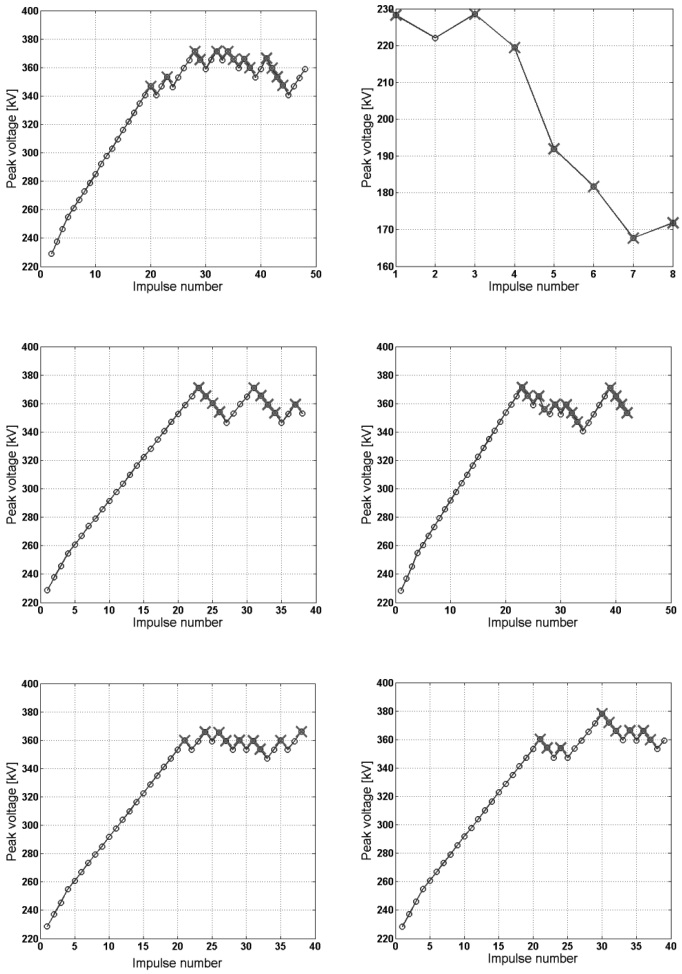

Figure A.21: Nanocomposite B retests - Top left: series 4, batch 2, electrode 1, Top right: series 4, batch 2, electrode 2, Middle left: series 4, batch 2, electrode 3, Middle right: series 4, batch 2, electrode 4, Bottom left: series 4, batch 2, electrode 5, Bottom right: series 4, batch 2, electrode 6

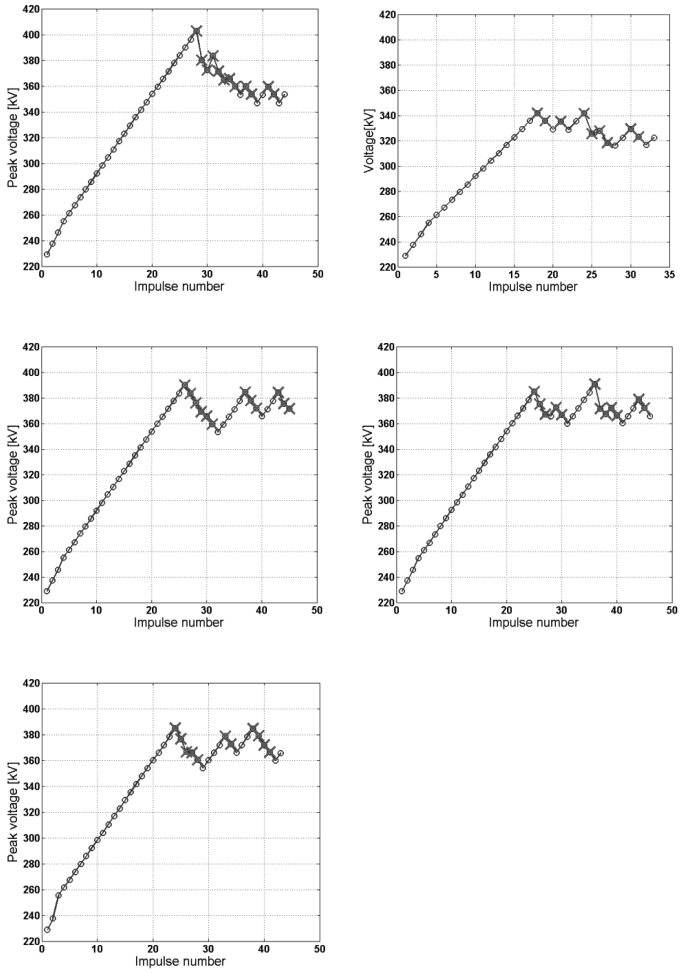

Figure A.22: Nanocomposite C - Top left: series 4, batch 1, electrode 7, Top right: series 4, batch 1, electrode 8, Middle left: series 4, batch 1, electrode 10, Middle right: series 4, batch 1, electrode 11, Bottom left: series 4, batch 1, electrode 12

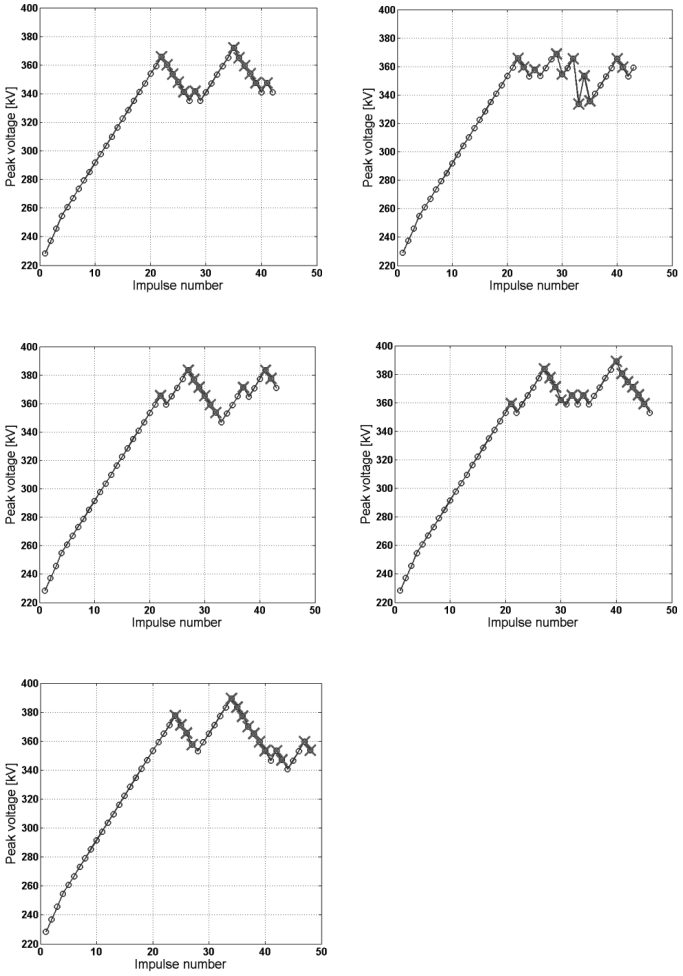

Figure A.23: Nanocomposite C retests - Top left: series 4, batch 2, electrode 7, Top right: series 4, batch 2, electrode 8, Middle left: series 4, batch 2, electrode 10, Middle right: series 4, batch 2, electrode 11, Bottom left: series 4, batch 2, electrode 12

A.3

Series 5 – Medium and large size electrodes with PA11 and thick epoxy coatings

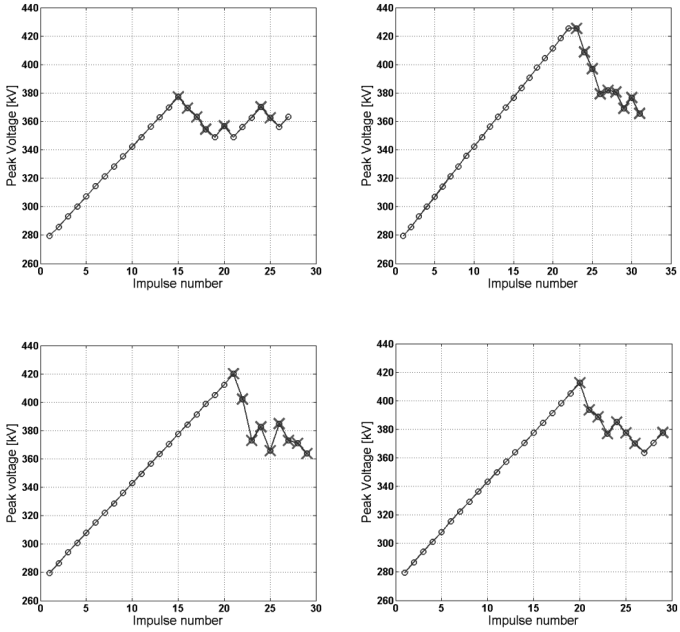

Figure A.24: Medium size PA11 – Top left: series 5, batch 1, electrode 1, Top right: series 5, batch 1, electrode 2, Bottom left: series 5, batch 1, electrode 3, Bottom right: series 5, batch 1, electrode 4

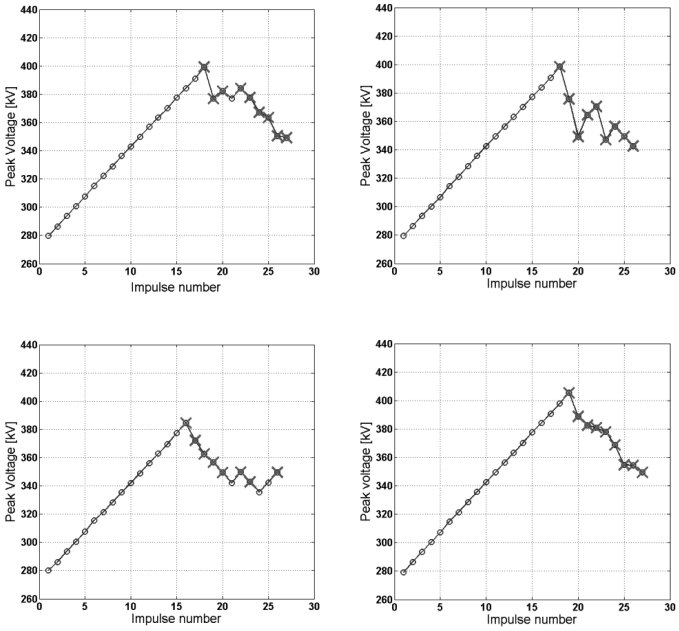

Figure A.25: Medium size PA11 – Top left: series 5, batch 2, electrode 1, Top right: series 5, batch 2, electrode 2, Bottom left: series 5, batch 2, electrode 3, Bottom right: series 5, batch 2, electrode 4

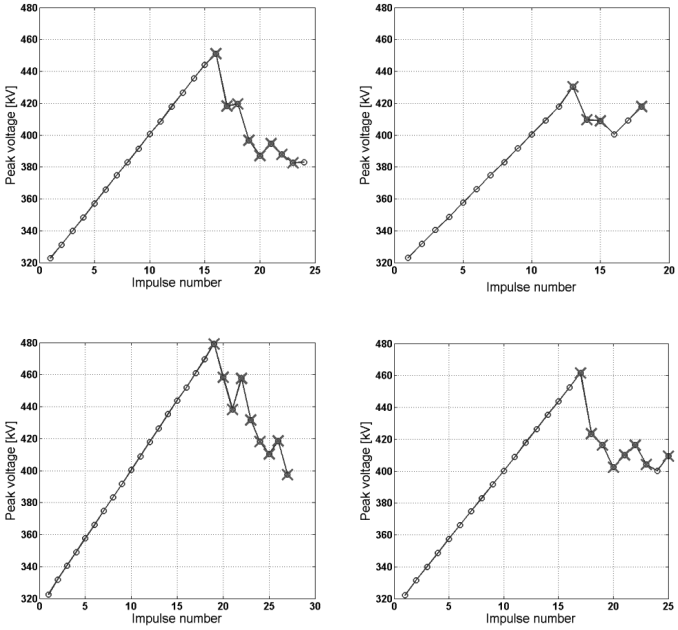

Figure A.26: Large size PA11 – Top left: series 5, batch 3, electrode 1, Top right: series 5, batch 3, electrode 2, Bottom left: series 5, batch 3, electrode 3, Bottom right: series 5, batch 3, electrode 4

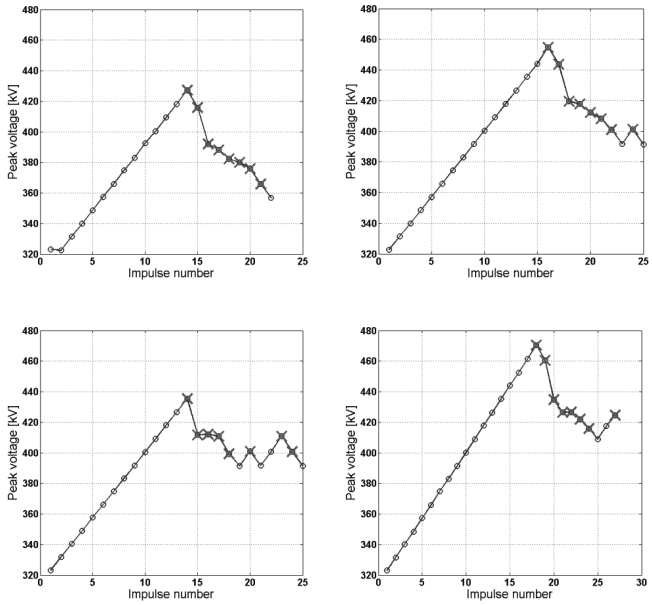

Figure A.27: Large size PA11 – Top left: series 5, batch 4, electrode 1, Top right: series 5, batch 4, electrode 2, Bottom left: series 5, batch 4, electrode 3, Bottom right: series 5, batch 4, electrode 4

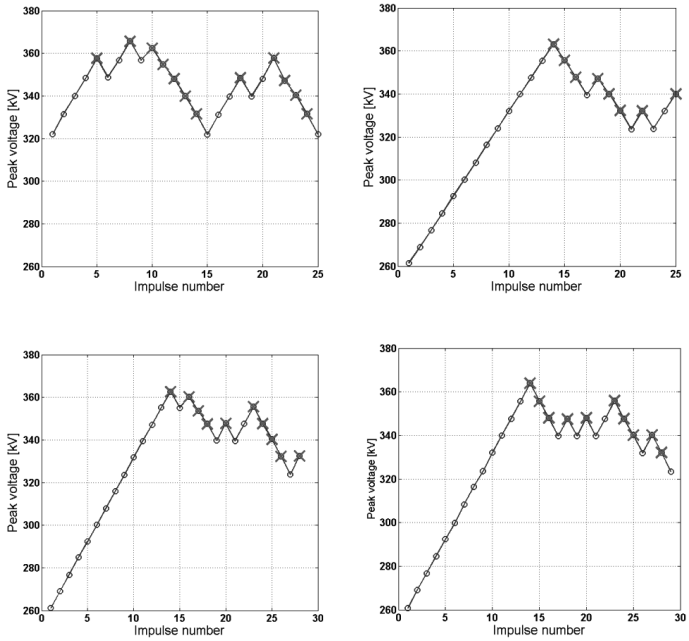

Figure A.28: Large size thick epoxy – Top left: series 5, batch 5, electrode 1, Top right: series 5, batch 5, electrode 2, Bottom left: series 5, batch 5, electrode 3, Bottom right: series 5, batch 5, electrode 4

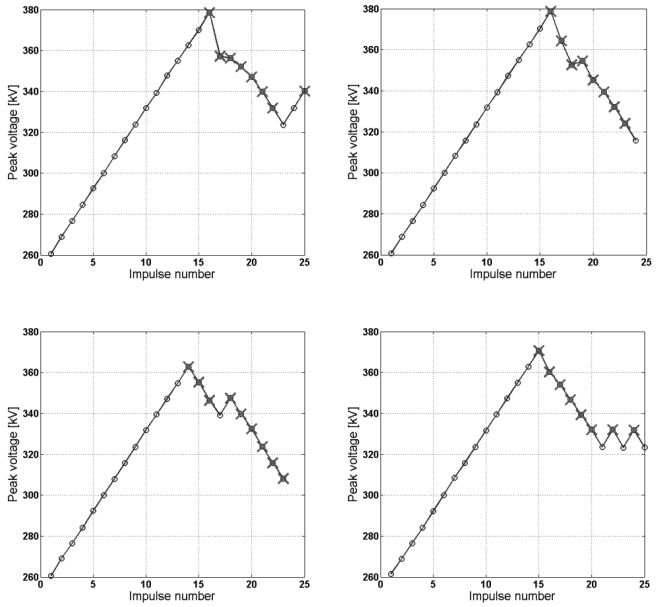

Figure A.29: Large size thick epoxy – Top left: series 5, batch 6, electrode 1, Top right: series 5, batch 6, electrode 2, Bottom left: series 5, batch 6, electrode 3, Bottom right: series 5, batch 6, electrode 4

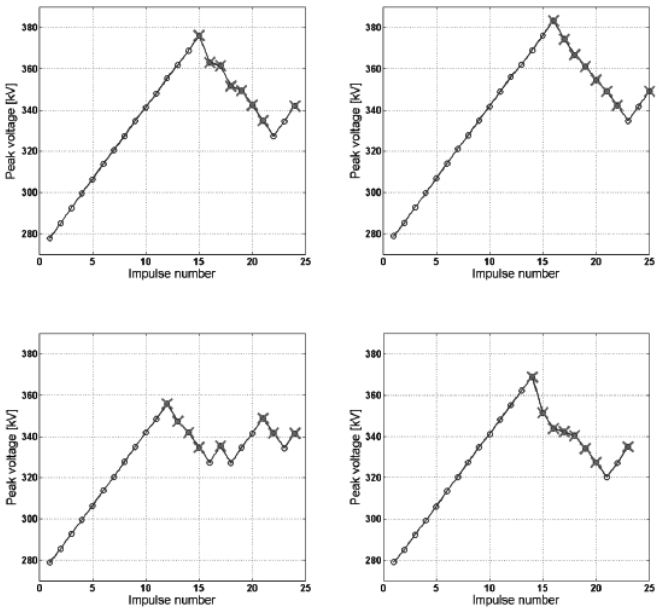

Figure A.30: Medium size thick epoxy – Top left: series 5, batch 7, electrode 1, Top right: series 5, batch 7, electrode 2, Bottom left: series 5, batch 7, electrode 3, Bottom right: series 5, batch 7, electrode 4

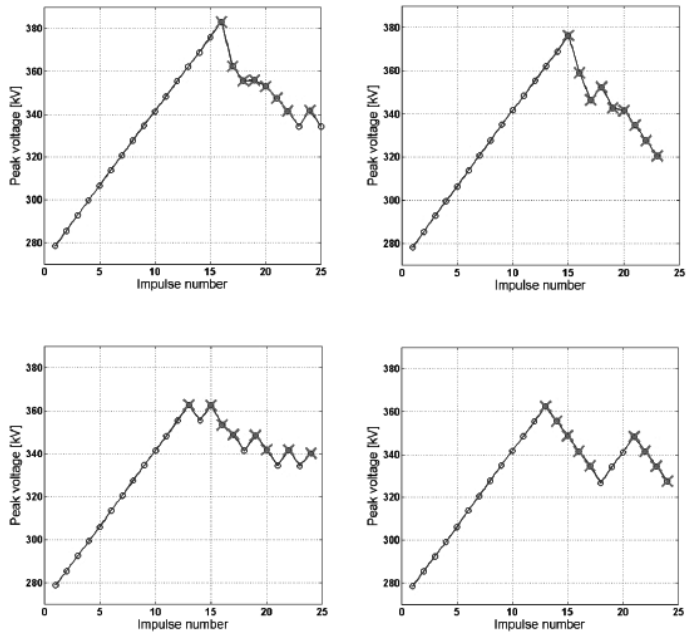

Figure A.31: Medium size thick epoxy – Top left: series 5, batch 8, electrode 1, Top right: series 5, batch 8, electrode 2, Bottom left: series 5, batch 8, electrode 3, Bottom right: series 5, batch 8, electrode 4

Bibliography

[1] P. Forster, V. Ramaswamy, P. Artaxo, T. Berntsen, R. Betts, D. W. Fahey, J. Haywood, J. Lean, D. C. Lowe, G. Myhre, J. Nganga, R. Prinn, G. Raga, M. Schulz, and R. V Dorland, "Changes in Atmospheric Constituents and in Radiative Forcing in: Climate Change 2007: The Physical Science Basis.," in ***Contribution of Working Group I to the Fourth Assessment Report of the Intergovernmental Panel on Climate Change***, 2008.

[2] Y. Kieffel, F. Biquez, and P. Ponchon, "Alternative gas to sf 6 for use in high voltage switchgears: g3," in ***Cired, 23rd International conference on electricity distribution***, 2015, pp. 15–18.

[3] M. Hyrenbach, T. Hintzen, P. Müller, and J. Owens, "Alternative gas insulation in medium-voltage switchgear," in ***Cired, 23rd International conference on electricity distribution***, 2015, pp. 15–18.

[4] G. Baldo and G. Pesavento, "Impulse Performance of Air Gaps in Series with Thick Insulating Layers," in ***5th International Symposium on High Voltage Engineering, Braunschweig, Germany***, 1987.

[5] A. T. de Wit, "The application of dielectric coatings in gas insulated switchgear," master thesis, TU Delft, 2010.

[6] H. Hama, K. Inami, T. Ootsuka, Y. Shimizu, E. Nagao, K. Oosumi, and M. Yoshimura, "Improvement of SF6 gas insulated system by applying thick dielectric-layered electrode and its application to high voltage equipment," in ***Gaseous Dielectrics X***, 2004, pp. 319–328.

[7] H. Hama and S. Okabe, "Cross-sectional Study between SF6 and Eco-friendly Gases on Dielectric Coated Electrodes for Real-size Gas Insulated Switchgear," ***IEEE Trans. Dielectr. Electr. Insul.***, vol. 19, no. 1, pp. 253–262, 2012.

[8] M. Hikita, S. Ohtsuka, N. Yokoyama, S. Okabe, and S. Kaneko, "Effect of Electrode Surface Roughness and Dielectric Coating on Breakdown Characteristics of High Pressure CO2 and N2 in a Quasi-Uniform Electric Field," ***IEEE Trans. Dielectr. Electr. Insul.***, vol. 15, no. 1, pp. 243–250, 2008.

[9] C. Lederle and J. Kindersberger, "The influence of surface roughness and dielectric coating on AC and DC Breakdown Voltage in SF6," in ***Proceedings of the XIVth International Symposium on High Voltage Engineering, Tsinghua University, Beijing, China***, 2005, vol. I-02.

[10] C. Lederle and J. Kindersberger, "The influence of surface roughness and coating on the Impulse Breakdown Voltage in SF6," in ***2004 Annual Report Conference on Electrical Insulation and Dielectric Phenomena***, 2004, pp. 522–525.

[11] C. Lederle, J. Kindersberger, and E. Kynast, "Influence of surface state and thin dielectric coating on the insulation properties of a coaxial electrode arrangement in SF6," in ***XVth International***

Symposium on High Voltage Engineering, University of Ljubljana, Elektroinstitut Milan Vidmar, Ljubljana, Slovenia, 2007, vol. T9-342.

[12] J. Marold, J. Kindersberger, and U. Krüsi, "Impulse voltage breakdown properties of electrodes with thick dielectric coatings in SF6," in ***XVth International Symposium on High Voltage Engineering, University of Ljubljana, Elektroinstitut Milan Vidmar, Ljubljana, Slovenia***, 2007, vol. T9-75.

[13] M. M. Morcos, S. Zhang, M. Holmberg, and K. D. Srivastava, "On the use of dielectric coatings in particle-contaminated gas insulated switchgear," in ***7th International Conference on Solid Dielectrics, Eindhoven, The Netherlands***, 2001, pp. 54–57.

[14] M. M. Morcos, S. Zhang, K. D. Srivastava, and S. M. Gubanski, "Dynamics of Metallic Particle Contaminants in GIS with Dielectric-Coated Electrodes," ***IEEE Trans. Power Deliv.***, vol. 15, no. 2, pp. 455–460, 2000.

[15] J. D. Morgan and M. Abdellah, "Impulse breakdown of covered cylinders in SF6 and SF6-gas mixtures," ***IEEE Trans. Electr. Insul.***, vol. 23, no. 3, pp. 467–473, 1988.

[16] Y. J. Park and K. J. Lim, "Impulse Breakdown Characteristics of Dry-Air under Quasi-Uniform Field at the Coated Electrode System," in ***Proceedings of the 18th International Symposium on High Voltage Engineering, Seoul, South Korea***, 2013, pp. 1728–1731.

[17] T. Rokunohe, T. Kato, M. Hirose, and T. Ishiguro, "Development of Insulation Technology in Compact SF6 Gas-Filled Bushings: Development of Compact 800-kV SF6 Gas-Filled Bushings," ***Electr. Eng. Japan***, vol. 171, no. 1, pp. 19–27, 2010.

[18] T. Rokunohe, Y. Yagihashi, K. Aoyagi, T. Oomori, and F. Endo, "Development of SF6-Free 72.5 kV GIS," ***IEEE Trans. Power Deliv.***, vol. 22, no. 3, pp. 1869–1876, 2007.

[19] T. Rokunohe, Y. Yagihashi, F. Endo, and T. Oomori, "Fundamental Insulation Characteristics of Air, N2, CO2, N2/O2 and SF6/N2 Mixed Gases," ***Electr. Eng. Japan***, vol. 155, no. 3, pp. 9–16, 2006.

[20] J. Y. Sim, J. H. Kwon, Y. J. Park, and K. J. Lim, "Impulse Breakdown Characteristics of the Air in Rod-Plane Electrode System with Covered Rod as Silicone Rubber," in ***Proceedings of the 18th International Symposium on High Voltage Engineering, Seoul, South Korea***, 2013, pp. 1545–1548.

[21] S.-Y. Woo, K.-R. Kwon, K.-B. Seo, and J.-H. Kim, "Effect of Dielectric Coating on Breakdown Characteristics in Switchgear," in ***Proceedings of the 18th International Symposium on High Voltage Engineering, Seoul, South Korea***, 2013, pp. 1371–1374.

[22] T. Yasuoka, M. Sato, Y. Hoshina, A. Shimamura, and M. Shiiki, "Improvement of Gaseous Insulation Performance by Gas/Solid Composite Insulation in High-Pressure CO2," in ***Proceedings of the 18th International Symposium on High Voltage Engineering, Seoul, South Korea***, 2013, pp. 1387–1391.

[23] T. Yoshida, M. Miyagawa, I. Ohshima, N. Masaki, and S. Yanabu, "Increase of Breakdown Voltage Due to Composite Insulation in SF6 Gas," ***Electr. Eng. Japan***, vol. 111, no. 6, pp. 36–45, 1991.

[24] J. H. M. Blennow, "Active High Voltage Insulation," phdthesis, Chalmers University of Technology, 2000.

[25] H. J. M. Blennow, M. L.-Å. Sjöberg, M. Å. S. Leijon, and S. M. Gubanski, "Electric Field Reduction Due to Charge Accumulation in a Dielectric-Covered Electrode System," ***IEEE Trans. Dielectr. Electr. Insul.***, vol. 7, no. 3, pp. 340–345, 2000.

[26] F. Mauseth, "Charge accumulation in rod-plane air gap with covered rod," PhD thesis, Norwegian University of Science and Technology NTNU, 2006.

[27] S. Kainaga, T. Miyamoto, M. Yoshimura, and T. Tsurimoto, "Characteristics of Charge Accumulation on Coated Electrode in SF 6 Gas," in ***15th International Conference on Electrical Machines and Systems***, 2012.

[28] R. J. Allen and K. H. Schoenbach, "Increased Hold-Off Voltage in Vacuum Gaps with Coated Electrodes," in ***1996 IEEE Annual Report - Conference on Electrical Insulation and Dielectric Phenomena, San Fransisco***, 1996.

[29] L. Jedynak, "Vacuum Insulation of High Voltages Utilizing Dielectric Coated Electrodes," ***J. Appl. Phys.***, vol. 35, no. 6, pp. 1272–1733, 1964.

[30] G. V. N. Kumar, J. Amarnath, and B. P. Singh, "Behavior of Metallic Particles in a Single Phase Gas Insulated System with Dielectric Coated Electrodes," in ***2008 International Conference on Condition Monitoring and Diagnosis, Beijing, China***, 2008.

[31] J. Y. Kim, Y. M. Kim, B. Y. Seok, J. H. Kwon, and K. J. Lim, "A Study on the Lightning Impulse Breakdown Characteristics of Dry Air for Design of Eco-Friendly Electric Power Apparatus," in ***Proceedings of the 18th International Symposium on High Voltage Engineering, Seoul, South Korea***, 2013, pp. 1392–1396.

[32] A. Kumada, S. Matsuoka, S. Yokoyama, K. Hidaka, N. Inoue, T. Donen, and M. Tsukima, "Calculation Model of Sparkover Voltage with Covered Electrode System in Dry Air," in ***Proceedings of the 18th International Symposium on High Voltage Engineering, Seoul, South Korea***, 2013, pp. 1403–1408.

[33] L. Ming, M. Leijon, and T. Bengtsson, "Factors Influencing Barrier Effects in Air-gaps," in ***9th International Symposium on High Voltage Engineering (ISH), Graz Convention Centre, Graz, Austria***, 1995, no. 2168.

[34] K. Jhure and E. Kynast, "High Pressure N2, N2/CO2 and CO2 Gas Insulation in Comparison to SF6 in GIS Applications," in ***Proceedings of the XIVth International Symposium on High Voltage Engineering, Beijing, China***, 2005.

[35] Y. Hoshina, M. Sato, M. Shiiki, M. Hanai, and E. Kaneko, "Lightning impulse breakdown characteristics of SF6 alternative gases for gas-insulated switchgear," ***Sci. Meas. Technol. IEE Proc.***, vol. 153, no. 1, pp. 1–6, 2006.

[36] F. H. Kreuger, ***Industrial High DC Voltage***. Delft University Press, 1995.

[37] R. H. Fowler and L. W. Nordheim, "The effect of the image force on the emission and reflexion of electrons by metals," ***Proc. R. Soc. London A***, vol. 121, pp. 626–639, 1928.

[38] A. Pedersen, "The effect of surface roughness on breakdown in SF6," ***IEEE Trans. Power Appar. Syst.***, vol. PAS-94, no. 5, pp. 1749–1754, 1975.

[39] F. H. Kreuger, ***Industrial High Voltage, part 1, 2 and 3***. Delft University Press, 1991.

[40] JIS, "JIS B 0601 Geometrical Product Specifications (GPS) - Surface texture: Profile method - Terms, definitions and surface texture parameters." 1994.

[41] ISO, "ISO 4287 Geometrical Product Specifications (GPS) - Surface texture: Profile method - Terms, definitions and surface texture parameters." 1997.

[42] A. H. Cookson and O. Farish, "Particle-initiated Breakdown between Coaxial Electrodes in Compressed SF6," ***IEEE Trans. Power Appar. Syst.***, vol. PAS-92, no. 3, pp. 871–876, 1973.

[43] T. Hattori, M. Honda, H. Aoyagi, N. Kobayashi, and K. Terasaka, "A Study on Effects of Conducting Particles in SF6 Gas and Test Methods for GIS," ***IEEE Trans. Power Deliv.***, vol. 3, no. 1, pp. 197–204, 1988.

[44] F. Endo, T. Yamagiwa, T. Ishikawa, and M. Hosokawa, "Particle-Initiated Breakdown Characteristics and Reliability Improvement in SF6 Gas Insulation," ***IEEE Trans. Power Deliv.***, vol. PWRD-1, no. 1, pp. 58–65, 1986.

[45] K. D. Srivastava, M. H. E. Tan, A. Jaksts, and R. G. van Heeswijk, "Effect of Dielectric Coatings on Metallic Particle Movement in Compressed Sulfur Hexafluoride Gas," in ***Annual Report Conference on Electrical Insulation and Dielectric Phenomena***, 1977, pp. 448–455.

[46] S. Meijer, "Partial Discharge Diagnosis of High-Voltage Gas-Insulated Systems," Delft University of Technology, 2001.

[47] A. A. Azer and R. P. Comsa, "Influence of Field Nonuniformity on the Breakdown Characteristics of Suliur Hexafluoride," ***IEEE Trans. Electr. Insul.***, vol. 8, no. 4, pp. 136–142, 1973.

[48] I.-A. Tsekmes, "Analysis of the Mechanisms Determining the Thermal and Electrical Properties of Epoxy Nanocomposites for High Voltage Applications," Delft University of Technology, 2016.

[49] "International Electrotechnical Commission," "IEC 60060-1 High-voltage test techniques part 1: General definitions and test requirements." 2010.

[50] International Electrotechnical Commission, "IEC 60243-1 Electric strength of insulating materials - Test methods - Part 1: Tests at power frequencies." 2013.

[51] N. Wiegart, L. Niemeyer, F. Pinnekamp, W. Boeck, J. Kindersberger, R. Morrow, W. Zaengl, M. Zwicky, I. Gallimberti, and S. A. Boggs, "Inhomogeneous field breakdown in GIS - The prediction of breakdown probabilities and voltages - Part I: Overview of a theory for inhomogeneous field breakdown in SF6," ***IEEE Trans. Power Deliv.***, vol. 3, pp. 923–930, 1988.

[52] B. Alijagic-Jonuz, "Dielectric properties and space charge dynamics of polymeric high voltage DC insulating materials," Delft University of Technology, 2007.

[53] I. D. Maxwell and R. A. Pethrick, "Dielectric Studies of Water in Epoxy Resins.," ***J. Appl. Polym. Sci.***, vol. 28, no. 7, pp. 2363–2379, 1983.

[54] F. Kremer and A. Schönhals, ***Broadband Dielectric Spectroscopy***. Springer-Verlag, Berlin, 2003.

[55] R. M. Neagu, E. Neagu, N. Bonanos, and P. Pissis, "Electrical Conductivity Studies in Nylon 11," ***J. Appl. Phys.***, vol. 88, no. 11, pp. 6669–6677, Dec. 2000.

[56] R. M. Neagu, E. Neagu, A. Kyritsis, and P. Pissis, "Dielectric Studies of Dipolar Relaxation Processes in Nylon 11," ***J. Phys. D. Appl. Phys.***, vol. 33, pp. 1921–1931, 2000.

[57] T. Maeno, T. Futami, H. Kushibe, T. Takada, and C. M. Cooke, "Measurement of spatial charge distribution in thick dielectrics using the pulsed electroacoustic method.," ***IEEE Trans. Electr. Insul***., vol. 23, no. 3, pp. 433–439, 1988.

[58] Y. Li, M. Yasuda, and T. Takada, "Pulsed Electroacoustic Method For Measurement Of Charge Accumulation In Solid Dielectrics," ***IEEE Trans. Dielectr. Electr. Insul.***, vol. 1, no. 2, pp. 188–195, 1994.

[59] IEC, "IEC 62539 Guide for the statistical analysis of electrical insulation breakdown data," ***International Electrotechnical Commission***. 2007.

[60] D. Van Der Born, P. H. F. Morshuis, J. J. Smit, and A. Girodet, "The influence of thin dielectric coatings on LI and AC breakdown strength in SF6 and dry air," ***Proc. IEEE Int. Conf. Solid Dielectr. ICSD***, pp. 287–290, 2013.

[61] J. M. Meek and J. D. Craggs, ***Electrical Breakdown of Gases***. At the Clarendon Press Oxford, 1953.

[62] T. W. Dakin and D. Berg, "Theory of Gas Breakdown," ***Prog. Dielectr.***, vol. 4, pp. 153–198, 1962.

[63] W. Mosch and W. Hauschild, ***Hochspannungsisolierungen mit Schwefelhexafluorid***. Berlin: VEB Verlag Technik, 1979.

[64] A. Pedersen, I. W. McAllister, G. C. Crichton, and S. Vibholm, "Formulation of the streamer breakdown criterion and its application to strongly electronegative gases and gas mixtures," ***Arch. für Elektrotechnik***, vol. 67, pp. 395–402, 1984.

[65] A. Pedersen, "Criteria for spark breakdown in sulfur hexafluoride," ***IEEE Trans. Power Appar. Syst.***, vol. 89, no. 8, pp. 2043–2048, 1970.

[66] E. H. R. Gaxiola, "Dielectric Breakdown in Insulating Gases - Space Charge effects and Non-Uniform Fields," PhD thesis, Eindhoven University of Technology, 1999.

[67] M. Abdel-Salam, H. Anis, A. El-Morshedy, and R. Radwan, ***High Voltage Engineering: Theory and Practice***. New York: Marcel Dekker Inc., 2000.

[68] E. Kuffel, W. S. Zaengl, and J. Kuffel, ***High Voltage Engineering Fundamentals***. Butterworth-Heinemann, 2000.

[69] M. Beyer, W. Boeck, K. Möller, and W. Zaengl, ***Hochspannungstechnik, Theoretische und praktische Grundlagen für die Anwendung***. Springer-Verlag, Berlin, 1986.

[70] K. Petcharaks, "A Contribution to the Streamer Breakdown Criterion," in ***International Symposium on High Voltage Engineering***, 1999, no. 3, pp. 369–372.

[71] G. Eriksson, "Easy Evaluation of Streamer Discharge Criteria," in ***Proceedings of the 2012 COMSOL Conference in Milan***, 2012.

[72] N. Wiegart, L. Niemeyer, F. Pinnekamp, W. Boeck, J. Kindersberger, R. Morrow, W. Zaengl, M. Zwicky, I. Gallimberti, and S. A. Boggs, "Inhomogeneous field breakdown in GIS - The prediction of breakdown probabilities and voltages - Part III: Discharge development in SF6 and computer model of breakdown," ***IEEE Trans. Power Deliv.***, vol. 3, no. 3, pp. 939–946, 1988.

[73] N. Wiegart, L. Niemeyer, F. Pinnekamp, W. Boeck, J. Kindersberger, R. Morrow, W. Zaengl, M. Zwicky, I. Gallimberti, and S. A. Boggs, "Inhomogeneous field breakdown in GIS - The prediction of breakdown probabilities and voltages - Part II: Ion density and statistical time lag," ***IEEE Trans. Power Deliv.***, vol. 3, no. 3, pp. 931–938, 1988.

[74] F. A. M. Rizk and M. B. Eteiba, "Impulse Breakdown Voltage-Time Curves of SF6 and SF6 - N2 Coaxial-Cylinder Gaps," ***IEEE Trans. Power Appar. Syst.***, vol. 101, no. 12, pp. 4460–4471, 1982.

[75] P. Simka, "Dielectric Coordination of High Voltage Gas Circuit Breakers," PhD thesis, ETH Zürich, 2011.

List of Publications

1. **D. van der Born** and J.J. Smit, "Evaluation of breakdown test procedures for self-restoring insulation types", Submitted, International Symposium on High Voltage Engineering, Buenos Aires, Argentina, 2017
2. **D. van der Born**, P.H.F. Morshuis, J.J. Smit and A. Girodet, "Negative LI Breakdown Behavior of Electrodes with Thin Dielectric Coatings in Dry Air at High Pressure", IEEE Conference on Electrical Insulation and Dielectric Phenomena, pp. 82-85, Des Moines, Iowa 2014.
3. **D. van der Born**, I.A. Tsekmes, P.H.F. Morshuis, J.J. Smit and A. Girodet, "Influence of Thick Epoxy Nanocomposite Coatings on Lightning Impulse Breakdown Behavior in Air.", IEEE Conference on Electrical Insulation and Dielectric Phenomena, pp. 86-89, Des Moines, Iowa, 2014.
4. **D. van der Born**, P.H.F. Morshuis, J.J. Smit and A. Girodet, "Evaluation of AC and LI Breakdown Strength of Electrodes with Thick Dielectric Coatings in SF_6 and Dry Air", International Symposium on High Voltage Engineering, pp. 1466-1471, Seoul, Korea, 2013.
5. **D. van der Born**, P.H.F. Morshuis, J.J. Smit and A. Girodet, "The Influence of Thin Dielectric Coatings on LI and AC Breakdown Strength in SF6 and Dry Air", IEEE International Conference on Solid Dielectrics, pp. 287-290, Bologna, Italy, 2013.
6. **D. van der Born**, I.A. Tsekmes, P.H.F. Morshuis, J.J. Smit, T.J. Person and S.J. Sutton, "Evaluation of Apparent Trap-Controlled Mobility and Trap Depth in Polymeric HVDC Mini-Cables", IEEE International Conference on Solid Dielectrics, pp. 242-245, Bologna, Italy, 2013.
7. I.A. Tsekmes, **D. van der Born**, P.H.F. Morshuis, J.J. Smit, T.J. Person and S.J. Sutton, "Space Charge Accumulation in Polymeric DC Mini-Cables", IEEE International Conference on Solid Dielectrics, pp. 452-455, Bologna, Italy, 2013
8. L.A. Chmura, **D. van der Born**, P.H.F. Morshuis and J.J. Smit, "Life curves for new and thermally aged oil-impregnated paper insulation", IEEE Electrical Insulation Conference, pp. 45-48, Ottawa, ON, Canada, 2013

9. **D. van der Born**, I.A. Tsekmes, P.H.F. Morshuis, J.J. Smit, T.J. Person and S.J. Sutton, "Evaluation of Space Charge Accumulation Processes in Small Size Polymeric Cable Models", IEEE Conference on Electrical Insulation and Dielectric Phenomena, pp. 669-672, Montreal, QC, Canada, 2012
10. T.J. Person, S.J. Sutton, **D. van der Born** and P.H.F. Morshuis, "Temperature and Stress Effects on Charge Accumulation and Transport in Extruded Insulation Compositions", Cigré Canada Conference, Montreal, QC, Canada, 2012

Acknowledgements

At the moment of writing these acknowledgements, six years and three months have passed since I joined the former high voltage technology and management group at Delft University of Technology for my master thesis project and subsequently for my PhD project. It has been a very nice experience for me to work in such a magnificent and spacious high voltage laboratory in which it was possible to perform an extensive amount of experiments related to high voltage engineering and materials science. I enjoyed every moment working with the employees, PhD students and master students in the group and the lab. The atmosphere was always welcoming and cooperative. Everybody was eager to help each other with their work and experiments.

First of all, I would like to express my gratitude towards my daily supervisor Peter Morshuis, who always provided support, knowledge and inspiration for me and my fellow students. The creativity of Peter has always been endless, which provided us with the ideas to perform more interesting experiments. Secondly, I would like to deeply thank Johan Smit, my promotor, who supported me greatly in the writing of this thesis and the finishing of my PhD project. He always read the chapters with great care and gave valuable comments on both the writing, the contents and the scientific significance of the thesis.

I would like to thank my fellow PhD student Alex Tsekmes for the great cooperation we had in the production and subsequent testing of the thick nanocomposite coatings. We always had a good laugh while working on our research projects and it was always a pleasure to work with Alex. With respect to the experiments in the lab I would like to express my gratitude towards the lab manager Paul van Nes, to Wim Termorshuizen and to Aad van der Graaf for being there to support my experiments, to build test setups and to produce components for the setups. The three of you always inspired me in the design of experiments and provided a great atmosphere to work in.

With respect to the project I would like to thank GE/Alstom Grid and the SuperGrid Institute for making this research project possible. Moreover, I would like to express my

gratitude towards Alain Girodet, Paul Vinson and Thomas Berteloot who provided support, materials and ideas for this research, especially for the breakdown model.

I would like to thank my fellow roommates and colleagues Lukasz, Muhannad, Qikai, Dhiradj, Ravish, Roy, Thomas, Roman and Huifei who provided a pleasant atmosphere and who were also great sparring partners for research related topics. Furthermore, I am grateful of the opportunity given by my current employer, DNV GL in Arnhem, to successfully finish my PhD thesis.

Finally, I would like to thank Elise for her support and understanding in stressful time periods and for encouraging me to finish this thesis.

Curriculum Vitae

Dennis van der Born was born in Alphen aan den Rijn, the Netherlands. He received his diploma in electrical engineering, track electrical power engineering (MSc), from Delft University of Technology, the Netherlands, in 2011. The topic of his master thesis is the accumulation and depletion of space charge in small size polymeric HVDC cable models. The research mainly consisted of space charge measurements, conduction current measurements and dielectric spectroscopy. Dennis started his PhD research on the application of dielectric coatings in gas insulated switchgear in the department of Electrical Sustainable Energy in September 2011. His research interests mainly consist of electrical breakdown of gaseous and solid dielectrics, failure of gas insulated switchgear and the electrical polarisation behaviour of solid dielectrics. In 2015 Dennis joined DNV GL as a consultant in the field of electromagnetic compatibility, human exposure to electromagnetic fields and insulation coordination of overhead lines and power cables.